Photoelectrochemical and Photocatalytic Water Oxidation using Metal Oxides

By

Joseph E. Yourey

A dissertation submitted in partial fulfillment
Of the requirements for the degree of
Doctor of Philosophy
(Chemistry)
In the University of Michigan
2014

Doctoral Committee
Assistant Professor Bart M. Bartlett, chair
Professor Mark Banaszak Holl
Assistant Professor Stephen Maldonado
Associate Professor Jamie D. Phillips

To my friend Anthony J. Miles

ACKNOWLEDGEMENTS

I'd first like to thank my family for their love and support. Mom and Dad, thank you for encouraging me to continue my education and always expecting the best. Your admirable work ethic has inspired all of your children. I'd also like to thank my siblings; Tony, Will, Becky, Luke, and extended family. I never have as much fun as when I am with all of you.

I would like to thank my research advisor, Bart Bartlett. Man, we made an awesome team. I first chose to work for you because of your incredible drive and dedication to science. But since then, your scientific and personal support has been incredible. The active role you've played in my progress and the opportunities you've provided are some of the most important things you could've done for me throughout my career. Thank you for always looking out for me. You are an incredible mentor, teacher and friend, and I am proud to have worked in your group. I'm excited to see where your lab goes over the many next years.

I would also like to thank my committee; Professors Mark Banaszak Holl, Stephen Maldonado, and Jamie Phillips. Thank you for your dedication to my progress and for providing honest and positive feedback. I'm also grateful to all of the members of the Bartlett lab. I could not have asked for better colleagues. You have all made graduate school so much fun and I will always miss these years. Tanya, I couldn't have done it without you. I will always remember sitting in the dark room praying for something to work when running our LSVs. Emily, the way you conduct yourself in every facet of your life is admirable. Thank you for managing our lab-- I will always be appreciative of that. Doodle, you are still one of the best scientists I have ever met and a wonderful friend, good luck bud. Kayla, it has been a pleasure collaborating with you and even more fun arguing with you. You are a great friend and I really do think we deserve siblings of the year. Ben, you are a great lab mate, friend, and most importantly soccer teammate. I will always respect your ability to think, keep up the hard work and I know you will be

successful. Jimmy and Charles, I am excited to see where you two guys take our lab. Good luck and keep working as hard as you do. I also want to thank the undergraduate students who worked in the lab. Joshy-poo, I could not have asked for someone better to work with. Thank you for all of your hard work and always letting me bash on you. Michael, Bones, Scott T, Elaine, Joel, Scott B, Wes, and Kris; seeing you all in lab always makes my day. Good luck with everything you do. I'd also like to thank the post docs I have worked with, Brendan, Yenting, and Vinod.

Next I'd like to thank Dotie for all of your guidance and devotion. The experience I have gained while working with you is invaluable, and I could not have gotten to where I am today without all of the help you've given me over the years. Thank you for asking me to work with you on the various projects; you made me a better teacher. Roy Wentz, beyond all of the incredible work you have done toward creating cells for my research, you were an even better friend. Thank you for all the times we went fishing, hunting, and chatting in your office. Finally, thank you to the rest of the U of M chemistry staff, all of your hard work is appreciated.

I'd also like to thank particular professors from my past educational experiences. Thank you two both of my undergraduate chemistry research advisors Professor Toby Chapman and Dr. Larry Friedman. Without your help, I would have never found my love for research. Thank you Professor Goldie for letting me serve as a UTU, you taught me the importance of being a great teacher.

Finally I'd like to thank all of the friends I have made throughout graduate school. Cam, Sam, Chun-man, Matt, Nomaan, Lebowski, Renata, and the many others. You all have made my experience here memorable and I will always be grateful for our friendships. Chelsea, you are an incredible woman and I am lucky to be with you. Thank you for your support throughout graduate school, particularly with my writing.

TABLE OF CONTENTS

LIST OF FIGURES

LIST OF TABLES

LIST OF ABBREVIATIONS

AMT	ammonium metatungstate
ALD	atomic layer deposition
CB	conduction band
CO_2	carbon dioxide
CV	cyclic voltammetry
CVD	chemical vapor deposition
e^-/h^+	electron/hole pair
EIS	electrochemical impedance spectroscopy
EDX	energy dispersive X-ray spectroscopy
E_F	Fermi level
E_{fb}	flat band potential
E_g	band gap
EPR	electron paramagnetic resonance spectroscopy
F	Faraday's constant
FTO	fluorinated tin oxide
GO	graphene oxide
HOMO	highest occupied molecular orbital
HTR	hydrothermal
ICP-AES	inductively coupled plasmas atomic emission spectroscopy
IR	infra-red
KB_i	potassium borate
KP_i	potassium phosphate
LSV	linear sweep voltammetry
LUMO	lowest unoccupied molecular orbital
L_p	minority carrier diffusion length
MB	methylene blue
N_D	donor density
NHE	normal hydrogen electrode
ORR	oxygen reduction reaction
PEC	photoelectrochemical
PL	photoluminescence
RGO	reduced graphene oxide
RHE	reversible hydrogen electrode
SEM	scanning electron microscopy
STH	solar to hydrogen
TEM	transmission electron microscopy
U	interatomic repulsion energy
UV	ultraviolet
VB	valence band

Vis	visible
V_{oc}	open-circuit voltage
W_D	depletion width
XPS	X-ray photoelectron spectroscopy
XRD	X-ray diffraction

LIST OF APPENDICES

ABSTRACT

Photoelectrochemical (PEC) water splitting is a sustainable and environmentally friendly method for the conversion of solar energy. However, in order to drive the paradigm shift toward these new sources of energy, this process needs to be cost competitive with current technologies. This thesis focuses on developing oxides capable of using visible light to drive water splitting. The major contribution of the work presented in this thesis focuses on the development of $CuWO_4$ as a visible light absorbing oxide for PEC water splitting.

Various synthetic methods were developed to evaluate the PEC properties of $CuWO_4$ including a sol-gel spin casting and electrochemical deposition method. The experimental results show that $CuWO_4$ is capable of converting visible light ($\lambda > 500$ nm) into photocurrent, driving water oxidation at its surface. $CuWO_4$ is chemically stable over extended periods of illumination, particularly in a borate buffer. $CuWO_4$ electrodes are also selective to performing water oxidation in the presence of competing electron donors such as Cl^-, a common ion in terrestrial water. In order to show water oxidation using only the sun's input, a Z-scheme approach was targeted. On the oxygen evolution side, $CuWO_4$ can photochemically drive water oxidation with the reduction of an electron acceptor in solution.

New phases and composite oxides were synthesized and tested for performing photocatalytic water oxidation in the presence of IO_3^-, an electron acceptor. Bronze phase TiO_2 chemically bonded to reduced graphene oxide is capable of oxidizing water with significantly enhanced rates compared to native TiO_2-bronze. Hydrothermally synthesized $PbCrO_4$ rods loaded with Pt and RuO_2 co-catalysts were also discovered to be competent light absorbing oxides for performing photocatalytic water oxidation under simulated solar irradiation. Finally, a wolframite solid solution $Zn_{1-x}Cu_xWO_4$ (x = 0–1) was synthesized using a Pechini citric-acid assisted sol-gel method. The photocatalytic

properties of this series were tested, and the solid-solution behavior of this series was confirmed using optical spectroscopy and magnetism.

CHAPTER 1

Introduction

1.1 Global Energy Challenge

One of the most important problems facing humanity in the 21st century is building an enduring, sustainable energy economy. Although fossil fuels can supply the estimated global energy demand well into the foreseeable future, this strategy has catastrophic environmental implications due to carbon dioxide (CO_2) emissions, a leading contributor to the greenhouse gas effect.[1] In addition to the environmental costs of burning fossil fuels, it is apparent that many foreign policy decisions are based on delivering a constant supply of oil to the United States.[2] Currently, the United States is nearly 75 % energy independent, however renewables are only responsible for about 9% of our annual energy consumption.[3,4] The technology of renewable energy also has economic benefits such as the reduced health and environmental restoration costs, job creation, and the intellectual property.[5] Even though the cost of renewable energy is dropping, it is still the major limitation for the implementation of these technologies. Continuous technological advances are needed to make renewable energy cost-competitive with fossil fuels and drive the evolution of how we consume energy. Sunlight is an ideal energy source because it is, for all practical purposes, completely sustainable and delivers more energy to earth in one hour than is consumed globally per year.[6] Although solar energy holds great promise, its large scale integration requires the efficient conversion of light into storable, usable forms of energy.

There has been substantial research in conversion technologies for carbon-neutral energy formation such as biomass production from green algae,[7,8] photovoltaic devices for electricity production,[9,10] and water splitting, or the direct photoelectrochemical (PEC) conversion of water into its constituent elements, H_2 and O_2.[11,12] All of these

methods will need to contribute as we push toward an energy independent nation which relies solely on sustainable sources. Water splitting, though, will have the farthest reaching impact for the following reasons. The ability to generate H_2 from water has vast uses in the energy sector beginning with its storage in a liquid fuel to replace gasoline. There is a need for H_2 to use in fuel-cells, resulting in more efficient and decentralized method of electricity production compared to combusting fossil fuels. Finally, H_2 is used in industrial processes including the Haber-Bosch cycle and Fisher-Tropsh synthesis, meaning that there is an immediate method for implementing renewably formed H_2.

Currently, 96% of H_2 produced is derived from fossil fuels, and the United States produces approximately 50 tons H_2/day.[13,14] PEC water splitting is the most direct mechanism in which H_2 can be produced from H_2O and this technology can potentially replace natural gas reformation as our major H_2 source. The reagents, water and sunlight are abundant, as the annual requirement of water to supply the necessary energy in the form is H_2 is only 0.01 % of annual rainfall, or 2×10^{-6} % of the water in the world's oceans.[15] The products, H_2 and O_2, can be produced at separate electrodes, thus alleviating the safety concerns with forming large quantities of reactive gases in the same chamber. PEC water splitting can be carried out at room temperature and most importantly, the inorganic materials used to construct water splitting devices offer a degree of chemical robustness and durability that is difficult to achieve in organic or biological systems. This is crucial as the mechanism for sustainable energy conversion must be cost-efficient.[16] Developing globally viable catalytic materials for this process is the primary focus of my thesis.

Water splitting is an endergonic process requiring an energy input of 237 kJ/mol of water. It is further complicated by the kinetic limitations associated with the four-electron oxidation of water which proceeds through highly corrosive and reactive intermediates.[17] Sunlight can provide the necessary energy input. However, that energy needs to be efficiently collected through absorption processes and transferred into a water molecule to break its chemical bonds. Semiconductors comprise a class of inorganic materials capable of converting solar energy into electrical energy to do work.

1.2 Semiconductor Electrodes for Energy Conversion

Throughout this thesis, I will show how absorbing light in a semiconductor can disrupt equilibrium and drive chemical reactions at the surface of the semiconductor. This provides a mechanism for the direct conversion of solar energy into a usable fuel. Semiconductors possess bands, which describe available energy states in which electrons can conduct through a solid. The bands of a semiconductor form as the number of discrete energy levels that originally comprised the orbitals in a molecule is increased by approximately 10^{23} and translational symmetry is taken into consideration, as dictated by Bloch theory.[18] Band structure is the link that connects structure and bonding to the resulting electronic, magnetic, and optical properties of a solid. A semiconductor has conducting properties between that of an insulator and a conductor, and importantly forms a rectifying junction when placed in an electrolyte solution.

Metal oxides are the class semiconducting materials in which this thesis focuses and therefore will be the context for much of the discussion. In many semiconducting oxides the metal in its highest oxidation state, and therefore the t_{2g} and e_g orbitals are unoccupied. These predominantly metal based orbitals comprise the conduction band (CB) minimum. A conduction band is analogous to the lowest unoccupied molecular orbital (LUMO). The valence band (VB) of an oxide is typically derived from the filled 2p orbitals of the O^{2-} ligand, and is analogous to the highest occupied molecular orbital (HOMO). The band gap (E_g) is the energy gap between the VB and CB. The band structure of a semiconductor is presented in Figure 1.1. The electronic structure of oxides is distinct from most covalent semiconductors, such as Si, and leads to many of the desired properties such as stability toward corrosion and passivation. In d^0 oxides, such as the commonly studied TiO_2, this gap is typically large ($E_g > 3$ eV), and therefore these materials are not intrinsic semiconductors. That means that without an imperfection or added dopant, these materials are in fact insulating. However, the beauty in oxides is that they are never perfect, and these crystallographic defects lead to their semiconducting properties.

For example, oxygen vacancies typically result in some fraction of the metal component in the oxide being reduced. The reduced metal contributes that donor level that exists in a state just below the conduction band minimum. This results in the Fermi

level (E_F) being higher in energy. This donor is typically ionized at room temperature, and the extra electron resides in the conduction band.[19] These extra electrons are predominantly responsible for conducting current, and therefore most oxide semiconductors are considered *n*-type. In an *n*-type semiconductor, electrons are the majority carrier and holes are considered the minority carrier. The donor density (N_D), or extra number of electrons, controls the electrostatics at the electrode/electrolyte interface and is measurable.

The next challenge in understanding the photoelectrochemistry of semiconductors is clarifying what happens when an *n*-type semiconductor comes into contact with an electrolyte solution. The electrode/electrolyte interface is described by the same physical quantities that describe a Schottky barrier.[20] When the electrode is submerged in an electrolyte, the Fermi levels of the two systems must equilibrate. That is, the electrochemical potential of the solution and E_F of the semiconductor become the same on both sides of the interface. This process is described in Figure 1.1.

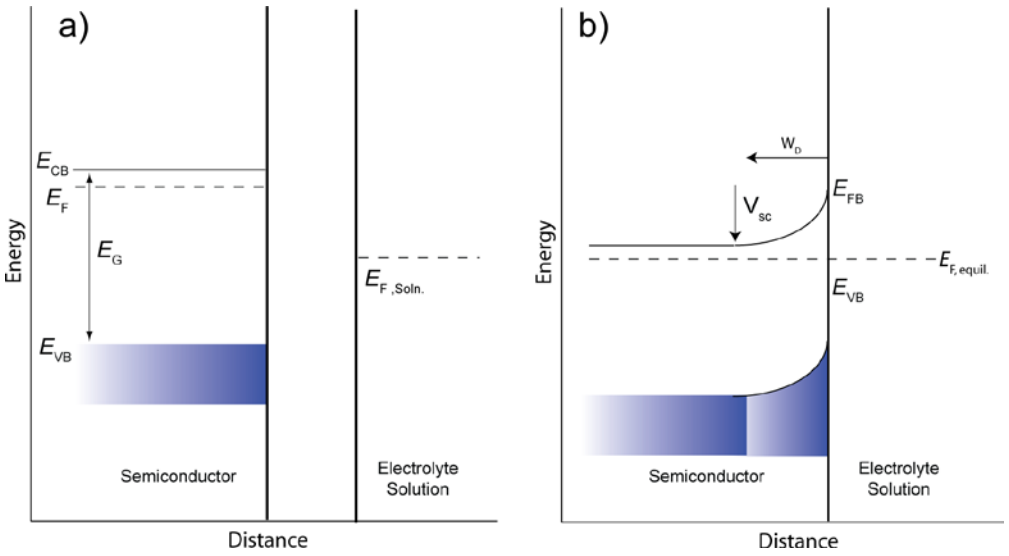

Figure 1.1 The formation of a junction between an n-type semiconductor and an electrolyte solution
The two images depict a) the separated systems and b) after equilibration

E_F of an *n*-type semiconductor is typically at higher potential energy than that of the solution. Therefore, in order to reach equilibrium, electrons from the semiconductor must dump into solution, lowering E_F and disrupting the charge neutrality of the semiconductor. This forms a built in voltage (V_{sc}) of the semiconductor which is

quantified as the difference in electrostatic potential between the surface of the semiconductor and its bulk.[21] After equilibrium is reached, the surface of the *n*-type semiconductor has been depleted of majority carriers and is positively charged with respect to the bulk, forming a depletion region. This charge difference produces an electric field, and the N_D dictates the width of the depletion region (W_D).

The electron/hole pairs (e^-/h^+) that form under illumination can face a certain fate based on how far into the bulk of the semiconductor they are created. Figure 1.2 illustrates certain locations of light absorption in an *n*-type semiconductor.

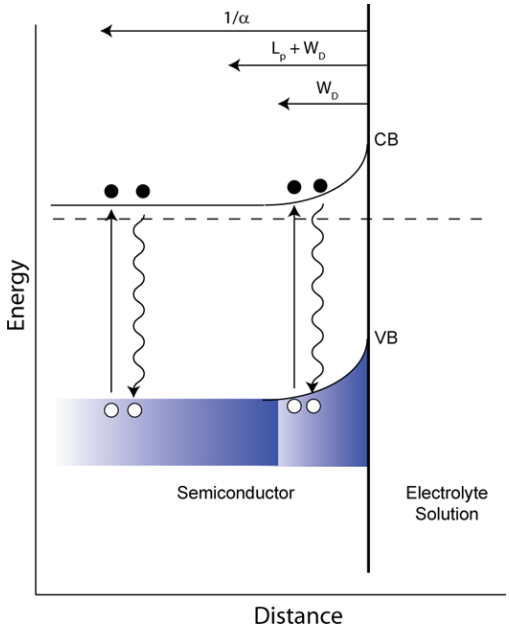

Figure 1.2 Photogeneration of e–/h+ pairs in the bulk and depletion layer of an n-type semiconductor
Created of e–/h+ pairs due to photon absorption in the bulk and depletion region are indicated by the straight line, whereas recombination is expressed as wavy lines.

In Figure 1.2, the *x*-axis represents distance from the semiconductor/electrolyte interface into the bulk of the material. Nearly all e^-/h^+ pairs created into the bulk of the semiconductor (at a distance equal to 1/α) will recombine. In metal oxides, only those e–/h+ pairs that are created within the depletion region (W_D) or very close to the depletion region ($L_p + W_{D)}$ have a chance to remain separated. L_p is the minority carrier diffusion length and this value is highly dependent on the material. L_p can range from very small (1-10 nm) to 100s of nm, though in most cases, L_p of oxides is smaller than that of other inorganic non-oxides due to lower charge carrier mobility.[22]

Under illumination, these e–/h+ pairs create an unequal distribution of charge, disrupting the equilibrium at the semiconductor/electrolyte interface. The formed photovoltage drives a photocurrent. When an *n*-type semiconductor performs water oxidation, h^+ are driven to the surface to oxidize water (equation 1) and e^- are driven through the external circuit via the back contact to the counter electrode, performing proton reduction (equation 2). This results in overall water splitting (equation 3)

$$H_2O + 4h\nu \rightarrow 2H^+ + \tfrac{1}{2}O_2 + 2e^- \qquad E° = 1.23 \text{ V RHE} \qquad 1)$$

$$2H^+ + 2e^- \rightarrow H_2 \qquad E° = 0 \text{ V RHE} \qquad 2)$$

$$H_2O + 4h\nu \rightarrow \tfrac{1}{2}O_2 + H_2 \qquad E° = -1.23 \text{ V RHE} \qquad 3)$$

1.3 Photoelectrochemical Water Splitting

PEC water splitting combines the light harvesting ability of a semiconductor with the chemically active surface of an electrolyzer into a single device, leading to lower overall device costs. Second, a PEC cell does not have to operate at such high overpotentials, providing a higher upper limit of energy conversion efficiencies. Currently, many devices at the research level require the input of electrical energy to drive water splitting reaction at an appreciable rate; however this results in a loss of efficiency. The majority of this thesis focuses on PEC water splitting, but of course the eventual goal is to drive water splitting using only the sun's energy. Many methods are under pursuit to form devices capable of water splitting and these approaches will be put into context in section 1.5 with specific focus on one approach I have worked on.

The first example of PEC water splitting was by Fujishima and Honda using TiO_2 in 1972.[23] In their experiments, a single crystal of rutile-phase TiO_2 generated a photovoltage of approximately 0.5 V, was 0.1 % efficient at an applied bias and generated approximately 0.1 mA/cm^2 of photocurrent. A photoanode must have a band gap and band edge positions that are suitable for driving water oxidation. The fundamental criteria that TiO_2 meets are that it possesses suitable electronic properties to efficiently collect the created charge carriers, and its O(2p) valence band lies at electrochemical potentials sufficiently more positive than O_2/H_2O (1.23 V RHE). A final criterion met by TiO_2, and most oxides, is that they are stable against oxidative decomposition under illumination. Semiconducting non-oxides such as CdS and GaP suffer oxidative decomposition mechanisms during the harsh conditions of water oxidation. This mechanism typically proceeds via a valence band hole that preferentially

oxidizes the anion (S^{2-}, P^{3-}) rather than water.[24] For that reason, all signs point to oxides as viable materials capable of the long term stability required for practical use.[25]

Although metal oxides are the most stable materials for this reaction, traditional metal oxides have valence band edges that are much too low in energy with respect to the water oxidation potential (1.23 V RHE), resulting in an enormous overpotential (> 1.7 V). Consequently, metal oxides with valence bands comprised predominantly of O (2p) orbitals have band gaps that are only responsive to UV light (<400nm). This is one criterion for PEC water splitting that TiO_2, and most metal oxides, do not meet. Many large band gap semiconductors have been discovered for overall water splitting,[26] and some reach quantum efficiencies greater than 50% when illuminated with single wavelength length of supra band-gap energy.[27] However, when illuminated with solar energy, these wide band gap materials suffer from inherently low efficiency because the sun's output in the UV portion of the solar spectrum is minimal (Figure 1.3) In order to become viable and meet the energy demand, a water splitting system should be near 10 % solar to hydrogen (STH) efficient, stable over an extended period of time, and more importantly stay cost-competitive with fossil fuels.[28,29] Figure 1.3 shows that as the band gap of the light absorbing oxide decreases, the theoretical STH efficiency increases.

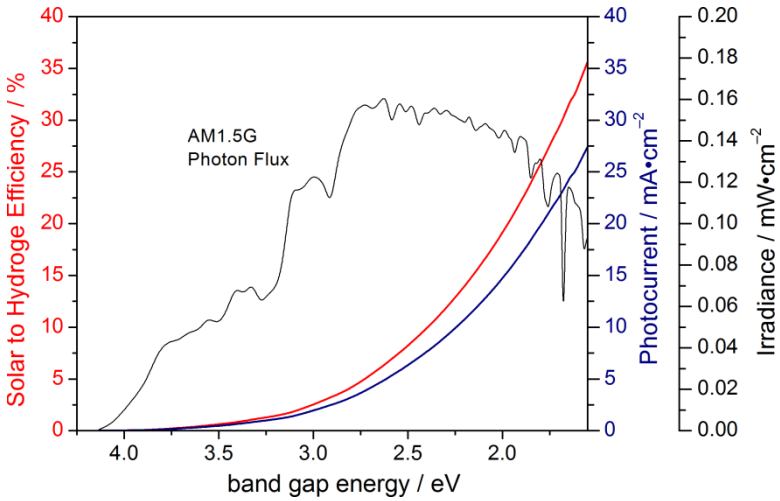

Figure 1.3 STH efficiency and photocurrent maximum based on band gap and AM1.5G illumination
This figure presents the maximum STH efficiency (red), the maximum photocurrent capable of being generated (blue) and the solar flux (black) in the visible portion of the solar spectrum.

The solar output in the visible part of the solar spectrum is significantly greater than the UV, 47% *vs.* 4%. As this reaction relies on absorbing light, the greater number of photons absorbed the higher the theoretical efficiency of a system. The target goal of 10% STH efficiency also necessitates the use of a material that absorbs in the visible portion of the solar spectrum. Though Figure 1.3 assumes perfect light absorption, quantitative conversion and Faradaic efficiency, all of which are unlikely conditions, the message remains the same: only by employing oxides that absorb visible light can high STH efficiency be obtained. The development of low band-gap oxide photoanodes is the primary focus of my thesis.

1.4 Approaches to Forming Visible-Light Absorbing Oxides

Over the past forty years, there have been many approaches toward increasing visible light absorption in metal oxides. The classic and well-studied method is through doping into wide band gap semiconductors. Metal cations are substituted into large band gap semiconductors resulting in colored oxides. These materials have been stringently surveyed as both photoelectrodes and photocatalysts, and the formation of these colored domains is the result of defect structure in the catalyst.[30] These states allow for new absorption processes that take place in the visible portion of the solar spectrum. Doped oxides are often successful as photocatalysts for the degradation of organic dye, mostly because these trap states are capable of facile electron transfer to organic species in solution.[31] However, the significant amount of doping needed for light absorption becomes detrimental to sustaining photocurrent in an electrode material, and in many cases the native oxide performs better as a photoanode. The uncompensated aliovalent doping is detrimental to the generated photocurrent because the defects lead to reduced crystallinity and larger effective masses of charge carriers, thus increased rates of carrier recombination. Recently, co-alloying for charge compensation has proven successful.[32,33] Both a cation and anion are substituted into the crystal and the anion compensates the charge mismatch of the metal dopant, resulting in greater metal solubility without increased defect structure.

Regardless, doping does not result in a band shift, but rather the formation of new absorption pathways in the visible portion of the solar spectrum.[34] One additional drawback of these new absorption events is that their resulting absorptivity coefficients

are low, meaning that even though visible light absorption is taking place, it is inefficient. One method to circumvent the low absorption associated with doping is through the formation of solid solutions.

A solid solution is a homogenous crystalline structure in which a significant amount of one or more types of atoms may be substituted for the original atoms without changing the structure. A solid solution allows one to tailor the dopant atom concentration and control the absorption properties of the resulting solid. Additionally, high amounts of molar substitution in a solid solution may also improve the conduction properties of a material without compromising the host's structural integrity. One example of a quaternary solid solution is the wurtzite phase $(Zn_{1-x}Ga_x)(O_{1-x}N_x)$. By controlling the mole ratio of ZnO to GaN (which are both large band gap semiconductors), a significant decrease is band gap is realized.[35,36] One conclusion of this solid solution was that the valence band is no longer predominantly O(2p) or N(2p) in character, rather a hybridized band forms between the metal d orbitals and anion p orbitals, raising the valence band maximum in energy. In this thesis, a solid-solution was targeted to evaluate the synergy of combining light absorption with a suitable electronic structure. The results of this work are presented in Chapter 5.

A third method to form visible light absorbing oxides is to form ternary phases (ABO_x) whose valence band maximum is not predominantly comprised of O 2p orbitals. In this case, the valence band will often consist of metal based orbitals hybridized with O 2p. Also, oxy-nitrides, such as TaON and $LaTiO_2N$, are targeted ternary phases as they also do not possess strictly O (2p) based valence bands, but rather N (2p) and O (2p) states form the valence band.[37,38] The properly chosen ternary phase has the added effect of possessing a higher energy valence band, all without adding states below the conduction band minimum. This concept is described in Figure 1.4

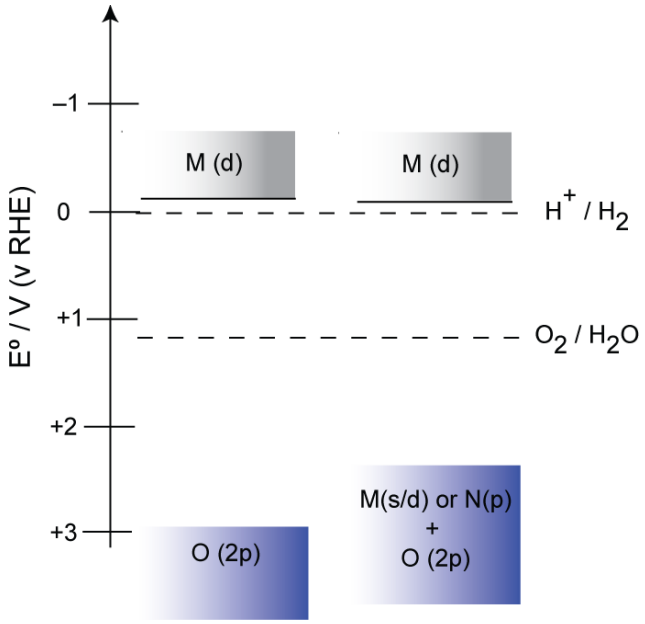

Figure 1.4 Band structure of oxide semiconductor comparing purely O (2p) to M (s/d) + O(2p) based valence band

In Figure 1.4, the metal based s or d orbitals hybridize with O(2p) orbitals, raising the overall energy of the valence band. This is a more desirable method for shrinking the band gap compared to lowering the conduction band energy. Most oxides possess a conduction band edge that sits close to or below the H^+/H_2 redox couple, and lowering the conduction band minimum shifts the open-circuit potential of the cell (V_{oc}) more positive with respect to H^+/H_2. As V_{oc} becomes more positive, the required input of electrical voltage required to drive water splitting will be greater.

The most important requirement in forming a ternary phase semiconductor is that the M(s/d) orbitals must be sufficiently electronegative to effectively hybridize with the oxygen based orbitals in the band structure. This prevents the formation of a constricted, metal based orbital between the O(2p) orbital and the conduction band. Most ternary phase semiconducting oxides are derived from oxyanions (BO_x^{n-}) in which the empty valence orbitals of the d^0/d^{10} metal component (B) form the conduction band. The valence band is typically formed from filled, or nearly filled, s or d orbitals of the metal cation (A^{n+}) component of the ternary phase. One example of this type that shows promise as a photoanode for PEC water oxidation is $BiVO_4$. The Bi(6s) orbitals dominate the valence band maximum, forming a 2.5 eV band gap material.[39]

Ternary oxides and oxynitrides are becoming an attractive avenue for research directed toward forming new visible light absorbing phases for PEC water splitting. Some other examples are the main group tungstates (Bi_2WO_6, $SnWO_4$)[40,41], stannate phases such as Cd_2SnO_4,[42] bismuth containing phases $BiCu_2VO_6$,[43] $CuBi_2O_4$,[44] and many new ternary phases which are being targeted through the use of combinatorial methods.[45–47] This thesis focuses on the 1st-row transition metal tungstates (AWO_x), inspired by the many advantageous PEC properties associated with WO_3 as a semiconductor for PEC water oxidation. The synthesis, characterization, and photoelectrochemistry of CuWO4 are the focus of Chapter 2 and 3.

1.5 Methods for Overall Water Splitting

With forty years of research and many milestones, one thing has become apparent: no single material will perform all of the necessary duties to efficiently and cost-effectively split water into its constituent elements. Much of this thesis focuses on PEC water splitting, where both solar and electrical energy are used to generate water splitting photocurrents. Other research focuses on performing water splitting by adding voltages across multiple light absorbers. These methods include *p*-*n* photolysis, where an *n*-type photoanode and *p*-type photocathode are circuited in series to perform unassisted water splitting. Most of the research in this field uses non-oxide materials. These devices initially show high conversion efficiencies, but suffer from instability over long periods of illumination.[48] Other methods form buried junctions where a photovoltaic material delivers the extra voltage to the photoanode to perform water splitting.[49] Finally, photovoltaic panels are being coated with a protecting oxide layers and combined to electrocatalysts.[50] In most cases, it seems that oxide-based photoanodes produced by cost-effective methods are still necessary to perform water oxidation robustly and economically viable. This thesis presents one method toward the end of water splitting without the need for an applied bias. It is a Z-scheme approach that is discussed further in Chapter 4. This method does not use two light absorbers in series to generate > 1.23 eV, but rather separates the two half reactions of water splitting both spatially and energetically, akin to natural photosynthesis. The results presented are on photoelectrodes, but the Z-scheme approach has also shown promise in the field of photocatalysis using powders suspended in solution. Within this thesis, the results toward

water splitting at no applied bias are all for one half of water splitting, accomplishing water oxidation while reducing an electron acceptor in solution.

1.6 Photocatalytic and Photoelectrochemical Water Oxidation

Powdered oxide photocatalysts are encouraging because the costs associated with large scale production of H_2 by this method is minimal compared to water splitting using paneled devices.[29] This fact arises from the comparative simplicity of the system; in powder photocatalysis, the catalyst material is simply stirred into the solution to create a suspension and then illuminated. Many synthesis methods for forming powdered photocatalysts are easily scalable and are considerably cheaper than the current methods for forming high quality thin-film devices. Also, when targeting new phases there are many synthesis methods in which a scientist can easily control properties such as particle size, morphology and crystallinity.

However, when developing new phases for use in photocatalytic or PEC water splitting, full characterization is imperative to understanding the advantages or limitations associated with a new material. With an electrode, it is possible to determine the relative energy of its band positions experimentally, rather than relying solely on calculations. By performing photoelectrochemistry, one can connect many of the experimental observations to the fundamental properties of the oxide, providing a roadmap for improvements. And, these synthetic or electrode improvements can be correlated to the descriptions of a semiconductor discussed earlier. This has been crucial for a material like hematite, where doping and morphology control led to a significant enhancement of its PEC performance, revitalizing this material as a photoanode. Such investigations are difficult on powders alone, and lead to disparity in presenting results across the field.

The information gleaned by performing PEC measurements on new materials is easily translatable to many other researchers in the field. PEC experiments are more easily benchmarked and experimental parameters can be standardized.[51] This is important for understanding gains, particularly with respect to visible light absorption. For example, if one filters all UV light from an experiment, then shows that visible light absorption results in catalytic turnover in this doped oxide using > 400 nm light, the result is meaningless for understanding how efficient that entire material is under simulated solar irradiation. Electrodes also allow one to more easily test certain hypotheses about a

particular material. If the goal is to increase efficiency under visible light, measuring the photocurrent action spectrum directly provides this information. These diagnostic techniques provide insight into the PEC material properties.

Using a photoelectrode, other important parameters such as stability over long periods of use and selectivity for performing water splitting are measurable and important to report. As stated, oxides seem to be the only materials capable of performing long-term photolysis of water when in direct contact with the electrolyte solution. However, this must be proven and long-term PEC stability experiments (controlled potential coulometry) provide this information directly. Also during long-term illumination experiments, the selectivity and stoichiometry of the chemical reaction can be easily monitored and compared. Along with stability, the selectivity to perform water oxidation has been assumed in many early studies on new photoactive materials. However, this isn't always true, and current research efforts also focus on ensuring that an electrode is selective when performing water oxidation. For example, competing anion oxidation (such as Cl^- to Cl_2) is one possible competing oxidation pathway and though forming Cl_2 has its utilities, it is not water splitting and therefore should be reported as such. This thesis compares the selectivity of our electrodes to the current state of art to ensure that the charge passed during a PEC experiment is in fact going to perform water oxidation.

Finally, this thesis focuses on various synthesis methods to create electrodes. One challenge of performing PEC experiments on polycrystalline oxide electrodes is ensuring that the mechanical structure of the electrode is sound. Though challenging, forming competent polycrystalline oxide photoelectrodes has become a major part of the effort to form cost-effective and scalable methods to form thin-films devices. Throughout this thesis, I will present synthetic methods which were chosen due to the resulting morphology, thickness, and purity of the formed electrode. Synthesis methods can also allow one to mitigate the disadvantageous properties of a newly developed material. For example, certain morphologies allow for maximum light absorption while maintaining short distance for charge carriers to travel, reducing the rates of recombination.[52,53] This helps alleviate the charge-transport limitations associated with oxides. Once a material is discovered and shows promising fundamental properties, controlling the physical parameters of the electrode can lead to significant gains in performance.

1.7 Scope of this Thesis

This thesis is structured on the synthesis and PEC characterization of visible light absorbing ternary oxides for water oxidation. Chapter 2 presents the various synthesis methods and physical and electrochemical characterization of $CuWO_4$, a material I have spent the majority of my thesis working on. Chapter 3 then presents PEC experiments conducted on $CuWO_4$ to highlight its advantages as a photoanode and compare the results we attain using this material to its congener WO_3. Specifically, this chapter focuses on the long-term stability of $CuWO_4$ as a photoanode and measuring its efficiencies for water oxidation. Chapter 4 focuses on using $CuWO_4$:WO_3 composite electrodes in a Z-scheme method to perform water oxidation with concomitant $[Fe(CN)_6]^{3-}$ at no applied bias. Chapter 5 focuses on $Zn_{1-x}Cu_xWO_4$, a transition metal tungstate solid solution. This chapter presents the optical and magnetic characterization of $Zn_{1-x}Cu_xWO_4$ as well as photocatalytic studies using $Zn_{1-x}Cu_xWO_4$ powders and PEC measurements on $Zn_{1-x}Cu_xWO_4$ photoanodes. Finally, Chapter 6 presents collaborative work using TiO_2-bronze as a composite photocatalyst that shows high rates of water oxidation with IO_3^- reduction when combined with reduced graphene oxide. Chapter 6 also presents the motivation, synthesis, and photocatalytic water oxidation experiments on $PbCrO_4$ rods. Following the thesis, there are appendices containing supporting data pertinent to each chapter. They are separated by chapter and appendix A-E is each for Chapter 2-6, respectively. The appendix figures are referenced throughout each chapter.

1.8 References

1. Wigley, T. M.; Richels, R.; Edmonds, J. A. Economic and Environmental Choices in the Stabilization of Atmospheric CO_2 concentrations *Nature*, **1996**, *379*, 240-243
2. Powering American's Defense: Energy and the Risks to National Security, **2009**
3. Monthly Energy Review, Energy Information Administration, March **2012**
4. Renewables 2013 Global Status Report. Renewable Energy Policy for the 21st Century, REN 21, **2013**
5. Dollars from Sense: The Economic Benefits of Renewable Energy, produced for the U.S. Department of Energy by the National Renewable Energy Laboratory, **1997**
6. Lewis, N. S.; Nocera, D. G. Powering the Planet, Chemical Challenges in Solar Utilization *Proc. Natl. Acad. Sci. USA* **2006**, *103*, 15729-15735
7. Demirbas, M. F. Biofuels from Algae for Sustainable Development *Applied Energy* **2011**, *88*, 3473-3480

8. Koller, M.; Salerno, A.; Tuffner, P.; Koinigg, M.; Boechzelt, H.; Schober, S.; Schnitzer, H.; Mittelbach, M.; Barunegg, G. Efficient Implementation of Micro-Algae for Sustainable Environmental and Economic Development *Current Topics in Biotechnology* **2011**, 6, 71-82
9. El Charr, L.; Lamont, L. A.; El Zein, N. Review of Photovoltaic Technologies *Renewable and Sustainable Rev.* **2011**, *15*, 2165-2175
10. Tian, B.; Kempa, T. J.; Lieber, C. M. Single Nanowire Photovoltaics *Chem. Soc. Rev.* **2009**, *38*, 16-24
11. Li, Z.; Luo, W.; Zhang, M.; Feng, J.; Zou, Z. Photoelectrochemical Cells for Solar Hydrogen Production: Current State of Promising Photoelectrodes, Methods to Improve their Properties, and Outlook *Energy Environ. Sci.*, **2013**, *6*, 347-370
12. Kudo, A.; Miseki, Y. Heterogeneous Photocatalyst Materials for Water Splitting *Chem. Soc. Rev.* **2009**, *38*, 253-278
13. Hydrogen and Fuel Cells: The US Market Report, The National Hydrogen Association, **2010**
14. Hydrogen, IHS report, **2010**
15. Van de Krol, R.; Grätzel, M. *Photoelectrochemical Hydrogen Production*, Springer: New York, 2011
16. James, B. D.; Baum, G. N.; Perez, J.; Baum, K. N. Technoeconomic Analysis of Photoelectrochemical (PEC) Hydrogen Production, DOE Final Report, **2009**
17. Turner, J. A. A Realizable Renewable Energy Future *Science*, **1999**, *285*, 697-689
18. Omar, M. A. *Elementary Solid State Physics: Principles and Applications*; Addison-Wesley: New York, 1993; p 179-183
19. Dmochowski, J. E. Donors in Semiconductors–Are they understood in Electronic Era? *J. Phys.: Conference Series* **2007**, *79*, 012010-14
20. Gerischer, H. Electrochemical Photo and Solar Cells Principles and Some Experiments *J. Electroanal. Chem. And Interfacial Chem.*, **1975**, *58*, 263-274
21. Bisquert, J.; Cendula, P.; Bertoluzzi, L.; Gimenez, S. Energy Diagram of a Semiconductor/Electrolyte Junctions *J. Phys. Chem. Lett.*, **2014**, *5*, 19840-19848
22. Memming, R. Electrochemical Decomposition of Semiconductors. In *Semiconductor Electrochemistry*, Wiley-VCH Verlag GmbH: 2007; pp. 16-18, p 373
23. Fujishima, A.; Honda, K. Electrochemical Photolysis of Water at a Semiconductor Electrode *Nature* **1972**, *238*, 37-38
24. Gerisher, M.; Mindt. W. The Mechanisms of the Decomposition of Semiconductors by Electrochemical Oxidation and Reduction *Electrochimica Acta*, **1968**, *13*, 1329-1341
25. D. B. Alexander, P. J. Kulesza, I. Rutkowska, R. Solarska, J. Augustynski, *J. Mater. Chem.* 2008, **18**, 2298
26. Osterloh, F. E. Inorganic Materials as Catalysts for Photochemical Splitting of Water *Chem. Mater.* **2008**, *20*, 35-54
27. Kato, H.; Asakura, K.; Kudo, A. Highly Efficient Water Splitting into H2 and O2 over Lanthanum-Doped NaTaO3 Photocatalysts with High Crystallinity and Surface Nanostructure *J. Am. Chem. Soc.* **2003**, *125*, 3082-3089

28. Bard, A. J.; Fox, M. A. Artificial Photosynthesis: Solar Splitting of Water to Hydrogen and Oxygen *Acc. Chem. Res.* **1995**, *28*, 141-145
29. Pinaud, B. A.; Benck, J. D.; Seitz, L. C.; Forman, A. J.; Chen, Z.; Deutsch, T. G.; James, B. D.; Baum, K. N.; Baum, G. N.; Ardo, S.; Wang, H.; Miller, E.; Jaramillo, T. F. Technical and Economic Feasibility of Centralized Facilities for Solar Hydrogen Production Via Photocatalysis and Photoelectrochemistry. *Energy Environ. Sci.* **2013**, *6*, 1983-2002.
30. Martyanov, I. N.; Uma, S.; Rodrigues, S.; Klabunde, K. J. Structural Defects Cause TiO_2-Based Photocatalysts to be Active in Visible Light *Chem. Commun.* **2004**, 2476-2477
31. Etacheri, V.; Seery, M. K.; Hinder, S. J.; Pillai, S. C. Highly Visible Light Active $TiO_{2-x}N_x$ heterojunction Photocatalysts *Chem. Mater.* **2010**, *22*, 3843-3853
32. Yin, W.-J.; Tang, J.; Wei, S.-H.; Al-Jassim, M. M.; Turner, J.; Yan, Y. Band Structure Engineering of Semiconductors for Enhanced Photoelectrochemical Water Splitting: The case of TiO_2 *Phys. Rev. B* **2010**, *82*, 045106-6
33. Breault, T. M.; Bartlett, B. M.; Lowering the Band Gap of Anatase-Structured TiO2 by Coalloying with Nb and N: Electronic Structure and Photocatalytic Degradation of Methylene Blue Dye *J. Phys. Chem. C* **2012**, *116*, 5986-5994
34. Choi, W.; Termin, A.; Hoffman, M. R. The Role of Metal Ion Dopants in Quantum-Sized TiO2: Correlation between Photoreactivity and Charge Carrier Recombination Dynamics *J. Phys. Chem* . **1994**, *98*, 13669-13679
35. Maeda, K.; Takata, T.; Hara, M.; Saito, N.; Inoue, Y.; Kobayashi, H.; Domen, K. GaN:ZnO Solution as a Photocatalyst for Visible-Light-Driven Overall Water Splitting *J. Am. Chem. Soc.* **2005**, *127*, 8286-8287
36. Maeda, K.; Teramura, K.; Lu, D.; Takata, T.; Saito, N.; Inoue, Y.; Domen, K. Characterization of Rh-Cr Mixed-Oxide Nanoparticles Dispersed on $(Ga_{1-x}Zn_x)(N_{1-x}O_x)$ as a Cocatalyst for Visible-Light-Driven Overall Water Splitting *Chem. Mater.* **2006**, *110*, 13753-13758
37. Fang, C. M.; Orhan, E.; de Wijs, G. A.; Hintzen, H. T.; de Groot, R. A.; Marchand, R.; Saillard, J.-Y.; de With, G. The Electron Structure of Tantalum (Oxy)Nitrides TaON and Ta3N5 *J. Mater. Chem. A* **2001**, *11*, 1248-1252
38. Zhang, F.; Yamakata, A.; Maeda, K.; Moriya, Y.; Takata, T.; Kubota, J.; Teshima, K.; Oishi, S.; Domen, K. Cobalt-Modified Porous Single-Crystalline LaTiO2N for Highly Efficient Water Oxidation under Visible Light *J. Am. Chem. Soc.* **2012**, *134*, 8348-8351
39. Walsh, A.; Yan, Y.; Huda, M. N.; Al-Jassim, M. M.; Wei, S.-H. Band Edge Electron Structure of $BiVO_4$: Elucidating the Role of the Bi s and V d Orbitals *Chem. Mater.* **2009**, *21*, 547-551
40. Visible-Light-Induced Degradation of Rhodamine B by Nanosized Bi_2WO_6 *J. Phys. Chem. C* **2005**, *109*, 22432-22439
41. Photophysical, Photoelectrochemical, and Photocatalytic Properties of Novel SnWO4 Oxide Semiconductors with Narrow Band Gaps *J. Phys. Chem. C* **2009**, *113*, 10647-10653

42. Despande, A.; Kelkar, S.; Rayalu, S.; Ogale, S. Orthorhombic/cubic Cd_2SnO_4 Nanojunctions: Enhancing Solar Water Splitting Efficiency by the Suppression of Charge Recombination *J. Mater. Chem. A* **2014**, *2*, 492-499
43. Bismuth-Copper Vanadate $BiCu_2VO_6$ as a novel photocatalyst for Efficient Visible-Light-Driven Oxygen Evolution *ChemPhysChem* **2005**, *6*, 2499-2502
44. Low Temperature Grown $CuBi_2O_4$ with Flower Morphology and its Composite with CuO Nanosheets for Photoelectrochemical Water Splitting *J. Mater. Chem. A* **2014**, *2*, 3661-3668
45. Wu, Y.; Laxic, P.; Hautler, G.; Persson, K.; Ceder, G. First Principles High Throughput Screening of Oxynitrides for Water-Splitting Photocatalysts *Energy Environ. Sci.* **2013**, *6*, 157-168
46. Kusama, H.; Wang, N.; Miseki, Y.; Sayama, K. Combinatorial Search for Iron/Titanium-Based Ternary Oxides with a Visible-Light Response *J. Combi. Chem.* **2010**, *12*, 356-362
47. Jiang, C.; Wang, R.; Parkinson, B. A. Combinatorial Approach to Improve Photoelectrodes Based on $BiVO_4$ *ACS Combi. Sci.* **2013**, *15*, 639-645
48. Khaselev, O.; Turner, J. A. A Monolithic Photovoltaic-Photoelectrochemical Device for Hydrogen Production via Water Splitting *Science* **1998**, *280*, 425-427
49. Abdi, F. F.; Han, L.; Smets, A. H. M.; Zeman, M.; Dam, B.; van de Krol, R. Efficient Solar Water Splitting by Enhanced Charge Separation in a Bismuth Vanadate-Silicon Tandem Photoelectrode *Nat. Commun.* **2013**, *4*, 2195
50. Reece, S. Y.; Hamel, J. A.; Sung, K.; Jarvi, T. D.; Esswein, A. J.; Pijpers, J. J. H.; Nocera, D. G. Wireless Solar Water Splitting Using Silicon-Based Semiconductors and Earth-Abundant Catalysts *Science* **2011**, *334*, 645-648
51. Chen, Z.; Dinh, H. N.; Miller, E. Photoelectrochemical Water Splitting: Standards, Experimental Methods, and Protocols, Springer, New York: **2013**
52. Zhang, K.; Shi, X.; Kim, J. K.; Lee, J. S.; Park, J. H.; Inverse Opal Structure Structured α-Fe2O3 on Graphene Thin-Films: Enhanced Photo-Assisted Water Splitting *Nanoscale*, **2013**, *5*, 1939-1944
53. Kelzenberg, M. D.; Boettcher, S. W.; Petykiewicz, J. A.; Turner-Evans, D. B.; Putnam, M. C.; Warren, E. L.; Spurgeon, J. M.; Briggs, R. M.; Lewis, N. S.; Atwater, H. A. Enhanced Absorption and Carrier Collected in Si Wire Arrays for Photovoltaic Applications *Nat. Mater.* **2010**, *9*, 239-244

CHAPTER 2

Synthesis, Physical Characterization and Electronic Structure Determination of $CuWO_4$

Portions of this chapter have been published:
Yourey, J. E.; Bartlett, B. M. *J. Mater. Chem.* **2011**, *21*, 7651-7660. Reproduced by permission of the Royal Society of Chemistry.
http://pubs.rsc.org/en/Content/ArticleLanding/2011/JM/C1JM11259G

Reproduced with permission from Yourey, J. E.; Pyper, K, J.; Kurtz, J. B.; Bartlett, B. M. *J. Phys. Chem. C.* **2013**, *117*, 8708-8718. Copyright 2013 American Chemical Society
http://pubs.acs.org/doi/abs/10.1021/jp402048b

2.1 Introduction

The research goal of this thesis was to design new oxide materials which could serve as photoactive electrodes for the oxidation of water. When surveying the literature, WO_3 was identified as a promising standalone material and therefore served as a starting point for targeting new candidates. WO_3 is a high performing photoanode capable of generating significant photocurrents at an applied bias when illuminated. WO_3 possesses a relatively high Hall e^- mobility (10 $cm^2\ V^{-1}\ s^{-1}$)[1] and long minority-carrier diffusion length (0.3 – 4.2 μm)[2,3] compared to other oxides such as TiO_2 and α-Fe_2O_3. One explanation of these advantageous properties is the contribution of the diffuse W (5d) orbitals that make up the conduction band in WO_3. Therefore, research focused on targeting new materials that contained W in a 6+ oxidation state with the intention of these empty states serving as the conduction band. There are numerous synthetic methods for forming competent photoanodes of WO_3 on transparent conducting substrates, and these served as a starting point for our syntheses. The main limitation of WO_3 is its large band gap, which results in only a fraction of visible light absorption and a low theoretical

solar to hydrogen (STH) efficiency (7%), described in Figure 1.3. WO_3 begins to absorb at approximately 475 nm (E_g = 2.75 eV), which is just into the blue part of the solar spectrum.[4]

There are particular strategies for increasing visible light absorption in wide band gap semiconductors such as WO_3. Metal and/or non-metal doping increases visible light absorption, but in most cases these absorption events are due to defects which result in low absorptivity coefficients and high charge carrier recombination.* Rather than use a doping approach, ternary tungstate materials were targeted. The hypothesis was that 1st row transition metal tungstates (AW_xO_y) would show increased visible light absorption as a result of charge transfer events. Ideally, absorption in these semiconducting oxides would result in electron transfer from a predominantly cation-based valence band to a higher energy W (5d) conduction bands. This electronic transition is a charge transfer and therefore should result in collectable carriers.

There is evidence of tungstate materials that show photocatalytic activity under illumination. Many of these materials are made from d^{10}/d^0 A^{n+} cations, which results in wide band gap semiconductors. Among them, $PbWO_4$ particles have been shown to decompose H_2O photocatalytically under UV illumination when properly loaded with a co-catalyst.[5] Bi_2WO_6 has also received attention as a photocatalyst for H_2 formation and organic dye degradation, and more recently as a photoanode for the oxidation of water.[6–9] Finally, $ZnWO_4$, which crystallizes into the wolframite crystal structure and possesses a high energy conduction band (-0.4 V RHE), has been shown to be an active catalyst for organic dye degradation.[10–12] When evaluating the wide band gap tungstates, the high photocatalytic activity is likely due to the high energy conduction band (< 0 V RHE). These materials are energetically capable of forming the super oxide radical under illumination which subsequently degrades the organic species in solution.

The 1st row transition metal tungstates AWO_4 (A = Mn, Fe, Co, Ni, Cu, Zn) all crystallize into the monoclinic wolframite structure. $CuWO_4$ is as an exception since Jahn-Teller distortion causes a transition from monoclinic to triclinic crystal symmetry. These tungstates (except for $ZnWO_4$) all absorb in the visible part of the solar spectrum as seen in Figure 2.1.

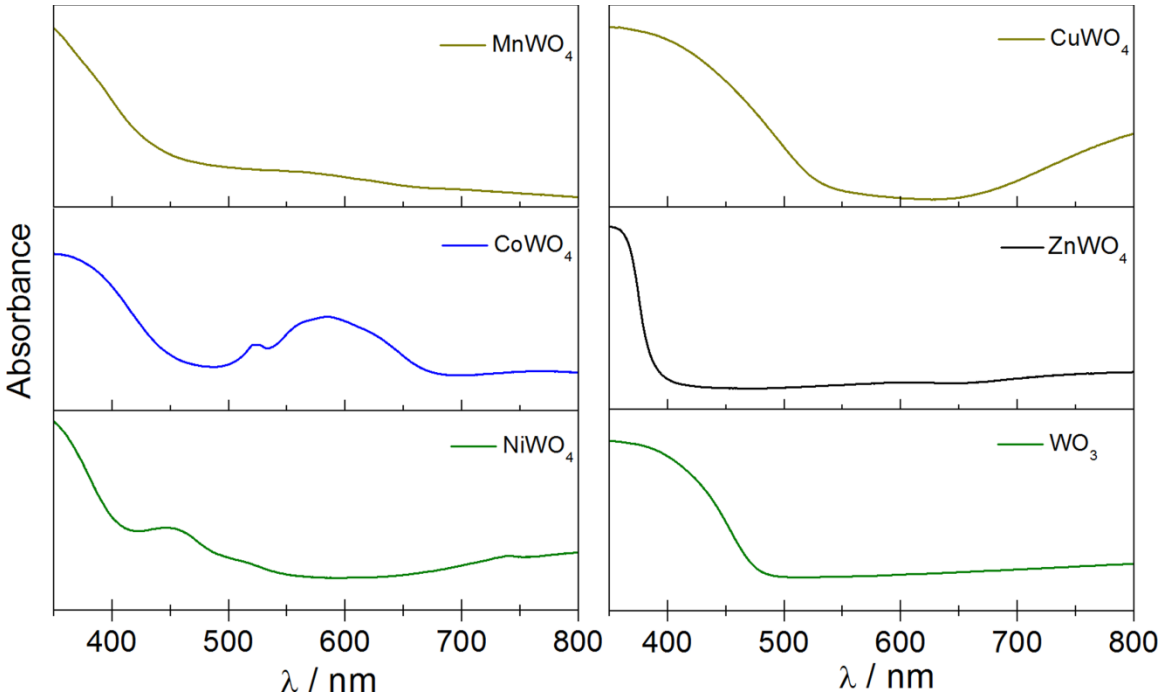

Figure 2.1 Absorption Spectra of AWO_4 and WO_3 powders

More importantly, the presented spectra show the charge transfer absorptions (the onset is seen at approximately 450, 475, 425, and 550 nm for Mn, Co, Ni, and $CuWO_4$, respectively) in addition to the typical *d-d* transitions commonly observed in the metal salts. The wolframite structure is made up of distorted octahedrally coordinated A^{2+} and W^{6+} cations. The transition metal octahedra are bridged through corner sharing oxygen atoms. Each individual metal's octahedra is edge sharing and translates along the *c*-axis (Figure 2.2).

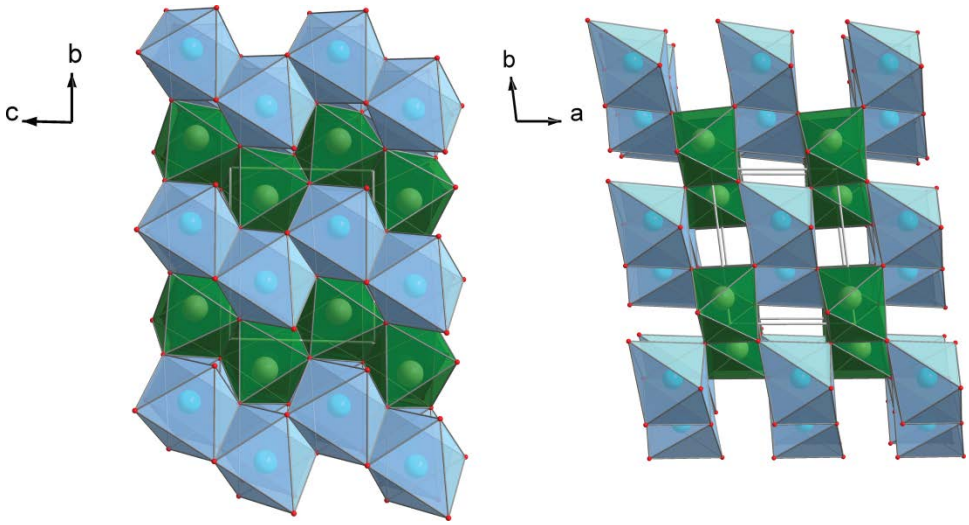

Figure 2.2 Crystal Structure of $CuWO_4$

The Cu and W octahedra are colored in green and blue, respectively
Left: The structure looking down *a* showing the parallel running zig-zag chains of edge sharing octahedra for each metal
Right: The structure looking down *c* showing the corner shared W and Cu octahedra

There are examples of the visible light absorbing tungstate nanoparticles being used for the photocatalytic degradation of organic dyes, with $CuWO_4$ most often showing the highest rates of activity when using visible light (again, $ZnWO_4$ is more active under UV illumination).[13,14] $NiWO_4$ and $CoWO_4$ have been used in electrocatalytic H^+ reduction and H_2O oxidation, respectively; however the reports show that $NiWO_4$ and $CoWO_4$ are not successful photocatalysts.[15,16] $MnWO_4$ is also not a successful photocatalyst; however it does have unique multiferroic properties.[17–19] $CuWO_4$ was targeted as a potential photoanode for water oxidation due to the early reports of single crystalline electrodes showing a photoresponse, the more current examples of successful photocatalytic dye degradation, and finally because $CuWO_4$ has the lowest energy band gap determined from UV-Vis spectroscopy.

The research goal in targeting polycrystalline $CuWO_4$ photoanodes is to develop a method to test the viability of smaller band-gap ternary oxides containing W for photoelectrochemical water oxidation. We are interested in identifying the advantages of this class of materials in comparison to the current state of art to understand how the presence of a transition metal influences the material's photoelectrochemical properties toward water oxidation. Furthermore, it was a goal to develop new synthetic methods for complex oxides for use in various applications. Electrochemical deposition is a low-cost and reliable method for forming electrode materials. Electrochemical deposition helps ensure ohmic contact between the oxide and substrate since the deposition is controlled by the transfer of electrons between the two. Furthermore, electrochemical deposition has many controllable parameters, which allows for further controlling the oxide growth. There is a body of literature on preparing WO_3 by electrochemical methods,[20] and because Cu^{2+} is redox active in aqueous solutions, we chose this synthetic method as a route for the formation of $CuWO_4$ photoanodes.

In this chapter, the synthesis of a $CuWO_4$ electrode is accomplished through electrochemical deposition. X-ray photoelectron spectroscopy (XPS) was used to characterize the amorphous as-deposited electrode and understand the mechanism of

deposition. The crystalline electrode was used to determine the position of the conduction and valence band of $CuWO_4$ with respect to the normal hydrogen electrode (NHE). Finally, systematically studying $CuWO_4$'s photoelectrochemical (PEC) properties highlights some of the advantageous properties of this material in comparison to the native WO_3.

2.2 Electrochemical Synthesis and Physical Characterization of $CuWO_4$ Electrodes

The first synthetic effort was producing electrochemically deposited $CuWO_4$ photoanodes. This electrochemical synthetic method was used due to the stated advantages as well as the literature precedent for WO_3 photoanodes from which these methods were adapted. Thin films of $CuWO_4$ are deposited onto FTO conducting substrates by electrodeposition under controlled potentiometry illustrated in Figure 2.3.

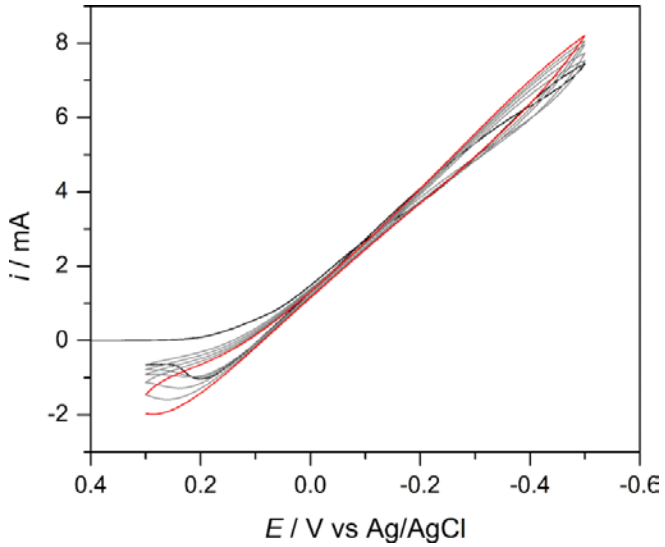

Figure 2.3 Electrochemical deposition co-reducing amorphous electrode material

Copper oxide and tungsten oxide are co-deposited at potentials between –0.5 V and +0.3 V (vs Ag/AgCl at pH 1.1) and the redox couples for Cu^{2+}/Cu^{+} and $W_2O_{11}^{2-}/WO_3$ are 0.08 V and –0.1 V versus Ag/AgCl at pH 1 respectively (Figure A.1). Deposition from the peroxytungstate $W_2O_{11}^{2-}$ has been previously reported in the literature.[20] Therefore the chemical reactions occurring at the electrode surface during the cathodic sweep are:

$$2Cu^{2+}(aq) + H_2O(l) + 2e^- \rightarrow 2Cu_2O(s) + 2H^+(aq) \quad (1)$$

$$W_2O_{11}^{2-}(aq) + 10H^+(aq) + 8e^- \rightarrow \quad 2WO_3(s) + 5H_2O(l) \quad (2)$$

The amorphous film deposited under ambient conditions is a heterogeneous mixture of Cu_2O, CuO and WO_3. This formulation is supported by X-ray photoelectron spectra, in

which signatures for Cu^{+}, Cu^{2+} and W^{6+} are observed as seen in Figure A.2. The Cu^{2+} present in the as-deposited film was due to oxidizing Cu_2O to CuO upon the anodic sweep.[21] Most important, after annealing the thin films at 500 ºC for 2 h, the bright yellow, crystalline $CuWO_4$ resulted from the reactions:

$$Cu_2O(s) + 2WO_3(s) + ½\ O_2(g) \rightarrow 2CuWO_4(s) \quad (3)$$

$$CuO(s) + WO_3(s) \rightarrow CuWO_4\ (s) \quad (4)$$

A photograph of the electrodeposited films before and after annealing is provided in Figure 2.4.

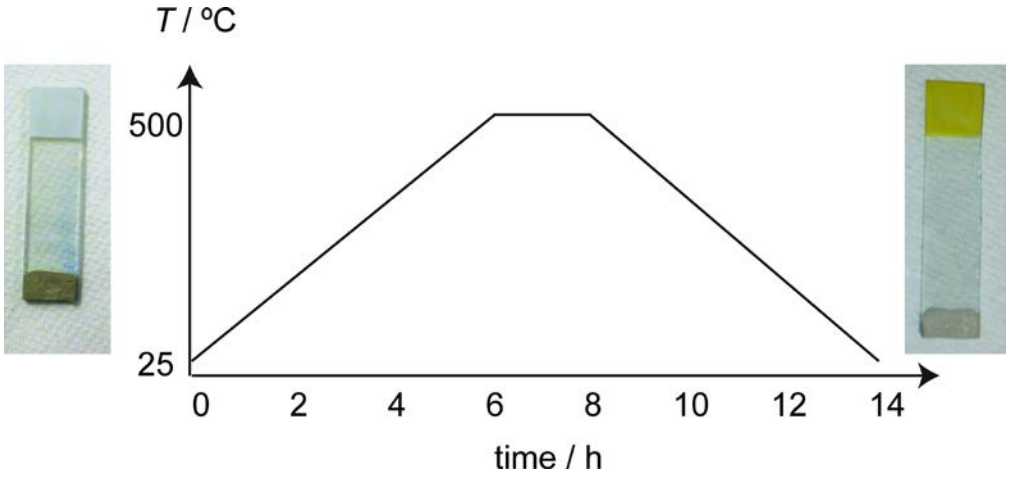

Figure 2.4 Heating scheme for the crystallization of $CuWO_4$ electrodes.
The ramp rate was ~1.3 ºC/min and the annealing temperature was kept at 500 ºC for 2 h

The composition of the films is determined by ICP-AES analysis. Analyzing three individual films provides a W:Cu ratios of 1.29, 1.35, and 1.99. However, a single film contains less than 1 mg of material which must be digested in 8 M NaOH then acidified for analysis, which pushes the detection limit of the analyzer. Therefore, by digesting six films to increase the signal, a W:Cu ratio of 1.20 is observed, consistent with the XRD analysis in which a slight excess of W in the form of WO_3.

The XPS survey scan for the annealed film is shown in Figure A.3. In the annealed thin films, we observe one set of lines for tungsten by XPS. $W(4f_{7/2})$ and $W(4f_{5/2})$ occur at binding energies of 34.5 eV and 36.9 eV, respectively in Figure A.4. The peak energies are consistent with W^{6+} standard peaks.[22] The Cu(2p) region shows $Cu(2p_{3/2})$ and $Cu(2p_{1/2})$ peaks at 934 and 954 eV as well as three satellite peaks, well understood for oxides of Cu^{2+}.[23] Finally, the O(1s) region can be deconvoluted with two Gaussian peaks: lattice oxide is the higher intensity peak at 529 eV and the shoulder at

531 eV is attributed to surface hydroxide, a typical feature observed in metal oxide thin films.

The X-ray diffraction pattern of the annealed films is illustrated in Figure A.5. $CuWO_4$ crystallizes in the centrosymmetric space group P–1,[24] and the corresponding Miller indices calculated from the single crystal structure are included in the figure. For comparison, we prepared a microcrystalline powdered sample by the high temperature solid-state reaction of stoichiometric quantities of CuO and WO_3 at 800 ºC for 2 h. The structures of $CuWO_4$ and WO_3 are well-known and XRD suggests that our films are slightly W-rich, supported by the shoulder in the (011) reflection at ~24.1º 2θ, as well as (022) reflection seen at 33.24º 2θ, unique to WO_3. The diffraction patterns of $CuWO_4$ and WO_3 are difficult to distinguish as both crystallize in similar structures.[25]

The $CuWO_4$ thin films prepared by electrodeposition show an average thickness of 2–3 μm determined by profilometry and supported by the cross-sectional SEM image of Figure 2.5. The top-down image shows a highly porous material consisting of aggregated particles ranging from 200-500 nm with a more densely packed layer of the same composition underneath.

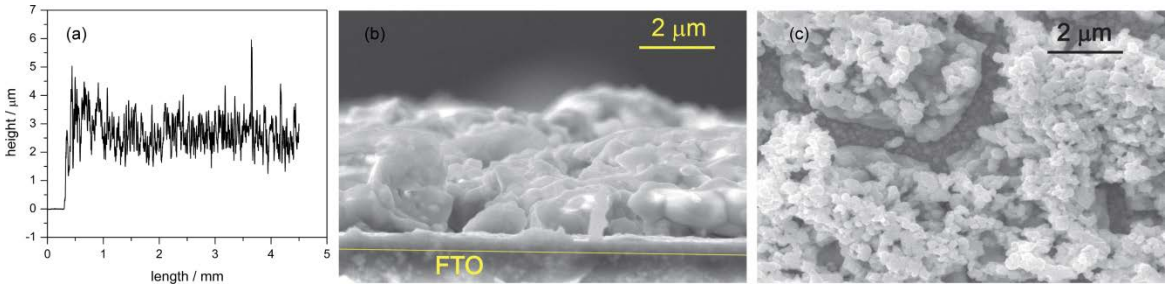

Figure 2.5 Profile (a), cross-sectional SEM image (b), and top-down SEM image (c) of a CuWO4 electrode.

The STEM elemental map seen Figure 2.6 shows an even distribution of Cu and W throughout the annealed material rather than distinct islands of either individual oxide.

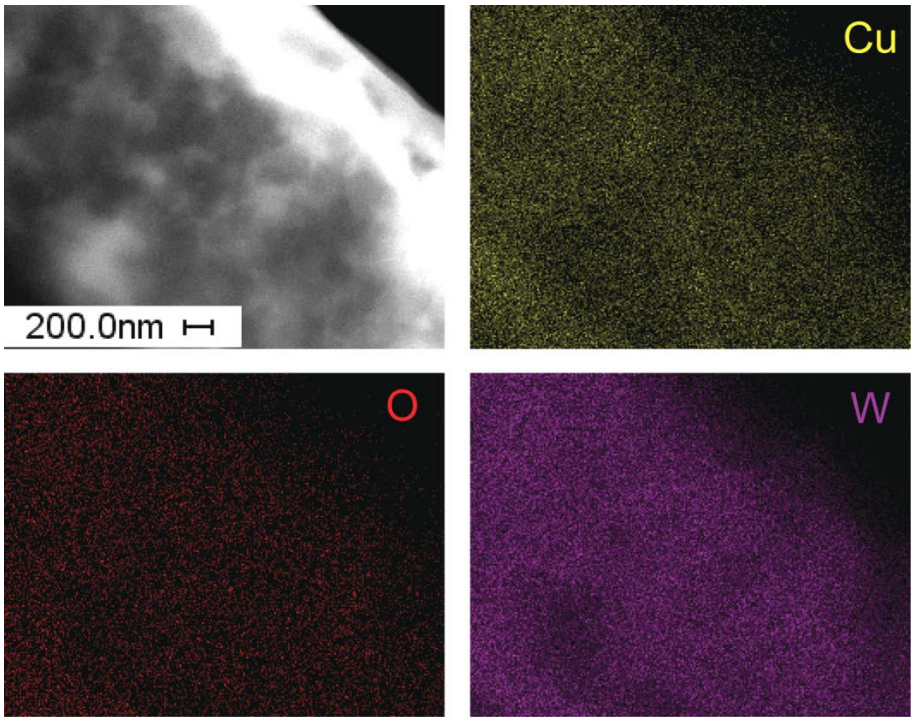

Figure 2.6 Cross-sectional TEM image (top left) with element mapping of Cu (yellow), W (purple), and O (red) proceeding clockwise.

Electronic absorption spectra of $CuWO_4$ thin films were collected using an integrating sphere in diffuse reflectance mode and compared to WO_3 electrodes prepared by electrochemical deposition.

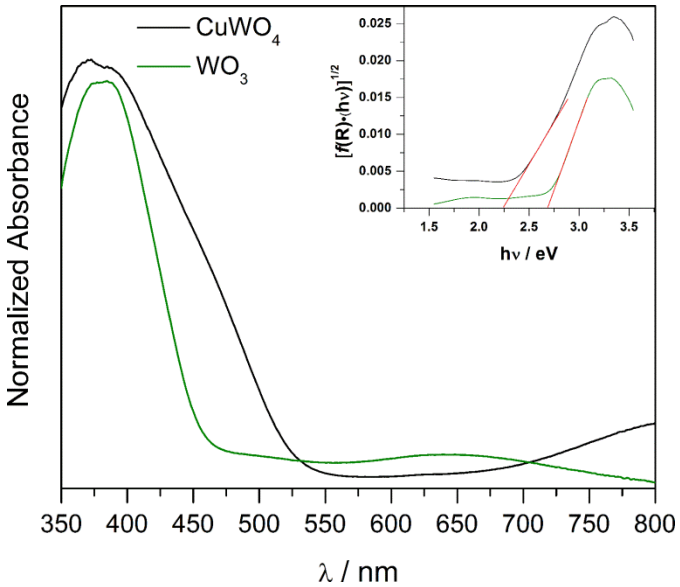

Figure 2.7 Electronic absorption spectra for $CuWO_4$ and for WO_3 electrodes. Inset. Tauc plot for the electrodes showing indirect gaps.

Figure 2.7 shows an absorption tail out to roughly 550 nm for $CuWO_4$, an initial indication that the optical band gap is approximately 2.3 eV, given by the mathematical relationship, E (eV) = 1240 / λ (nm). This transition is assigned as the MMCT associated with hybridized O(2p) + Cu(3d) valence band and the conduction band. The gradual increase in absorbance as opposed to a very sharp increase strongly suggests that this material has an indirect band gap.[26] Accordingly, transforming the reflectance spectrum into a Tauc plot (inset of Figure 2.7) shows that $CuWO_4$ indeed shows an indirect gap of 2.3 eV, representing a bathochromic shift of 0.45 eV compared to the indirect gap of WO_3. Notably, this band gap is similar to what has been measured for other $CuWO_4$ thin films27 as well as single crystals.[26,28] In addition to the MMCT bands, $CuWO_4$ shows low energy, localized *d-d* bands within the Jahn-Teller distorted CuO_6 octahedra from 700–800 nm.[29] This absorption band is typical of Cu^{2+}, and is comparable to the absorption spectrum observed for aqueous Cu^{2+} salts.[30]

2.3 Sol-Gel Synthesis of $CuWO_4$

This synthesis method produces $CuWO_4$ photoanodes by spin casting a viscous precursor solution. This method was targeted for several reasons. First, spin casting is a straight forward and scalable method for electrode synthesis. Physical properties of the electrode such as thickness are easily controllable through spin rates and number of depositions. Control of electrode thickness is important for $CuWO_4$ because the material has an indirect band gap, and therefore a thicker electrode with maintained PEC performance is desired to maximize absorption. In terms of composition, the stoichiometry of the tungstate can be easily controlled through the concentration of precursors used during the preparation. This is important for the results of PEC experiments conducted in Chapter 3 to elucidate some of the fundamental properties of $CuWO_4$ regarding stability and selectivity when performing PEC water oxidation. Electrochemical deposition resulted in films that were slightly W rich, which could provide mislead electrode stability and Faradaic efficiency results. This synthetic method is also useful as it provides a route to synthesize complex tungstate solid solutions, AA′WO4 where the stoichiometry of the cation can be varied amongst the first row transition metal tungstates. This will play a more significant role in Chapter 5 when complex tungstates are formed using an adaptation of this synthesis. Furthermore, in

many cases, when a metal cation is mixed in solution with a metal oxoanion, precipitation of the amorphous oxide results. The choice of unreactive precursors provides a route to maintain the solubility and stability of the casting solution. This method could also be amended for other ternary oxide precursors, and adaptations are currently used in our laboratory.

In order to produce the $CuWO_4$ thin film electrodes, a mixture of $Cu(NO_3)_2 \cdot 3H_2O$ and AMT in a 12:1 (v/v) ethylene glycol : water mixture was heated at 95 ºC to form a solution that turned from light blue to green in color. Upon heating in air, the water evaporates, which decreases the solubility of AMT. Control experiments have shown show that cupric nitrate is unreactive upon heating (a light blue solution persists), but heating AMT results in a chemical change such that a brown precipitate forms upon cooling. In the AMT and cupric nitrate reactant mixture, the precursor solution becomes stable and transparent at temperatures greater than 90 ºC after a 150-minute induction period. When this precursor solution is cooled to room temperature, a white precipitate forms. This process is initially reversible; however, after four hours the precipitate does not dissolve when reheated. A similarly colored green solution has been observed in a precipitation reaction between Na_2WO_4 and $Cu(NO_3)_2$ in ethylene glycol.[31] In that co-precipitation, equimolar Na_2WO_4 dissolved in the minimal volume of H_2O and was added to a solution of $Cu(NO_3)_2$ dissolved in ethylene glycol, forming an analogous dark green color before fully precipitating. By forming a more viscous precursor through heating and adding Triton-X, the solution is amenable to spin casting onto FTO.

The thin films were crystallized by annealing at 550 ºC for 1 h and the X-ray diffraction pattern recorded in **Figure A.6** matches that of pure phase $CuWO_4$, but with relative intensities of the Bragg reflections that are distinct from those obtained on powdered samples. There is greater intensity observed for the (0 1 *l*) family of Bragg planes, indicating preferred orientation. Poly(ethylene) glycol has been shown to serve as a structure-directing agent in WO_3 formed from colloidal precursors,[32–35] and we surmise that a similar process is taking place in our system. Most important, $CuWO_4$ prepared from this sol-gel method does not show any WO_3 impurity phase by X-ray diffraction, typically seen as a shoulder at 24.1 º2θ and a unique reflection at 33.2 º2θ (Cu Kα X-ray source). Energy dispersive X-ray analysis (EDX) indicates a pure material with a W:Cu

ratio of 1.05:1±0.03 taken as an average from three measured areas on four different samples. The stoichiometry of the electrode was further corroborated using ICP-AES in which the W:Cu ratio was measured to be 1.06:1.

The high-resolution SEM image presented in Figure 2.8 indicates that sol-gel chemistry results in nanoparticulate electrodes composed of 190 ± 30 nm (longer axis) × 79 ± 15 nm (shorter axis) interconnected crystallites. Other isostructural AWO_4 powders formed between 500 and 550 ºC are typically close to this size.[31]

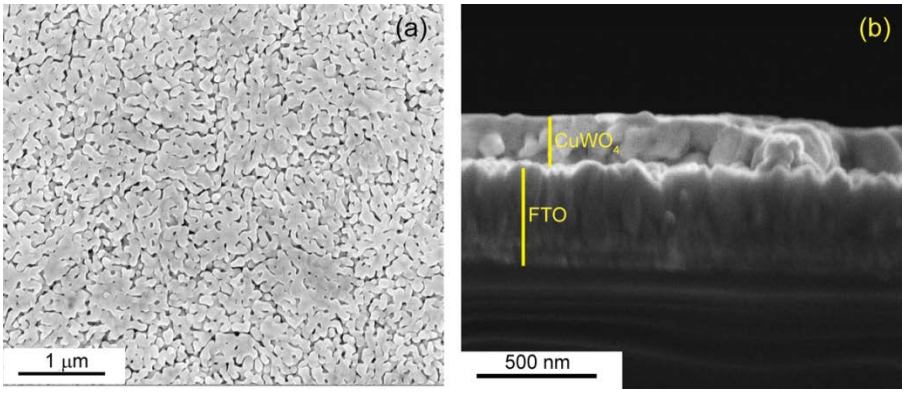

Figure 2.8 Top down (a) and cross-sectional (b) SEM images of $CuWO_4$ on FTO.

SEM imaging also confirms that $CuWO_4$ electrodes are uniform in coverage and the cross sectional SEM shows that the film is ~200 nm thick on top of the FTO substrate. The morphology of interconnected particulates, rather than a dense matte layer, is important for the PEC performance and though each crystallite is larger typically observed for WO_3 electrodes, the morphology is similar to WO_3 prepared from colloidal precursors as well as other oxides prepared by sol-gel methods. [36,37]

The prepared electrodes are slightly opaque yellow crystalline solids with the onset of an absorption edge at 550 nm, which extends into the UV region of the spectrum as shown in Figure 2.9. Figure 2.9 also presents the current efficiency of CuWO4 at an applied bias of 1.23 V RHE. The data shows that the onset of absorption in the thin film corresponds to photocurrent generation. This result and the photoelectrochemistry of CuWO4 will be discussed in more detail within Chapter 3.

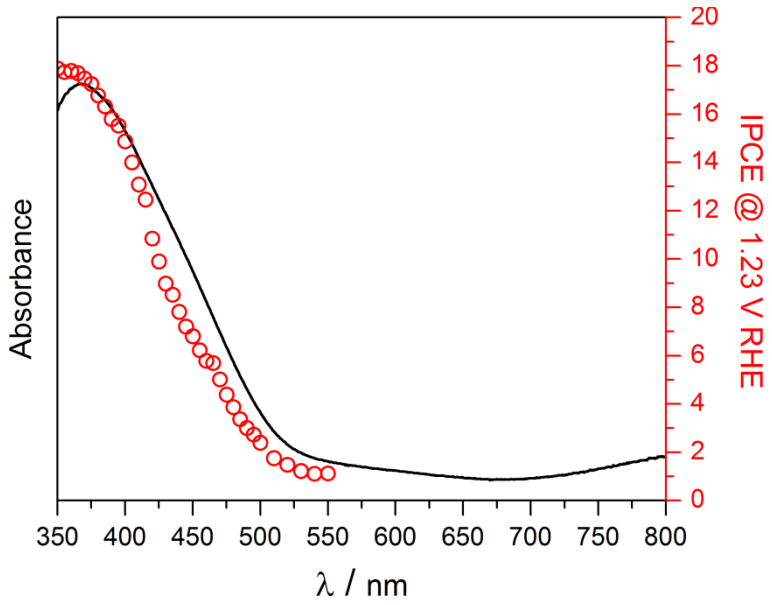

Figure 2.9 UV-vis diffuse reflectance spectrum (black line) and photoaction spectrum (red circles) of $CuWO_4$ thin films.

An indirect band-gap Tauc plot estimates a band-gap energy, E_g, of 2.45 eV. This band gap is slightly higher than $CuWO_4$ prepared by electrochemical deposition (Figure 2.7) and spray pyrolysis,[38] but thin films are known to have slightly larger experimental band gap compared to their powder counterparts or thicker films due to a shorter path length for absorption.[39] The lack of absorption in the 200 nm thin films is further supported by 1) a band-gap energy for thin films that is larger than what is measured for bulk material, 2) the near zero absorptivity at wavelengths greater than 525 nm and 3) the lack of strong *d-d* transitions typically observed at wavelengths longer than 650 nm in powdered CuWO4.[40]

2.4 Electronic Structure of $CuWO_4$

In order to elucidate the electronic structure of $CuWO_4$, electronic absorption spectroscopy is used in conjunction with electrochemical impedance spectroscopy. Using these two methods, the band gap, E_g, as well as the positions of the conduction and valence bands is elucidated in a semiconducting material. Though, determining the exact energy position of the band edges requires measuring the ionization potential and electron affinity in vacuum, EIS provides a close approximation of the conduction band edge in an n-type semiconductor. Electrochemical impedance spectroscopy (EIS) is used to determine the flat band potential in a semiconductor, which as per the Mott-Schottky

relationship. EIS was measured over a frequency range 0.1 to 100 Hz in the DC potential range –0.1 to + 0.5 V (vs Ag/AgCl at pH 7) and capacity calculated as a function of frequency according to the equation:

$$C_{sc} = -\frac{1}{2\pi f Z_{im}} \tag{5}$$

where f is the frequency of the experiment and Z_{im} is the imaginary component of the impedance. Capacitance values are input into the Mott-Schottky relation:

$$\frac{1}{{C_{sc}}^2} = \frac{2}{e\varepsilon\varepsilon_0 N_D}\left(E - E_{fb} - \frac{k_B T}{e}\right) \tag{6}$$

where C_{sc} is the total capacitance in the space-charge depletion layer, E is the applied potential, E_{fb} is the flat-band potential, N_D is the majority-carrier density, and T is temperature. The remaining constants carry their typical meanings such that $2/e\varepsilon_0 = 1.41 \times 10^{32}$ V•cm/C^2 and $k_B T/e = 0.0257$ V at 298 K. E_{fb} is determined from the x-intercept of the plot $1/({C_{sc}}^2)$ versus E, $E_0 = E_{fb} + (k_B T/e)$ and the majority-carrier density is calculated from the slope, where $d({C_{sc}}^{-2})/dE = 2/(e\varepsilon\varepsilon_0 N_D)$. For ε, the dielectric constant of $CuWO_4$, we use 83, the literature value obtained for a pressed pellet prepared from single crystals.[41] From the data shown in Figure 2.10, we obtained a flat band potential of –0.17 V vs Ag/AgCl at pH 7, 0.42 V RHE.

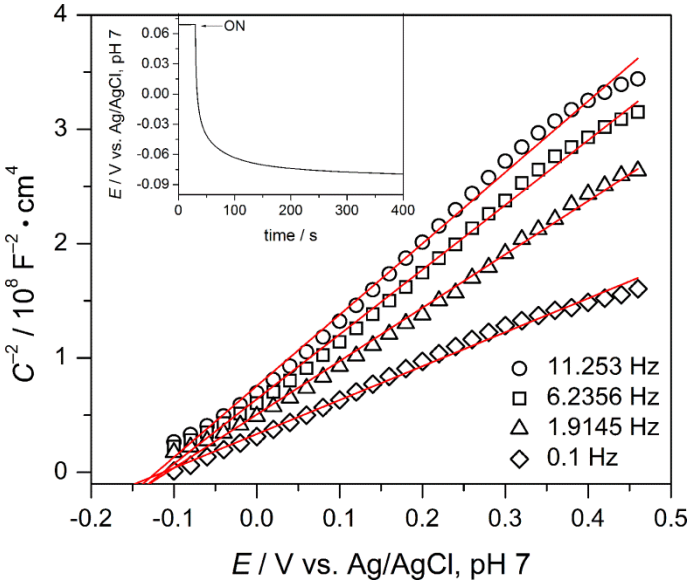

Figure 2.10 Capacitance–voltage profiles for a $CuWO_4$ electrode in a 0.1 potassium phosphate buffer (pH 7) vs Ag/AgCl.
Inset. Open-circuit potential upon intense light illumination.

This significant result is further validated with the onset potential observed in the photocurrent experiments and the open circuit potential of the cell when illuminated, shown in the inset of Figure 2.10.[42] Both syntheses provide similar measured flat band potentials, though there is some frequency dispersion in the measured value at higher frequencies. Frequency dispersion is often observed in polycrystalline electrodes, and can make the results more difficult to interpret. In $CuWO_4$, The agreement of the $C^{-2} - E$ response for a range of lower (0.1 – 10 Hz) frequencies over three orders of magnitude and the near unity values of the slopes in the observed Bode plots (Figure A.7) validates using a simple RC circuit in series with an additional resistance to model the electrode (Randle's circuit). Figure A.8 further validates the energy position of the conduction band in $CuWO_4$. Using an electrode prepared from a cleaved single crystal of $CuWO_4$ in an electrolyte containing a equi-molar $Fe(CN)_6^{3-/4-}$, the measured flat band potential in $CuWO_4$ is 0.4 V RHE. Using the single crystal in an electrolyte with a well-defined redox potential, minimal frequency dispersion is seen at higher frequencies and the measured flat band potential is consistent up to 10,000 Hz. These measurement conditions are not feasible using the polycrystalline electrodes because exposed FTO electrochemically oxidizes/reduces the redox mediator in solution.

The measured donor density of $CuWO_4$ varies by synthesis. In the single crystal prepared into an electrode, the donor density was determined to be approximately 5×10^{18} cm^{-3}. This was lower in comparison to N_D measured on sol-gel $CuWO_4$ (1×10^{20} cm^{-3}) and the electrochemically deposited electrodes (3×10^{21} cm^{-3}). The higher donor density is possibly be due to the highly porous electrode surface in which there may be more than $1cm^2$ active surface area. Additionally, $d(C_{sc}^{-2})/dE$ varies slightly by the frequency used to construct the Mott-Schottky plot, and because it was necessary to use lower frequencies that fit the Randle's circuit, these values may be further inflated. Finally, because these electrodes are polycrystalline in nature, the defect structure may be higher than a single crystal, further resulting in an increased measured donor density.

The electrochemical impedance and electronic absorption experiments yield the electronic structure illustrated in Figure 2.11. Figure 2.11 is plotted with respect to the normal hydrogen electrode (NHE) at pH 0. The experimental data measured at pH 7 vs Ag/AgCl is converted using the Nernst equation and Figure A.9 validates that $CuWO_4$

shows a Nernstian response with respect to solution pH, showing a slope of 0.062 V/decade when measuring the change in open-circuit voltage under illumination at various pH.

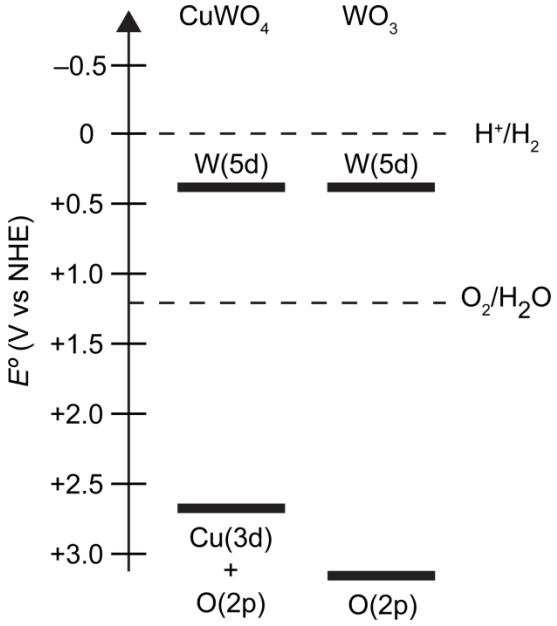

Figure 2.11 Experimentally determined band diagrams for $CuWO_4$ and WO_3.

The proclivity for $CuWO_4$ to act as a photocatalyst for water splitting was surveyed nearly 30 years ago, but the material was abandoned because experimental results led the authors to assert that the valence band is purely atomic O(2p) in character.[43] Since that report, the electronic structure of $CuWO_4$ has been investigated, and a strong Cu(3d) orbital contribution to the valence band is predicted from first principles DFT calculations.[44] Notably, the dispersion in the valence band is ca. 7.7 eV, much wider than the O(2p) band. In addition to the Cu contribution near the valence band maximum edge, the bottom of the valence band is calculated to have significant W(5d) character.

There are conflicting reports about the composition of the conduction band. In reference 44, W(5d) orbitals compose the minimum of the conduction band with a small contribution of O(2p) and Cu(3d) orbitals, indicating a W(5d)←Cu(3d) MMCT as the dominant absorption event as seen in Figure 2.12a. Other reports indicate that $CuWO_4$ is a charge transfer insulator, presenting the major absorption event as a LMCT from a predominantly O(2p) based valence band into a Cu(3d) dominated conduction band,

indicated in Figure 2.12b.[45] However, another study suggests that the unoccupied Cu(3d) state resides approximately 1 eV above the valence band maximum with minimal W(5d) contribution, leading to a *d-d* absorption of significantly lower energy than the main absorption found near 2.3 eV.[46] One major influence of these varying calculations is the spectral redistribution of the Cu(3d) states which change in energy as a result of the spin interactions between ferromagnetic (along b) or antiferromagnetic (along c) neighboring Cu centers.[47,48] Second, the differences in the resulting band structures also arises from the interatomic repulsion energy (*U*) associated with Cu^{2+} in the crystal structure. In oxides containing Cu^{2+}, *U* is typically greater than the *d* orbital width and causes a splitting into two Hubbard bands.[49] Applying a Hubbard term, *U*, to the calculations alters the energy position of the filled and unfilled Cu(*3d*) bands in the electronic structure. In the literature used to provide the possible electronic structures, *U* ranges from 4 eV to 7 eV depending on the calculation and influences the resulting depictions of the electronic structure. Furthermore, the elongation of the z-axis results in differences in orbital overlap which causes further splitting of the e_g states, resulting in thin, filled and partially filled orbitals at different energies within the gap.[47] This tetragonal distortion of the Cu–O octahedron does however lead to the smaller band gap observed in $CuWO_4$ compared to the other metal tungstates.

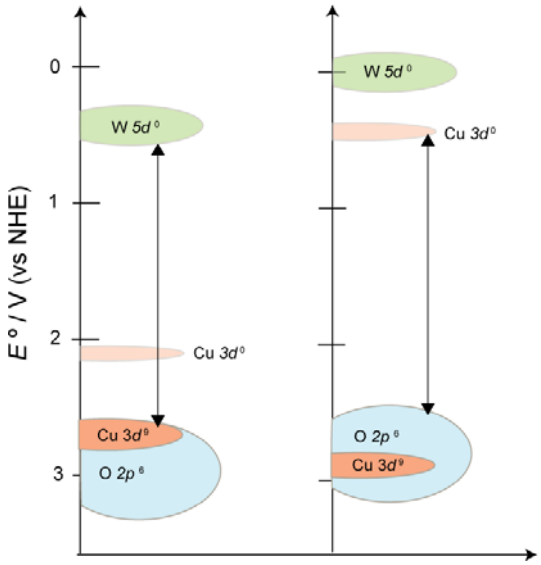

Figure 2.12 Depiction of two possible electronic structures of $CuWO_4$
These electronic structures match the DFT calculations and include the measured E_{fb}. This figure also indicates the charge transfer events capable of creating photocurrent

Our experimental electrochemical impedance data shows that the valance band edge is raised by nearly 0.5 V compared to that in pure WO_3, giving credence to the Cu(*3d*) contribution. In addition, the flat band potential of $CuWO_4$, +0.4 V (vs RHE), matches directly that of WO_3 reported in the literature[50] as well as experimental data collected on an electrodeposited WO_3 film prepared in our lab. This insinuates W(5d) orbitals strongly contribute to the conduction band. In both original theory papers, the calculated band gaps are 1.9 eV and 1.5 eV for references 44 and 46 respectively, and are in reasonably good agreement with previous papers that cite the gap at 2.3 eV[28] and 2.0 eV[27,43] as well as our experimental gap of 2.3 eV.

From our initial discovery, there have been subsequent calculations done to validate our claim as to the electronic structure of $CuWO_4$.[47,51,52] The general consensus is that the transition beginning at 550 nm is a W(5d)←Cu(3d) MMCT and the low energy transition edge seen approximately at 700 nm is a localized Cu(3d) *d-d* transition. Though these calculations approximate the optical properties of $CuWO_4$, electrochemical and photoelectrochemical studies indicate that Cu(3d) states near the conduction band play a significant role in dictating the electrode properties of this material. In order to get a more detailed picture of the electrochemical properties of $CuWO_4$ at energies near the conduction band, cyclic voltammetry (CV) was performed on $CuWO_4$ in both N_2 and O_2 sparged cells, and compared to similar conditions using WO_3 and FTO electrodes. The cyclic voltammogram recorded in Figure 2.13 provides details on role of Cu near the conduction band of $CuWO_4$.

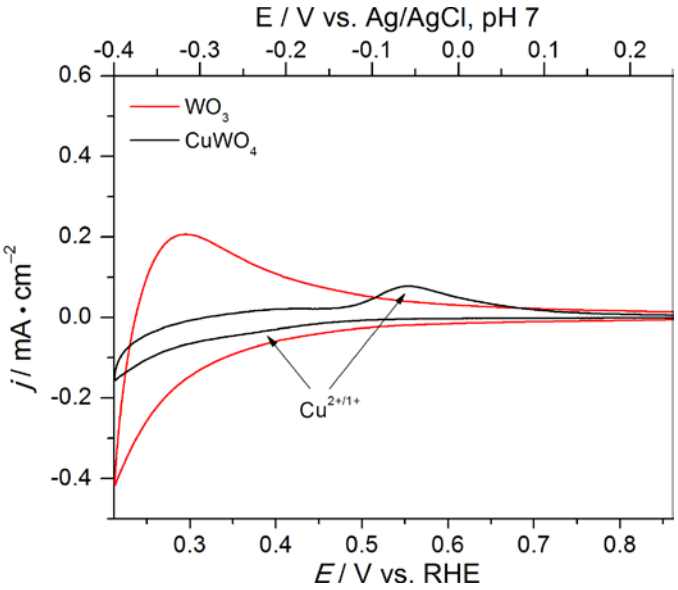

Figure 2.13 CV of $CuWO_4$ and WO_3 in an N_2 purged cell in the dark

$CuWO_4$ shows a quasi-reversible couple with peak potentials, E_{pc} = 0.38 V and E_{pa} =0.55 V in an N_2-purged cell. A similar CV experiment performed on a WO_3 electrode of similar thickness shows no such waves; rather, H^+ insertion and extraction is observed, as has been documented.[53] Furthermore, there is no color change observed in the $CuWO_4$ electrode from yellow to dark blue, typical for W^{6+} reduction. This is not surprising since wolframite is not known to intercalate protons.[54] When the electrochemical potential is swept to more reductive potentials, the redox chemistry of $CuWO_4$ becomes more obvious **Figure A.10**. Also, no discernible waves are observed on a blank FTO electrode. Comparatively, $ZnWO_4$ and $CoWO_4$ show no such redox chemistry, even in an expanded electrochemical window (Figure A.11) further suggesting that the redox chemistry near the conduction band edge is Cu^{2+} based. With these experimental results, it was concluded that this set of peaks in $CuWO_4$ corresponds to $Cu^{2+/1+}$, suggesting that Cu (*3d*) orbitals states exist in the lower energy portion of the conduction band. This conclusion was further verified through comparison of calculations which determine the thermodynamic oxidation and reduction potentials of semiconductors in aqueous solutions.[55] The reduction potential of $CuWO_4$ is due to $Cu^{2+/1+}$ which was predicted to be at potentials just more negative than the conduction band edge.

In the presence of O_2, a catalytic O_2-reduction wave is observed at 0.50 V (–0.11 V *vs.* Ag/AgCl, pH 7) on $CuWO_4$, which again is distinct from WO_3 and FTO electrodes, as seen in Figure 2.14.

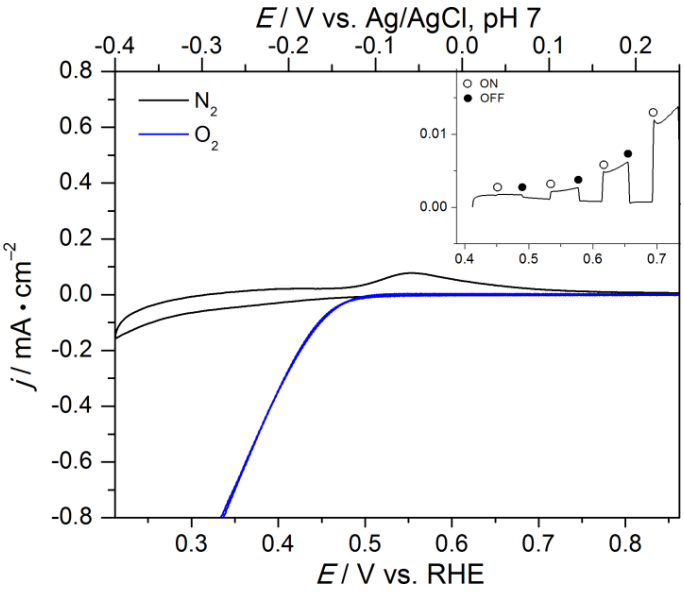

Figure 2.14 CV on $CuWO_4$ in a N_2 and O_2 purged cell
Inset shows the onset of photocurrent in a linear sweep voltammogram on $CuWO_4$ under illumination.

The photocurrent onset potential for PEC water oxidation (presented in the inset of Figure 2.14) also occurs near this potential, 0.46 V (–0.15 V *vs.* Ag/AgCl), further indicating that this Cu-based redox couple dictates both the onset of photocatalysis as well as the dark electrocatalysis of O_2 reduction. Mixed metal tungstates have been shown to be active materials for the electrocatalytic reduction of H^+ to H_2 and Cu is a known metal to be active for electrocatalytic reductions as it proceeds through a $Cu^{2+/1+/0}$. Therefore it is feasible that $CuWO_4$ is active for the catalytic reduction of O_2. The performance of $CuWO_4$ can be evaluated through Tafel slope analysis for the oxygen reduction reaction (ORR). At lower current densities, $CuWO_4$ has a Tafel slop of 67 mV/decade. At higher current densities, the slope increases to 117 mV/decade, indicating a decrease in rate at higher overpotentials (Figure A.12). These experimental slopes closely correlate to the common rate determining steps for the ORR on Pt/PtO_x catalysts.[56] The low slope region corresponds to a pseudo two electron rate determining step, whereas a slope of 120 mV/decade means the first electron transfer is the rate determining step.[57] It is known that the small slope (60 mV/dec.) at higher potentials

corresponds to the reaction taking place at Pt covered with an oxide (PtO_x) whereas the larger slope corresponds to a Pt^0 surface.[56] Interestingly, this change in slope on $CuWO_4$ may be due to the reduction of the catalytic sites from Cu^{2+} to Cu^0 because the changeover potential from low to high slope is close to the measured reduction potential for $CuWO_4$. Though these rates of catalysis are reasonably high on $CuWO_4$, the overpotential required for onset is much greater than what is seen on noble metal catalysts such as Pt and Pd.[58,59] Regardless, there is potential for $CuWO_4$ as a low-cost ORR catalyst that is capable of high temperature cycling, unlike noble metals that are unstable catalysts at higher temperatures. At room temperature and at -0.6 V vs Ag/AgCl (0.1 V RHE), the $CuWO_4$ electrode is not stable for more than ten minutes performing ORR at pH 7 (Figure A.13). In fact, a colorization of the electrode takes place from yellow to copper colored, indicating the reduction of Cu^{2+} to Cu^0. This process is exacerbated in acidic solutions where $Cu^{2+/0}$ is more likely than $Cu^{2+}/^{1+}$. The presence of Cu redox chemistry indicates that the $CuWO_4$ contains Cu(*3d*) character near the conduction band edge, and these states are responsible for many of the fundamental properties of $CuWO_4$ presented in Chapter 3.

2.5 Conclusion

This chapter presents the rational design for targeting specific oxides to serve as photoelectrodes for water oxidation. My research began with a survey of known, promising materials motivated by the goal of increasing visible light absorption while maintaining competency as a semiconducting material. This chapter presents two synthesis methods which add to the body of literature for oxide synthesis and were continuously used through the majority of my thesis work. These methods of synthesis are considered inexpensive and industrially relevant methods to deposit oxide materials onto conducting substrates. The presented methods present insight into the electrochemical role of copper within $CuWO_4$. This chapter presents a methodology for targeting ternary phase oxide materials which contain predominantly metal based valence bands rather than traditional oxygen (2p) orbitals. These low energy metal orbitals must sufficiently hybridize with oxygen orbitals to provide a continuous valence band, rather than discrete d states which possibly plague the use of other 1st row transition metal tungstates. Most importantly, the experiments conducted on $CuWO_4$ helped lay the

foundation for methods of physical and experimental characterization that our lab follows on a newly synthesized material.

2.6 Outlook

Since the results presented in Chapter 2 have been published, there has been progress on the use of tungstate materials in PEC water oxidation. Various synthetic methods have been used to form $CuWO_4$ photoanodes including a co-sputtering approach and modified electrochemical deposition routes.[52,60–62] The electrochemical experiments conducted on these synthesized electrodes show that the properties presented in Chapter 2 are intrinsic to $CuWO_4$ and independent of synthesis method or resulting morphology. As research has continued to progress, composite electrode materials have been formed using $CuWO_4$ to improve on the PEC properties. Multi-walled carbon nanotubes (MWCNT) have been incorporated with $CuWO_4$ to form a light absorbing/charge collecting composite electrode by spray deposition.[63] This composite electrode shows improved photocurrent generation over the native electrode and high photostability. *p*-CuO/*n*-$CuWO_4$ junctions have been formed, capable of photoelectrochemical photocurrent switching (PEPS).[64] Additionally, research groups have taken advantage of the higher energy valence band found in $CuWO_4$ to form heterojunctions with increased electronic fields to help separate charge carriers. Such an example is a $BiVO_4$-$CuWO_4$ heterojunction,[65] and current efforts in our laboratory are aimed at forming WO_3-$CuWO_4$ junctions that use an induced electric field, as well as the chemoselectivity of $CuWO_4$ to form an electrode with high Faradaic efficiencies for O_2 production. As will be presented in the following chapter, the intrinsic properties of $CuWO_4$ lead to advantageous photoelectrochemistry such as increased selectivity for water oxidation under illumination.

2.7 Experimental Methods

Electrochemical Synthesis of $CuWO_4$. All reagents were purchased from Sigma Aldrich and used as received with no further purification. Composite photoanodes were prepared via electrodeposition from a 25 mL bath composed of 25 mM $Cu(NO_3)_2 \cdot 3H_2O$ and 25 mM $H_2W_2O_{11}$. The acidic peroxytungstate precursor was synthesized by dissolving metallic tungsten powder (0.95 g) in 10 mL of 30% hydrogen peroxide in a cold water bath. After complete dissolution, excess peroxide was decomposed using a

platinum mesh catalyst (4 cm^2), evident when no more bubbles evolved from the platinum mesh. The solution was quantitatively transferred and diluted to 25 mM in a 70:30 water:2-propanol mixture. The pH of the starting mixture was approximately 1.9, and the acidity of the final deposition solution was adjusted to pH 1.1 by adding 2–3 mL of 5% nitric acid solution. Films were electrodeposited onto soda-lime glass coated with a 400 nm fluorinated tin oxide (FTO) conducting layer purchased from Pilkington Glass (Tec 15 2.2 mm thick, 12–14 Ω) after being cleaned by sonication in ethanol, then acetone for 20 min each. Amorphous white films were prepared by submerging a 1 cm^2 area in a stirred stock solution. The potential was swept from +0.3 V to –0.5 V for 6 complete cycles, passing ~0.5–0.6 C total charge versus a Ag/AgCl reference electrode at pH 1.1 and 25 ºC using a CH Instruments 660C Electrochemical Workstation. These films were subsequently annealed in air at 500 ºC for 2 h using an MTI box furnace. The films were heated and cooled at a rate of approximately 1.3 ºC/min. After annealing, the resulting bright yellow films were used in all subsequent experiments. Control tungsten oxide films were electrodeposited from the same deposition solution as the copper(II) tungstate films, with the notable exception that no cupric nitrate precursor was employed. These films were deposited potentiostatically at –0.6V for 6 minutes in a non-stirred solution, experimentally passing ~0.55 C total charge. These films were annealed using the same heating scheme described above, resulting in films ca. 600 nm thick as determined by profilometry.

Sol-Gel Synthesis of $CuWO_4$.

All reagents were purchased from Sigma Aldrich and used as received with no further purification. The $CuWO_4$ photoanodes were prepared via spin-casting the sol-gel precursors onto a fluorinated tin oxide (FTO) substrate. FTO was purchased from Pilkington Glass (Tec 15 2.2 mm thick, 12–14 Ω/sq.) and was cleaned by sonication in ethanol and acetone for 20 min each, and then rinsed with de-ionized water and dried under N_2. First, 1.00 mmol of $Cu(NO3)_2 \cdot 3H_2O$ was dissolved into 1.2 mL of ethylene glycol in a 20 mL scintillation vial. Next, 1.00 mmol of tungsten in the form of ammonium metatungstate hydrate ($(NH_4)_6H_2W_{12}O_{40} \cdot 4H_2O$, AMT) was added to the vial. 0.1 mL of H_2O was then added, and the mixture was sonicated and stirred to dissolve the AMT. Finally, 0.025 g of Triton-X 100 non-ionic surfactant was added to the mixture,

forming a blue solution. The vial was stirred and heated in an oil bath at 95 ºC to form a dark green solution. After heating for at least 2.5 h, 25 µL of the green precursor solution was dropped onto 1 cm^2 of masked FTO and spun for 10 min at 1200 rpm immediately followed by 2000 rpm for 3 s to remove excess liquid from the edges; the 1 cm^2 area was centered over the Laurell spin coater (model WS-400B06NNP/LITE). The casted electrodes were annealed at 550 ºC for 1 h, with 1 h ramp and cool times. This heating scheme was optimized for photoelectrochemical performance. Electrical contact was made by attaching copper wire (Fisher Scientific) using silver print II (GC electronics) to exposed FTO. Finally, the electrode was sealed using Hysol 1C epoxy at the end of a piece of glass tubing through which the wire had been fitted.

Physical Characterization. X-ray diffraction patterns were recorded on a Brüker D8 Advance diffractometer equipped with a graphite monochromator, a Lynx-Eye detector, and parallel beam optics using Cu-Kα radiation (λ = 1.54184 Å). Patterns were collected using a 0.6 mm incidence slit, with a step size and scan rate of 0.04º/step and 0.5 s/step respectively. Phases were identified as $CuWO_4$ (JCPDF 72-0616) and WO_3 (JCPDF 72-0677) using MDI Jade version 5.0. Observed $CuWO_4$ Bragg reflections were compared to those calculated from the single crystal X-ray structure.[66]

UV-Vis spectra were recorded using an Agilent-Cary 5000 spectrophotometer equipped with an external diffuse reflectance accessory. Spectra were recorded in reflectance mode and presented as normalized absorbance. Tauc plots were then generated using the Kubekla-Munk function, $F(R) = (1–R)^2/2R$. Film thickness was determined by profilometry using a Dektak 6 M Surface Profilometer.

Scanning electron microscopy images were obtained using an FEI Nova Nanolab SEM/FIB with an accelerating voltage of 10 kV. X-ray photoelectron spectra were recorded on a Kratos XPS (8 mA, 14 keV, Monochromatic Al). All peaks were calibrated to C(1s) at 284.5 eV. The XPS data was fit using CasaXPS program. Peaks were fit with a Shirley background using a GL(30) fit. Transmission electron microscopy was performed using a JEOL 2010F instrument. XTEM samples were prepared as follows. Film surfaces were adhered using M-bond 610 adhesive. The sample was then cut to an appropriate size and mechanically ground until it was sufficiently thin. Finally, it was polished with a precision ion polishing system (Gatan) and mounted onto a slotted

titanium grid using M-bond 610 adhesive. Energy dispersive X-ray analysis spectra (EDX) of sol-gel $CuWO_4$ were collected using a Hitachi S-3200N SEM with an accelerating voltage of 25 kV, a secondary electron (SE) detector and a working distance of 15 mm. Spectra were quantified using EDAX genesis software and the Cu K and W L emission lines were used. The determined atomic ratio of W:Cu was 1.05:1±0.03. Spectra were collected for 180 live seconds with a dead time (% DT) less than 40% collecting on average 4000 cps. The atomic ratio was also quantified using a 10 kV accelerating voltage to minimize the contribution of the FTO and SiO under layers. The resulting atomic ratio of W to Cu was 1.04 ± 0.05 using the Cu L and W M emission lines.

ICP-AES elemental analysis for Cu and W was obtained using a Perkin-Elmer Optima 2000DV instrument. Electrochemically deposited $CuWO_4$ electrodes were digested in 8 M NaOH, and then acidified using HNO_3. The atomic ratio of Cu to W in the film was determined using an average of the two most intense emission lines for each metal: 324.752 and 327.393 nm for Cu; 207.912 and 224.876 nm for W. ICP-AES elemental analysis for Cu and W in sol-gel $CuWO_4$ was obtained using a Perkin-Elmer Optima 2000DV instrument. The material from four films was used for the experiment. First, the four films were placed in a 20 mL scintillation vial, and 2 mL of 30% H_2O_2, 1 mL of HNO_3 (69%) and 2 mL of H_2O were added. Then, the vial was heated to 80 ºC and stirred. Over time, 1 – 2 mL of additional H_2O_2 was added as the mixture was dissolving. Finally, it was allowed to cool, and the solution was diluted with H_2O to 10 mL total for use. The emission lines used were 324.752 nm and 224.876 nm for Cu and W, respectively.

Impedance measurements were performed using an Autolab PGSTAT302N electrochemical workstation equipped with a frequency response analysis (FRA) module version 4.9 in a pH 7 potassium phosphate solution. A sinusoidal 10 mV excitation waveform was used to measure the impedance characteristics of the electrode (10 kHz–0.1 Hz), scanning from 1.0 to –0.1 V vs Ag/AgCl.

2.8 References

1. Berak, J. M.; Sienko, M. J. Effect of Oxygen-Deficiency of Electrical Transport Properties of Tungsten Trioxide Crystals. *J. Solid State Chem.*, **1970**,*2*, 109-133
2. Reyes-Gil, K. R.; Wiggenhorn, C.; Brunschwig, B. S.; Lewis, N. S. Comparison between the Quantum Yields of Compact and Porous WO_3 Photoanodes, *J. Phys. Chem. C*, **2013**, *117*, 14947-14957
3. Wang, H.; Lindgren, T. He, J.; Hagfeldt, A.; Lindquist, S.-E. Photoelectrochemistry of Nanostructured WO_3 Thin Film Electrodes for Water Oxidation: Mechanism of Electron Transport, *J. Phys. Chem. B*, **2000**, *104*, 5686-5696
4. Schoonman, J.; van de Krol, R. Nanostructured Materials for Solar Hydrogen Production. *U. P. B. Sci. Bull., Series B*, **2011**, *73*, 31-43 ISSN: 1454-2331
5. Kadowaki, H.; Saito, N.; Nishiyama, H.; Kobayahsi, H.; Shimodaira, Y.; Inoue, Y. Overall Splitting of Water by RuO_2-Loaded $PbWO_4$ Photocatalyst with $d^{10}s^2$-d^0 Configuration. *J. Phys. Chem. C* **2007**, *111*, 439-444.
6. Amano, F.; Nogami, K.; Abe, R.; Ohtani, B. Preparation and Characterization of Bismuth Tungstate Polycrystalline Flake-Ball Particles for Photocatalytic Reactions. *J. Phys. Chem. C* **2008**, *112*, 9320-9326.
7. Amano, F.; Yamakata, A.; Nogami, K.; Osawa, M.; Ohtani, B. Visible Light Responsivle Pristin Metal Oxide Photocatalyst: Enhancement of Activity by Crystallization under Hydrothermal Treatment. *J. Am. Chem. Soc.* **2008**, *130*, 17650-17651.
8. Bhattacharya, C.; Lee, H. C.; Bard, A. J. Rapid Screening by Scanning Electrochemical Microscopy (SECM) of Dopants for Bi_2WO_6: Improved Photocatalytic Water Oxidation with Zn Doping. *J. Phys. Chem. C* **2013**, *117*, 9633-9640.
9. Zhang, L.; Bahnemann, D. Synthesis of Nanovoid Bi_2WO_6-2D Ordered Arrays as Photoanodes for Photoelectrochemical Water Splitting. *ChemSusChem* **2013**, *6*, 283-290.
10. Fu, H.; Lin, J.; Zhang, L.; Zhu, Y. Photocatalytic Activities of a Novel $ZnWO_4$ Catalyst Prepared by a Hydrothermal Process. *Appl. Catal., A* **2006**, *306*, 58-67.
11. Shi, R.; Wang, Y.; Li, D.; Xu, J.; Zhu, Y. Synthesis of $ZnWO_4$ Nanorods with [100] Orientation and Enhanced Photocatalytic Properties. *Applied Catal., B* **2010**, *100*, 173-178.
12. He, D.; Zhang, X.; Xie, T.; Zhai, J.; Li, H.; Chen, L.; Peng, L.; Zhang, Y.; Jiang, T. Studies of Photo-Induced Charge Transfer Properties of $ZnWO_4$ Photocatalyst. *Appl. Surf. Sci.* **2011**, *257*, 2327-2331.
13. Schmitt, P.; Brem, N.; Schunk, S.; Feldmann, C. Polyol-Mediated Synthesis and Properties of Nanoscale Molybdates/Tungstates: Color, Luminescence, Catalysis. *Adv. Funct. Mater.* **2011**, *21*, 3037-3046.
14. Montini, T.; Gombac, V.; Hameed, A.; Felisari, L.; Adami, G.; Fornasiero, P. Synthesis, Characterization and Photocatalytic Performance of Transition Metal Tungstates. *Chem. Phys. Lett.* **2010**, *498*, 113-119.

15. Selvan, R. K.; Gedanken, A. The Sonochemical Synthesis and Characterization of $Cu_{1-x}Ni_xWO_4$ Nanoparticles/Nanorods and their Application in Electrocatalytic Hydrogen Evolution. *Nanotech.* **2009**, *20*, 105602-105609
16. Jia, H.; Stark, J.; Zhou, L. Q.; Ling, C.; Sekito, T.; Markin, Z. Different Catalytic Behavior of Amorphous and Crystalline Cobalt Tungstate for Electrochemical Water Oxidation. *RSC Adv.* **2012**, *2*, 10874-10881.
17. Ye, F.; Fishman, R.; Fernandez-Baca, J.; Podlesnyak, A.; Ehlers, G.; Mook, H.; Wang, Y.; Lorenz, B.; Chu, C. Long-Range Magnetic Interactions in the Multiferroic Antiferromagnet $MnWO_4$. *Phys. Rev. B* **2011**, *83*. 140401-4.
18. Meddar, L.; Josse, M.; Maglione, M.; Guiet, A.; La, C.; Deniard, P.; Decourt, R.; Lee, C.; Tian, C.; Jobic, S.; Whangbo, M.-H.; Payen, C. Increasing the Phase-Transition Temperatures in Spin-Frustrated Multiferroic $MnWO_4$ by Mo Doping. *Chem. Mater.* **2012**, *24*, 353-360.
19. Solovyev, I. V. Origin of multiferroicity in $MnWO_4$. *Phys. Rev. B* **2013**, 87. 144403-7.
20. Muelenkamp, E.A. Mechanism of WO_3 Electrodeposition from Peroxy-Tungstate Solution *J. Electrochem. Soc*., **1997**, *144*, 1664-1671.
21. Wu, L.; Tsiu, L.; Sqami, N.; Zangari, G. Photoelectrochemical Stability of Cu_2O Films *J. Phys. Chem. C*, **2010**, *114*, 11551-11556.
22. Bilogen, P.; Pott , G. T. X-ray Photoelectron Spectroscopy Study of Supported Tungsten Oxide *J. Catal.*, **1973**, *30*, 169-174.
23 Novakov, T. X-ray Photoelectron Spectroscopy of Solids; Evidence of Band Structure *Phys. Rev. B* **1971**, *3*, 2693-2698.
24. Kihlborg, L.; Gebert, E. $CuWO_4$, a Distorted Wolframite-Type Structure *Acta Crystallogr., Sect. B* **1970**, *26*, 1020-1026.
25. Tanisaki, S. Crystal Structure of Monoclinic Tungsten Trioxide at Room Temperature *J. Phys. Soc. Jpn*. **1960**, *15*, 573-581.
26. Lacomba-Perales, R.; Ruiz-Fuertes, J.; Errandonea, D.; Martínez-García, D.; Segura, A. Optical Absorption of Divalent Tungstates *Europhys. Lett*. **2008**, *83*, 37002 (5p).
27. Pandey, P. K.; Bhave, N. S.; Kharat, R. B.; Spray Deposition Process of Polycrystalline Thin Films of $CuWO_4$ and Study on its Photovoltaic Electrochemical Properties Mater. Lett., **2005**, *59*, 3149-3155.
28. Doumerc, J.-P.; Hejtmanek, J.; Chaminade, J.-P.; Pouchard, M.; Krussanova, M. A Photoelectrochemical Study of $CuWO_4$ Single Crystals *Phys. Status Solidi A* **1984**, *82*, 285-294.
29. Ruiz-Fuertes, J.; Sanz-Ortiz, M. N.; González, J.; Rodríguez, F.; Segura, A.; Errandonea, D. Optical Absorption and Raman Spectroscopy of $CuWO_4$ *J. Phys.: Conf. Ser*. **2010**, *215*, 012048-5.
30. Jorgensen, C. K. Aquo Ion Formation II. The First Transition Group in Ethanol *Acta. Chem. Scand.* **1954**, *8*, 175-191.
31. Schmitt, P.; Brem, N.; Schunk, S. Feldmann, C. Polyol-Mediated Synthesis and Properties of nanoscale Molybdates/Tungstates: Color Luminescence, Catalysis *Adv. Funct. Mater*. **2011**, *21*, 3037-3046.

32. Li, W.; Li, J.; Wang, X.; Ma, J.; Chen, Q. Photoelectrochemical and Physical Properties of WO_3 Films Obtained by the Polymeric Precursor Method. *Int. J. Hydrogen Energy* **2010**, *35*, 13137-13145
33. Cremonesi, A.; Djaoued, Y.; Barsani, D.; Lottici, P. P. Micro-Raman Spectroscopy on Polyethylene-Glycol Assisted Sol–Gel Meso and Macroporous WO_3 Thin Films for Electrochromic Applications. *Thin Solid Films* **2008**, *516*, 4128-4132
34. Yang, H.; Shang, F.; Gao, L.; Han, H. Structure, Electrochromic and Optical Properties of WO_3 Film Prepared by Dip Coating-Pyrolysis. *App. Surf. Sci.* **2007**, *253*, 5553-5557
35. Djaoued, Y.; Ashrit, P. V.; Badilescu, S.; Brüning, R. Synthesis and Characterization of Macroporous Tungsten Oxide Films for Electrochromic Application. *J. Sol-Gel Sci. Technol.* **2003**, *28*, 235-244
36. Santato, C.; Odziemkowski, M.; Ulmann, M.; Augustynski, J. Crystallographically Oriented Mesoporous WO_3 Films: Synthesis, Characterization, and Applications. *J. Am. Chem. Soc.* **2001**, *123*, 10639-10649
37. Hamd, W *et. al.* Mesoporous α-Fe_2O_3 Thin Films Synthesized via the Sol–Gel Process for Light-Driven Water Oxidation. *Phys. Chem. Chem. Phys.* **2012**, *24*, 13224-13232
38. Pandey, P. K.; Bhave, N. S.; Kharat, R. B. Spray Deposition Process of Polycrystalline Thin Films of $CuWO_4$ and Study on its Photovoltaic Electrochemical Properties. *Mater. Lett.* **2005**, *59*, 3149.
39. Kwong, W. L.; Savvides, N.; Sorrell, C. C. Electrodeposited Nanostructured WO_3 Thin Films for Photoelectrochemical Applications *Electrochim. Acta* **2012**, *75*, 371.
40. Yourey, J. E.; Kurtz, J. B.; Bartlett, B. M. Structure, Optical Properties, and Magnetism of the Full $Zn_{1-x}Cu_xWO_4$ ($0 \leq x \leq 1$) Composition Range *Inorg. Chem.* **2012**, *51*, 10394-10401.
41. Arora, S. K.; Mathew, T. Dielectric studies of $CuWO_4$ crystals *Phys. Status Solidi A* **1989**, *116*, 405-413.
42. Turner, J. A. Energetics of the Semiconductor-Electrolyte Interface *J. Chem. Ed*. **1983**, *60*, 327-329.
43. Benko, F. A.; MacLaurin, C. L.; Koffyberg, P. F. $CuWO_4$ and Cu_3WO_6 as Anodes for the Photoelectrolysis of Water *Mater. Res. Bull*. **1982**, *17*, 133-136.
44. Khyzhun, O. Y.; Bekenev, V. L.; Solonin, Y. M. First-Principles Calculations and X-ray Spectroscopy Studies of the Electronic Structure of $CuWO_4$. *J. Alloys Cmpd.* **2009**, *480*, 184-189.
45. Huda, M. N.; Al-Jassim, M. M.; Turner, J. A. Mott Insulators: An Early Selection Criterion for Materials for Photoelectrochemical H2 Production. *J. Renewable Sustainable Energy* **2011**, *3*, 053101-10.
46. Lalić, M. V.; Popović, Z. S.; Vukajlović, F. R. Ab Initio Study of Electronic, Magnetic and Optical Properties of $CuWO_4$ Tungstate *Comput. Mater. Sci.* **2011**, *50*, 1179-1186.
47. Lalić, M. V.; Popović, Z. S.; Vukajlović, F. R. Electronic Structure and Optical Properties of $CuWO_4$: An Ab Initio Study. *Comput. Mater. Sci*. **2012**, *63*, 163-167.

48. Forsyth, J. B.; Wilkinson, C.; Zvyagin, A. I. The Antiferromagnetic Structure of Copper Tungstate, $CuWO_4$ *J. Phys.: Condens. Matter* **1991**, *3*, 8433-8440.
49. Goodenough, J.B. Interpretation of the Transport Properties of Ln_2NiO_4 and Ln_2CuO_4 Compounds *Mat. Res. Bull*. **1973**, *8*, 423-431.
50. Desilvestro, J.; Grätzel, M. Photoelectrochemistry of Polycrystalline *n*-WO3: Electrochemical Characterization and Photoassisted Oxidation Processes *J. Electroanal. Chem*., **1978**, *238*, 129-150.
51. Kuzmin, A.; Kalinko, A.; Evarestov, R. A. Ab Initio Lcao Study of the Atomic, Electronic and Magnetic Structures and the Lattice Dynamics of Triclinic Cuwo4. Acta Materialia **2013**, *61*, 371-378.
52. Hill, J. C.; Ping, Y.; Galli, G. A.; Choi, K.-S. Synthesis, Photoelectrochemical Properties, and First Principles Study of *n*-Type $CuW_{1-x}Mo_xO_4$ Electrodes Showing Enhanced Visible Light Absorption. *Energy Environ. Sci*. **2013**, *6*, 2440-2446.
53. Schirmer, O. F.; Wittwer, V.; Baur, G.; Brandt, G. Dependence of WO_3 Electrochromic Absorption on Crystallinity. *J. Electrochem. Soc.* **1977**, 124, 749-753
54. Fujioka, Y.; Frantti, J.; Asiri, A. M.; Obaid, A. Y.; Jiang, H.; Nieminen, R. M. Structural Properties of Pure and Nickel-Modified Nanocrystalline Tungsten Trioxide. *J. Phys. Chem. C* **2012**, *116*, 17029-17039
55. Chen, S.; Wang, L.-W. Thermodynamic Oxidation and Reduction Potentials of Photocatalytic Semiconductors in Aqueous Solutions *Chem. Mater.*, **2012**, *24*, 3659-3666
56. Wakabayshi, N.; Takeichi, M.; Itagaki, M.; Uchida, H.; Watanabe, M. Temperature-Dependence of Oxygen Reduction Activity at a Platinum Electrode in an Acidic Electrolyte Solution Investigated with a Channel Flow Double Electrode *J. Electroanal. Chem.*, **2005**, *574*, 339-346
57. Song, C.; Zhang, J.; In *PEM Fuel Cell Electrocatalysts and Catalyst Layers*; Zhang, J.; Springer: New York, **2008**; p 113-116
58. Paulus, U. A.; Schmidt, T. J.; Gasteiger, H. A.; Behm, R. J. Oxygen Reduction on a High-Surface Area Pt/Vulcan Carbon Catalyst: A Thin-Film Rotating Ring-Disk Electrode Study *J. Electroanal. Chem.*, **2001**, *495*, 134-145
59. Oishi, K.; Savadogo, O. Electrochemical Investigation of Pd-Co Thin Films Binary Alloy for the Oxygen Reduction Reaction in Acid Medium *J. Electroanal. Chem.* **2013**, *703*, 108-116
60. Chang, Y.; Braun, A.; Deangelis, A.; Kaneshiro, J.; Gaillard, N. Effect of Thermal Treatment on the Crystallographic, Surface Energetics, and Photoelectrochemical Properties of Reactively Cosputtered Copper Tungstate for Water Splitting *J. Phys. Chem. C* **2011**, *115*, 25490-25495.
61. Gaillard, N.; Chang, Y.; Braun, A.; DeAngelis, A. Copper Tungstate ($CuWO_4$)–Based Materials for Photoelectrochemical Hydrogen Production. Mater. Res. Soc. Symp. Proc. **2012**, *1446*, 19-24.
62. Hill, J. C.; Choi, K.-S. Synthesis and Characterization of High Surface Area $CuWO_4$ and Bi_2WO_6 Electrodes for Use as Photoanodes for Solar Water Oxidation. *J. Mater. Chem. A* **2013**, *1*, 5006-5014

63. Gaillard, N.; Chang, Y.; DeAngelis, A.; Higgins, S.; Braun, A. A Nanocomposite Photoelectrode Made of 2.2 eV Band Gap Copper Tungstate ($CuWO_4$) and Multi-Wall Carbon Nanotubes for Solar-Assisted Water Splitting. *Int. J. Hydrogen Energy* **2013**, *38*, 3166-3176.
64. Zheng, J. Y.; Song, G.; Kim, C. W.; Kang, Y. S. Facile Preparation of *p*-CuO and *p*-CuO/*n*-$CuWO_4$ Junction Thin Films and Their Photoelectrochemical Properties. *Electrochim. Acta* **2012**, *69*, 340-344.
65. Pilli, S. K.; Deutsch, T. G.; Furtak, T. E.; Brown, L. D.; , J. A.; Herring, A. M. $BiVO_4$/$CuWO_4$ Heterojunction Photoanodes for Efficient Solar Driven Water Oxidation *Phys. Chem. Chem. Phys.* **2013**, *15*, 3273-3278.
66. Klein, S.; Weitzel, H. J. PERNOD – Ein Programm zur Vergeinerung von Kristallstrukturparametern aus Neutronenbeugungspulverdiagrammen *J. Appl. Crystallogr.* **1975**, *8*, 54-59.

CHAPTER 3

Detailed Photoelectrochemical Study of $CuWO_4$

Portions of this chapter have been published:
Reproduced with permission from Yourey, J. E.; Pyper, K, J.; Kurtz, J. B.; Bartlett, B. M. *J. Phys. Chem. C.* **2013**, *117*, 8708-8718. Copyright 2013 American Chemical Society
http://pubs.acs.org/doi/abs/10.1021/jp402048b

Reproduced with permission from Pyper, K. J.; Yourey, J. E.; Bartlett, B. M. *J. Phys. Chem. C.* **2013**, *117*, 24726-24732. Copyright 2013 American Chemical Society
http://pubs.acs.org/doi/abs/10.1021/jp408434v

Yourey, J. E.; Bartlett, B. M. *J. Mater. Chem.* **2011**, *21*, 7651-7660. Reproduced by permission of the Royal Society of Chemistry.
http://pubs.rsc.org/en/Content/ArticleLanding/2011/JM/C1JM11259G

3.1 Introduction

As mentioned at the end of chapter 2, there has been significant progress on the development of new methods for the synthesis of $CuWO_4$, along with composite and heterojunction electrodes. This chapter presents an in depth study its PEC properties for water oxidation. Specifically, this chapter is focused on electrode stability over long periods of illumination in neutral pH electrolytes. There is recent emphasis in PEC water splitting on finding electrolyte compositions that are compatible with both redox half reactions. Currently, PEC H_2 evolution on metal oxide photocathodes,[1–3] as well as overall water splitting on tandem devices[4,5] is often carried out at near-neutral pH. Therefore, an anode that possesses a larger window of pH stability is needed for incorporation into one of these systems, rather than being confined to strong acids or strong bases. The goal is to measure the Faradaic efficiency (i.e.–the selectivity of performing the desired redox reaction on an electrode). In conducting these studies, an electrolyte (potassium borate, KB_i at pH 7) not commonly used for PEC water oxidation

was identified as a promising buffer system for long term stability and high Faradaic efficiencies for O_2 formation. The results are presented in a manner of comparison to the native WO_3 and the fundamental differences in the electronic structure of $CuWO_4$ in comparison to WO_3 are connected to these PEC properties.

3.2 Photoelectrochemistry of $CuWO_4$

The ability of a semiconducting material to generate collectable charge carries is determined by the use of a photoaction spectrum. Figure 2.9 shows the external quantum efficiency of a sol-gel $CuWO_4$ photoanode at 1.23 V RHE along with the absorption spectrum of the electrode. The onset of measurable efficiencies begins at 530 nm, which corresponds to a band gap of 2.45 eV, approximately the same as the energy gap determined from the absorption spectrum in sol-gel $CuWO_4$. Again, this is slightly larger than what is measured on a thicker film or powdered counterparts but $CuWO_4$ is an indirect band gap material (α = 1715 cm^{-1} at 500 nm, calculated from electrochemically deposited $CuWO_4$, Figure B.1), and therefore a film of nearly 6 μm is required for complete photon absorption at longer wavelengths. However, even in thicker, electrochemically deposited films, $CuWO_4$ still has low quantum efficiencies at these longer wavelengths (Figure B.1). This is possibly because the penetration depth (indirectly proportional to absorptivity coefficient) of photons is far beyond the depletion width (W_D), and the generated charge carriers suffer recombination in the bulk. Many electrodes with higher current densities require multiple layers but it becomes difficult to decipher whether the poorer performance observed in thicker $CuWO_4$ electrodes is due to poor charge transport or if this restriction is due to the mechanical challenges of electrode construction. The evidence for poor charge transport is supported by the similar PEC response of $CuWO_4$ regardless of synthetic methods and thickness when illuminated with AM1.5G irradiation, as seen in Figure 3.1. Only the fraction of light absorbed near or in the depletion width in $CuWO_4$ results in collected charge.

Linear sweep voltammetry (LSV) is a typical experiment conducted in our laboratory to evaluate the ability of a photoanode to perform water oxidation under illumination. This experiment allows for the determination of onset potential, as well as the current density generated as a function of applied bias to an electrode. The shape of photocurrent generated during LSV provides insight into the overall efficiency of an

electrode, and the observed transient photocurrent under chopped light illumination provides insight into surface recombination events. LSV performed on $CuWO_4$ photoanodes as a function of pH establishes the propensity of $CuWO_4$ to photooxidize water in various electrolytes. Figure 3.1 provides a voltammogram on both electrochemically deposited and sol-gel $CuWO_4$ photoanodes in a pH 7 phosphate buffer, a typical electrolyte system used for studying photoelectrochemistry of oxide photoanodes.

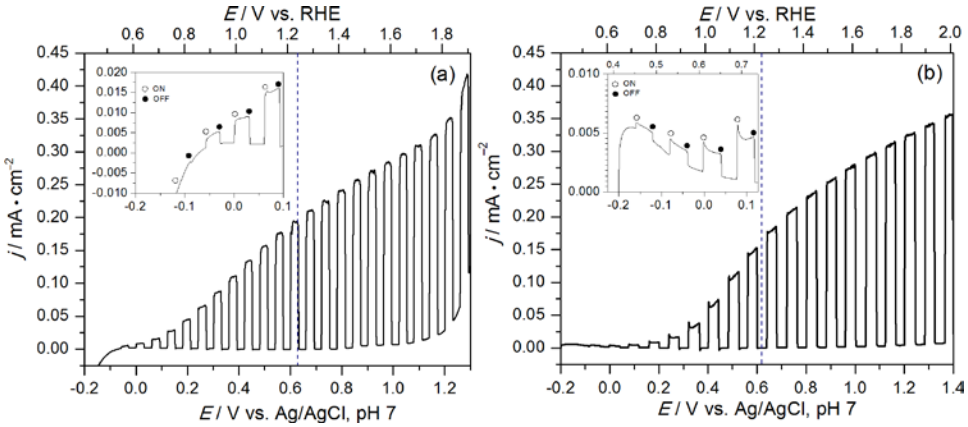

Figure 3.1 LSV trace of $CuWO_4$ electrodes prepared by a) electrochemical deposition and b) sol-gel spin casting under chopped illumination

The experiment was conducted in 0.1 M potassium phosphate buffer (pH 7) and the thermodynamic potential for water oxidation (1.23 V RHE) is noted by the blue line. **Inset.** Expansion of LSV to illustrate the onset of photocurrent

Under the application of simulated solar light, the onset of photocurrent begins at –0.15 V vs. Ag/AgCl (0.48 V RHE) in both electrodes. For comparison purposes, the top axis converts the potential using the Ag/AgCl reference electrode in aqueous solution at pH 7 to the reversible hydrogen electrode (RHE = NHE at pH 0) using the equation:

$$E_{RHE} = E_{Ag/AgCl} + 0.0591\ V \bullet pH + 0.199\ V \quad (5)$$

Electrochemically deposited $CuWO_4$ shows higher photocurrents at lower applied biases in comparison to sol-gel electrodes, which could be due to the presence of WO_3. WO_3 electrodes show a stronger take off of photocurrent in comparison to $CuWO_4$. Both electrodes show a similar near linear shape in the onset of photocurrent which indicates a sluggish kinetics of water oxidation. This slow onset in comparison to an ideal exponential take-off reduces the fill-factor and leads to lower overall efficiencies for

energy conversion. This slow onset of current indicates a large charge-transfer resistance to perform water oxidation at smaller applied biases, and by using a kinetically faster reactant such as H_2O_2, the photocurrent generated at lower potentials is slightly enhanced (Figure B.2).

Under simulated solar irradiation, a current density of 0.20 mA/cm^2 and 0.15 mA/cm^2 is observed at the thermodynamic potential (+0.62 V vs. Ag/AgCl, pH 7) in electrochemically deposited and sol-gel electrodes, respectively. Again, similar PEC properties are observed as the current densities generated in $CuWO_4$, regardless of synthesis, and are always on the same order of magnitude. This is also confirmed amongst the recent literature on various synthetic preparations of $CuWO_4$. In the dark, however, no current is passed until a bias of 1.1 V (2.125 V RHE) is applied. $CuWO_4$ requires an overpotential of 0.6 V to oxidize water in the dark. As can be seen in figure, the representative voltammogram of sol-gel synthesized $CuWO_4$ does not show such an early and strong onset of dark electrolysis, but rather electrolysis is very slow and begins 0.1 V more positive. This initial result indicated that $CuWO_4$ could perform electrocatalytic water oxidation; however a Tafel evaluation of the current generated reveals that this density is not sustained and is likely due to the oxidation of surface species on the electrode. After a short bulk electrolysis experiment, the dark current generated in $CuWO_4$ decreases significantly, as seen in Figure B.3. The Tafel slope for the dark electrolysis of water on $CuWO_4$ is very high (> 200 mV/decade), and is likely due to breakdown in reverse bias. For comparison the Tafel slope of $CoWO_4$, which is considered a water oxidation electrocatalyst, after annealed at 200 ºC has a slope of 60 mV/decade and 112 mV/decade after 500 ºC annealing.[16]

The charge-transfer resistance to water oxidation at the electrode-electrolyte interface, R_{ct}, was studied to understand the slow onset of current seen in a linear sweep voltammogram. R_{ct} was measured under 1-sun illumination using EIS methods at potentials where only photocurrent is generated due to PEC water oxidation.

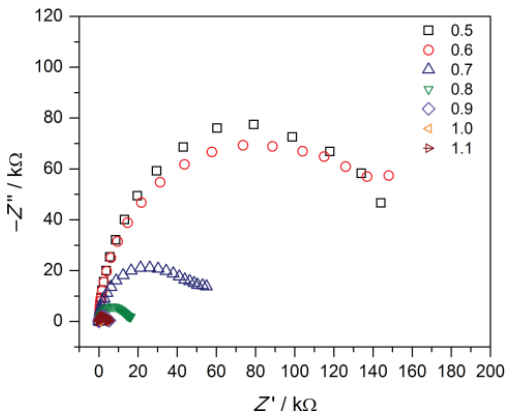

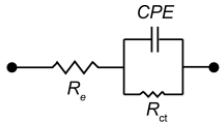

E / V *vs.* RHE	R_{ct} / Ω•cm^{-2}	*CPE-P* (α)	*CPE-T* (Q / s$^{\alpha}$•Ω^{-1}cm^{-2})	τ_{rxn} / s
0.5	162,210	0.966	3.25E-5	5.48
0.6	156,350	0.958	2.01E-5	3.2
0.7	51,940	0.936	2.04E-5	1.1
0.8	14,831	0.902	2.35E-5	0.30
0.9	4,927	0.892	2.35E-5	0.10
1.0	3,552	0.917	1.84E-5	0.046
1.1	4,675	0.950	1.40E-5	0.060

Figure 3.2 (a) Nyquist plot of EIS data under illumination at varying applied bias and (b) table of quantified circuit parameters.
The experiment was conducted on $CuWO_4$ thin films in 0.1 M KP_i buffer at pH 7 and AM1.5G irradiation at 100 mW/cm^2.

Under illumination, photocurrents start to generate in $CuWO_4$ at ~ 0.45 V RHE. However, the Nyquist plot presented in Figure 3.2a shows that not until the applied bias exceeds 0.7 V RHE under illumination does R_{ct} decrease significantly. In fact, from 0.9 – 1.1 V R_{ct} reaches a constant value of ~4,600 Ω. The calculated R_{ct} values and time constants, τ_{rxn}, of the water oxidation half reaction are tabulated in Figure 3.2b. This result led to a more thorough investigation of the electrode-electrolyte interface during PEC water oxidation. The circuit model seen in Figure 3.2 is one of the more straight forward circuits used to evaluate the overall resistance to electron transfer. This work continued through collaboration with my colleague, Kayla Pyper, and further analysis reveals a more detailed system. Specifically, by evaluating the capacitive elements under several illumination intensities, and using multiple methods to evaluate the EIS data, we determined that a mid-gap state dictates the photoelectrochemical properties of $CuWO_4$, which will be discussed in section 3.3.[6]

As the pH of the buffered electrolyte decreases, the photocurrent at a set potential (vs. Ag/AgCl) decreases, shown in Figure 3.3.

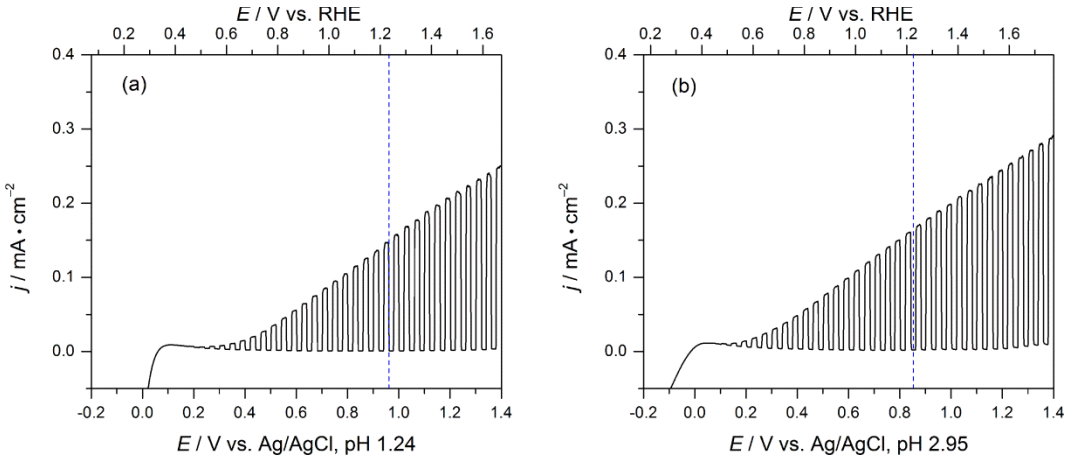

Figure 3.3 LSV trace of a $CuWO_4$ electrode under chopped illumination measured in 0.1M $HClO_4$ (a) and 0.1M acetate buffer (b).
The thermodynamic potential for water oxidation (1.23 V RHE) is noted by the blue line.

In a pH 3 acetate buffer electrolyte solution, the onset of photocurrent shifts anodically to +0.1 V, with a dark cathodic current at potentials less than 0.1 V (vs Ag/Cl). Here, the chopped light experiment shows that no dark anodic current is observed upon sweeping out to +1.4 V, but that the photocurrent at the thermodynamic potential is 0.16 mA/cm^2. Similarly, in a pH 1 solution of 0.1 M perchloric acid, there is no dark anodic current in the scanned potential window, and the photocurrent density at the thermodynamic potential is similar (0.15 mA/cm^2). These results are one of the first indicators of the selectivity for water oxidation using $CuWO_4$ in comparison to its congener, WO_3. WO_3 is known to oxidize certain species in solution which are kinetically more accessible, such as acetate and perchlorate, resulting in large current density increases in comparison to solely performing water oxidation. In the LSV traces seen above, the current density and shape of the curve is similar regardless of electrolyte species. This comparison of selectivity on $CuWO_4$ to WO_3 will be discussed further in section 3.5. Figure B.4 shows nearly superimposable LSV traces in a KPi buffer at pH 3, 5 and 7 when plotted vs. RHE, reaffirming $CuWO_4$'s Nernstian response to solution pH.

3.3 EIS studies of a mid-gap state in $CuWO_4$

The sol-gel $CuWO_4$ electrodes were used to further investigate the capacitive elements of the electrode/electrolyte interface under illumination when performing water oxidation. These experiments concluded that the onset of photocurrent was dictated by

the presence of a mid-gap state that participates in water oxidation. A schematic of the electron transfer processes can be seen in Figure 3.4.

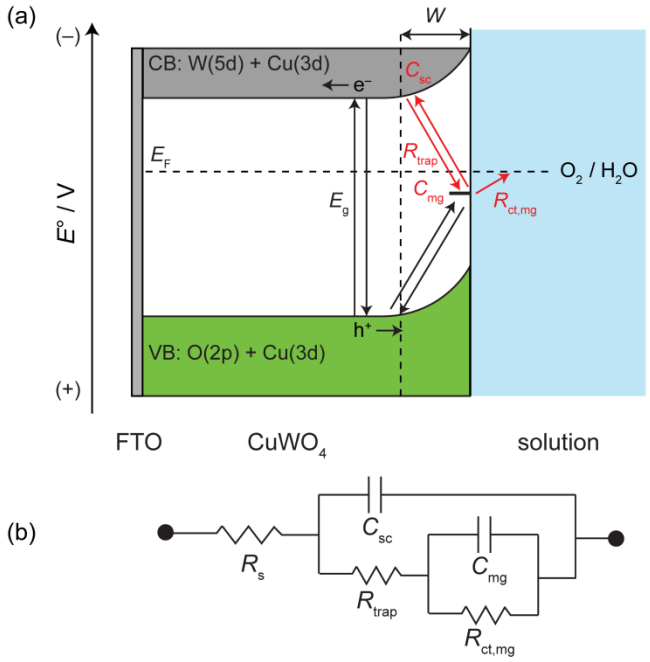

Figure 3.4 (a) Electron transfer events in $CuWO_4$ during water oxidation and (b) electrical circuit modeled to fit the EIS data.

Furthermore, the circuit used to fit the data in the potential range of interest is presented in Figure 3.4b. This circuit differs from the initial circuit described in Figure 3.2b in that an additional RC circuit was added in series to the existing parallel association. This equivalent circuit accurately models the photoelectrochemical data, and the EIS results agree well with recent theory in which PEC water splitting on a semiconductor film electrode proceeds through a mid-gap state.[7]

In this thesis, the major conclusions of the EIS studies will be briefly presented as they pertain to PEC water oxidation on $CuWO_4$, but a more in depth discussion of the results can be found in reference 12. Using EIS, the region from 0.8 – 1.0 V RHE was modeled using circuit presented in Figure 3.4b to gain insight into the cause for the large overpotential and sluggish onset of photocurrent. By measuring the overall capacitance of the electrode as a function of a large frequency range (Mott-Schottky analysis), electronic transitions, such as those to a mid-gap state that typically take place on a longer time scale can be observed. As seen in Figure 3.5, a change in slope to a near constant capacitance between 0.8 – 1.0 V suggests Fermi level pinning due to a mid-gap state.[8]

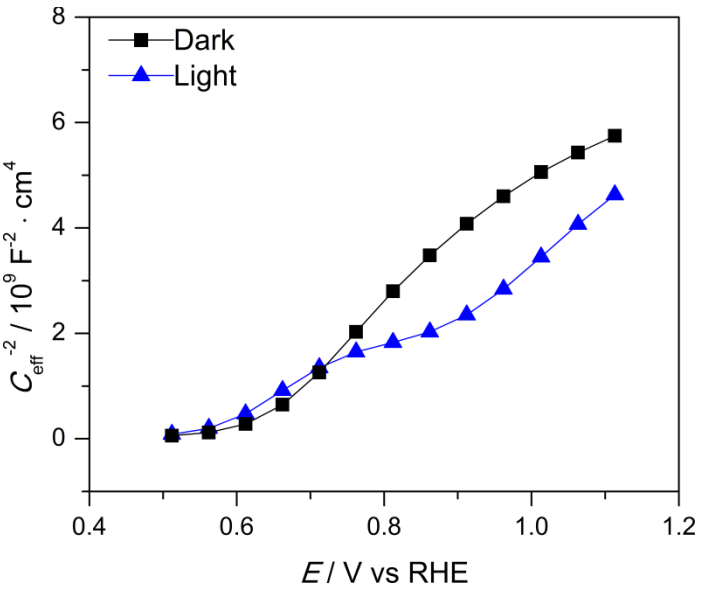

Figure 3.5 Mott-Schottky analysis of $CuWO_4$ at 100 Hz in a pH 7 0.5 M KB_i buffer.

The change to near zero slope in the Mott-Schottky analysis is more prevalent under illumination at higher frequencies, but these changes can also be identified at lower frequencies in the dark, suggesting that this mid gap state in $CuWO_4$ is permanent.[9–11]

A Nyquist plot evaluates the impedance due to charge transfer resistance (Z') and impedance due to capacitance (Z'') as a function of frequency. An example Nyquist plot of $CuWO_4$ at 0.96 V RHE under illumination, as seen in Figure 3.6, presents two separate semicircles which indicate two separate charge-transfer events occurring at the electrode surface.

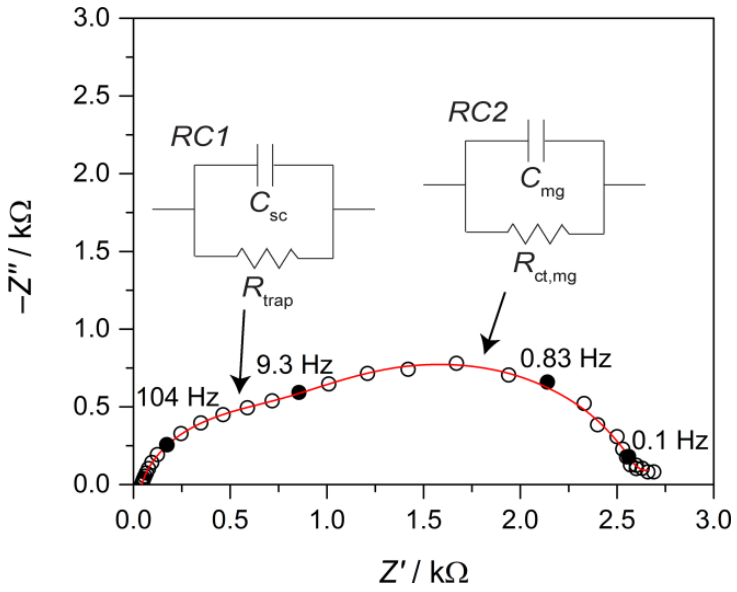

Figure 3.6 Nyquist plot of $CuWO_4$ at 0.96 V RHE under AM1.5G illumination

The two separate semicircles are further evidence for the presence of a mid-gap state participating in the mechanism of electron transfer during photoelectrochemical water oxidation on $CuWO_4$. Each process corresponds to an *RC* circuit: *RC1* is attributed to non-Faradaic capacitive events in the depletion region, and the second semicircle, *RC2*, commonly represents the interaction with the solution, where a Faradaic reaction can be monitored.[12] Non-Faradaic processes typically respond to higher frequency perturbations since interacting with the solution is prevented by the fast voltage switching. The opposite is true for Faradaic processes which need lower-frequency perturbations to measure interfacial electron transfer. Construction of a Bode plot allowed for monitoring the change in capacitive processes as a function of the applied potential and more than one capacitive event can be deconvoluted in a plot of phase angle vs. log frequency.

Finally, the pathway of electron transfer was determined by quantifying the various resistances and capacitances of both the space charge region and mid-gap state in $CuWO_4$ (Figure B.5). The quantified values were acquired from the output of the fit to the Nyquist data using the model circuit. As the Fermi level was unpinned in $CuWO_4$ near 1 V RHE, there is a sharp decrease in the capacitance of the mid-gap state which is found to be concomitant with an increase in photocurrent. These observations all in concert suggest a process where electrons from water are stored in the mid-gap state under illumination then, at higher applied biases, holes from the valence band are

transferred to the state resulting in successful water oxidation. The build-up of charge in the mid gap state suggests that photogenerated holes reaching the surface state is a rate-limiting process in $CuWO_4$. The mechanism of water oxidation proceeding on $CuWO_4$ is hypothesized to be different than on WO_3, which leads to the distinct photoelectrochemical properties discussed in section 3.4. These differences provide some of the advantageous properties observed on $CuWO_4$, particularly the stability of the electrode under illumination.

3.4 Chemical Stability of $CuWO_4$

The Faradaic efficiency and photostability of $CuWO_4$ photoanodes were evaluated by varying the pH of a KP_i buffer solution (pH 3, 5 and 7). When producing O_2 from H_2O, the Faradaic efficiency is determined by taking the total charge passed during the experiment and dividing by $4F$ (F = Faraday's constant 96485 C/mol e^-) because it is a four electron oxidation. Photostability measurements were carried out under simulated 1-sun illumination (AM1.5G 100 mW/cm^2), whereas Faradaic efficiency measurements were carried out at 3-sun illumination (300 mW/cm^2) to increase the O_2 signal in the fluorescence detector used for quantifying the produced O_2. In a pH 7 KPi buffer, sol-gel prepared $CuWO_4$ photoanodes are more stable in acid (pH 3 and at pH 5) than at pH 7 in 0.1 M KP_i, as seen in **Figure 3.7**.

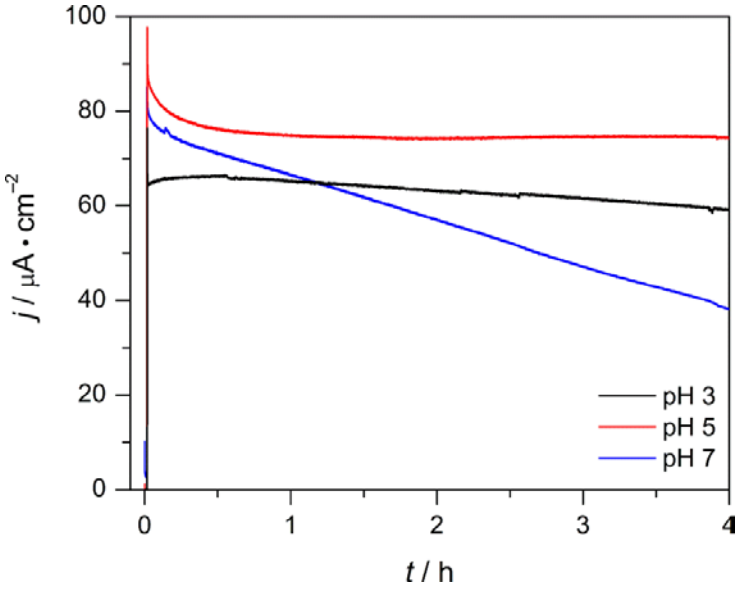

Figure 3.7 j–t curves oxidation on $CuWO_4$ films in 0.1 M KPi at 1.23 V RHE under AM1.5G illumination at 100 mW/cm^2

Over a 4-hour illumination period, $CuWO_4$ maintains 90% and 88% of its initial steady-state current at pH 3 and 5, respectively. However, at pH 7, j_{ph} drops to only 49% of the initial steady-state current. Regardless of the pH, $CuWO_4$ shows high Faradaic efficiencies for O_2 production as seen in Figure 3.8: 87, 79, and 100% for pH 3, 5, and 7 in KP_i buffer respectively.

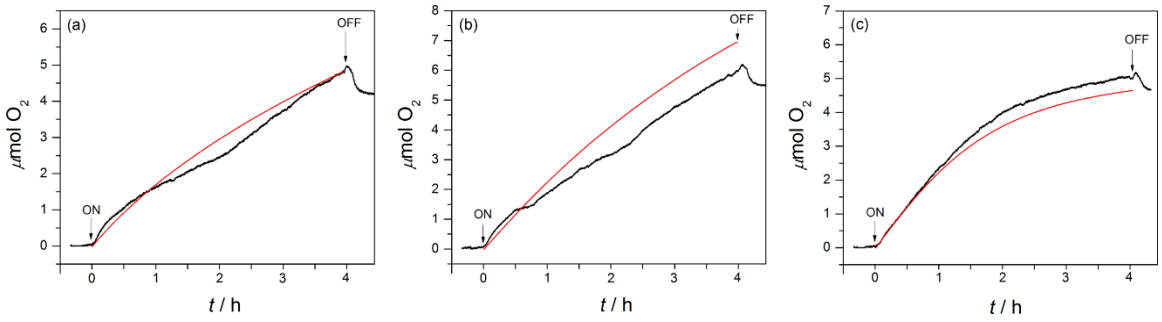

Figure 3.8 O_2-detection experiments for water oxidation on $CuWO_4$ films
The experiments were carried out in 0.1 M KPi buffer at 1.23 V under AM1.5G illumination at 300 mW/cm2: pH 3 (a), pH 5 (b); pH 7 (c).

To shed more light on the source of $CuWO_4$ photoanode degradation, a methanol oxidation experiment was carried out in pH 7 KP_i buffer containing 20% MeOH by volume. This experiment allows for an answer to the question: at pH 7, does $CuWO_4$ undergo acid-base chemistry giving rise to photocurrent decay over time in KP_i, or do intermediates generated during water photooxidation (but not methanol oxidation) lead to decay? Figure B.6 shows that $CuWO_4$ is quite stable when oxidizing methanol in a pH 7 KP_i buffer, with $j_{ph} \sim 125$ μA/cm^2 that decays less than 6% after 4 h of constant illumination. This enhanced stability indicates that although pH may be a contributing factor for catalyst degradation when oxidizing water at pH 7, it is not the major culprit. This result is in agreement with Figure 3.14 which determined that in the dark, $CuWO_4$ is chemically stable at pH 7.

A second question emerges regarding electrode stability in buffered solutions. At pH 7, is it the proton (pH) or the anion of the buffer that results in degradation? To address this question, a potassium borate buffer, KB_i at pH 7 was prepared. The long-term illumination results indicate that a pH 7 in KB_i, $CuWO_4$ photoanodes show excellent stability, illustrated in Figure 3.9.

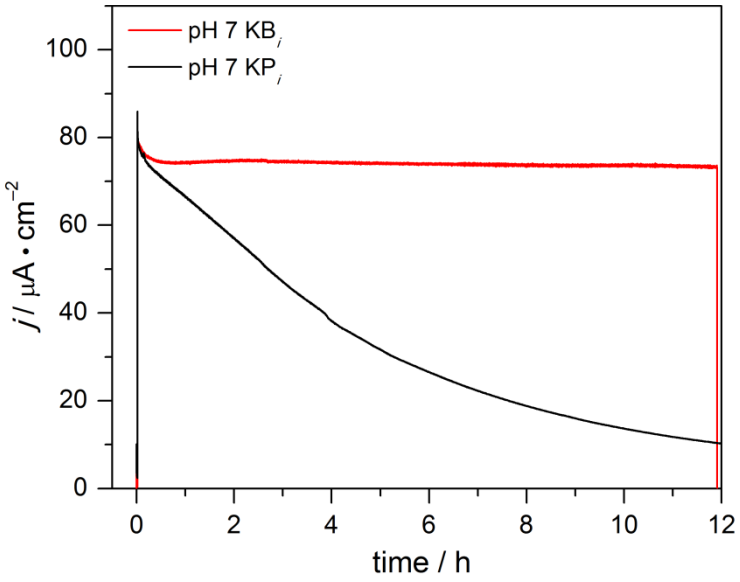

Figure 3.9 *j*–t curve comparison between water oxidation in pH 7 KBi (red) and KP_i (black)
The experiment was conducted at 1.23 V RHE and under AM1.5G illumination at 100 mW/cm^2.

The electrode maintains 93% of its initial photocurrent density (j_{ph}) after 12 h of continuous 1-sun illumination. In contrast, in pH 7 KP_i buffer, j_{ph} drops 50% after 4 h, and only 15% of the initial photocurrent remains after 12 h of continuous illumination. Additionally, $CuWO_4$ maintains a high Faradaic efficiency (96%) for O_2 evolution at pH 7 in KB_i, plotted in Figure 3.10. These results show that the phosphate anion, not pH negatively affects the stability of $CuWO_4$ in aqueous electrolyte.

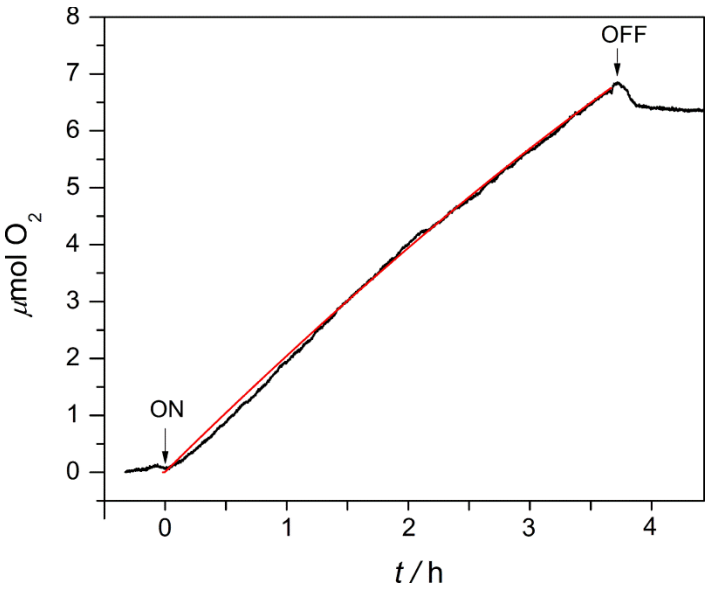

Figure 3.10 O_2-detection experiments for water oxidation on CuWO4 films in a pH 7 KBi buffer.
The experiment was carried out at 1.23 V RHE at 300 mW/cm^2. Black and red lines represent measured O_2 and theoretical yield based on coulometry respectively.

The relative stability of $CuWO_4$ in a KB_i buffer in comparison to a KP_i buffer is intriguing and the presented work contributes to the growing empirical knowledge of how the electrolyte functions in PEC oxidations—particularly with regard to electrode stability. For example, WO_3 photoanodes illuminated in acidic solutions containing sulfate and chloride are quite stable, but show low Faradaic efficiency for water oxidation due to competitive anion oxidation.[13] At higher pH, the Faradaic efficiency of WO_3 for water oxidation increases, but it then suffers from its own acid-base instability. Also, interest is growing in carbonate buffers and the stability and rates of water oxidation on $BiVO_4/SnO_2/WO_3$,[14] TiO_2,[15] and $CuWO_4/BiVO_4$[16] photoanodes have been measured over extended periods of illumination. The phosphate and borate buffers employed show that the interaction between the anion and the electrode surface plays a larger role on stability than does pH alone. Although the phosphate ion negatively affects electrode stability for water oxidation on $CuWO_4$, methanol oxidation proceeds with minimal degradation. This observation indicates that either anion interactions with the electrode surface or the basicity of the anion affects long-term stability. The speciation of inorganic phosphate, P_i, in a 0.1 M KP_i solution at pH 7 is 0.061 M $H_2PO_4^-$ and 0.039 M HPO_4^{2-}. In contrast, for inorganic borate, B_i, a 0.1 M KB_i solution at pH 7 is composed of 0.0993

M H_3BO_3 and 0.0007 M $H_2BO_3^-$. pK_1 of phosphoric acid, H_3PO_4, is 2.12, whereas pK_1 of boric acid, $B(OH)_3$, is 9.24. Slightly higher photocurrent is observed in the LSV in pH 7 KP_i in comparison to KB_i (Figure B.7) which is likely due to the ionic strength difference of the electrolyte used. Adding NaCl or Na_2SO_4 as supporting electrolytes increases the ionic strength of the electrolyte, supported by the increase in photocurrent in those experiments, presented in Figure B.8.

The interaction of the electrolyte with the surface of $CuWO_4$ during a long-term illumination experiment was probed by SEM. Figure 3.11 shows the surfaces before and after illumination in 0.1 M KP_i and KB_i at pH 7.

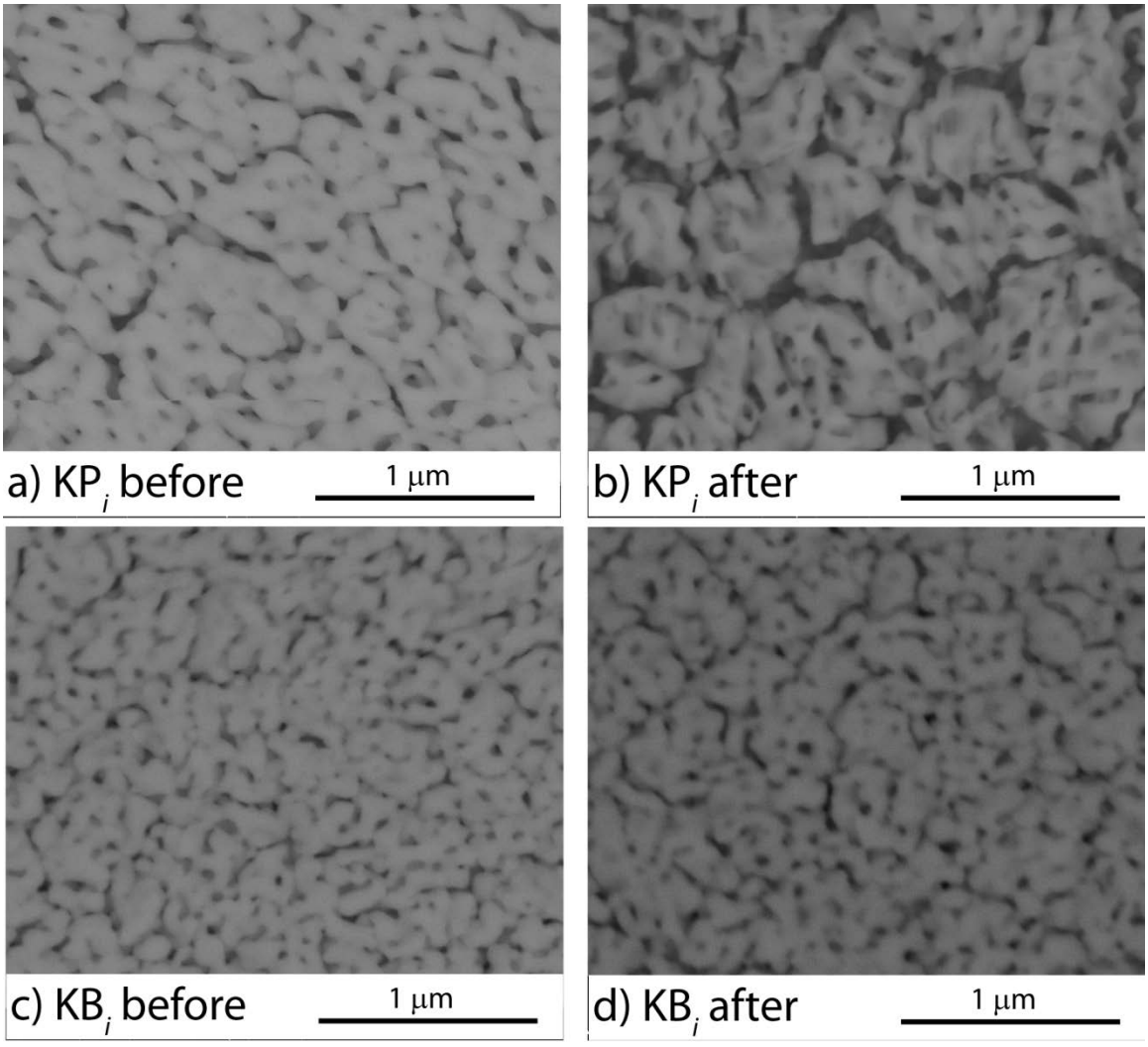

Figure 3.11 SEM studies of $CuWO_4$ surface in a) KP_i before and after b) illumination for 12 h at pH 7, and c) KB_i before and after d) illumination for 12 h at pH 7

Before illumination, the surface is made of uniformly distributed $CuWO_4$ crystallites, typical of the sol-gel electrode. After 12 h of illumination in pH 7 KP_i, the surface of the film is significantly altered. The crystallites have been thinned and look like they are dissolving into the electrolyte. There is also is increased cracking on the film surface and the FTO substrate is more exposed. This physical alteration of the electrode surface takes place over the 12 h illumination period as the current density decreases significantly. In a KB_i electrolyte, the surface of the electrode is virtually unchanged during the 12 h illumination period. The current density is maintained and the $CuWO_4$ crystallites do not show any significant sign of degradation. There may be a slight increase in area between the crystallites, but that does not result in a decrease of photocurrent.

The films were also studied by XPS to evaluate the change in the electrode surface during prolonged PEC water oxidation as seen in Figure 3.12.

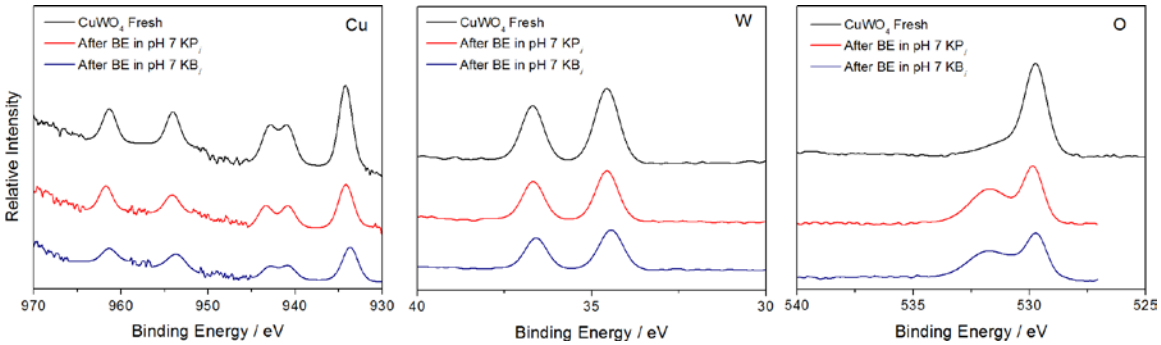

Figure 3.12 XPS of fresh $CuWO_4$ compared to $CuWO_4$ after 12 h illumination in pH 7 Kb_i and KP_i

The Cu (2p) and W (4f) peaks are not altered during prolonged illumination. This hints that there are no significant oxidation state changes in Cu^{2+} and W^{6+}, which is expected. The O(1s) peak however, shows a significant change during the course of the experiment. The peak indicative of OH^- (531.8 eV) increases in relative intensity compared to lattice oxygen (529.8 eV). During prolong PEC water oxidation, the surface of the electrode becomes predominantly OH^-. Comparatively, there is no major difference in the O, Cu, or W species found on the electrodes tested in KB_i vs. KP_i. This hints that no new species were formed other than the change in surface termination. The presence of P and B was also tested for using XPS. However, no unique peaks indicative of phosphate or borate adsorption onto the surface, or a new phosphorus/boron containing species was identified. This indicates the formation of phosphorus containing species on the surface is

not a degradation mechanism in these electrodes. However the experimental results directly show that the presence of KP_i leads to the degradation of the electrodes.

The importance of photon flux on the stability of $CuWO_4$ electrodes was evaluated. At three times the sun's output, $CuWO_4$ degrades more rapidly. Though the rate of degradation increases in both KP_i and KB_i buffers under 3-sun illumination, the same trend of stability is observed as pH is varied: electrodes maintain 60, 70, and 16 % of the initial photocurrent in pH 3, 5, and 7 KP_i buffers, respectively, seen in Figure B.9, and $CuWO_4$ maintains 74% of the initial photocurrent density in pH 7 KB_i buffer (Figure B.10) under 3-sun illumination. This behavior again confirms the relative stability of $CuWO_4$ photoanodes in KB_i buffer in comparison to KP_i. The rates of degradation and the decay curve in pH 3 and 5 KP_i and pH 7 KB_i are similar, where pH 7 KP_i has a more distinct decay curve.

The accumulation of charge at the surface due to the higher photon flux may contribute to a faster rate of degradation, which is evident in the LSVs recorded under 100 *vs*. 300 mW/cm^2 in Figure B.11. Besides the obvious increase in photocurrent under higher irradiance, an additional difference between the two *j-E* profiles is the significant transient photocurrent at higher irradiance, demonstrating increased recombination on the time-scale of the LSV experiment (the scan rate is 20 mV/s). This accumulated, chemically unproductive charge may lead to faster degradation. Of course, charge recombination goes undetected in the bulk electrolysis experiments at steady state since this charge is not collected. So, although it will not contribute to the measured Faradaic efficiency, recombination may still play a role in the electrode stability. One additional note is that in all photostability (j_{ph}–t) experiments at 1.23 V RHE, the current returns to ≤ 1 μA/cm^2 without a large cathodic response regardless of pH or irradiance after turning off the light source. Small cathodic transient currents are evident at lower potentials in the LSV, but at 1.23 V RHE, there is minimal recombination when the light is chopped off. Another consideration in evaluating $CuWO_4$ photoanodes at 100 mW/cm^2 (1-sun) *vs*. 300 mW/cm^2 (3-sun) illumination is the stability as a function of total charge passed (moles of H_2O produced). In KB_i buffer at pH 7 with no added NaCl, $CuWO_4$ photoanodes pass 4.59 C at 1-sun for 12 h *vs*. 3.85 C at 3-suns for 4 h. That is, more charge is passed at lower irradiance with no degradation, and the total charge passed is

not detrimental to the stability. This behavior is also true with added 100 mM NaCl: 3.17 C *vs*. 2.65 C are passed under the same conditions. Therefore it is not likely that the same degradation pathways describe both the buffer effect and the irradiance effect.

3.5 Photoelectrochemistry of $CuWO_4$ in Comparison to WO_3

These presented results are significant in developing a comparison between $CuWO_4$ and WO_3 to identify unique photoelectrochemical properties in tungstate photoanodes. When we first began studying $CuWO_4$, electrochemically deposited electrodes contain a slight excess of W in the form of WO_3, mentioned in section 2.2. This necessitated further comparison between the two materials and led to the discovery of the advantages associated with using $CuWO_4$. Specifically, increased light absorption due to a smaller band gap and increased stability of these electrodes are two properties in which many PEC results are focused.

In order to evaluate the relationship between the smaller band gap and the ability to convert lower energy photons into photocurrent, LSV experiments were performed. Figure 3.13 is a comparison between electrodeposited $CuWO_4$ and WO_3 photoanodes under various cut off filters. With a band gap of 2.7 eV, WO_3 will be incapable of generating photocurrent for light having wavelengths greater than 475 nm.

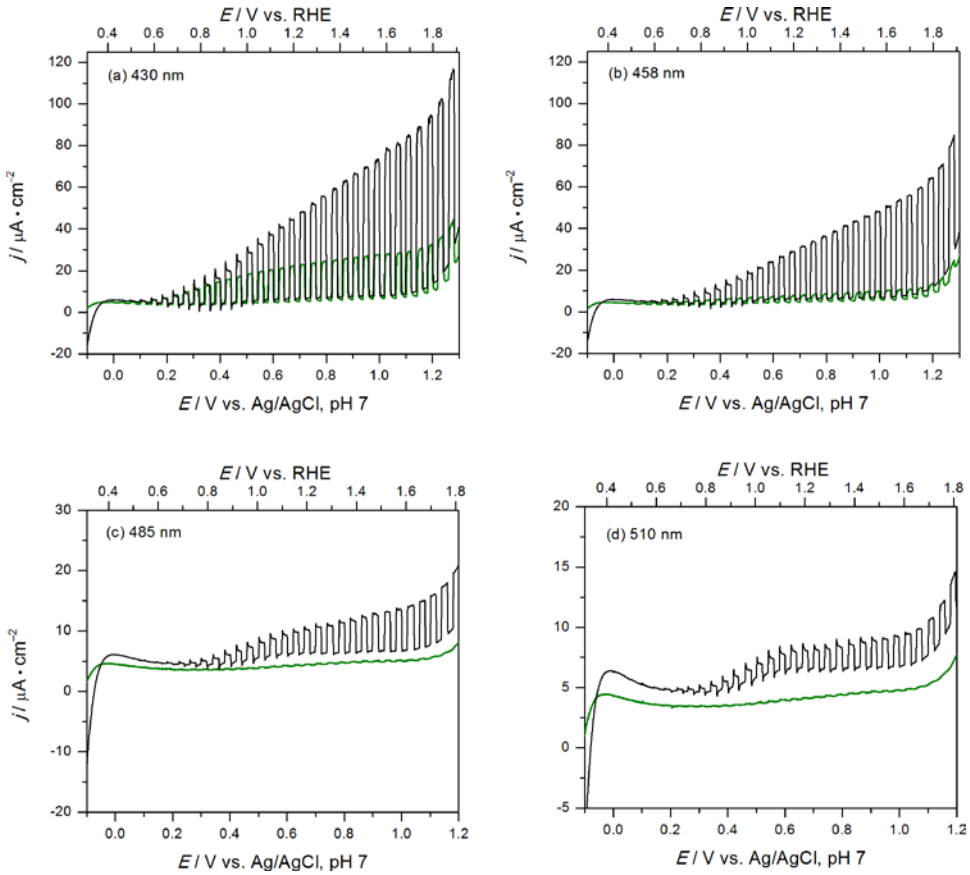

Figure 3.13 LSV of $CuWO_4$ (black) and WO_3 (green) electrodes using a series of cut-off filters under chopped illumination measured in 0.1 M KPi buffer (pH 7).
The cut-off filters used are 430 nm, 458 nm, 485 nm, and 510 nm in panels (a)–(d)

Figure 3.13c and d show that for $\lambda > 485$ nm, WO_3 has negligible photocurrent while $CuWO_4$ demonstrates photoinduced current, indicated by the square wave form observed in the chopped light experiment with the 485 and 510 nm cutoff filters applied. Figure Figure 3.13b and c show that photocurrent in $CuWO_4$ significantly drops between a 458 nm and 485 nm cutoff filter. This again is likely due to low photon absorptivity and collection of charge carriers in the bulk. Regardless, the result of this experiment was important as it helped justify our efforts for studying tungstate anodes, and confirmed that lower energy MMCT's are capable of generating sufficient photovoltages capable of splitting water.

Our research also focuses on the relative stability of new materials we produce in our lab compared to the current precedent. The first study we conducted was to measure

the chemical stability of $CuWO_4$ in comparison to WO_3. WO_3 is an Arrhenius acid and is known to decompose under neutral or basic conditions according to the reaction:

$$WO_3(s) + H_2O(l) \rightarrow WO_4^{2-}(aq) + 2H^+(aq) \quad (8)$$

Our hypothesis was that because $CuWO_4$ in an insoluble tungstate (K_{sp} = 1.3 × 10^{-8} in H_2O at 22 ºC)[17] it would show increased stability in comparison to WO_3 at pH 7 in the dark. Performing linear sweep voltammetry on a freshly prepared $CuWO_4$ film followed by storing the film in KP_i electrolyte for 12 hours, then repeating the sweep shows only a slight decrease in the photocurrent density (0.17 to 0.15 mA/cm^2 at +0.5 V vs. Ag/AgCl), illustrated in Figure 3.14. The same experiment performed on a WO_3 film shows that the photocurrent decreases dramatically from 0.17 to 0.03 mA/cm^2. This experiment is repeatable using a sol-gel $CuWO_4$ electrode and Figure B.12 shows that over 80% of the photocurrent is retained after soaking in a pH 7 KP_i electrolyte solution overnight.

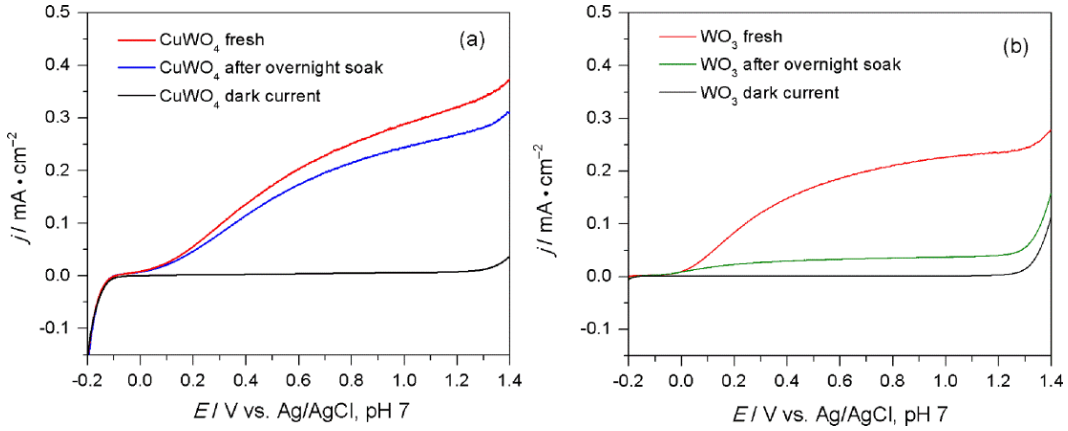

Figure 3.14 LSV trace of $CuWO_4$ (a) and WO_3 (b) in 0.1M KP_i at pH 7

Though there is an abundance of literature on WO_3 evaluating its efficiency for PEC water oxidation on a short time scale, there hadn't been a study evaluating its photostability as a function of time. Therefore, we also wanted to evaluate the relative stability of $CuWO_4$ in comparison to WO_3 under illumination in a pH 7 electrolyte.

Bulk electrolysis experiments performed under AM 1.5G illumination demonstrate that $CuWO_4$ films in electrolyte solutions at pH 7 are more photostable in comparison to WO_3. Figure 3.15 compares the current density observed as a function of illumination time in KP_i buffer for electrodeposited $CuWO_4$ and WO_3.

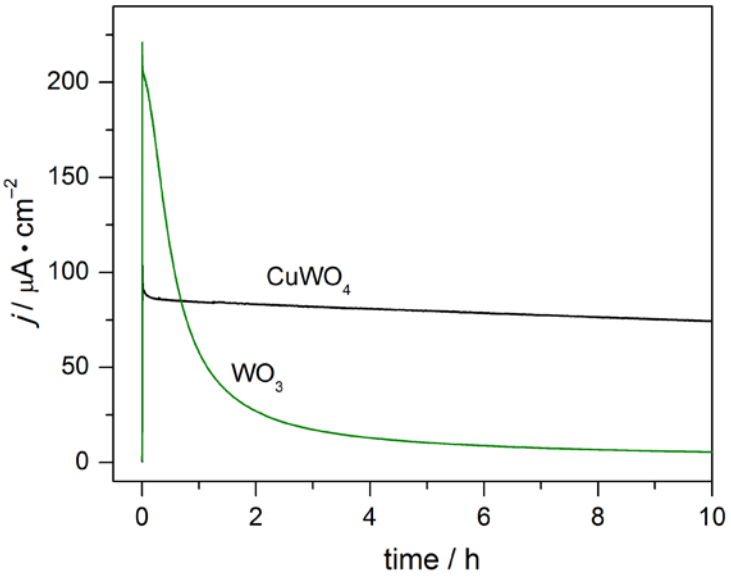

Figure 3.15 *j*-t comparison of electrochemically deposited $CuWO_4$ and WO_3 at 0.5V vs Ag/AgCl in 0.1 M KP_i (pH 7).

The results of Figure 3.15 typify $CuWO_4$ in comparison to WO_3 photoanodes for PEC water splitting. WO_3 photoanodes produce significantly greater photocurrents initially in comparison to $CuWO_4$, but in a relatively short timescale, these electrodes degrade and an irreversible loss of photocurrent is observed. $CuWO_4$ on the other hand, shows increased stability when performing water oxidation. Electrochemically deposited $CuWO_4$ photoanodes do not show infinite stability in pH 7 phosphate buffer and as discussed the, stability of $CuWO_4$ is dependent on the electrolyte composition and pH. However, the electrochemically deposited $CuWO_4$ electrodes do show an increased relative stability when compared to sol-gel $CuWO_4$ electrodes. One potential explanation of the slightly differing results could be the relative electrode thickness and robustness. Electrochemically deposited electrodes are much more robust and although degradation takes place, the degradation processes are not as rapid on such a timescale, and over the 12 h illumination period electrochemically deposited electrodes do not suffer significant from degradation. Additionally, the stability experiments conducted on the sol-gel electrodes were performed at potentials nearly 150 mV more positive than the electrochemically deposited electrode. And, as will be discussed in Chapter 4, at zero applied bias even composite $CuWO_4$-WO_3 electrodes show improved stability when compared to applied bias chemistry.

Sol-gel $CuWO_4$ photoanodes show very high stability over a 12 h illumination period in a pH 7 KBi buffer. Therefore, a comparison experiment was conducted using a sol-gel $CuWO_4$ electrode in comparison to a sol-gel WO_3 electrode. The stability of $CuWO_4$ in pH 7 KB_i buffer in comparison to that observed for WO_3 shows a dramatic improvement. Figure 3.16 shows that only 8% WO_3's its initial photocurrent remains after 12 h. Furthermore, WO_3 degrades more rapidly in phosphate buffer at pH 1, 3, and 5,[18] providing another PEC distinction between $CuWO_4$ and WO_3.

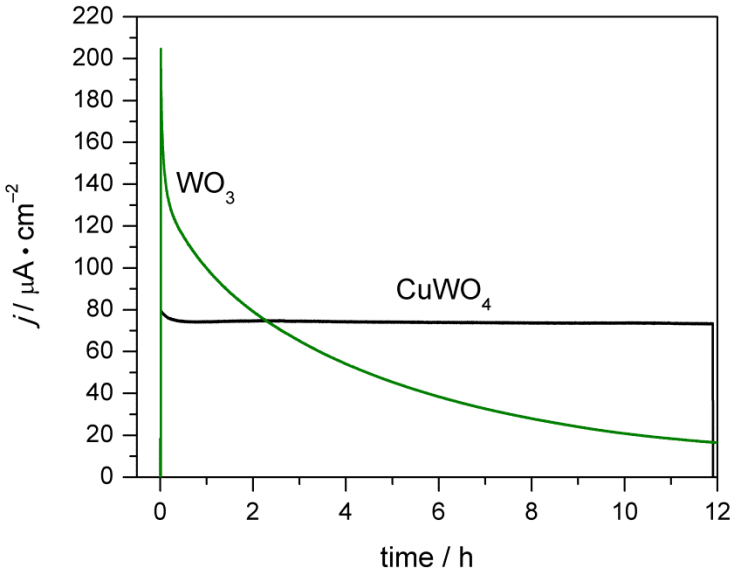

Figure 3.16 *j*-t comparison of $CuWO_4$ and WO_3 electrodes in KB_i buffer
The experiment was conducted at 1.23 V RHE in 0.1 M KBi buffer at pH 7 under 100 mW/cm^2 AM1.5G illumination.

In additional to photostability, chemoselectivity is now recognized as a key metric in assessing new materials for solar water oxidation. The growing emphasis to demonstrate that the product of PEC water splitting reactions is indeed oxygen led to a competition study between $CuWO_4$ and WO_3 in the presence of Cl^- ions. This competing anodic reaction is a major limitation for WO_3, considering the planet's most abundant salt electrolyte is sodium chloride (sea water is 2% chloride by mass). Photoanodes that preferentially oxidize anions rather than water often show unusually high photostability. In contrast to this observation, $CuWO_4$ photoanodes show Faradaic efficiency for water oxidation that is near unity in equimolar KB_i and NaCl at pH 7, advancing its attraction as a photoanode, shown in Figure 3.17a.

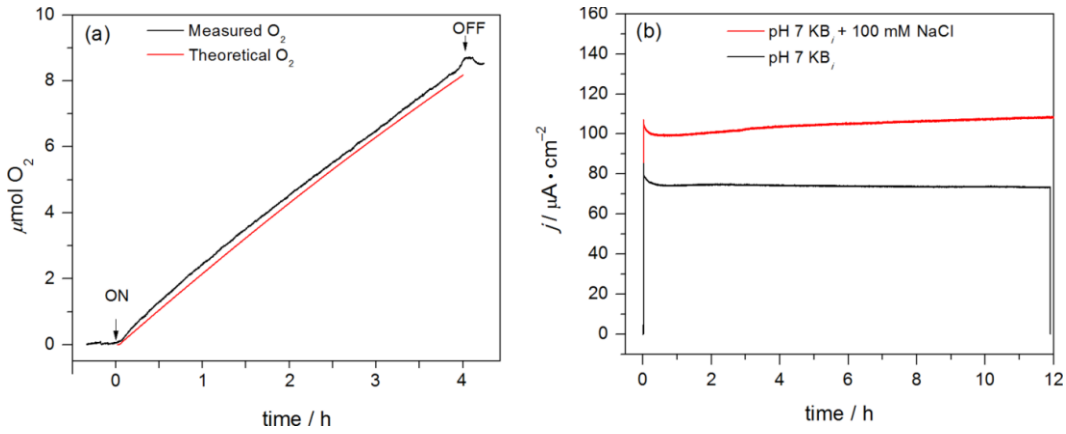

Figure 3.17 O_2 experiment (a) and *j*-t comparison of $CuWO_4$ in KB_i buffer under AM1.5G 100 mW/cm2 illumination

Additionally, the *j-t* profiles in 0.1 M KB_i and 0.1 M KB_i with 100 mM NaCl are stable under 100mW/cm^2 (Figure 3.17b) irradiation and similar under 300 mW/cm^2 (Figure B.13) irradiation, hinting that the same reaction is occurring on the electrode surface. These results were also confirmed in a pH 5 KP_i buffer, where similar faradaic efficiencies and decay profiles were observed with and without 100 mM NaCl (Figure B.14–16) A quantitative analysis for Cl_2 by a standard starch-iodide test was conducted and unambiguously shows that WO_3 performs quantitative Cl^- oxidation (100% Cl_2 Faradaic efficiency) in 0.1 M NaCl at pH 5, whereas $CuWO_4$ performs H_2O oxidation in pH 7 KB_i with 100 mM NaCl ($\leq$ 2% Cl_2 detected). Images of the PEC cells after the experiment (Figure 3.18) clearly show the presence of I_3^- after injection of $NaI_{(aq)}$ into the cell to produce Cl_2.

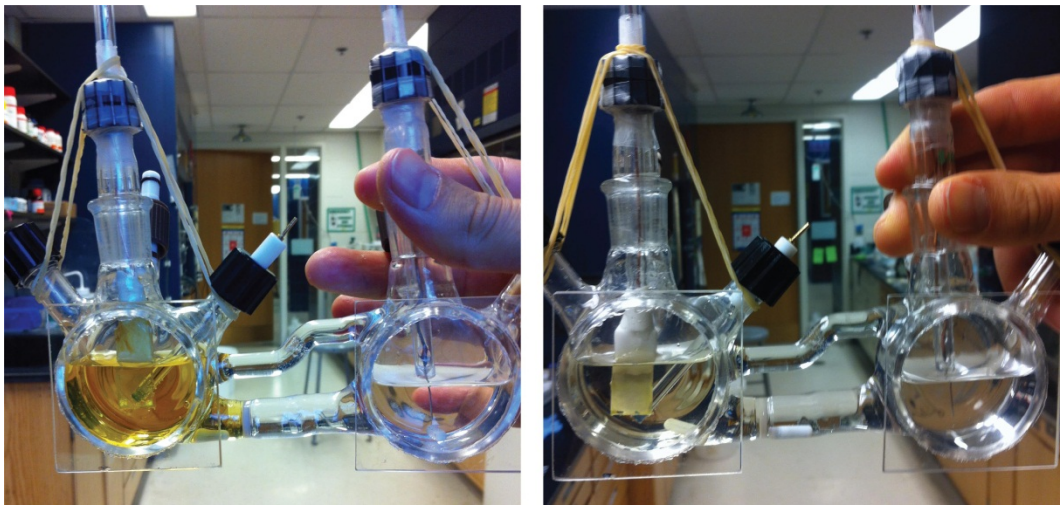

Figure 3.18 Images of PEC cells after *j*-t experiment using WO_3 (left) and $CuWO_4$ (right) in buffer containing Cl^-
The WO_3 experiment was conducted in pH 5 solution containing 0.1 M NaCl and the $CuWO_4$ experiment was conducted in a 0.1 M KB_i buffer containing 0.1 M NaCl

The properties of $CuWO_4$ in comparison to WO_3 regarding efficiency and stability photoanodes may be due to the distinct differences in the electronic structure of the two materials. The atomic orbital parentage of the valence bands in these two materials differ. In $CuWO_4$, Cu(3d) and O(2p) states dominate the top of the valence band, raising its energy nearly 0.5 eV compared to WO_3, whose valence band is predominantly O(2p) in character. More importantly, as discussed in section 3.3, water oxidation is mediated by a mid-gap state on $CuWO_4$. The sluggish kinetics of this mid-gap state may decrease the driving force for Cl^- oxidation. Furthermore, if water species are adsorbed on surface states in $CuWO_4$, e^- transfer between $H_2O_{(ads)}$ and the electrode surface would be more facile than transfer to Cl^-. Additionally, the Cu-based states may be a cause for the increased stability on $CuWO_4$. A known degradation pathway in WO_3 is the formation of W-peroxy species during PEC water splitting, which leads to degradation of the electrode surface and a loss of activity. In $CuWO_4$ rather, Cu-states participating directly in the mechanism of water oxidation may circumvent the peroxy-based degradation process leading to more stable photoanodes.

3.6 Conclusion

It was shown that the onset potential for photooxidation of water is dictated by a Cu-based redox couple positioned at 0.45 V *vs.* RHE. EIS measurements were utilized to

monitor the process of e^- transfer taking place and a mid-gap state that dictates the PEC properties of $CuWO_4$. This state was identified by comparing a deduced electrochemical circuit to theory. The chemical stability of $CuWO_4$ was evaluated and it was shown that in 0.1 M KP_i buffer, $CuWO_4$ photoanodes show better stability at lower pH and have a Faradaic efficiency for O_2 production of 87, 79, and 100 % at pH 3, 5, and 7 respectively. An electrochemically deposited $CuWO_4$ shows greater stability in comparison to sol-gel $CuWO_4$. Moreover, in a pH 7 KB_i buffer, there is minimal degradation after 12 h of continuous photoelectrochemical water oxidation under 100mW/cm^2 illumination, indicating that the electrolyte composition is an important determinant of long-term stability. In the presence of chloride, the Faradaic efficiency remains high in both KP_i and KB_i buffers, important for the potential use of sodium chloride as a suitable electrolyte in large scale use. This chapter also presented a side by side comparison of the PEC properties of $CuWO_4$ in comparison to WO_3. First, it was learned that the $CuWO_4$ is significantly more stable in the dark when stored in a pH 7 electrolyte when compared to WO_3. This was evaluated experimentally by conducting voltammetry before and after storing the electrode. Under illumination, $CuWO_4$ is significantly more stable when compared to WO_3, regardless of electrolyte composition. More importantly, the Faradaic efficiency of $CuWO_4$ is near unity in Cl^- containing solutions, unlike WO_3 which preferentially oxides the anion found in solution.

3.7 Outlook

The research presented in this chapter was toward a more quantitative analysis of the physical properties of $CuWO_4$ photoanodes. One of the obvious drawbacks of the PEC results presented on $CuWO_4$ are the lower current densities generated, and consequently the lower efficiencies for solar energy conversion. In order to address these limitations on $CuWO_4$, the next step is to understand the fundamental charge carrier properties of $CuWO_4$ and connect these properties to improved synthetic methods. Such work has been accomplished on α-Fe_2O_3.[19] When first used as a photoanode, α-Fe_2O_3 was synthesized by similar methods presented in this thesis and the attained photocurrent densities were similar. Through stringent doping control and higher order synthetic methods, such as atomic layer deposition (ALD) and chemical vapor deposition (CVD), the photocurrent densities achieved on α-Fe_2O_3 have increased an order of magnitude

over the past decade. The major challenge of forming tungstates by these methods is the optimization of the experimental parameters to ensure stoichiometric deposition of all the elements. Also, we have not yet identified and quantified a suitable dopant for $CuWO_4$. Doping d^0 4^+ in α-Fe_2O_3 increases donor density and improves PEC properties. Similarly, a 3^+ dopant for Cu^{2+} in $CuWO_4$ may show a similar result and lead to higher PEC properties. Furthermore, doping with a significantly smaller ion compared to Cu^{2+} may contract the crystal structure. This contraction will lead to greater orbital overlap of Cu(*3d*) orbitals and result in increased charge hopping.[20] There are DC conductivity experiments on $CuWO_4$ as a function of temperature,[21,22] and it is known that the crystal significantly contracts under pressure,[23] but there is yet to be a connection between a compressed unit cell of $CuWO_4$ and improved conductivities. It also should be noted that in principle, low doping should not increase the conduction as greatly as high doping/alloying. But, alloying in $CuWO_4$ does not result in such enhancements (*vide infra*). Therefore, low doping amounts (< 1%) may be a possible route for increased PEC performance as a result of increased donor density and crystal structure contraction.

Accordingly, the potential of fully optimized $CuWO_4$ photoanodes has not yet been realized, and the ultimate performance may be significantly higher than α-Fe_2O_3. With a mechanism to more precisely measure the charge carrier dynamics of electrodes prepared by these methods, doping can then be implemented in order to see further improvements in PEC properties. Pulsed laser deposition has been used to synthesize $CuWO_4$ with moderate success and insignificant increases in photocurrent densities. The PLD method for deposition has resulted in still planar $CuWO_4$ electrodes. In order to circumvent some of the present limitations, micro-structuring the electrodes may result in significant enhancement in the resulting PEC properties.

One approach toward this end is to form thin layers or sufficiently small nanoparticles of $CuWO_4$ attached to a 3D current collector. This has already been shown to work with $CuWO_4$; nanoparticles are dispersed on MWCNT's.[24] In this case, the light absorbing $CuWO_4$ is no longer planar with respect to the FTO and charge transfer to a current collector is more facile compared to a planar electrode. Additionally, the small (25 nm) $CuWO_4$ particles do not suffer as much bulk recombination as thicker planar electrodes. Overall light absorption is still high as these particles are dispersed throughout

the MWCNT network. A similar approach in our laboratory is to form a network of conducting oxide (aluminum doped zinc oxide, AZO) on top of which thin layers of $CuWO_4$ can be deposited. Now, there is an increased active surface in comparison to the planar electrodes. The hierarchical structure will allow for greater overall photon absorption while maintaining the shorter distance between $CuWO_4$ and the conducting AZO/FTO.

One major questions still to answer is whether or not the mid-gap state and Cu(*3d*) contributions to the electron structure will always continue to limit generated photocurrents. If sluggish onsets of photocurrents (and thus huge loss in overall STH efficiency) cannot be circumvented, the advantageous stability properties of this material may never be fully realized for high power conversion PEC water splitting. These limitations have been circumvented by various methods. The most recent is incorporating an electrocatalyst at the surface of the oxide, separating the tasks of light absorption/charge transport with the chemical reaction. I have tried incorporating catalysts such as cobalt phosphate (Co*P*$_i$), cobalt borate (CoB_i) and iron oxyhydroxide (FeOOH) without success to date. Although, the transport properties of $CuWO_4$ such as diffusion length and electron mobility have not yet been connected to the ideal amount of co-catalyst to be deposited. This information is useful for realizing optimized photocurrents in other catalyst/semiconductor systems, and may lead to successful increases in performance in $CuWO_4$. Additionally, passivation of the mid-gap state by a thin oxide layer may prevent charge trapping and lead to increased STH efficiencies in $CuWO_4$. This process has been proven successful on non-oxides as well as α-Fe_2O_3. Surface passivation layers by sputtering and atomic layer deposition are being pursued in our laboratory and a thickness-controlled layer may prove useful on $CuWO_4$. Finally, there is a growing field using the stability that a heterogeneous oxide affords in the presence of O_2 to create a much greener and cheaper catalyst for industrially relevant organic transformations. The selectivity on $CuWO_4$ due to the higher energy valence band and mid-gap state may be translated to other photodriven chemical reactions. Particularly in reference to transformations that must not over oxidize the desired product. Most oxides such as TiO_2 and WO_3 produce hydroxide radicals upon illumination. This is because of the highly oxidizing hole formed in the O(*2p*) orbitals are

sufficiently positive in voltage. This may lead to over oxidation and undesired product formation. The holes formed at the valence band or mid-gap state in $CuWO_4$ which are not O(*2p*) based may lead to oxidative transformations that stop at a certain level of progression and are much more desired.

3.8 Experimental

Photoelectrochemistry on Electrochemically Deposited $CuWO_4$

Photoelectrochemical measurements were performed in a custom-built, three-electrode Pyrex glass cell with a quartz viewing window. The cell contained the working thin-film photoanode, the Ag/AgCl reference electrode, and a platinum mesh counter electrode. For water oxidation, the supporting electrolyte was a pH 7 buffered solution of 0.1 M potassium phosphate (61.5 % K_2HPO_4 and 38.5 % KH_2PO_4). pH-dependent photoelectrochemical measurements were performed using 0.1 M Na_2SO_4 (pH 6), a 0.1 M acetate buffer (pH 3), and 0.1 M $HClO_4$ (pH 1) electrolyte solutions. Oxidation of methanol was carried out in a 10% solution of methanol in 0.1 M Na_2SO_4. In all cases, electrical contact to the working electrode was achieved using CG Electronics Silver Print II and a stainless-steel alligator clip. Linear sweep voltammetry was performed using a CH Instruments 660C Electrochemical Workstation; current was recorded as a function of potential when scanned anodically from –0.2 V to +1.4 V (versus Ag/AgCl) at a sweep rate of 10 mV/s. The light source was a Newport-Oriel 150 W Xe arc lamp fitted with an AM 1.5G filter to simulate incident solar radiation. The photoanode was placed 2 cm from the fiber optic source, and a 0.3 cm^2 spot was irradiated through the quartz window. The lamp power was measured to be 82 mW, giving an irradiance of 270 mW/cm^2. Therefore, all reported current densities are corrected to 100 mW/cm^2 illumination.

Photoelectrochemistry on Sol-Gel $CuWO_4$

Photoelectrochemistry was performed using a CH Instruments 660 C Electrochemical Work-station. All photoelectrochemical (PEC) measurements were performed in custom built cells with quartz viewing windows. 3-electrode voltammetry experiments were performed using the working $CuWO_4$ thin-film photoanode, a Ag/AgCl (Sat. KCl) reference electrode, and a Pt auxiliary electrode. The scan rates for cyclic voltammetry in the dark and linear sweep voltammetry under illumination were 50 mV/s and 20 mV/s

respectively. The supporting electrolyte in all PEC experiments was 0.1 M KPi to pH 3, 5, or 7, or 0.1 M KB_i at pH 7, prepared by adding an appropriate amount of KOH to H_3BO_3. The buffer solution was purged with N_2 prior to PEC measurements. A 1 cm^2 area of $CuWO_4$ from the front-side was irradiated through a quartz window. Of note is that there is no discernible difference in photocurrent when illuminating the electrode from the front- vs. back-side. We attribute the similar photocurrent response to the thinness of our $CuWO_4$ electrodes resulting in negligible directionality of charge-carrier collection. Freshly prepared electrodes were employed to start each experiment, but a direct comparison of the photocurrent generated in a single $CuWO_4$ photoanode in each electrolyte solution is provided in the SI. The light source was a Newport-Oriel 150W Xe arc lamp fitted with an AM1.5G filter (Newport). The lamp power was adjusted to 100 mW/cm^2 (except for O2 detection experiments described below) using an optical power meter (Newport 1918-R) equipped with a thermopile detector (Newport 818P-015-19). Photocurrent measurements to determine the band-gap energy were performed under monochromatic light (Newport Cornerstone 260 ¼m Monochromator). The measured photocurrent as a function of wavelength was performed at 1.23 V RHE in 0.1 M KP_i pH 7 electrolyte. The data was transformed and is presented as the square root of the photocurrent generated to depict an indirect-gap Tauc plot.

Electrochemical impedance spectroscopy analysis was carried out with an Eco Chemie Autolab PGSTAT302N potentiostat with a frequency-response analysis (FRA) module. Measurements were taken from –0.1 to 0.5 V vs. Ag/AgCl at pH 7 in 100 mV increments with a 5-minute equilibration time at each potential. A range of frequencies between 65,000 and 0.01 Hz was used with a 10 mV amplitude perturbation. Data were fit using Zview software. The light source was a Newport-Oriel 150 W Xe arc lamp fitted with an AM 1.5G filter to simulate incident solar radiation at 100 mW/cm^2.

Oxygen Evolution Measurements

Oxygen detection was performed in a custom built two-compartment cell separated by a fine frit. For O_2-detection experiments, the $CuWO_4$ working electrode, Ag/AgCl reference electrode, and fluorescence probe (FOSSPOR 1/8″ Ocean Optics Inc.) were sealed in one compartment, separated from the Pt auxiliary electrode. O_2 detection experiments were carried out at 1.23 V RHE in 0.1 M electrolyte using an AM1.5G filter

and custom built water filter. The power was adjusted to be 300 mW/cm2. The number of moles of O_2 produced was determined using the ideal gas law using the measured volume of the head space, the temperature recorded using a NeoFox temperature probe, and the partial pressure of O_2 recorded by the FOSSPOR fluorescence probe. Dissolved O_2 in the solution was accounted for through Henry's law using the measured partial pressure of O_2 and the volume of solution in the cell. Throughout the experiment, the solution was stirred to aid O_2 dissociation from the working electrode. The working electrode compartment contained 20 mL of electrolyte and 22 mL of head space. The fluorescence probe was calibrated with a 2-point calibration (0.00%, and 20.9%) using Neo-Fox software (Ocean Optics Inc.). Before beginning the experiment, % O_2 was recorded for 20 min to ensure the cell was sealed completely from the atmosphere and to create a baseline, and then measured for a period of time after the light was turned off. An important note is that during O_2 measurements, some O_2 is detected that was not produced photoelectrochemically, but was detected because of drift in the fluorescence probe's calibration as the temperature slightly increases over the course of illumination. Fluctuation is observed in control experiments in which the Faradaic efficiency of O_2 production was measured for electrolysis of water on plain FTO under illumination. Based on these control experiments, the uncertainty in measurements may account for errors as high as 10 % in the reported Faradaic efficiencies, particularly at low O_2 levels. Faradaic efficiency was determined by dividing the measured moles of O_2 by the theoretical yield, which is determined by dividing the total charge passed during the experiment by 4F (4-electron oxidation, F = Faraday's constant, 96,485 C/mol e–).

Chlorine Gas Detection

In order to determine whether Cl_2 gas was formed from oxidation of Cl^- in saline solution, a starch-iodide test was used. In this method, quantitative Cl_2 gas analysis was conducted after performing bulk electrolysis in a two-compartment cell. The results from $CuWO_4$ films in pH 7 0.1 M KBi buffer containing 0.1 M NaCl were compared to those from a WO_3 film prepared by sol-gel methods in a pH 5 0.1 M NaCl electrolyte (WO3 is not stable at pH 7). 20 mL of electrolyte was mixed with 5 mL of 0.25 M KI, diluting to 25 mL such that the concentration of I^- is 50 mM. I^- reacts with dissolved Cl^2 according to the balanced equation: $2I^-_{(aq)} + Cl_{2(g)} \rightarrow 2Cl^-_{(g)} + I_{2(aq)}$. 5 mL of the resulting solution

was titrated against 10 mM $Na_2S_2O_3$ with added starch as the iodine indicator: $I_{2(aq)} + 2S_2O_3^{2-}{}_{(aq)} \rightarrow S_4O_6^{2-}{}_{(aq)} + 2I^-_{(aq)}$. Comparing the coulometry with the titration results show that Cl_2 gas formation is quantitative (100%) for WO_3 and $\leq 2\%$ for $CuWO_4$.

3.9 References

1. Paracchino, A.; Laporte, V.; Sivula, K.; Gratzel, M.; Thimsen, E. Highly Active Oxide Photocathode for Photoelectrochemical Water Reduction. *Nat. Mater.* **2011**, *10*, 456-461.
2. Joshi, U. A.; Palasyuk, A. M.; Maggard, P. A. Photoelectrochemical Investigation and Electronic Structure of a *p*-Type $CuNbO_3$ Photocathode. *J. Phys. Chem. C*. **2011**, *115*, 13534-13539.
3. Hahn, N. T.; Holmberg, V. C.; Korgel, B. A.; Mulllins, C. B. Electrochemical Synthesis and Characterization of *p*-$CuBi_2O_4$ Thin Film Photocathodes. *J. Phys. Chem. C.* **2012**, *116*, 6459-6466.
4. Tong, L.; *et. al.* Sustained Hydrogen Generation using a dye-sensitized NiO Photocathode/$BiVO_4$ Tandem Photo-Electrochemical Device. *Energy Environ. Sci.* **2012**, *5*, 9472-9475.
5. Lin, C.-Y.; Lao, Y.-H.; Mersch, D.; Reisner, E. Cu_2O/NiO_x Nanocomposite as an Inexpensive Photocathode in Photoelectrochemical Water Splitting. *Chem. Sci.* **2012**, *3*, 3482- 3487.
6. Pyper, K. J.; Yourey, J. E.; Bartlett, B. M. Reactivity of CuWO4 in Photoelectrochemical Water Oxidation is Dictated by a Mid-gap Electronic State *J. Phys. Chem. C* **2013**, *117*, 24726-24732
7. Bertoluzzi, L.; Bisquert, J. Equivalent Circuit of Electrons and Holes in Thin Semiconductor Films for Photoelectrochemical Water Splitting Applications *J. Phys. Chem. Lett.* **2012**, *3*, 2517-2522.
8. Mahé, E.; Rouelle, F.; Darolles, I.; Devilliers, D. Electrochemical Characterization of Silicon Electrodes: Part 1: Capacitance-voltage Method *J. New Mat. Electr. Sys.* **2006**, *9*, 257-268.
9. Klahr, B.; Gimenez, S.; Fabregat-Santiago, F.; Hamann, T.; Bisquert, J. Water Oxidation at Hematite Photoelectrodes: The Role of Surface States *J. Am. Chem. Soc.* **2012**, *134*, 4294-4302.
10. Hens, Z. The Electrochemical Impedance of One-Equivalent Electrode Processes at Dark Semiconductor|Redox Electrodes Involving Charge Transfer through Surface States. 1. Theory *J. Phys. Chem. B* **1999**, *103*, 122-129.
11. Hens, Z.; Gomes, W. The Electrochemical Impedance of One-Equivalent Electrode Processes at Dark Semiconductor|Redox Electrodes Involving Charge Transfer through Surface States. 2. The n-GaAs/Fe^{3+} System as an Experimental Example
12. Orazem, M.E.; Tribollet, B. *Electrochemical Impedance Spectroscopy*, John Wiley & Sons, Inc., **2008**; Chp. 13; pp. 330
13. Mi, Q.; Zhanaidarova, A.; Brunschwig, B. S.; Gray, H. B.; Lewis, N. S. A Quantitative Assessment of the Competition between Water and Anion Oxidation at

WO_3 Photoanodes in Acidic Aqueous Electrolytes. *Energy Environ. Sci.* **2012**, *5*, 5694-5700
14. Saito, Rie.; Miseki, Y.; Sayama, K. Highly Efficient Photoelectrochemical Water Splitting using a Thin Film Photoanode of $BiVO_4/SnO_2/WO_3$ Multi-Composite in a Carbonate Electrolyte. *Chem. Commun.* **2012**, *48*, 3833-3835
15. Kong, D.-S.; Zhang, Z.-D.; Wang, J.; Wang, C.; Zhao, X.; Feng, Y.-Y.; Li, W.-J. A Photoelectrochemical Study on the Features of Carbonate-Catalyzed Water Oxidation at Illuminated TiO_2/Solution Interface. *J. Solid State Electrochem.* **2013**, *17*, 69-77
16. Pilli, S. K.; Deutsch, T. G.; Furtak, T. E.; Brown, L.; Turner, J. A.; Herring, A. M. $BiVO_4/CuWO_4$ Heterojunction Photoanodes for Efficient Solar Driven Water Oxidation. *Phys. Chem. Chem. Phys.* **2013**, 15, 3273-3278
17. Grobler, S. R.; Suri, S. K. Solubilities of the Molybdates and Tungstates of Copper(II) in Water by Ion-Selective Electrodes *J. Inorg. Nucl. Chem.* **1980**, *42*, 51-53
18. Hill, J. C.; Choi, K.-S. Effect of Electrolytes on the Selectivity and Stability of *n*-Type WO_3 Photoelectrodes for Use in Solar Water Oxidation. *J. Phys. Chem. C* **2012**, *116*, 7612-7620
19. Sivula, K.; Le Formal, F.; Grätzel, M. Solar Water Splitting: Progress Using Hematite (α-Fe2O3) Photoelectrodes *ChemSusChem* **2011**, *4*, 432-449

20 Huda, M. N.; Al-Jassim, M. M.; Turner, J. A. Mott Insulators: An Early Selection Criterion for Materials for Photoelectrochemical H_2 Production. *J. Renewable Sustainable Energy* **2011**, *3*, 053101-10.

21 Gonzalez, C. M.; Dunford, J. L.; Du, X.; Post, M. L. Characterization of Carrier States in $CuWO_4$ Thin-Films at Elevated Temperatures using Conductometric Analysis *J. Solid. State. Chem.* **2013**, *201*, 35-40

22 Mathew, T.; Batra, N. M; Arora, S. K. Electrical Conduction in $CuWO_4$ Crystals *J. Mater. Sci.*, **1992**, *27*, 4003-4008

23 Ruiz-Fuertes, J.; Friedrich, A.; Pellicer-Porres, J.; Errandonea, D.; Segura, A.; Morgenroth, W.; Haussuhl, E.; Tu, C.-Y.; Polian, A. Structure Solution of the High-Pressure Phase of $CuWO_4$ and Evolution of the Jahn-Teller Distortion *Chem. Mater.*, **2011**, *23*, 4220-4226

24 Gaillard, N.; Chang, Y.; DeAngelis, A.; Higgins, S.; Braun, A. A Nanocomposite Photoelectrode Made of 2.2 eV Band Gap Copper Tungstate ($CuWO_4$) and Multi-Wall Carbon Nanotubes for Solar-Assisted Water Splitting. *Int. J. Hydrogen Energy* **2013**, *38*, 3166-3176.

CHAPTER 4

Water Oxidation on a $CuWO_3$–WO_4 Composite Electrode in the Presence of $[Fe(CN)_6]^{3-}$: Toward Solar Z-Scheme Water Splitting at Zero-Bias

Portions of this chapter have been published:
Reproduced with permission from Yourey, J. E.; Kurtz, J. B.; Bartlett, B. M. *J. Phys. Chem. C*, **2012**, *116*, 3200. Copyright 2012 American Chemical Society
http://pubs.acs.org/doi/abs/10.1021/jp211409x

4.1 Introduction

Water splitting to generate chemical fuels such as hydrogen using semiconductor photoelectrodes is a long-standing problem that addresses an urgent societal need.[1] However, the experiments presented in the first part of this thesis are applied bias photo*electro*chemical water splitting which leads to a loss in efficiency (Equation 1).

$$\eta(E_{app}) = \frac{j(E^0 - E_{app})}{P_{AM1.5G}} \times 100\% \qquad 1)$$

The applied bias (E_{app}) is subtracted from E^o (1.23 V for water splitting) resulting in an inherent loss of efficiency, even before losses due to recombination. The flat-band potential (E_{fb}) of $CuWO_4$ is + 0.4 V (RHE), meaning that this material is incapable of water splitting without the applied bias; electrons in the conduction band minimum do not have enough energy to reduce protons (Equation 2).

$$2H^+ + 2e^- \rightarrow H_2 \qquad E^o = 0.0 \text{ V (RHE)} \qquad 2)$$

One approach to circumvent the need for the applied bias is to separate the two half reactions of water splitting. Rather than reducing H^+, another electron accepting species whose E^o is more positive than 0 V RHE, and by requirement the E_{fb} of the semiconducting material. Therefore, the overall photovoltage required is less than 1.23 V

and water oxidation is achieved without the need for an applied bias. This highly reversible and stable electron species will then be subsequently re-oxidized by the other *p*-type photocathode used to photochemically form H_2 on its surface. A depiction of the energy levels required for the photoanode, photocathode, and redox mediator, as well as a schematic of a possible device configuration for this process can be seen in Figure 4.1.

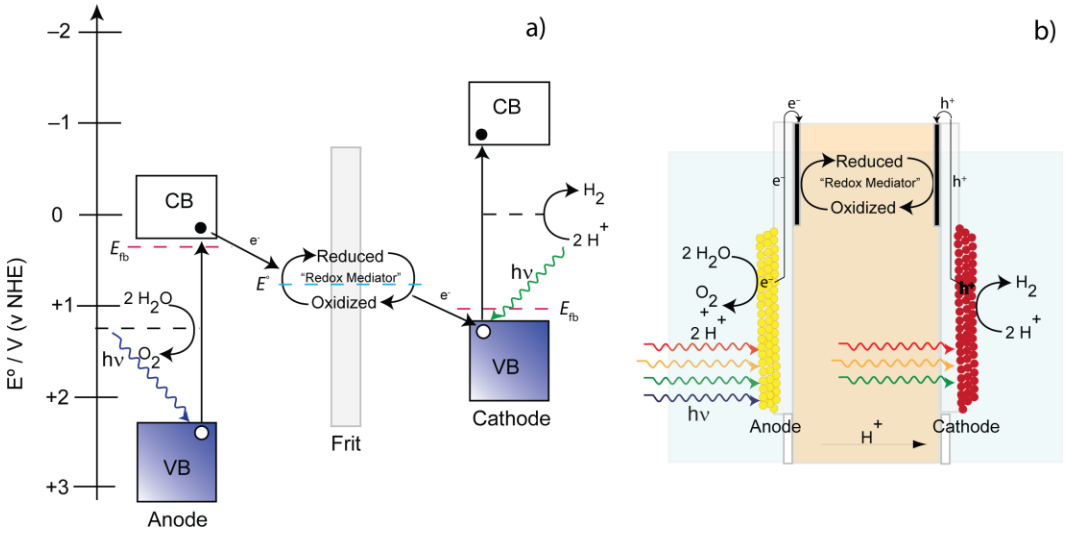

Figure 4.1 Band picture a) and device b) for overall water splitting using two light absorbing photoelectrodes and a redox mediator

Figure 4.1a illustrates the energy requirements for performing this series of light-driven photochemical reactions. Akin to photosynthesis, the Z-scheme of electron transfer can be seen. E_{fb} of the *n*-type photoanode must be at potentials more reducing than E^o of the redox mediator. Likewise, E_{fb} of the *p*-type photocathode must be at potentials more oxidizing the $E^{o\prime}$ of the redox mediator. Figure 4.1b illustrates a device which back contacts two photoelectrodes to a pool of dissolved redox mediator. Light is first impingent on the photoanode which is on a transparent conducting oxide, harvesting higher energy photons. Light passes through the pool of mediator and upon the photocathode which ideally harvests the lower energy photons. The photoexcited electrons and holes are transferred to a back-contacted electrode in the pool reducing and oxidizing the redox mediator. Additionally, the three compartments are separated by a frit preventing the transfer of the mediator into either side compartment while still allowing for the flow of protons, preventing competing photochemical reactions taking place on either surface. This device isn't ideal for a few reasons including competing photon

absorption by the redox mediator and *i*R drop due to the fritted separation of the two compartments, but it does fulfill the requirements for achieving Z-scheme overall water splitting at no applied bias. Using two light sources by splitting the impingent light is one method to alleviate the competing photon absorption, and using low-resistance membranes can remove a significant portion of the *i*R drop between the solutions.

Z-scheme water splitting is receiving significant attention in the powdered photocatalyst community.[2–5] Photocatalytic powders for both half reactions are suspended in a solution containing both the oxidized and reduced form of the mediator and illuminated. This methodology has particular advantages, specifically device and materials cost,[6] but using a thin-film electrode allows one to identify drawbacks and, more importantly establish a road map for better materials design. Additionally, electrolyte compatibility issues can be circumvented through the physical separation of the two light harvesting electrodes. This chapter presents the synthesis of a WO_3-$CuWO_4$ composite electrode and a photoelectrochemical study of one half of the aforementioned Z-scheme, water oxidation with concomitant redox mediator reduction. Specifically, the work focuses on water oxidation with concomitant ferricyanide reduction at neutral pH using only simulated sunlight. Ferricyanide is a suitable electron acceptor because it is stable and highly reversible. Also, its pH independence presents some interesting results as the driving force for reduction can be tuned with changing E_{fb} in $CuWO_4$ as a function of pH. The balanced half reactions (Equations 3-4) and overall reaction (Equation 5) are:

$$2H_2O \rightarrow O_2 + 4H^+ + 4e^- \qquad E^{o\prime} = 0.82 \text{ V (pH 7)} \qquad 3)$$

$$4[Fe(CN)_6]^{3-} + 4e^- \rightarrow 4[Fe(CN)_6]^{4-} \qquad E^{o\prime} = 0.44 \text{ V (pH 7)} \qquad 4)$$

$$2H_2O + 4[Fe(CN)_6]^{3-} \rightarrow O_2 + 4H^+ + 4[Fe(CN)_6]^{4-} \qquad E^{o\prime} = -0.38 \text{ V (pH 7)} \qquad 5)$$

where the reported potentials $E^{o\prime}$ are versus the hydrogen electrode at pH 7. At pH 7, E_{fb} of $CuWO_4$ is at higher energy than $E^{o\prime}$ of ferricyanide. The O_2/H_2O couple is calculated from the Nernst equation and the $[Fe(CN)_6]^{3-/4-}$ was measured in KP_i buffer at the concentrations used in this study (Figure C.1).

4.2 Synthesis and Characterization of $CuWO_4$-WO_3 Composite Electrodes

In order to raise the current density generated in our electrodes, we turned to a composite film with a composition of nearly 1:1 $CuWO_4$:WO_3 (2:1 W:Cu) to retain the visible light harvesting ability of $CuWO_4$ but to improve the kinetics of electron transfer from water. There is a significant body of literature focusing on 3*d* transition metal

oxides for which charge-carrier kinetics can be enhanced by preparing heterostructures.[7–10] Pertinent examples to PEC water oxidation are $BiVO_4$-WO_3, $ZnWO_4$-WO_3, and Fe_2O_3-WO_3 composites which possess increased visible light absorption and faster rates compared to either native metal oxide. Our $CuWO_4$-WO_3 composite is prepared by modifying the electrodeposition synthesis presented in section 2.2. To increase the WO_3 mole fraction in the resulting electrode, the starting Cu^{2+} and $W_2O_{11}^{2-}$ precursor concentrations were altered and the pH of the deposition bath was adjusted to 1.25, slightly higher than that of the solution giving the 1.2:1 ratio. Additionally, the parameters of the controlled potentiometry experiment used to deposit the electrode were slowed from 50 mV/s to 10 mV/s and the number of cycles was decreased from six to two total cycles (Figure C.2). This 2:1 mixture in the composite electrode led to the highest photocurrent densities after comparing the atomic ratios of W:Cu in a series of prepared electrodes. The composition, morphology, and structure of the composite material were characterized using SEM, XRD, and EDX spectroscopy. The atomic ratio of W to Cu was determined by quantifying the Cu-K and W-L lines of an EDX spectrum. By evaluating six different samples prepared from three independent deposition baths, we have determined the W:Cu ratio to be 2.03 ± 0.21 (Figure C.3). The electrodeposited electrode is a 2-3 μm thick, polycrystalline film, which results in a highly porous surface (Figure C.4). The X-ray diffraction pattern confirms the presence of crystalline $CuWO_4$ and WO_3 phases (Figure C.5). WO_3 was identified by peak splitting seen at *ca.* 24º 2θ. However, the relative intensities of the diffraction pattern indicate that the crystalline component is predominantly $CuWO_4$ in nature leading to optical properties and photoelectrochemistry typical of $CuWO_4$, but distinct from WO_3.

4.3 Photoelectrochemistry

In order to examine the prospect of a $CuWO_4$-WO_3 composite anode to perform as a photoanode for water oxidation, spectral response of the material was taken in a pH 7 buffered solution of 0.1 M potassium phosphate (61.5% K_2HPO_4 and 38.5% KH_2PO_4) containing 25 μM $[Fe(CN)_6]^{3-}$. These mimic the conditions under which the bulk photolysis experiments were performed. The spectral response and its product with the solar flux density give the absorbed photon flux density, illustrated in Figure 4.2. The

highlight of this measurement is the 7% efficiency to perform zero-bias water oxidation at 400 nm

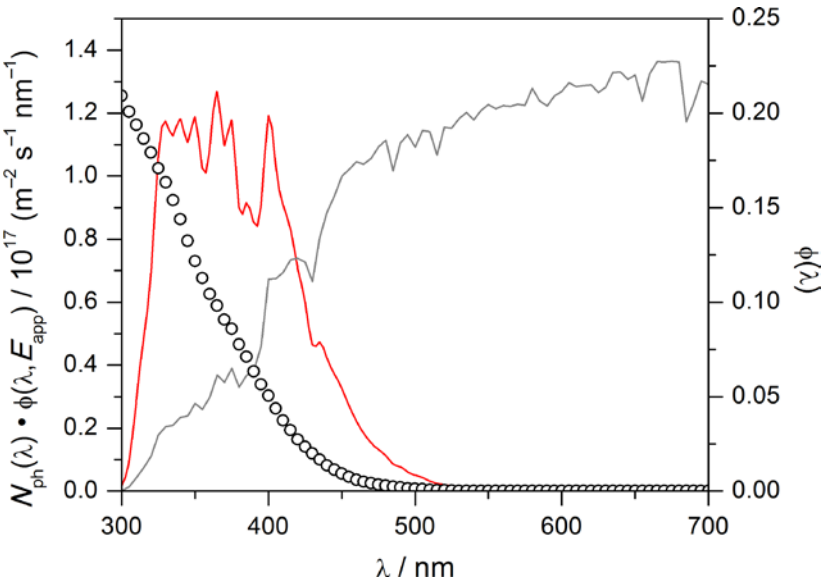

Figure 4.2 Spectral response of $CuWO_3$-WO_4 in pH 7 KP_i containing $[Fe(CN)_6]^{3-}$ (black) and the absorbed photon density (red).
The solar flux density is illustrated in gray for reference. It is drawn to scale, but its explicit units are not shown.

The integrated absorbed photon flux density is determined to be 1.34×10^{19} s^{-1} m^{-2}. As seen previously, from the spectral response, absorption into the MMCT band does not result in much collected current out to 550 nm. Nonetheless the chemical stability afforded by the $CuWO_4$-containing electrode provides the impetus for exploring further the photoelectrochemistry of the material, underscored by the photostability and Faradaic efficiency of the electrodes.

Next, voltammometric and potentionstatic experiments using a 3-electrode setup evaluate the composite photoanode performance in only pH 7 KP_i buffer. In Figure 3, the linear sweep voltammogram shows anodic photocurrent density of *ca*. 0.3 mA/cm^2 at the thermodynamic potential for water oxidation, 0.618V vs Ag/AgCl at pH 7 (1.23 V vs RHE).

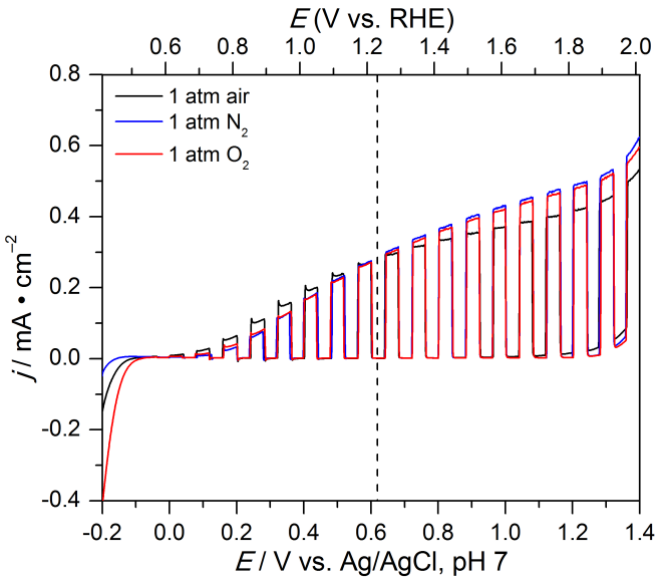

Figure 4.3 Chopped-light LSV trace of a $CuWO_4$–WO_3 photoanode in a pH 7 KP_i buffer under various atmospheres.
The experiment was conducted under AM1.5G illumination and the thermodynamic potential for water oxidation is indicated by the dashed line.

This is approximately double the current generated using a sol-gel $CuWO_4$ electrode, yet the shape of the LSV trace is similar. Regardless of synthesis, the shape of the LSV trace amongst the various electrodes is very similar, showing the fundamental electrochemistry associated with $CuWO_4$. Since the potential of the cell depends on the O_2 partial pressure according to the Nernst equation, an LSV trace was recorded in a cell open to ambient room conditions as well as with bubbling N_2 at 1 atm and O_2 at 1 atm. Neither the current nor the onset potential are changed substantially either in the dark or upon illumination. However, at 0.5 V RHE the catalytic onset of oxygen reduction is seen in an O_2 saturated cell. In ambient air, this catalytic current is decreased, and in 1 atm N_2 the reduction of the electrode is seen at slightly more negative potentials. Again, this Cu based redox event dictates the onset of photocurrent and the dark electrocatalytic reduction of oxygen. Importantly, this behavior is reproduced in any typical electrode, regardless of the exact Cu:W elemental ratio.

To demonstrate that oxygen is indeed evolved at the thin film photoanode under 100 mW/cm^2 AM1.5G (1-sun) illumination, Figure 4.4 shows the results of an O_2-detection experiment using a 3-electrode setup at an applied bias of 0.5 V (vs Ag/AgCl).

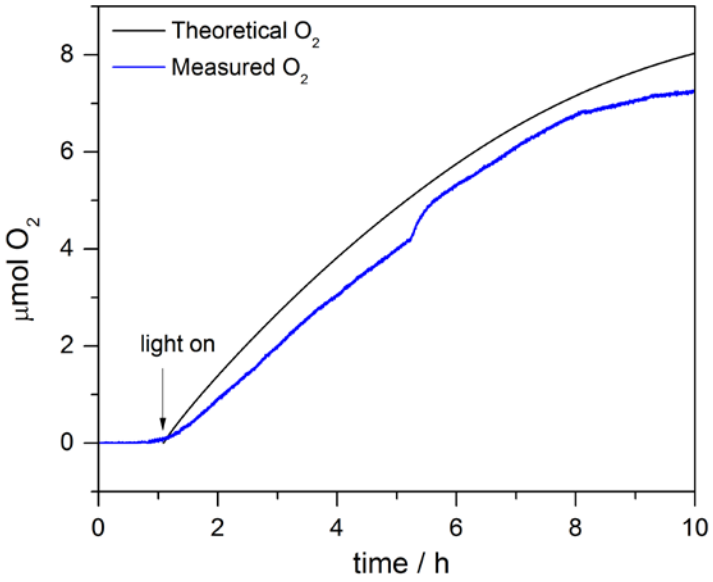

Figure 4.4 O_2 evolution from an aqueous KP_i solution at +0.5 V (vs Ag/AgCl) using a $CuWO_4$-WO_3 photocatalyst.

An applied bias is required to evolve O_2 from water since the flat band potentials of both $CuWO_4$ and WO_3 are more positive than the H^+ reduction potential. Notably, no O_2 is observed prior to illumination at 0.5 V (Ag/AgCl), indicated by the arrow. Upon illumination, the O_2 signal increases above background almost immediately, and over the 8 h illumination period, a Faradaic efficiency of 80-95% is measured over the duration of the experiment. The composite electrode is composed of *ca.* 0.5 mg of material, therefore a stoichiometric reaction would yield only 0.16 µmol O_2, and we observe a 10-fold increase in this yield after ~2 h of continuous illumination, indicating that we are in fact catalyzing the decomposition of water, and not the decomposition of our electrode. Interesting is that even though these electrodes possess nearly half WO_3, the Faradaic efficiency for O_2 is high and significantly more stable (Figure C.6) than a plain WO_3 electrode under similar conditions. These results indicate that charge transfer may take place from WO_3 to $CuWO_4$ due to the electric field caused by $CuWO_4$'s higher energy valence band, as illustrated in Figure 4.5 depicting $CuWO_4$ as the site for the chemical reaction taking place.

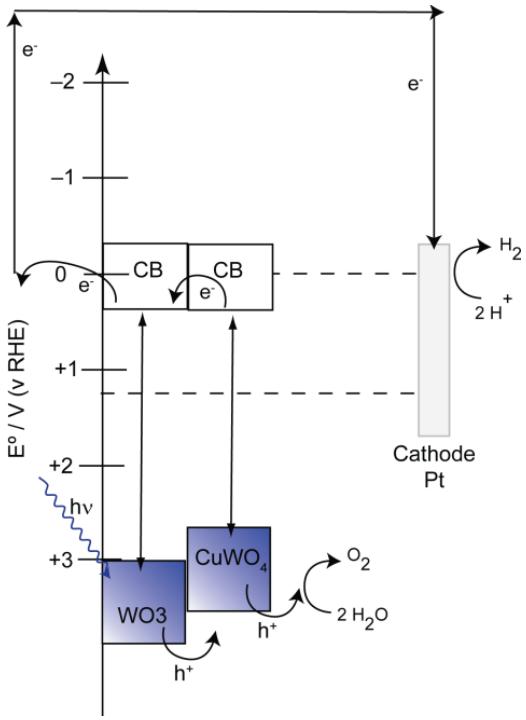

Figure 4.5 Depiction of a $CuWO_4$-WO_3 heterojunction

After establishing the photoelectrochemistry of water splitting with an applied bias, we evaluated the capability of the composite photoanode to perform water oxidation in the presence of ferricyanide using only a 2-electrode system. Figure 4.6 shows the photoelectrochemical response in the *j*-*V* curve of the composite photoanode in 0.1 M pH 7 KP_i buffer both with and without ferricyanide.

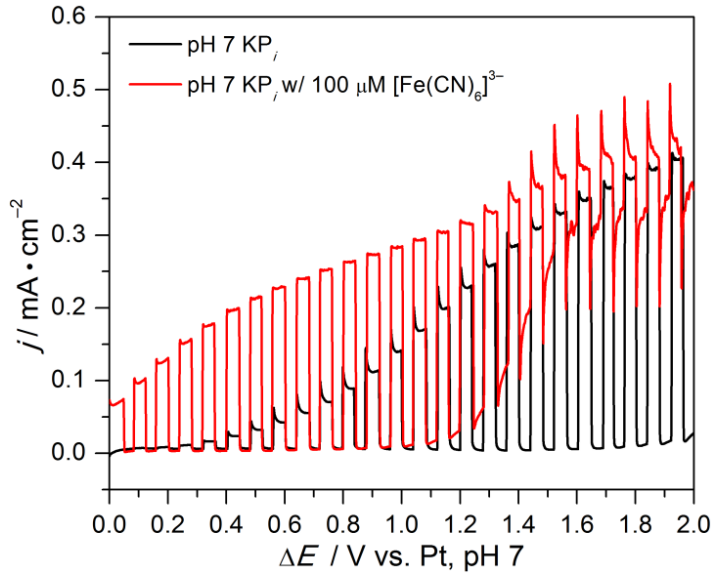

Figure 4.6 Two-electrode LSV trace of aqueous solutions containing 0.1 M KP$_i$ electrolyte (black) and electrolyte plus 100 μM $[Fe(CN)_6]^{3-}$ (red). Potentials are reported against the platinum auxiliary electrode.

First, the onset of electrolytic water oxidation (i.e.—dark current) begins at a less positive potential in the presence of ferricyanide (1.10 V vs. the Pt auxiliary electrode) than in its absence (1.95 V vs. Pt). It is also notable that this difference (0.85 V) is equal to the change in potential between performing water electrolysis (1.23 V) and water oxidation with ferricyanide reduction (0.38 V at pH 7). Under 1-sun illumination without ferricyanide, there is no anodic photocurrent until we apply an external bias. However with ferricyanide present, there is ~60 μA of photocurrent generated at no applied bias. Figure C.7 repeats the data shown in Figure 4.6 using a 1:1 $[Fe(CN)_6]^{3-/4-}$ mixture both at 100 μM concentration; the *j*-*E* characteristics are again essentially unchanged at these concentrations.

This is an important result because of the possibility of competitive photoxidation of $[Fe(CN)_6]^{4-}$ rather than water. First, the low concentration of ferrocyanide may prevent it from being a serious competitor for surface holes. Testing this directly is difficult because at higher concentrations, competitive photon absorption becomes dominating. The second reason falls under the same logic as to why $CuWO_4$ is selective for water oxidation rather than Cl^-. Hole transfer into solution from the mid-gap state may prevent outer sphere charge transfer between the surface and ferrocyanide, leaving bound water as the ultimate electron donor. These results are consistent with studies using $CuWO_4$

single crystals in the presence of various electron donors such $FeCl_2$, $[W(CN)_8]^{4-}$, $[Mo(CN)_8]^{4-}$. During these voltammetry experiments, there was no evidence of unique photochemical oxidation of these various electron donors, but again the voltammetry traces were similar to water oxidation.

4.4 Steady-state Zero-bias Water Oxidation in the Presence of $[Fe(CN)_6]^{3-}$

Although voltammetry is useful for determining the onset potential and the overpotential for a chemical reaction occurring under photocatalytic conditions, the technological end goal of this research is to generate stable materials to carry out solar water oxidation under short-circuit (zero-bias) conditions. First, to more clearly show that water oxidation and concomitant ferricyanide *can* be photodriven on the surface of a $CuWO_4$-WO_3 composite electrode, a zero-bias bulk electrolysis was conducted under chopped-light illumination. Figure 4.7 unequivocally shows that in a solution containing KP_i electrolyte only, no photocurrent is generated when illuminated. This is clearly observed over the first 200 s of the experiment.

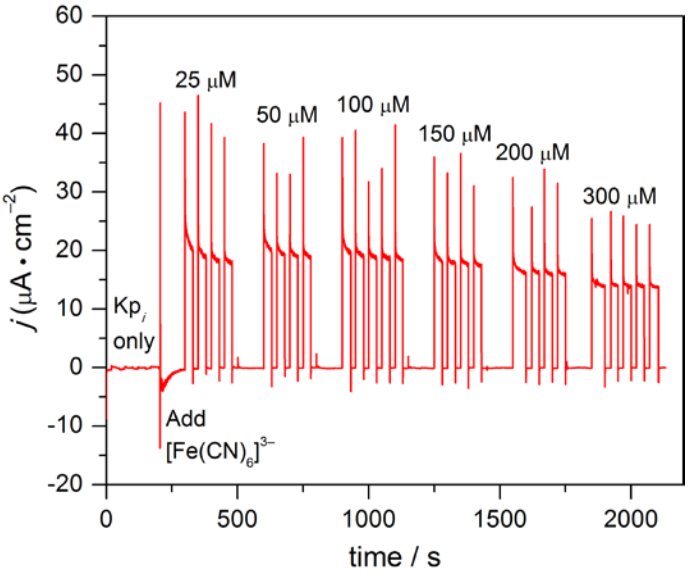

Figure 4.7 Incremental addition of $[Fe(CN)_6]^{3-}$ in a 100mM KP_i solution using a $CuWO_4$-WO_3 photoanode in a 2-electrode cell while conducting a chopped light bulk electrolysis experiment at 0 V vs Pt mesh auxiliary electrode.

After the addition of ferricyanide, sustained photocurrent is generated upon chopping the light. The generated photocurrent is sustained as more aliquots of ferricyanide are added, making the solution more concentrated in electron donor. However, when the solution becomes more concentrated than 150 μM, there is a decrease in photocurrent due to

competing photon absorption. For the reduction half reaction, the disappearance of $[Fe(CN)_6]^{3-}$ was monitored using UV-Vis spectroscopy (λ_{max} = 420 nm) as a function of time. Figure 4.8 compares $[Fe(CN)_6]^{3-}$ disappearance and the coulometry of the reaction in two cells—one in which only the oxidized form, $[Fe(CN)_6]^{3-}$, is present at 200 μM concentration, and the other in which both $[Fe(CN)_6]^{3-}$ and $[Fe(CN)_6]^{4-}$ are each present at 200 μM concentration.

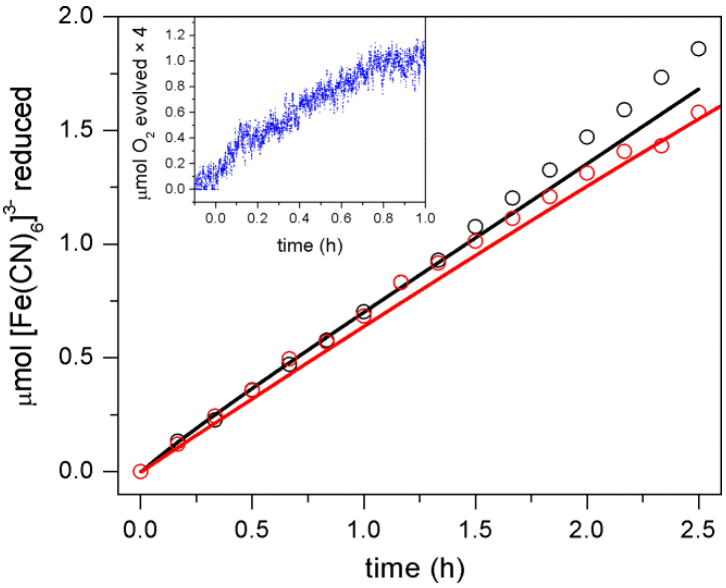

Figure 4.8 Faradaic efficiency of water oxidation and ferricyanide reduction under short-circuit conditions.
Black and red circles represent solutions containing 200 μM $[Fe(CN)_6]^{3-}$ and 200 μM $[Fe(CN)_6]^{3-}$ + 200 μM $[Fe(CN)_6]^{4-}$ respectively. The solid lines record the charge passed in each experiment. **Inset.** O_2 evolution monitored for the first hour of illumination in the presence of 200 uM $[Fe(CN)_6]^{3-}$.

The increase in concentration is necessary to quantify $[Fe(CN)_6]^{3-}$ reduction over a significantly long timeframe. Near the end of the experiment, the observed quantity of ferricyanide reduced appears to exceed the theoretical yield slightly in each experiment, which can be attributed to minor solvent loss as we remove and reintroduce aliquots of solution during the experiment. There is continuous N_2 flow throughout the duration of the experiment in order to keep the cell free of atmospheric oxygen as well as to prevent competitive O_2 reduction at the auxiliary electrode. Using our fluorescence probe in a separate experiment starting with 100 μM $[Fe(CN)_6]^{3-}$ in which no aliquots are removed, we measured the rate of water oxidation to be 0.25 μmol O_2 h^{-1}, illustrated in the inset of Figure 4.8. Here, the detected O_2 partial pressure is slightly higher than that supported by

the coulometry because the zero-bias experiment pushes the detection limit of our fluorescence probe. Nevertheless, the quantity of O_2 generated trends closely with ferricyanide reduction.

Ferricyanide continuously disappears throughout the course of the entire experiment (absorption spectra are presented in Figure 4.9), indicating that water oxidation is taking place with concomitant ferricyanide reduction at Pt.

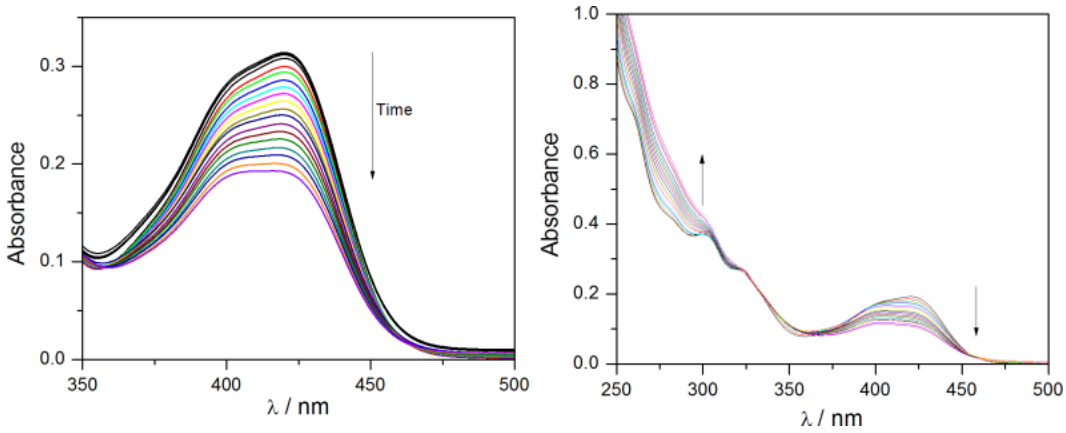

Figure 4.9 Absorption spectra showing the decrease in $[Fe(CN)_6]^{3-}$

The measured absorbance values are converted to concentration of $[Fe(CN)_6]^{3-}$ in solution using a constructed calibration curve. By taking the difference between initial and measured concentrations, the total µmoles of $[Fe(CN)_6]^{3-}$ reduced at each time interval is known through the volume of solution used in the experiment. In the left side of Figure 4.9, the dashed lines at the top represents a control experiment over a 3 h period in which a 200 µM $[Fe(CN)_6]^{3-}$ solution was illuminated without a $CuWO_4$-WO_3 electrode present. As expected, there was no decrease in $[Fe(CN)_6]^{3-}$ concentration. In the right side of Figure 4.9, the arrows describe the decrease of $[Fe(CN)_6]^{3-}$ (420 nm) and the formation of $[Fe(CN)_6]^{4-}$ (275 nm).

Figure 4.10 shows the steady-state photocurrent generated at zero bias in the presence of 200 µM $[Fe(CN)_6]^{3-}$ using a composite thin-film working electrode and Pt mesh auxiliary electrode.

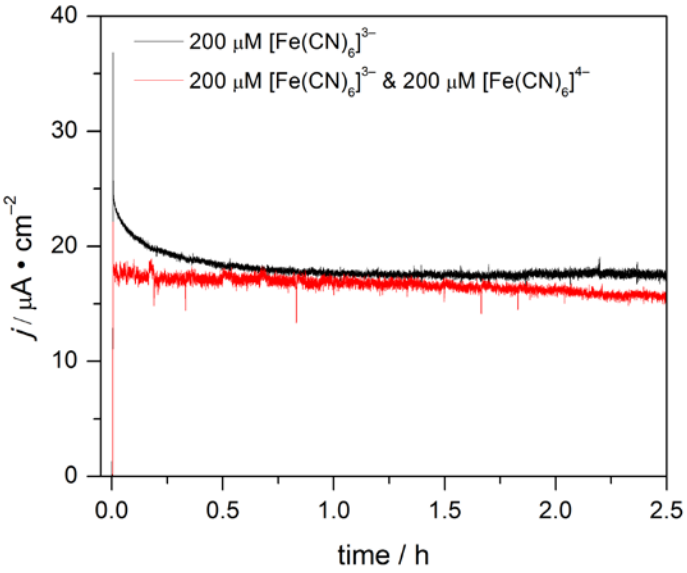

Figure 4.10 Steady-state photocurrent density measured during bulk photolysis at zero bias is in the presence of 200 μM $[Fe(CN)_6]^{3-}$ (black) and 200 μM each of both $[Fe(CN)_6]^{3-}$ and $[Fe(CN)_6]^{4-}$ (red).

Upon illuminating our 1 cm^2 electrode, a steady-state short-circuit current of 17 μA of steady state photocurrent is observed. Using the same two-electrode setup, a bias of 0.6 V is needed to generate O_2 at the same rate (with hydrogen evolution at the auxiliary electrode, illustrated in Figure C.8. $CuWO_4$ exhibits respectable stability when over the two hour illumination period under short-circuit conditions. $CuWO_4$ shows increased stability when performing water oxidation with ferricyanide reduction at short circuit when compared to the stability at an applied bias as seen in Figure C.6. The applied bias may be contributing to the rate of degradation in the electrode, or the electrode degrades faster as the surface turns over the reaction many more times.

Finally, the driving force for ferricyanide reduction can be tuned using the pH of the electrolyte solution. $CuWO_4$ in aqueous solution shows a Nernstian response to pH, whereas the [Fe(CN)6]3–/4–couple is pH-independent. Therefore, at higher pH, the $CuWO_4$-WO_3 composite show an increase in photocurrent when illuminated in the presence of ferricyanide under short-circuit conditions due to the larger driving force. Figure C.9 shows that at pH 3 (E_{fb} $CuWO_4$ = 0.07 vs Ag/AgCl and $E^{o\prime}$ of $[Fe(CN)_6]^{3-}$ = 0.225 V vs. Ag/AgCl) the electrode generates 5μA/cm^2 compared to pH 9 (E_{fb} $CuWO_4$ = – 0.7 V vs. Ag/AgCl and $E^{o\prime}$ of $[Fe(CN)_6]^{3-}$ = 0.225 V vs. Ag/AgCl) where it generates 45 μA/cm^2 of photocurrent. This observation is significant as one would want to tune the

rate of O_2 evolution to match the rate at which H_2 is being produced from a photocathode in a functioning device. Ferrocyanide has been previously shown to act as a sacrificial reductant for H_2 evolution on V_2O_5-doped TiO_2 in phosphate buffer, providing precedent for the other half of the Z-scheme and presenting some viability to this method for overall water splitting.[11]

4.5 Efficiency Calculations

Combining coulometry and O_2 yield with the spectral response and source power, we have determined the conversion efficiency. Taking into account the solar flux density $N_{ph}(\lambda)$ and the spectral response, $\phi(\lambda, E_{app})$ (also referred to as incident photon to current efficiency, IPCE) from Figure 4.2, the maximum conversion efficiency, η_{max}, is given by the equation:

$$\eta_{max} = \int_0^\infty N_{ph}(\lambda)\phi(\lambda, E_{app})d\lambda \bullet \frac{e(E^0 - E_{app})}{P_{AM1.5G}} \times 100\% \qquad 6)$$

where E^o is $E^{o\prime}$, the standard potential for the reaction (0.38 V from equation 3), E_{app} is the applied bias (0 V), e is the fundamental unit of charge (1.60×10^{-19} C), and $P_{AM1.5G}$ is the lamp power (1000 W/m^2). At short circuit, η_{max} is determined to be 0.082% for this reaction. We note here that the product of absorbed photon flux density (the integral of equation 6) and the fundamental charge supports a maximum current density, j_{max} of 214 μA/cm^2. However, our experimental steady-state current density of 17 μA/cm^2 (Figure 4.10) gives a conversion efficiency given by the formula:

$$\eta(E_{app}) = \frac{j(E^0 - E_{app})}{P_{AM1.5G}} \times 100\% \qquad 7)$$

of 0.0065% for no applied bias. This is on a par with the apparent quantum yield (AQY), described by the equation:

$$AQY = \frac{n \times \#\ molecules\ O_2\ evolved}{\#\ incident\ photons} \times 100\% \qquad 8)$$

where $n = 4$ for water oxidation. Using our data over the 1 hour illumination period from the inset of Figure 4.8, we measure an AQY of 0.038% (the same order of magnitude as $4 \times \eta$ (0.026%).

4.6 Conclusions

An electrodeposited 1:1 mixture of $CuWO_4$:WO_3 is chemically stable toward water oxidation. Under simulated 1-sun illumination, overall water splitting can be

accomplished with an applied bias of 0.5 V (vs. Ag/AgCl). More important, water oxidation occurs upon irradiating the photoanode under short-circuit conditions with concomitant reduction of ferricyanide. In order to generate photocurrents at zero-applied bias in an N_2 purged cell, ferricyanide must be present to serve as an electron acceptor. $CuWO_4$-WO_3 generates 17 $\mu A/cm^2$ of constant photocurrent over extended periods of illumination and the amount of ferricyanide reduced was quantified using UV-Vis spectroscopy. $CuWO_4$ is 7% efficient at 400 nm for the reaction with an overall apparent quantum yield of 0.38 % under simulated solar irradiation.

4.7 Outlook

This chapter presented one half of artificial photosynthesis using ferricyanide as an electron shuttle. The next steps should be toward the discovery of a competent photocathode capable of performing H^+ reduction with subsequent ferrocyanide oxidation. Cu_2O and Rh:$SrTiO_3$ are *p*-type oxides which have been studied for PEC hydrogen production. There are no studies performing the second half of the Z-scheme on these materials as electrodes, but Rh:$SrTiO_3$ is an active powdered catalyst for H_2 production and I^- oxidation. Next, optimization and device fabrication will allow for overall efficiency measurements and benchmarking this process. To increase the efficiency of the water oxidation half, higher performing photoanode materials such as WO_3 or $BiVO_4$ can be substituted for $CuWO_4$. These materials may show preferential oxidation of the redox mediator, but passivation of the surface with a selective electrocatalyst for water oxidation may prevent the back reaction from taking place. Also, controlled heterojunctions using $CuWO_4$ as an outer layer may form a more active electrodes with a selective surface. The presented measurements lay out a method for testing the various electrodes.

4.8 Experimental Methods

Synthesis of $CuWO_4$-WO_3 composite photoanodes

All reagents were purchased from Sigma Aldrich and used as received with no further purification. Composite photoanodes were prepared by electrodeposition from a 30 mL bath composed of 50 mM $H_2W_2O_{11}$ and 30 mM $Cu(NO_3)_2 \cdot 3H_2O$ in a 30% isopropanol solution. The pH of the starting mixture was approximately 1.7, and the acidity of the final deposition solution was adjusted to 1.2-1.25 by adding 1-2 mL of 20%

nitric acid solution. Amorphous white films composed of Cu_2O and WO_3 were deposited onto 1.1 cm^2 masked soda lime glass coated with 400 nm of fluorinated tin oxide (FTO) (Pilkington Glass, Tec 15 2.2 mm thick, 12-14 Ω/sq). The potential was swept from +0.3 V to -0.5 V (vs. Ag/AgCl) for 2 complete cycles at a scan rate of 10 mV/s at room temperature using a CH Instruments 660C Electrochemical Workstation. These films were immediately removed from the deposition solution and then annealed in air at 500 °C for 6 h using an MTI box furnace. The films were heated and cooled at a rate of approximately 2 °C/min. After annealing, the resulting films were cut to a 1.1 × 2 cm^2 piece and electrical contact was made by attaching copper wire (Fisher Scientific) using silver print II (GC electronics). Finally, the electrode was sealed using Hysol 1C epoxy at the end of a piece of glass tubing through which the wire has been fitted.

Material Characterization

X-ray diffraction was recorded on a Brüker D8 Advance diffractometer equipped with a graphite monochromator, a Lynx-Eye detector and parallel beam optics using Cu Ka radiation (λ = 1.54184 Å). Patterns were collected using a 0.6 mm incidence slit, with a step size and scan rate of 0.04 °/step and 0.5 s/step respectively. Phases were identified as $CuWO_4$ (JCPDF 72-0616) and WO_3 (JCPDF 72-0677) using MDI Jade version 5.0. Observed $CuWO_4$ Bragg reflections were compared to those calculated from the single crystal X-ray structure.

UV-Vis spectra were recorded using a Cary 5000 spectrophotometer (Agilent) equipped with an external diffuse reflectance accessory. Spectra were recorded in reflectance mode and transformed mathematically into absorbance. Tauc plots were then generated using the Kubelka-Munk function, $F(R) = (1–R)^2/2R$.

Scanning electron microscopy (SEM) images were collected using a Hitachi S-3200N SEM with an accelerating voltage of 15 kV. Energy dispersive X-ray analysis spectra (EDX) were collected using a Hitachi S-3200N SEM with an accelerating voltage of 15 kV, a back scattering electron (BSE) detector, and a working distance of 15 mm. Spectra were quantified using EDAX genesis software and the Cu K and W L emission lines were used.

Photoelectrochemistry

Photoelectrochemistry was performed using a CH Instruments 660C Electrochemical Workstation. All photoelectrochemical (PEC) measurements were conducted custom built single- or two- compartment cells illustrated in Figure S3. For 2-electrode measurements, the working thin-film photoanode and platinum mesh auxiliary electrode were placed in close proximity to one another. 3-electrode experiments were performed using the working thin-film photoanode, a Ag/AgCl reference electrode, and a Pt auxiliary electrode. The supporting electrolyte in all PEC experiments was a pH 7 buffered solution of 0.1 M potassium phosphate (61.5% K_2HPO_4 and 38.5% KH_2PO_4) with or without $[Fe(CN)_6]^{3-}$. To remove any additional redox active contaminants from the KP_i electrolyte and the Pt mesh auxiliary electrode, 2 V were applied between a Pt working and the Pt mesh auxiliary electrode prior to any experiment. Also, to remove all surface contaminants from the photoanode, all $CuWO_4$-WO_3 electrodes were illuminated in the pH 7 KP_i buffer for 1h at 0 V vs Pt mesh prior to performing any PEC measurements. The buffer solution was then purged with N_2 prior to photoelectrochemical measurements and an inert atmosphere was maintained during PEC experiments, unless otherwise noted. The light source was a Newport-Oriel 150W Xe arc lamp fitted with an AM1.5G filter (Newport) to simulate solar radiation. The photoanode was placed 2 cm from the fiber optic source and 1 cm^2 spot was irradiated through a quartz window. The lamp power was adjusted to 100 mW using an optical power meter (Newport 1918-R) equipped with a thermopile detector (Newport 818P-015-19).

Spectral response was recorded using a Newport-Oriel 150 W Xe arc lamp attached to a quarter-turn single-grating monochromator. Light was chopped at 20 Hz, and a quartz beam splitter was used to simultaneously record the light output with a separate Si photodiode to adjust for any fluctuations in lamp intensity. The experiment was conducted in 100 mM KP_i containing 25 µM $[Fe(CN)_6]^{3-}$ in an unstirred cell. A 2-electrode configuration was used with a $CuWO_4$-WO_3 working electrode and Pt mesh auxiliary electrode. The potential of the working electrode was poised at 0 V (vs Pt mesh) and the absolute photocurrent was measured by a digital PAR 273 potentiostat. The output current signal was connected to a Stanford Instruments SR830 lock-in amplifier,

and the output signals from the lock-in amplifier and the reference Si photodiode were fed into a computer controlled by custom-written LabVIEW software.

Oxygen Detection

Oxygen detection was performed in a custom built two-compartment cell separated by a fine frit. For applied bias experiments, the $CuWO_4$-WO_3 working electrode, Ag/AgCl reference electrode, and fluorescence probe (FOSSPOR 1/8″ Ocean Optics Inc.) were in one compartment, separated from the Pt auxiliary electrode. No bias experiments in the presence of $[Fe(CN)_6]^{3-}$ were performed in a custom built single compartment cell equipped with a $CuWO_4$-WO_3 working electrode, Pt mesh auxiliary electrode and FOSSPOR fluorescence probe. Throughout both sets of experiments, solutions were stirred at 400–1000 rpm to help O_2 dissociation from the working electrode as well as deliver fresh $[Fe(CN)_6]^{3-}$ to the Pt mesh auxiliary electrode. The single compartment cell contained 20 mL of Kp_i electrolyte and 19 mL of head space. The number of moles of O_2 produced was determined using the ideal gas law using the measured volume of the head space, temperature that was recorded using a NeoFox temperature probe, and the partial pressure of O_2 recorded with the FOSSPOR fluorescence probe as described above. Dissolved O_2 in the KP_i electrolyte solution was accounted for through Henry's law using the measured partial pressure of O_2 and the volume of solution in the cell.

4.9 References

1. Nozik, A. Photoelectrochemistry: Applications to Solar Energy Conversion *J. Annu. Rev. Phys. Chem.* **1978**, *29*, 189-222.
2. Abe, R.; Sayama, K.; Sugihara, H. Development of New Photocatalytic Water Splitting into H_2 and O_2 Using Two Different Semiconductor Photocatalysts and a Shuttle Redox Mediator IO_3^-/I^- *J. Phys. Chem. B* **2005**, *109*, 16052-16061.
3. Maeda, K.; Higashi, M.; Liu, D.; Abe, R.; Domen, K. Efficient Nonsacrificial Water Splitting through Two-Step Photoexcitation by Visible Light Using a Modified Oxynitride as a Hydrogen Evolution Photocatalyst. *J. Am. Chem. Soc.* **2010**, 132, 5858-5868.
4. Iwase, A.; Ng, Y. H.; Ishiguro, Y.; Kudo, A.; Amal, R. Reduced Graphene Oxide as a Solid-State Mediator in Z-Scheme Photocatalytic Water Splitting under Visible Light *J. Am. Chem. Soc.*, **2011**, *133*, 11054-11057
5. Maeda, K. Z-Scheme Water Splitting Using Two Different Semiconductor Photocatalysts *ACS Catal.*, **2013**, *3*, 1486-1503

6. Pinaud, B. A.; Benck, J. D.; Seitz, L. C.; Forman, A. J.; Chen, Z.; Deutsch, T. G.; James, B. D.; Baum, K. N.; Baum, G. N.; Ardo, S.; Wang, H.; Miller, E.; Jaramillo, T. F. Technical and Economic Feasibility of Centralized Facilities for Solar Hydrogen Production Via Photocatalysis and Photoelectrochemistry. *Energy Environ. Sci.* **2013**, *6*, 1983-2002.
7. Kronawitter, C. X.; Vayssieres, L.; Shen, S.; Guo, L.; Wheeler, D. A.; Zhang, J. Z.; Antoun, B. R.; Mao, S. S. A perspective on Solar-Driven Water Splitting with All-Oxide Hetero-Nanostructures *Energy Environ. Sci.* **2011**, *4*, 3889-3899.
8. Hong, S. J.; Lee, S.; Jang, J. S.; Lee, J. S. Heterojunction $BiVO_4/WO_3$ Electrodes for Enhanced Photoactivity of Water Oxidation *Energy Environ. Sci*. **2011**, 4, 1781-1787.
9. Li, P.; Zhao, X.; Jia, C.-j.; Sun, H.; Sun, L.; Cheng, X.; Liu, L.; Fan, W. $ZnWO_4$/BiOI Heterostructures with Highly Efficient Visible Light Photocatalytic Activity: The Case of Interface Lattice and Energy Level Match. *J. Mater. Chem. A* **2013**, *1*, 3421-3429
10. Leonard, K. C.; Nam, K. M.; Lee, H. C.; Kang, S. H.; Park, H. S.; Bard, A. J. $ZnWO_4/WO_3$ Composite for Improving Photoelectrochemical Water Oxidation. *J. Phys. Chem. C* **2013**, *117*, 15901-15910.
11. Kasem, K. K.; Dahn, M. Photodissociation of Water using Colloidal Nanoparticles of Doped Titanium (IV) Oxide Semiconductors for Hydrogen Production *Curr. Sci.* **2010**, *99*, 1068-1074.

CHAPTER 5

Structure, Optical Properties, and Magnetism of the Full $Zn_{1-x}Cu_xWO_4$ ($0 \leq x \leq 1$) Composition Range and the Application to Photochemistry

Portions of this chapter have been published:
Reproduced with permission from Yourey, J. E.; Kurtz, J. B.; Bartlett, B. M. *Inorg. Chem.*, **2012**, *51*, 10394. Copyright 2012 American Chemical Society
http://pubs.acs.org/doi/abs/10.1021/ic301607g

5.1 Introduction

The first row *d*-block tungstates, AWO_4, (A = Mn, Fe, Co, Ni, Cu, Zn) all crystallize in the wolframite structure,[1,2] which makes these materials an ideal tunable platform whose properties can be exploited through forming solid solutions. This chapter presents the optical and magnetic characterization of the wolframite solid solution series $Zn_{1-x}Cu_xWO_4$ prepared by traditional solid state methods as well as a modified Pechini sol-gel method. The particles prepared by the Pechini sol-gel synthesis were tested as photocatalysts for organic dye degradation. Furthermore, the series was evaluated as photoanodes for PEC water oxidation when prepared by a spin casting method. This work began as a continuation toward next generation tungstate electrodes to serve as light absorbing catalysts and photoanodes.

Zinc analogues were chosen because even though $ZnWO_4$ is a wide band gap semiconductor (3.4 eV), its direct band gap leads to high absorptivity. Furthermore, E_{fb} of $ZnWO_4$ resides at (–0.4 V vs. RHE), sufficiently more negative than $E°(H^+/H_2)$. Consequently, this material acts as an excellent UV photocatalyst for organic dye degradation,[3,4] In fact, its catalytic activity under UV illumination is quite high in comparison to the other UV light harvesting tungstates. The wolframite structure is typical of first row transition metals, and the larger band dispersion in wolframite

compared to scheelite (the other common tungstate crystal structure) results in a smaller effective mass, leading to higher charge carrier mobility.[5,6] With a high energy E_{fb}, the onset of photocurrent from a $ZnWO_4$ photoanode should also take place at lower applied biases. This is important because if it is coupled to another semiconductor, there will be higher photocurrents at the device's operating potential. $ZnWO_4$ possesses a valence band that is predominantly O (2p) in character and a conduction band that is W (5d) based. The band structures of $CuWO_4$ and $ZnWO_4$ are presented in Figure 5.1.

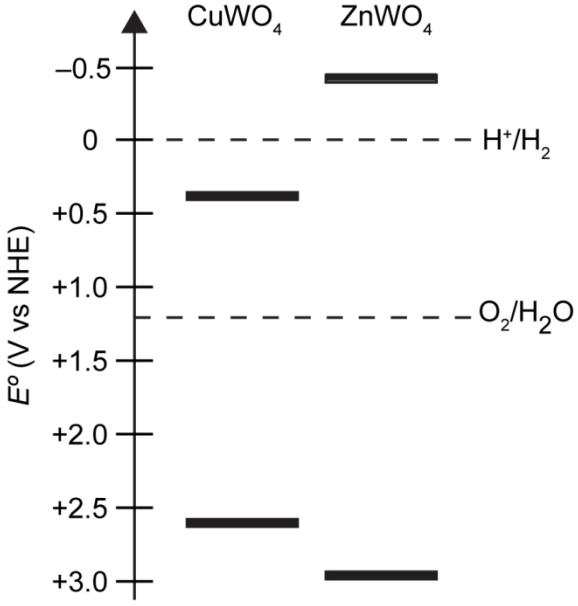

Figure 5.1 Band edges of $CuWO_4$ and $ZnWO_4$

The differences in the electronic structures of $CuWO_4$ and $ZnWO_4$ arise because of their *d*-electron counts, d^9 and d^{10}, respectively. Jahn-Teller distorted Cu^{2+} has a singly occupied $d_{x^2-y^2}$ orbital that likely contributes to the conduction band and diminishes the bulk conductivity. Yet, the strong absorption edge in the visible afforded by adding Cu(3d) character to the top of the valence band is necessary for getting efficient visible-light absorption. Therefore, the interplay between photon absorption and charge separation will dictate the optimal photocatalytic chemistry such as water oxidation or dye degradation.[7,8] By substituting zinc rather than another 1st-row transition metal, there are no additional ligand-field *d-d* transitions to serve as recombination centers. The overall hypothesis is that by systematically substituting Cu into $ZnWO_4$, a shift in E_{fb} would be accompanied by an increase in the valence band energy, leading to an increase in visible light in absorption.

As copper and zinc are substituted, the bond connectivity is scantly disrupted; pure $ZnWO_4$ crystallizes in the monoclinic space group *P*2/*c*. The Zn–O bond distances along *z* are 2.23 Å and 2.03 Å due to an eccentric Zn^{2+}.[9] Jahn-Teller effects cause an elongation of the Cu–O octahedra forming a distorted wolframite structure with *P*–1 symmetry. Accordingly, the Cu–O bond distances along *z* increase to 2.47 Å and 2.35 Å. The local octahedra for $CuWO_4$ and $ZnWO_4$ are presented in Figure 5.2.

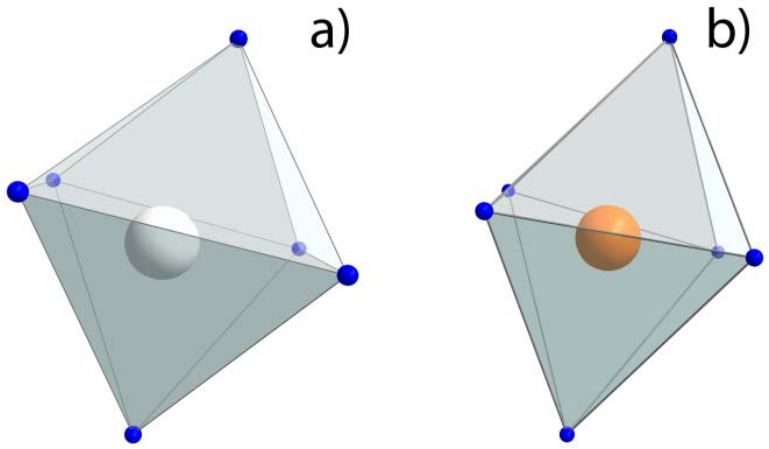

Figure 5.2 Zn–O a) and Cu–O b) octahedron in AWO_4

Research began by first developing an understanding of the entire composition range of the solid solution by optically and magnetically characterizing the series. In previous work, the series, $Zn_{1-x}Cu_xWO_4$ ($0 \leq x \leq 1$) prepared by direct precipitation has been determined to be a solid solution through crystallographic analysis using high-resolution Guinier powder X-ray diffraction[10] and by Rietveld analysis of the neutron diffraction pattern.[9,11] One highlight in this phase transition is the symmetry change of the crystal from *P*2/c to *P*–1 due to Jahn-Teller distortion of the Cu^{2+} cation. This transition is described as a ferroelastic transition, and is dependent on temperature and composition and has been modeled in terms of Landau theory using spontaneous strain to measure the order parameter.[12] The magnetic properties of $CuWO_4$[13–15] and of the $Zn_{1-x}Cu_xWO_4$ ($0.8 \leq x \leq 1$) series[16] have been investigated experimentally only to show that this system changes from an ordered antiferromagnet to a simple paramagnet as Zn^{2+} is substituted beyond the composition $Zn_{0.2}Cu_{0.8}WO_4$. $CuWO_4$ shows both long-range and short-range order that has been explained in a spin dimer analysis of the zig-zag CuO_4 chains. The work presented in this chapter correlates and optical and magnetic properties

of the solid solution to understand the transition from $CuWO_4$ to $ZnWO_4$ with the goal of connecting these properties to photocatalysis.

5.2 Synthesis, Structure, and Morphology of $Zn_{1-x}Cu_xWO_4$

The $Zn_{1-x}Cu_xWO_4$ series has been synthesized by traditional solid methods at 850 °C for 36 h as per the reaction:

$$x\mathrm{CuO} + (1-x)\mathrm{ZnO} + \mathrm{WO_3} \rightarrow \mathrm{Zn_{1-x}Cu_xWO_4} \qquad 1)$$

Annealing temperatures ≥ 850 °C have been used to synthesize $CuWO_4$, $ZnWO_4$ and other rare earth metal tungstates by traditional solid state methods. [6,17] Intermediate grinding helps to assure complete homogenization into a single phase, which we affirm by the indexed X-ray diffraction patterns. Of particular note, the diffraction patterns do not change after the second 12 h annealing for any samples with one exception, $x = 0.2$. This composition is close to $Zn_{0.78}Cu_{0.22}WO_4$, where the transition between the monoclinic $P2/c$ structure of $ZnWO_4$ and the triclinic $P\text{–}1$ of $CuWO_4$ is observed. For the materials prepared by the Pechini citric acid method according to the overall reaction (after annealing)

$$12\ \mathrm{A^{2+}}(aq) + \mathrm{H_2W_{12}O_{40}^{6-}}(aq) + 8\mathrm{H_2O}(l) \rightarrow\ 12\ \mathrm{AWO_4}(s) + 18\mathrm{H^+}(aq) \qquad 2)$$

Long heating times are not required to homogenously distribute Zn^{2+} and Cu^{2+} ions since this synthesis uses soluble aqueous precursors. One 3-hour annealing at 700 ºC is sufficient to obtain phase pure material (Figure D.1).

Compound purity is verified by ICP-AES analysis on the digested samples; data are presented in Table D**.1**. Figure 5.3 presents the diffraction data for the solid-state synthesized series in the range 14 – 27 °2θ.

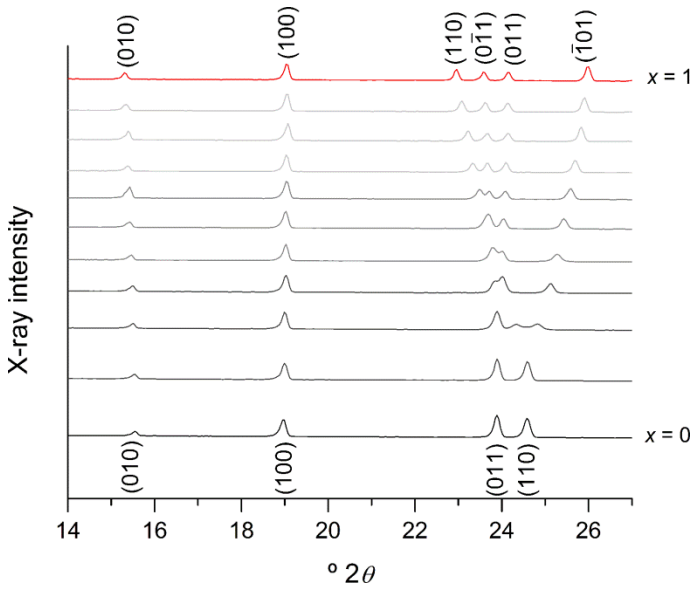

Figure 5.3 Indexed XRD patterns of $Zn_{1-x}Cu_xWO_4$ prepared by solid-state methods.

Notably, the Bragg reflections corresponding to the (010) and (100) planes do not change as a function of *x*. These planes are predominately related to the WO_6 octahedra, and therefore are not expected to change (Figure D.2). Between 23 and 26 °2θ, we observe the evolution of the de-symmetrization of the structure as Cu^{2+} is incorporated. The end-member composition $CuWO_4$, crystallizes in the lower symmetry *P*–1 space group, evidenced by the appearance of additional (0–11) and (–101) Bragg reflections. The (110) and (011) planes are predominately associated with the $A^{2+}O_6$ octahedra, and are therefore are most influenced in the transition from $ZnWO_4$ to $CuWO_4$ (Figure D.2). The (110) and (011) reflections shift from 24.5 to 23.0 °2θ and from 23.9 to 24.1° 2θ, respectively. SEM images of the $Zn_{1-x}Cu_xWO_4$ series are presented in Figure D.3. The average particle sizes for $CuWO_4$ and $ZnWO_4$ samples are approximately 5 µm and 1.5 µm, respectively for compounds prepared by solid-state reaction (1). Here, there is a gradual increase in particle size as *x* increases in the annealed samples. In contrast, materials prepared by the Pechini method in reaction (2) show a more uniform particle size of ~200 nm.

5.3 Optical Properties of $Zn_{1-x}Cu_xWO_4$

Figure 5.4 shows absorbance as a function of wavelength for the series.

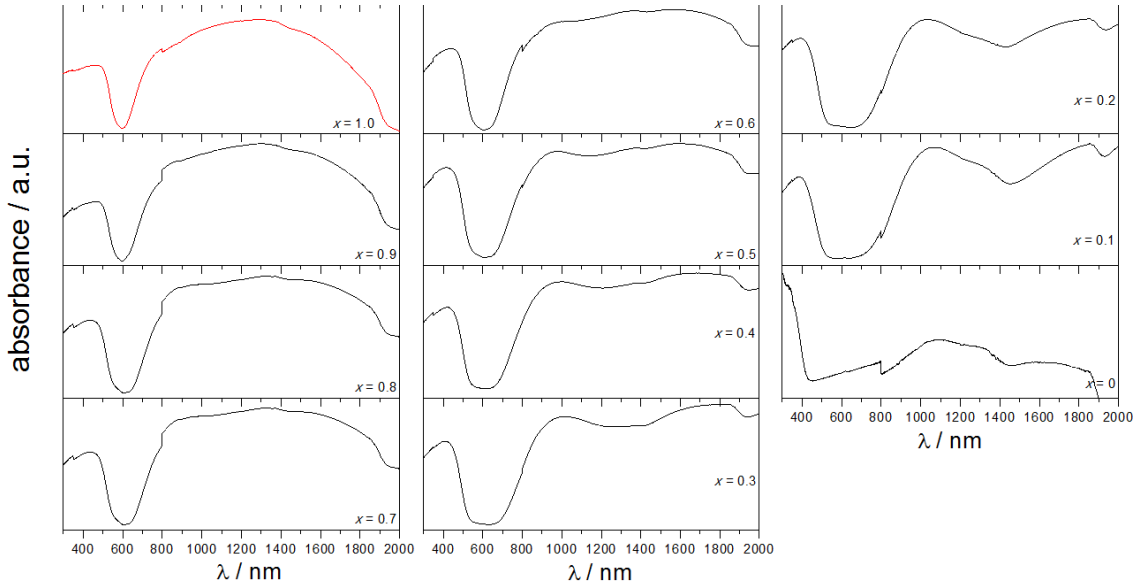

Figure 5.4 UV-Vis-NIR spectra of the $Zn_{1-x}Cu_xWO_4$ series.

The end member $ZnWO_4$ shows absorption attributed to the O(2p) → W(5d) LMCT edge at ~ 425 nm. In contrast, the $CuWO_4$ absorption edge begins at 550 nm as a result of a Cu(3d) → W(5d) MMCT, with localized Cu *d*-*d* transitions observed at ~625 nm and extending to longer wavelengths. Other compositions within the $Zn_{1-x}Cu_xWO_4$ series show absorption edges between those observed for the end member compositions $ZnWO_4$ and $CuWO_4$. As *x* increases, we observe a bathochromic shift in the characteristic charge-transfer absorption edge due to increasing Cu(3d) density near the top of the valence band and a possible shifting in E_{fb} to lower energy. Additionally, as *x* increases, a hypsochromic shift and concomitant increase in the intensity of the Cu *d*-*d* transitions is observed. $ZnWO_4$ and $CuWO_4$ are described as direct and indirect absorbing materials respectively; therefore we present a plot of band gap, E_g vs. *x* in Figure 5.5.

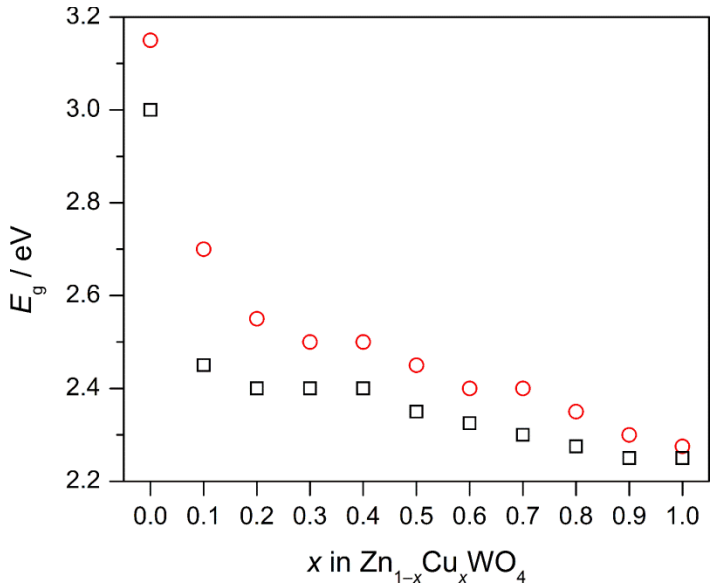

Figure 5.5 Direct (red circles) and indirect (black squares) band gap energies in the $Zn_{1-x}Cu_xWO_4$ series.

Both the direct and indirect fits to the band gap decrease linearly as x increases from to 0.1 to 1, illustrating that the intermediate compositions are composed of a random distribution of Cu and Zn on the cation sublattice, and are not simply a two-phase mixture of $CuWO_4$ and $ZnWO_4$. Notable in Figure 5.5 is the large decrease in the absorption spectrum once 10 mole percent Cu^{2+} is incorporated. This result will be discussed further in the context of the PEC results later, but it seems as Cu is added, the large change in band gap may be a result of new densities of states rather than a controlled shift in the W (5d) based conduction band. The initial large change may be due to the formation of a new, Cu(3d) based state and the later gradual decrease in E_g from x = 0.2–1 may be due to increasing Cu(3d) density at the valence band maximum. This is in disagreement with the original hypothesis which predicted a monotonic shift in absorption along the entire series. The measured band gap of $Zn_{0.9}Cu_{0.1}WO_4$ is only 0.2 eV greater than $CuWO_4$ described by the direct Tauc plot. This result is concurrent with the electrochemical data presented in section 2.4, where the conduction band of $CuWO_4$ contains significant Cu (3d) character.

We use far-IR spectroscopy to evaluate the local symmetry change as copper is substituted for zinc in the structure. As greater copper density is added, Jahn-Teller effects drive the tetragonal distortion of the $A^{2+}O_6$ octahedra, lowering the energy of the

entire system. Far-IR spectroscopy lets one evaluate this change and monitor the structure as it de-symmetrizes. The far-IR spectra are presented in Figure 5.6.

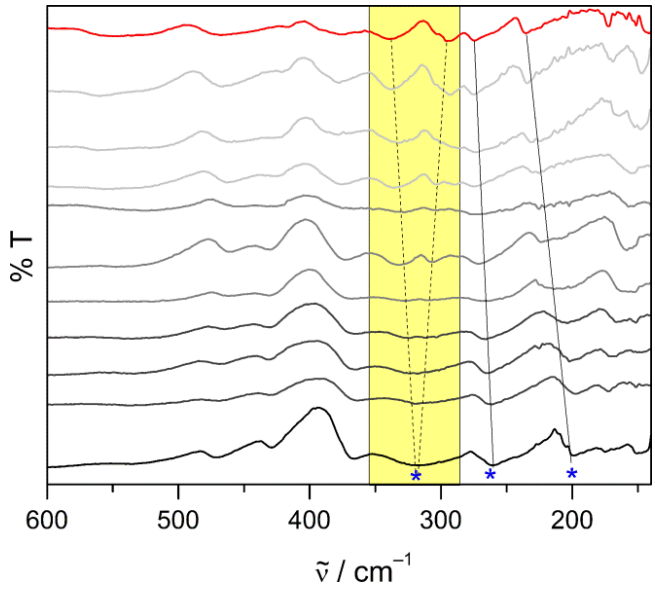

Figure 5.6 Far IR spectra of the $Zn_{1-x}Cu_xWO_4$ series.
$ZnWO_4$ is shown in black; $CuWO_4$ is shown in red. The highlighted area shows the evolution of the A_u symmetry mode as the structure evolves from P2/c ($ZnWO_4$) to P–1 ($CuWO_4$).

The $Zn_{1-x}Cu_xWO_4$ series is presented in the figure and the data are stacked for clarity. We identify the vibrational frequencies of the M^{2+}–O (M = Cu, Zn) stretches by comparing the end members to known literature[18–20] and evaluating the smooth transition from $ZnWO_4$ to $CuWO_4$ throughout the series. The symmetry of these systems is reduced because the divalent cation is off-centered,[11] but the vibrational modes of the Zn–O and Cu–O octahedra can be derived from C_{2h} and C_i site symmetry. Two medium-intensity Zn–O stretches in the $ZnWO_4$ structure appear at 200 cm^{-1} (B_u) and 260 cm^{-1} (B_u) and show a shift to higher energy as x increases; the lines in the figure are guides to the eye. In $CuWO_4$, the corresponding A_u stretches are observed at 235 and 275 cm^{-1}, respectively. The highlighted region of the figure shows that the strong-intensity A_u mode in $ZnWO_4$ observed at 320 cm^{-1} splits into two peaks at x = 0.3. In $CuWO_4$, the two stretches appear at 295 and 338 cm^{-1}. The peak splitting observed at x = 0.3, correlates to the changeover from $P2/c$ ($ZnWO_4$) to $P–1$ ($CuWO_4$) and the increase in energy between the two indicates a gradual change of the $A^{2+}O$ octahedra. The intensity and shape of the peaks in $ZnWO_4$ and $CuWO_4$ match that which has been discussed in the literature.[18] As

the peaks at 200 and 260 cm^{-1} undergo a hypsochromic shift with increasing *x*, there is no real change in their shape, whereas the broad peak originally found at 320 cm^{-1} splits into two medium-intensity peaks found at 295 and 338 cm^{-1} in $CuWO_4$. In $CuWO_4$, the peaks at 235, 275, and 295 cm^{-1} are medium intensity, and the peak at 338 cm^{-1} is stronger intensity. There are also symmetric oxygen-based A_u stretches uniting W–O octahedra in the zigzag chain at 425 and 470 cm^{-1} as well as tungsten-based low energy stretches at 150 and 170 cm^{-1} that again, do not shift significantly as *x* changes. Our results are similar to what has been described in the compound $Zn_{0.75}Cu_{0.25}WO_4$, where low temperature mid-IR studies highlight the *P*–1 to *P*2/*c* phase transition as a function of temperature.[12]

5.4 Magnetic Properties of $Zn_{1-x}Cu_xWO_4$

The magnetic properties of the 1st row transition metal wolframite series have been evaluated due to the ease of forming solid solutions. For example, the multiferroic tungstate, $MnWO_4$, has interesting magneto-electric properties, which have been altered by substituting other first row transition metal cations. In general, it has been shown that doping into $MnWO_4$ with both diamagnetic ions such as Zn^{2+} and Mg^{2+} as well as paramagnetic ions such as Fe^{2+} and Co^{2+} influences the ordering temperatures found within the $MnWO_4$ system: simply, diamagnetic ions decrease the ordering temperatures while paramagnetic ions increase the ordering temperatures. [21– 30]

In addition to substituting the divalent cation, anion substituted tungstates have been prepared such as the series $CuMo_{1-x}W_xO_4$ ($0 \leq x \geq 0.1$). In this series, there is a temperature-dependent first-order phase transition at ambient pressure.[31] Magnetic susceptibility coupled with neutron diffraction on the series $CuMo_{1-x}W_xO_4$ (x = 0.15, 0.25, 0.35) shows that the magnetic unit cell changes from one that is doubled along the *a* axis for x = 0.15, which is identical to $CuWO_4$, to one that is doubled along the *c* axis (x = 0.25, 0.35).[15] Additionally, a spin dimer analysis in $CuMo_{0.25}W_{0.75}O_4$ shows the magnetic unit cell should double along both *a* and *b*, distinct from the end-member compositions.[32,33] In this case, magnetic and thermochromic studies describe a system that does not maintain a complete solid solution throughout all concentrations of tungsten and molybdenum by identifying impurity phases through these experiments.

The magnetic structure of $CuWO_4$ is complex. At a molecular level, it is described as a spin dimer with zigzag chains of CuO_6 edge-sharing octahedra. The ordering transition below the Néel point arises from long-range 3-D antiferromagnetic ordering with a unit cell that doubles along the crystallographic *a* axis (Figure D.4). The dc susceptibility data for the series $Zn_{1-x}Cu_xWO_4$ are shown in Figure 5.7.

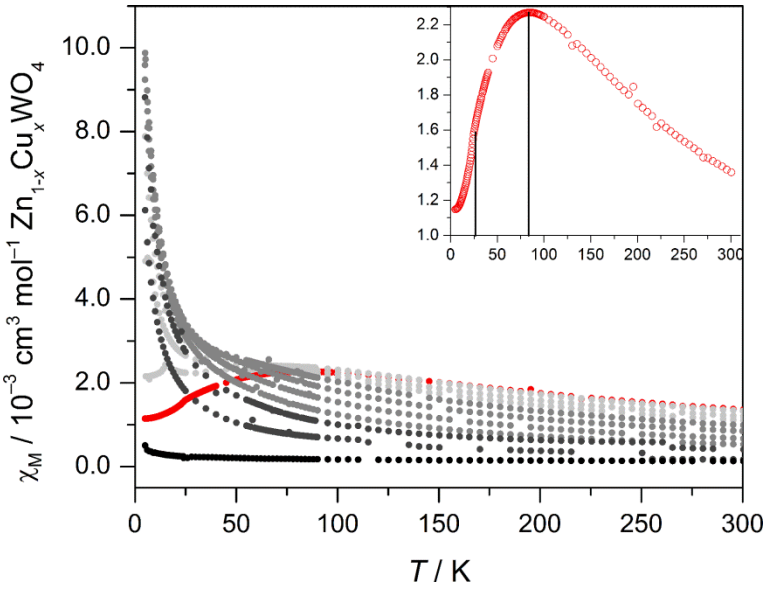

Figure 5.7 Molar susceptibility of the $Zn_{1-x}Cu_xWO_4$ series.
$ZnWO_4$ is shown in black, $CuWO_4$ is shown in red, and intermediate compositions are in gray. Inset magnifies the $CuWO_4$ data and shows two ordering transitions.

The end-member composition $CuWO_4$ shows a broad peak maximum at 82 K (Inset of Figure 5.7). Ac susceptibility experiments show no frequency-dependence in this maximum (Figure D.5 ruling out spin glass or spin liquid behavior associated with this transition). As the concentration of copper decreases, this transition temperature decreases to 69 K (x = 0.9) and to 59 K (x = 0.8). For compositions having $x < 0.8$, no discernible transition is observed. In order to obtain sufficient signal for these magnetically dilute samples, a strong measuring field (1 T) is required. Figure D.6 shows that for $CuWO_4$, there are no differences in the magnetic susceptibility arising from a 1 T measuring field compared to a more typical 1000 Oe (0.1 T) measuring field. The broad maximum at 85 K in the susceptibility at higher copper concentration has been well described in the literature, and this transition decreases monotonically with x. This transition in $CuWO_4$ is attributed to the strongest antiferromagnetic interaction of the spin units within the 2D sheets in $CuWO_4$, yet it does not lead to long range ordering.[13]

Rather, the high-temperature antiferromagnetic ordering above the Néel point found in $Zn_{1-x}Cu_xWO_4$ (x = 0.8, 0.9, 1) mimics the susceptibility behavior in CuO, which shows a similar type of ordering above its true Néel point.[34] This ordering has been interpreted as the transition from cooperative to non-cooperative magnetism, (*i.e.*—a transition from lattice- to molecular interactions at the Néel point) as described by Wucher.[35]

Various physical methods have been employed to determine the Néel temperature of $CuWO_4$, which is elusive by simple susceptibility measurements since there is no sharp maximum in $\chi_M(T)$. The disappearance of the (½ 0 0) magnetic Bragg reflection in $CuWO_4$ at 23 K using neutron diffraction is definitive, and matches the temperature at which an EPR signal disappears (24 K).[13,14] Although there is no such defining feature for T_N in the $\chi_M(T)$ plot, the first derivative $d\chi_M/dT$ shows a maximum at 23.5 K, which compares favorably to a T_N of 22.5 K reported by this method in the literature.[15] Then, the upturn in $\chi_M(T)$ below 3 K is ascribed to ferromagnetic interactions between Cu^{2+} ions within the same chemical cell, a common interaction observed for the first-row transition-metal tungstates (A = Fe, Co, Ni).[36] T_N was also determined from $d\chi_M/dT$ for x = 0.9 and 0.8: 14.5 K, and 5.5 K, respectively. The derivative plots, $d\chi_M/dT$ are presented in Figure D.7 for both the solid-state and Pechini synthesized compounds.

The observed changes in both the high-temperature transition and the Néel temperature for $Zn_{1-x}Cu_xWO_4$ (x = 0.8, 0.9, 1) are consistent with a magnetic Ising model.[37] Specifically, Néel points in Mn-, Fe-, and $CuWO_4$ shift to lower temperatures as described by these theories.[16] Interestingly, because of the complex magnetic properties of $CuWO_4$, it shows deviation from the ideal models using 1 or 2-dimensional systems in that the transition from an antiferromagnetically ordered material to a simple paramagnet occurs at such low dilution.

In order to evaluate the spin interaction between nearest-neighboring copper atoms, we performed Curie-Weiss analysis in the paramagnetic regime. Figure 5.8 shows a plot of the effective moment (μ_{eff}) and Weiss constant (Θ) as a function of x for the entire $Zn_{1-x}Cu_xWO_4$ series.

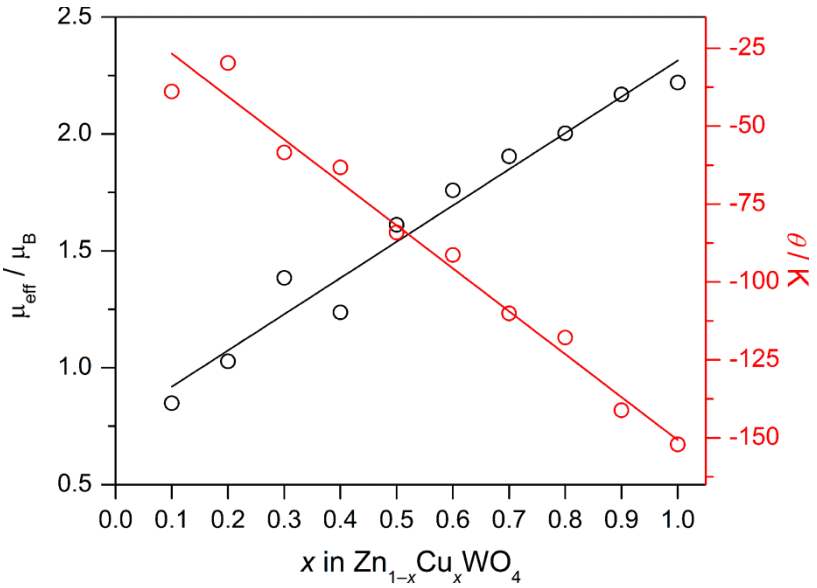

Figure 5.8 Trends in μ_{eff} and the Weiss constant, Θ in the series $Zn_{1-x}Cu_xWO_4$ prepared by solid-state synthesis.

The results show that the magnitude of the Weiss constant increases linearly from ~–39 K for x = 0.1 to –152 K for x = 1. Three effects are clear:

1. In $CuWO_4$, there is strong antiferromagnetic coupling of nearest-neighbor spins.
2. The variation of Θ with x reflects that the exchange interaction gets stronger as the number of paramagnetic Cu^{2+} centers increases.
3. As expected, the effective moment increases linearly with increasing copper concentration due to incorporating greater spin density in the compound.

A mean field theory treatment for $CuWO_4$ gives an average exchange constant J of –213 cm^{-1} according to the equation:

$$\Theta = \frac{z\,J\,S(S+1)}{3k_B} \qquad 3)$$

where z is the number of nearest neighbor spins (2 in the zigzag chains of the wolframite structure), S = ½ for Cu^{2+}, and k_B is the Boltzmann constant, 0.695 cm^{-1} K^{-1}. We note that this energy is on par with the sum of the intrachain interactions calculated by Koo and Whangbo (the sum of the exchange energies of intrachain antiferro- and ferromagnetic components in their DFT study is –282 cm^{-1}).[32] We note however, that the analysis in reference 32 is based on a more detailed spin dimer model that also explains the short-range order at 90 K in $CuWO_4$. We point out the similarity in coupling constants simply to demonstrate that the decrease in intrachain coupling as the Zn-

concentration increases in our materials may also explain that disappearance of any short-range order as *x* decreases.

Then, by evaluating the magnetic moment on a per mol copper basis for each compound in the series, the average magnetic moment was found to be 2.30 ± 0.19 μ_B, which is in good agreement with the observed magnetic moment for $CuWO_4$ of 2.23 μ_B. This result is in accord with our optical data, strongly demonstrating that copper- and zinc ions statistically distribute over common 2*i* Wyckoff sites on the lattice. Accordingly, susceptibility measurements provide a method for determining whether or not a mixed-metal tungstate is in fact a solid solution or a two-compound mixture, important for the intermediate compositions here and as well as for other 1st row transition metal tungstates where their X-ray diffraction patterns are virtually identical because these compounds do not Jahn-Teller distort.

We have prepared $Zn_{1-x}Cu_xWO_4$ (x = 0.8, 0.9, 1.0) by a Pechini sol-gel method in which the precursors are atomically mixed prior to annealing. We focus on the compositions with high Cu^{2+} concentration here since they have the smallest band gaps. For these compounds, Figure D.8 compares T_N, Θ, and μ_{eff} for the compounds prepared by both methods. The $\chi_M(T)$ plots are nearly superimposable (Figure D.9), and the derived magnetic properties match very closely, as presented in Table 5.1.

Table 5.1 Magnetic Properties of $Zn_{1-x}Cu_xWO_4$

Compound	μ_{eff} / μ_B	Θ / K	T_N / K	T_2 / K	ptcl size / μm
Solid-state Synthesis					
$CuWO_4$	2.22	−152	23.5	82	5–7
$Zn_{0.1}Cu_{0.9}WO_4$	2.17	−141	14.5	69	5–7
$Zn_{0.2}Cu_{0.8}WO_4$	2.00	−118	5.5	59	5–7
Pechini Synthesis					
$CuWO_4$	2.26	−155	23	80	0.2–0.5
$Zn_{0.1}Cu_{0.9}WO_4$	2.16	−145	13	62	0.1–0.5
$Zn_{0.2}Cu_{0.8}WO_4$	1.99	−116	5	55	0.1–0.5

As in the solid state preparation, T_N in materials prepared by the Pechini method decreases with decreasing copper concentration. The higher-temperature

antiferromagnetic ordering transition is also observed for the Pechini compounds, and again shows a shift to lower temperature with decreasing copper content. This ordering temperature varies slightly, which may be explained by subtle differences in particle size, which has been observed in CuO nanoparticles.[38] Notably, the effective moment and Weiss constant were also determined using the paramagnetic region of the $\chi_M(T)$ plot, and match those determined for the solid-state synthesized congeners.

To provide an example of how susceptibility measurements distinguish further between having a random distribution of copper and zinc on the common 2*i* Wyckoff sites from having a two-phase mixture of $CuWO_4$ and $ZnWO_4$, we prepared a SQUID sample composed of 50% $CuWO_4$ and 50% $ZnWO_4$ by mass. The $\chi(T)$ in Figure 5.9 compares the gram susceptibility for the 1:1 two-phase mixture, synthesized $Zn_{0.5}Cu_{0.5}WO_4$, and pure $CuWO_4$.

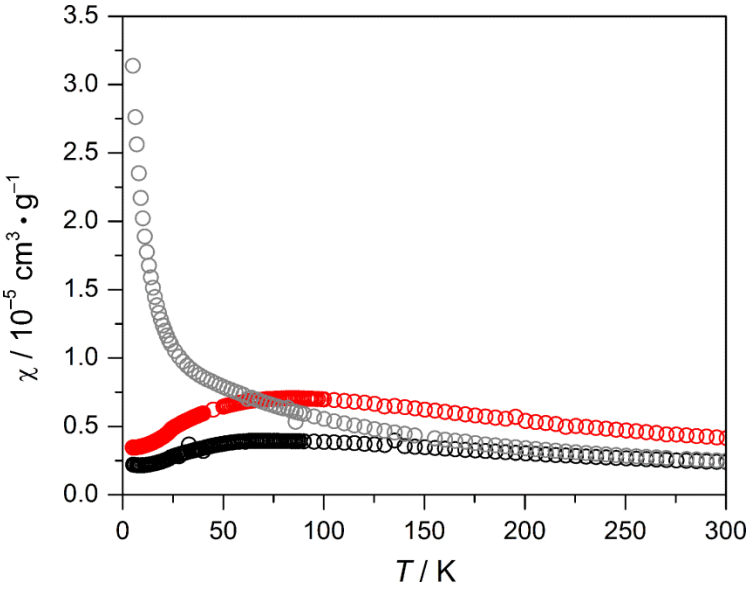

Figure 5.9 Comparison of the gram susceptibility of $CuWO_4$ (red), a 1:1 mixture of $ZnWO_4$:$CuWO_4$ (black), and the compound $Zn_{0.5}Cu_{0.5}WO_4$ (gray).

Of note is that the 1:1 mixture shows a susceptibility that is ~½ that of $CuWO_4$, but is otherwise indistinguishable. This is expected for $CuWO_4$ buried in a diamagnetic host matrix. In contrast, the synthesized compound $Zn_{0.5}Cu_{0.5}WO_4$ is distinct; it shows no discernible magnetic transitions.

The presented data have direct implication in understanding the electronic structure of water-oxidation photoanodes that have been prepared. The highest

performing (i.e.—highest current) photoanodes are composed of a 1:1 mixture of wolframite $CuWO_4$ and monoclinic WO_3, whose structure and composition we conclude by X-ray diffraction and elemental analysis. This composite mixture shows a similar result to Figure 5.9, where the susceptibility of the $CuWO_4$ phase is not disrupted by the presence of WO3, validating the physical mixture of phases compared to an alloyed phase. In order to understand how electronic structure impacts the kinetics on the $CuWO_4$ for water oxidation, PEC and photocatalysis studies on the $Zn_{1-x}Cu_xWO_4$ series will provide insight into the charge transport limitations of this system by incorporating a closed shell 2+ cation which does not contain potential trap states that arise at a bulk heterojunction, as is the case in our $CuWO_4$:WO_3 composite materials.

The optical data provides insight into the electronic structure of $Zn_{1-x}Cu_xWO_4$. Our results indicate a smooth transition in the series, though the large initial change in E_g with 10 mole % incorporation of Cu, hinting at the presence of Cu (3d) states within the gap. As more copper is incorporated into the structure, the greater the Cu(3d) density contributes to the top of the valence band. This raises the potential energy of the valence band, thereby lowering the overall band gap from $Zn_{1-x}Cu_xWO_4$ ($0.2 \leq x \leq 1$). The interplay between band edge positions (overpotential), band gap (photon flux), and band width (carrier mobility) determines rate in photocatalysis, and this forms the basis of evaluating this series as both photoanodes and photocatalysts for solar-driven water oxidation.

5.5 Photocatalysis on $Zn_{1-x}Cu_xWO_4$ powders

The Pechini synthesized $Zn_{1-x}Cu_xWO_4$ powders were tested as photocatalysts for organic dye degradation. Methylene Blue (MB) is a common organic dye used to evaluate the photocatalytic activity of semiconductors. It has been studied commonly on TiO_2[39] dye degradation is known to take place through radical based mechanisms facilitated by electron transfer from the semiconductor. The series was prepared in order to test our hypothesis that $Zn_{1-x}Cu_xWO_4$ solid solutions would show increased rates of dye degradation due to maintained visible light absorption (Cu^{2+}) and a high energy conduction band edge (Zn^{2+}). The results of MB degradation experiment are presented in Figure 5.10.

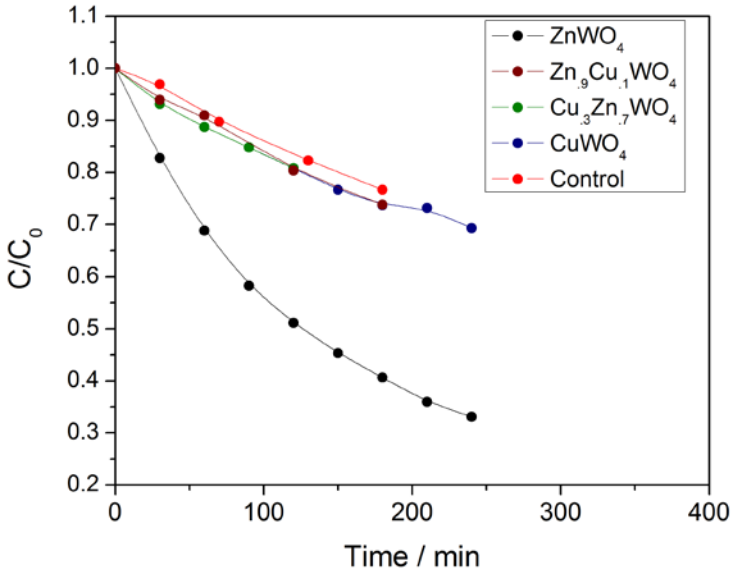

Figure 5.10 MB degradation experiments on $Zn_{1-x}Cu_xWO_4$ powders under 500 mW/cm^2 (5-sun) AM1.5G illumination.

Figure 5.10 presents the degradation results of some representative samples prepared by Pechini sol-gel methods. We focus on the low copper concentration regime because the measured band gap in these materials is sufficiently smaller than $ZnWO_4$, yet with higher amounts of zinc we hypothesized that the flat band potential would be higher energy, like $ZnWO_4$. The results show that using AM1.5G illumination, $ZnWO_4$ is still the most active tungstate material. In fact, once 10 mol % of copper is introduced, the activity decreases to that similar to $CuWO_4$, which is only slightly more active than baseline. An electrochemical and PEC study of $Zn_{1-x}Cu_xWO_4$ photoanodes will be discussed in section 5.6 and provide insight into this result. As discussed in the literature, $CuWO_4$ does show increased activity with respect to other visible light absorbing tungstates,[40] but this activity is still sufficiently lower than that of $ZnWO_4$. There is literature precedent for increasing activity in $ZnWO_4$ by adding Sn^{2+}.[41] However, in this manuscript, a UV cutoff filter ($\lambda \geq 420$ nm) prevents $ZnWO_4$ from absorbing any light, and thus it shows no photocatalytic activity. In our case, we are using an AM1.5G filter which attenuates the power of UV light to match the output of the sun.

The measured surface area of the Pechini sol-gel particles was approximately 10 m^2/g. This value is lower than $ZnWO_4$ prepared by hydrothermal reaction (HTR) methods (20–30 m^2/g).[42] Additionally, the MB adsorption was significantly lower in

Pechini sol-gel particles when compared to HTR prepared $ZnWO_4$. $ZnWO_4$ shows 93% adsorption of MB vs. 12% adsorption for HTR and Pechini synthesized particles, respectively. The quantity of dye adsorbed onto the oxide was quantified by UV-Vis spectroscopy. The decrease in solution concentration of dye after the addition of the oxide was measured and the difference in concentration was due to adsorption onto the oxide. Adsorption of the organic dye is crucial for successful catalysts and therefore we sought to prepare $Zn_{1-x}Cu_xWO_4$ by HTR methods to increase the surface area and adsorptive properties of the catalyst.

$ZnWO_4$ is typically prepared hydrothermally in a basic solution.[43] OH^- acts as a capping agent during crystallization because it adsorbs onto the [100] face of $ZnWO_4$.[42,44] Rods are typically formed and we sought to translate this growth mechanism to generate $CuWO_4$ and $Zn_{1-x}Cu_xWO_4$ rods. However, during crystallization in basic condition an undesired metastable phase, $Cu_2WO_4(OH)_2$ formed.[45] Therefore, a pH of 6 was necessary to form the desired phase. pHs lower than 6 solubilize the precursors and no solid product forms. Figure D.10 presents the diffraction results of the synthesis of $CuWO_4$ at pH 6 and 8. As can be seen, at pH 8 the undesired $Cu_2WO_4(OH)_2$ forms whereas pH 6 only hydrated $CuWO_4$ forms. Figure D.11 shows the corresponding SEM images of $CuWO_4$ prepared hydrothermally at pH 6 at 180 °C for 12h. MB adsorption was sufficiently increased in the $CuWO_4$ particles prepared by HTR methods in comparison to Pechini sol gel synthesis, 85 % adsorption vs 18 %, respectively. However, the rates of MB degradation were not influenced by this advantageous increase in MB adsorption and decrease in particle size, indicating still that under 500 mW/cm^2 (5-sun) AM1.5G illumination, $CuWO_4$ is not an active dye degradation catalyst.

The mechanism for dye degradation is commonly known to pass through two mechanisms. The photogenerated e^-/h^+ pair creates superoxide ($O_2^{\bullet-}$, $E°$ = –0.33 V NHE) and hydroxyl radicals ($OH^{\bullet}$, $E°$ = 2.38 V NHE), respectively. Either of these species begins the radical degradation of the organic dye. $ZnWO_4$ can potentially form both of these species, resulting in an active dye degradation catalyst. However, the electronic structure of $CuWO_4$ precludes the formation of $O_2^{\bullet-}$ and $OH^{\bullet}$, hindering its performance as a photocatalyst. The original hypothesis to form solid solutions possessing a suitable electronic structure for radical formation and a band gap in the visible was not recognized

in the $Zn_{1-x}Cu_xWO_4$ series. Many of these reasons are clearer through the experiments discussed in Chapter 3, which took place chronologically after these dye degradation experiments. Additionally, PEC experiments on $Zn_{1-x}Cu_xWO_4$ photoanodes which were also conducted prior to the EIS studies support those results. Cu (*3d*) states both in the conduction band as well as mid-gap dictate many of the fundamental PEC properties of $Zn_{1-x}Cu_xWO_4$ solid solutions.

5.6 Photoelectrochemical studies on $Zn_{1-x}Cu_xWO_4$

$Zn_{1-x}Cu_xWO_4$ photoanodes were synthesized using the sol-gel spin casting method used to form $CuWO_4$. The final Zn:Cu atomic ratio was simply controlled through the atomic ratio in the nitrate precursors chosen. The results of LSV traces conducted on representative members of the $Zn_{1-x}Cu_xWO_4$ series are presented in Figure 5.11.

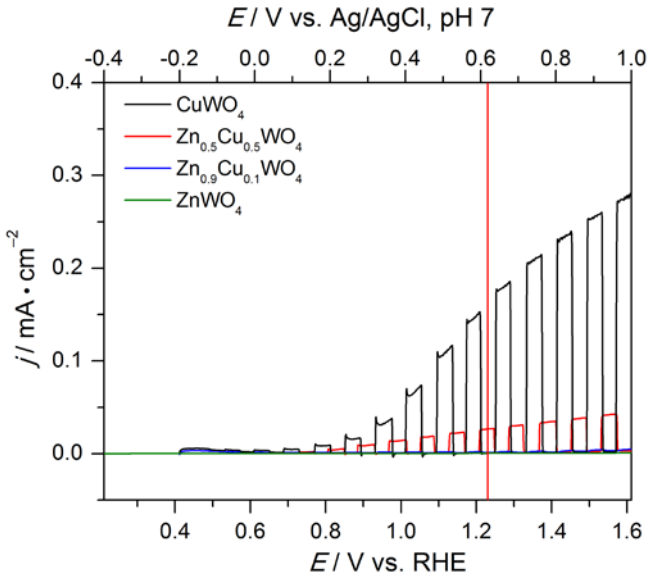

Figure 5.11 LSV traces of $Zn_{1-x}Cu_xWO_4$ photoanodes under AM1.5G illumination.

In this figure, the greater amount of zinc incorporated into the solid solution, the lower the photocurrent. $ZnWO_4$ is inactive as a photoanode under AM1.5G illumination, and also only shows minimal PEC response under illumination with an unfiltered Xe lamp. CV provides insight into how Cu(3*d*) states incorporate into the electronic structure of $Zn_{1-x}Cu_xWO_4$. Figure 5.12 presents CV traces of representative electrodes in a N_2 purged solution to identify the redox chemistry of copper in the solid-solutions generated in forward bias.

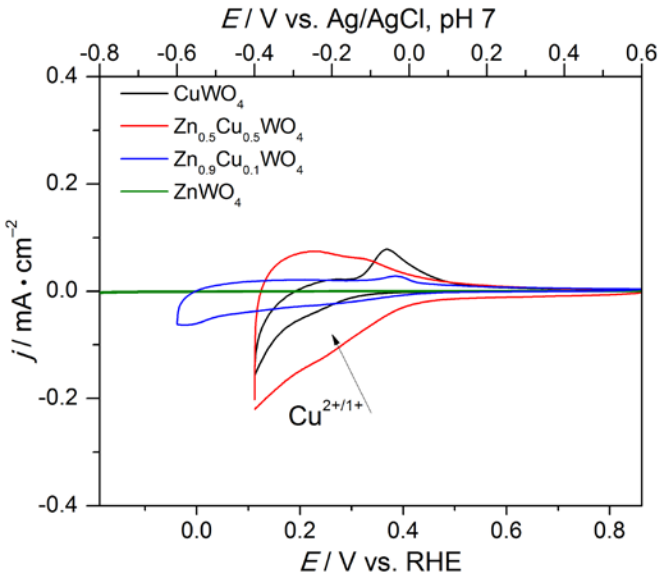

Figure 5.12 CV traces of $Zn_{1-x}Cu_xWO_4$ in N_2 purged cell in the dark

In Figure 5.12, $ZnWO_4$ shows zero redox chemistry in the experimental window, as indicated by the green trace. $Zn_{0.5}Cu_{0.5}WO_4$, $CuWO_4$, and $Zn_{0.9}Cu_{0.1}WO_4$ show a reduction at nearly the same potential in the CV trace. This reduction event is less prevalent on $Zn_{0.5}Cu_{0.5}WO_4$, and there seems to be more surface capacitance on the electrode (which may be an artifact of the chosen electrode), but it is identifiable in the CV trace. $Zn_{0.9}CuWO_4$ shows reduction beginning at similar potentials compared the other copper containing materials, but the current is smaller. On the return, an oxidation peak is seen again at the same potential as $CuWO_4$. This behavior also translates to the measured open-circuit voltages (OCP) measured on the various solid-solutions. $ZnWO_4$ has an OCP that is significantly more negative than any of the series containing copper (0.05 V RHE in N_2 purged KP_i under illumination). As copper is incorporated into the series, the measured OCP shifts toward more positive potentials and nearly matches that of pure-phase $CuWO_4$, again reaffirming that Cu(3*d*) states are dictating the PEC and electrochemistry of tungstate anodes. $Zn_{0.9}Cu_{0.1}WO_4$ has a measured OCP of +0.5 V RHE under AM1.5G illumination which is typical to $CuWO_4$.

The E_{fb} of $ZnWO_4$ and $Zn_{0.5}Cu_{0.5}WO_4$ was determined using Mott-Schottky analysis of the EIS data in order to approximate its band edge positions (Figure D.12). E_{fb} of $ZnWO_4$, $Zn_{0.5}Cu_{0.5}WO_4$, and $CuWO_4$ are –0.45 and , +0.10, and 0.45 V RHE, respectively. These values indicate that there are states shifting toward more positive

potentials with the incorporation of copper. The measurement may be probing the capacitance of W(5d) states which make up the conduction band in $ZnWO_4$ and a significant part of $CuWO_4$. In $Zn_{0.5}Cu_{0.5}WO_4$, the capacitance associated with the Cu(3d) states interrupts the measurement causing a deviation from linearity, and therefore the measured E_{fb} was constructed from a smaller voltage window. This result however, does trend with the original hypothesis as to the continuous evolution of the electronic structure between the two end members, but as seen in Figure 5.13, the Cu(3d) states add in at a constant energy level and do not change as a function of zinc content.

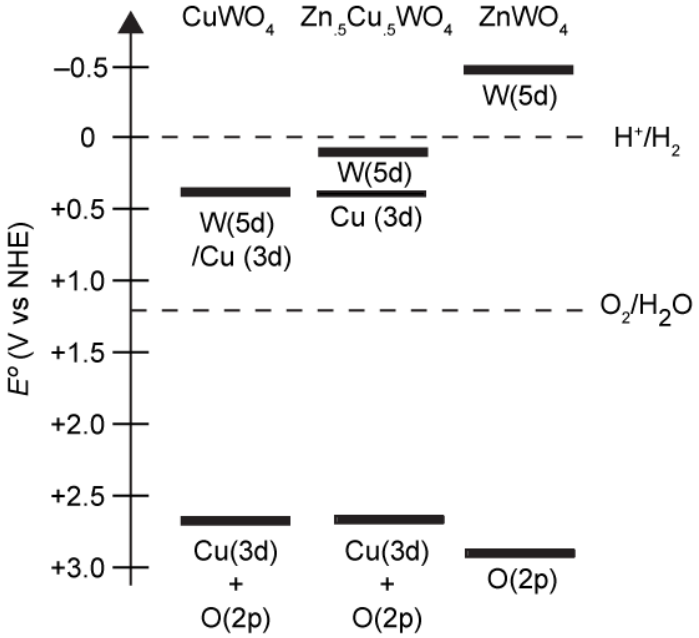

Figure 5.13 Band diagrams of $Zn_{1-x}Cu_xWO_4$ showing E_{fb} measured by Mott-Schottky analysis of EIS and the Cu (3d) states identified by CV.

There is a contrasting trend between the photocatalytic reactivity and PEC properties of the series. $CuWO_4$ is the most active photoanode, yet $ZnWO_4$ is the most active dye degradation catalyst. This can be explained by the fundamental phenomena required in order to have successful photocatalytic performance and PEC properties. As discussed, $ZnWO_4$ can form $O_2^{\bullet-}$ and $OH^{\bullet}$ under illumination, which results in a radical-based degradation of the organic dyes.[46] $CuWO_4$ however does not possess band edges at sufficient potentials to produce these highly reactive species. In $CuWO_4$ photoanodes however, the electrochemical bias applied provides the necessary driving force for the oxidation of water at the surface of the material. Furthermore, recombination is slow

enough where charge carriers can be collected and significant photocurrents are measured.

When zinc is substituted for copper, there is a decrease in the photocurrent response of the electrode. One possible explanation for this is the decrease in visible light absorption with increasing amounts of zinc. But, another plausible reason for the decrease in photocurrent is an increase in charge recombination rates. $ZnWO_4$ is a self-activating phosphor that exhibits a blue-green emission band under UV illumination.[47,48] Photoluminescence is an indicator of fast recombination, which may be plaguing the $ZnWO_4$ and $Zn_{1-x}Cu_xWO_4$ photoanodes. As a dye degradation photocatalyst, the rates of the chemical reactions are sufficiently quick that any charges trapped on the surface react with the solution species. But, as a photoelectrode, $ZnWO_4$ seems incapable of generating a significant photovoltage with high magnitudes of photocurrents.

5.7 Conclusion

This chapter presents an adapted Pechini citric acid sol-gel synthesis forming $Zn_{1-x}Cu_xWO_4$ particles. The optical and magnetic properties confirm the existence of a solid-solution rather than a two-phase mixture. Far-IR spectroscopy supports an elongation and desymmetrizing of the $A^{2+}O_6$ octahedra. The band gap of the series decreases monotonically as Cu^{2+} substitutes for Zn^{2+}. Finally, The effective moment (μ_{eff}) is commensurate with S = ½ Cu^{2+} for all compositions, and the magnitude of the Weiss constant (Θ) increases as x increases, further supporting a smooth transition from $ZnWO_4$ to $CuWO_4$ as x changes. This platform was used to evaluate the interplay between band-gap energy and charge transfer kinetics in photocatalysts for dye degradation and PEC water oxidation. The results show that $ZnWO_4$ is the most active photocatalyst for the degradation of MB, even under AM1.5G illumination. $CuWO_4$ however, is the most active photoanode for PEC water oxidation. The differences can be explained by the fundamental properties of the two end members.

5.8 Outlook

The efforts in $Zn_{1-x}Cu_xWO_4$ were toward the formation of a more active photocatalyst and/or photoanode. The experimental results demonstrate that Cu incorporation for increased visible light absorption adds significant Cu(3d) density at lower energy states. This decreases the rates of photocatalysis. These experimental results

can be correlated with theory to further understand how the densities of state are mixed when forming AA´WO4 solid solutions. Currently, there is no theory to describe these mixtures, but these results could justify the experimental observations on $Zn_{1-x}Cu_xWO_4$ and more importantly, point toward other possibly more successful AA´WO4 materials.

Another strategy is to leave the wolframite tungstate structure. Bi_2WO_6 crystallizes in an orthorhombic crystal structure, has a direct band gap of 2.8 eV, and possesses a conduction band comprised predominantly of W(5d) orbitals.[49] It is an incredibly active dye degradation catalyst under UV-Vis illumination[50], is selective the oxidation of glycerol to dihydroxyacetone,[51] and is receiving attention as a photoanode for PEC water oxidation.[52] I have shown that adding Cu^{2+} as a dopant increases visible light absorption, but have not studied the photocatalytic and PEC properties of this material. There also may be more suitable choices of dopants to increase visible light absorption, as this chapter presents some of the limitations of using Cu^{2+} as a source of visible light absorption. Anion doping using Mo forms visible light responsive $Bi_2W_{1-x}Mo_xO_6$ capable of dye degradation under visible illumination.[53]

Doped Bi_2WO_6 may be suitable as a dye degradation catalyst under visible light illumination though as a photoanode its, photoelectrochemistry may suffer due to forming these mid-gap trap states. E_{fb} of Bi_2WO_6 resides at 0 V RHE making it an attractive material with an early onset of photocurrent. There is an example of forming Bi_2WO_4 2D array photoanodes with improve PEC properties over the planar electrode.[54] Therefore, forming highly crystalline Bi_2WO_6 with a well-defined structure is an attractive approach toward a more active UV photoanode.

5.9 Experimental

Synthesis of $Zn_{1-x}Cu_xWO_4$

ZnO, CuO and WO_3 starting materials were purchased from Sigma Aldrich (>99%) and used as received. $Zn_{1-x}Cu_xWO_4$ ($0 \leq x \leq 1$) powders were prepared by solid state methods. 8 mmol of each W and A (A = Zn, Cu) were ground in an agate mortar and pestle, pressed into a pellet and annealed in an alumina crucible at 850 °C for 12 h, with heating and cooling ramp times of 4 h. After annealing, the samples were reground and re-annealed. This process was repeated once more for a total annealing time of 36 h

at 850 °C. The initial ratios of Cu:Zn were controlled to give the desired composition in the entire $Zn_{1-x}Cu_xWO_4$ series (x = 0, 0.1, 0.2, 0.3, 0.4, 0.5, 0.6, 0.7, 0.8, 0.9, and 1). Select compounds in the series were also synthesized by a Pechini-type citric acid sol-gel method. This synthesis was adapted from a method used to prepare rare-earth metal tungstates,[55] where the optimal molar ratio of citric acid to total metal cations was 1:1, and the citric acid to ethylene glycol ratio was 2:1. In a given experiment, 2 mmol of $A(NO_3)_2 \bullet xH_2O$ (A = Zn, Cu) and 2 mmol W from ammonia metatungstate were dissolved in 4 mmol of citric acid (3 M stock solution) and mixed with 2 mmol ethylene glycol. This solution was stirred and heated at 80 – 90 °C until the water evaporated, leaving a puffed gel. This gel was subsequently dried overnight in a vacuum oven at 60 – 70 °C. Finally, the dried gel was ground in an agate mortar and pestle and annealed at 700 °C for 3 h, with 2 h heating and cooling rates.

Physical, Optical, and Magnetic Characterization

X-ray diffraction patterns were recorded on a Brüker D8 Advance diffractometer equipped with a graphite monochromator, a Lynx-Eye detector, and parallel beam optics using Cu-Kα radiation (λ = 1.54184 Å). Patterns were collected using a 0.6 mm incidence slit, with a step size and scan rate of 0.04º/step and 0.5 s/step respectively. The phases were identified and indexed according to the reported crystal structure determined by Schofield *et al.* for the $Zn_{1-x}Cu_xWO_4$ series.[10] UV-Vis spectra were recorded using an Agilent-Cary 5000 spectrophotometer equipped with a Praying Mantis diffuse reflectance accessory. $BaSO_4$ was used as a baseline and samples were collected in a 1 cm diameter holder. In a measurement 50 mg of sample was diluted with 50 mg of $BaSO_4$ and packed on top of a $BaSO_4$ base to form a smooth surface flush with the holder. Spectra were recorded in reflectance mode and transformed mathematically into normalized absorbance. Tauc plots were then generated using the Kubekla-Munk function, $F(R) = (1-R)^2/2R$. Scanning electron microscopy (SEM) images were collected using a Hitachi S-3200N SEM with an accelerating voltage of 15 kV. Higher resolution SEM images were collected using a FEI Nova Nanolab SEM/FIB with an accelerating voltage of 10 kV. ICP-AES elemental analysis for Cu, Zn, and W was obtained using a Perkin-Elmer Optima 2000DV instrument, and sample prep was performed using a method described by Montini *et al.*[56] Initially, 12 mg of material was mixed into 1 mL 30% H_2O_2 (Fisher),

0.8 mL HNO_3 (69% Fisher) and 1 mL H_2O. The samples were then stirred and heated to 80 °C for 30 minutes and then cooled. This process was repeated, adding H_2O_2 and heating, until all materials were dissolved. As H_2O_2 was decomposed at high temperatures, H_2WO_4 began to precipitate out of solution, in which case more H_2O_2 was added to re-dissolve the H_2WO_4. Finally, the samples were diluted to 50 mL for storage with 1 mL extra H_2O_2 being added to prevent any precipitation. The emission lines used are 324.752 nm, 202.548 nm, and 239.708 nm for Cu, Zn, and W respectively.

Susceptibility measurements were performed on a Quantum Design MPMS-XL7 equipped with an Evercool^{TM} Dewar. ~100 mg of sample was suspended in ~100 mg eicosane (>99% Sigma-Aldrich) in a polycarbonate capsule. Measurements were collected under zero-field cooled conditions with a measuring field of 1 T in the temperature range 5 – 300 K to ensure sufficient signal-to-noise with magnetically dilute samples. The molar susceptibility was checked at lower measuring fields for the high Cu-containing materials for comparison, and the data are identical (*vide infra*). For each dc susceptibility data point, the average of three measurements of 32 scans over a 4 cm scan length was acquired. Data were corrected for the diamagnetism of the sample holder and eicosane, as well as for core diamagnetism using Pascal's constants. Susceptibility data were fit to the Curie-Weiss law for $T \geq 150$ K: $\chi_M = C / (T - \Theta)$ where C relates to the effective magnetic moment as $\mu_{eff} = 2.82\ C^{1/2}$. Ac susceptibility measurements were recorded under an ac field $H_{ac} = H_0 \sin(2\pi ft)$ for $H_0 = 3$ Oe and $f \sim 2$, 20, 200, and 1500 Hz.

Photocatalytic Experiments on $Zn_{1-x}Cu_xWO_4$

Catalysis experiments were conducted on 50 mg of powdered sample in 40 mL of 10 ppm MB. The solutions were allowed to reach equilibrium for 1h in the dark to account for adsorption of MB onto the powders. The change in concentration of MB was measured by monitoring the change in absorption at 420 nm. The cell was stirred and illuminated through a quartz window with 500 mW/cm^2 of AM1.5G illumination. Aliquots were taken out and the stated times and the solution was centrifuged at 3300 rpm for 5 minutes to separate any solid catalyst. An absorption spectrum and the percent change in concentration (= C/C_0) was measured and compared to the initial concentration of MB after adsorption (C_0).

Photoelectrochemical experiments were conducted under the provided experimental parameters. LSV traces were collected at 20 mV/s scan rate under AM1.5G illumination with an irradiance of 100 mW/cm^2. CV traces were conducted at 1 atm in the dark under continuous bubbling of N_2.

5.10 References

1. Keeling Jr., R. O. The Structure of $NiWO_4$ *Acta. Cryst.*, **1957**, *10*, 209-213
2. Macavei, J.; Schulz, H. The Crystal Structure of Wolframite Type Tungstates at High Pressure *Z. Kristallog*, **1993**, *207*, 193-208
3. Fu, H.; Lin, J.; Zhang, L.; Zhu, Y. Photocatalytic Activities of a Novel ZnWO4 Catalyst Prepared by a Hydrothermal Process *Appl. Catal., A* **2006**, *306*, 58-67.
4. Fu, H.; Chengsi, P.; Zhang, L.; Zhu, Y. Synthesis, Characterization and Photocatalytic Properties of Nanosized Bi_2WO_6, $PbWO_4$, and $ZnWO_4$ Catalysts *Mater. Res. Bull.* **2007**, *42*, 696-706.
5. Ouyang, S.; Kikugawa, N.; Chen, D.; Zou, Z.; Ye, J. A Systematical Study of Photocatalytic Properties of AgMo2 (M = Al, Ga, In) : Effects of Chemical Composition, Crystal Structures, and Electronic Structures *J. Phys. Chem. C* **2009**, *113*, 1560-1566.
6. Kim, D. W.; Cho, I.-S., Shin, S. S; Lee, S.; Noh, T. H.; Kim, D. H, Jung, S.; Hong, K. S. Electronic Band Structures and Photovoltaic Properties of MWO_4 (M = Zn, Ma, Ca, Sr) Compounds *J. Solid State Chem.* **2011**, *184*, 2103-2107.
7. Irie, H.; Watanabe, Y.; Hashimoto, K. Nitrogen-Concentration Dependence on Photocatalytic Activity of $TiO_{2-x}N_x$ *J. Phys Chem. B* **2003**, *107*, 5483-5486.
8. Huang, G.; Shi, R.; Zhu, Y. Photocatalytic Activity and Photolelectric Performance Enhancement for $ZnWO_4$ by Fluorine Substitution *J. Mol. Catal. A: Chem.* **2011**, *348*, 100-105.
9. Schofield, P. F.; Knigh, K. S.; Redern, S. A. T.; Cressey, G. Distortion Characteristics Across the Structural Phase Transition in $(Cu_{1-x}Zn_x)WO_4$ *Acta Crystollogr.* **1997**, *B53*, 102-112.
10. Schofield, P. F.; Redfern, S. A. T. Ferroelastic Phasse Transition in the Sanmartinite ($ZnWO_4$)-Cuproscheelite ($CuWO_4$) Solid Solution *J. Phys. Condens. Matter* **1992**, *4*, 375-388.
11. Redfern, S. A. T.; Bell, A. M. T.; Henderson, C. M. B.; Schofield, P. F. Rietveld Study of the Structural Phase Transition in the Sanmartinite ($ZnWO_4$)-Cuproscheelite ($CuWO_4$) Solid Solution (*Eur. J. Mineral.* **1995**, *7*, 1019-1028.
12. Redfern, S. A. T. Hard-Mode Infrared Study of the Ferroelastic Phase Transition in $CuWO_4$-$ZnWO_4$ Mixed Crystals *Phys. Rev. B* **1993**, *48*, 57615765.
13. Anders, A. G.; Zvyagin, A. I.; Kobets, M. I.; Pelikh, L. N.; Khats'ko, E. N.; Yurko, V. G. *Sov. Phys.-JETP* **1972**, *35*, 934.
14. Forsyth, J. B.; Wilkinson, C.; Zvyagin, A. I. the Antiferromagnetic Structure of Copper Tungstate, $CuWO_4$ *J. Phys.: Condens. Matter* **1991**, *3*, 8433-8440.
15. Ehrenberg, H.; Theissmann, R.; Gassenbauer, Y.; Knapp, M.; Wltschek, G.; Weitzel, Fuess, H.; Herrmanndörfer, T.; Sheptyakov, D. the Crystal and Magnetic Structure

Relationship in $Cu(W_{1-x}Mo_x)O_4$ Compounds with Wolframite-Type Structure *J. Phys.: Condens. Matter.* **2002**, *14*, 8573-8581.
16. Zvyagin, A. I.; Anders, A. G. Effect of Magnetic Dilution on the Critical temperature of Few Dimensional Antiferromagnetic $CuWO_4$ *Sov. Phys.-JETP* **1974**, *40*, 154.
17. Tomaszewicz, E.; Worztynowicz, A.; Kaczmarek, S. M. Subsilidus Phae Relations in $CuWO_4$-Gd_2WO_6 System *Solid State Sciences* **2007**, *9*, 43-51.
18. Clark, G. M.; Doyle, W. P. Infra-Red Spectra of Anhydrous Molybdates and Tungstates *Spectrochim. Acta* **1966**, *22*, 1441-1447.
19. Fomichev, V. V.; Kondratov, O. I. Vibrational Spectra of Compounds with the Wolframite Structure *Spectrochim. Acta* **1994**, *50A*, 1113-1120.
20. Ruiz-Fuertes, J.; Errandonea, D.;Locomba-Perales, R.; Segura, A.; Gonzalez, J.; Rodriquez, F.; Manjon, F. J.; Ray, S.; Rodriguez-Hernandez, P.; Munoz, A.; Zhu, Zh.; Tu, C. Y. High-Pressure Structural Phase Transitions in $CuWO_4$ *Phys. Rev. B* **2010**, *81*, 224115-10.
21. Obermayer, H. A.; Dachs, H.; Schröcke, H. Investigations Concerning the Coexistence of Two Magnetic Phases in Mixed Crystals (Fe, Mn)WO_4 *Solid State Commun.* **1973**, *12*, 779-784.
22. Wegner, F. On the Magnetic Phase Diagram of (Mn, Fe)WO_4 Wolframite *Solid State Commun.* **1973**, *12*, 785.
23. Zvyagin, A. I.; Anders, A. G. *Sov. Phys.-JETP* **1974**, *67*, 309.
24. Meddar, L.; Josse, M.; Deniard, P. La, C.; Andre, G.; Damay, F.; Petricek, V. Efect of Nonmagneetic Substituents Mg and Zn on the Phase Competition in the Multiferroic Antiferromagnet MnWO4 *Chem. Mater.* **2009**, *21*, 5203-5214.
25. Chaudhury, R. P.; Ye, F.; Fernandez-Baca, J. A.; Lorenz B.; Wang, Y. Q.; Sun, Y. Y.; Mook, H. A.; Chu, C. W. Robust Ferroelectric State in Multiferroic $Mn_{1-x}Zn_xWO_4$ *Phys. Rev. B* **2011**, *83*, 014401-6.
26. Ye. F.; Ren, Y.; Fernandez-Baca, J. A.; Mook, H. A.; Lynn, J. W.; Chaudhury, R. P.; Wang, Y.-W.; Lorenz, B.; Chu, C. W. Magnetic Switching and Phase Competition in the Multiferroic Antiferromagnet $Mn_{1-x}Fe_xWO_4$ *Phys. Rev. B* **2008**, *78*, 193101-4.
27. Chaudhury, R. P.; Ye. F.; Fernandez-Baca, J. A.; Wang, Y.-W.; Sun, Y. Y.; Lorenz, B.; Mook, H.A.; Chu, C. W. Magnetic and Multiferroic Phases of Single-Crystalline $Mn_{0.85}Co_{0.15}WO_4$ *Phys. Rev. B* **2010**, *82*, 184422-5.
28. Chaudhury, R. P.; Lorenz, B.; Wang, Y.-Q.; Sun, Y. Y.; Chu, C. W. Re-Entrant Ferroelectricity and the Multiferroic Phase Diagram of $Mn_{1-x}Fe_xWO_4$ *New J. Phys.* **2009**, *11*, 033036-10.
29. Song, Y. S.; Chung, J. H.; Park, J. M. S.; Choi, Y. N. Stabilization of the Elliptical Spiral Phase and the Spin-Flop Transition in Multiferroic $Mn_{1-x}Co_xWO_4$ *Phys. Rev. B*, **2009**, *79*, 224415-6.
30. Bahoosh Golrokh, S.; Wesselinowa, J. M. Ion Doping Effects in Multiferroic $MnWO_4$ *J. Appl. Phys.* **2012**, *111*, 083906-4.
31. Gaudon, M.; Carbonera, C.; Thiry, A. E.; Demourgues, A.; Deniard, P.; Payden, C.; Létard, J.-F.; Jobic, S. Adaptable Thermochromism in the $Cu_{1-x}W_xO_4$ Series ($0 \leq x \leq 1$): A Behavior Related to a First-Order Transition with a Transition Depending on *x* *Inorg. Chem.* **2007**, *46*, 10200-10207.

32 Koo, H.-J.; Whangbo, M.-H. Spin Dimer Analysis of the Anisotropic Spin Exchange Interactions in the Distorted Wolframite-Type Oxides $CuWO_4$, $CuMoO_4$-III, and $Cu(Mo_{0.25}W_{0.75})O_4$. *Inorg. Chem.* **2001**, *40*, 2161-2169.
33. Schwarz, B. C.; Ehrenberg, H.; Weitzel, H.; Fuess, H. Investigation on the Influence of particular Structure Parameters on the Anisotropic Spin-Exchange Interactions in the Distorted Wolframite-Type Oxides $Cu(Mo_xW_{1-x})O_4$ *Inorg. Chem.* **2007**, *46*, 378-380.
34. O'Keeffe, M.; Stone, F. S. The Magnetic Susceptibility of Cupric Oxide *J. Phys. Chem. Solids* **1962**, *23*, 261-266.
35. Wucher, J. *Acad. Sci. Paris* **1955**, *241*, 288.
36. Wilkinson, C. The Theory of the Spin-Density Patterson Function *Acta Crystallogr. A* **1973**, *29*, 449-452.
37. Oguchi, T.; Obokata, T. Theory of Magnetically Dilute Systems *J. Phys. Soc. Jpn.* **1969**, *27*, 1111-1116.
38. Punnoose, A.; Magnon, H.; Seehra, M. S.; Bonevich, Bulk to Nanoscale Magnetism and Exchange Bias in CuO Nanoparticles *J. Phys. Rev. B* **2001**, *64*, 174420-8.
39. Teh, C. M.; Mohamed, A. R. Roles of Titanium Dioxide and Ion-Doped Titanium Dioxide on Photocatalytic Degradation of Organic Pollutants (Phenolic Compounds and Dyes) in Aqueous Solutions: A Review. *J. Alloys Cmpd.* **2011**, *509*, 1648-1660
40. García-Pérez, U. M.; Martínez-de la Cruz, A.; Peral, J. Transition Metal Tungstates Synthesized by Co-Precipitation Method: Basic Photocatalytic Properties. *Electrochim. Acta* **2012**, *81*, 227-232.
41. Su, Y.; Zhu, B.; Guan, K.; Gao, S.; Lv, L.; Du, C.; Peng, L.; Hou, L.; Wang, X. Particle Size and Structural Control of $ZnWO_4$ Nanocrystals via Sn^{2+} Doping for Tunable Optical and Visible Photocatalytic Properties *J. Phys Chem. C* **2012**, *116*, 18508-18517.
42. Shi, R.; Wang, Y.; Li, D.; Xu, J.; Zhu, Y. Synthesis of Znwo4 Nanorods with [100] Orientation and Enhanced Photocatalytic Properties. *Applied Catal, B* **2010**, *100*, 173-178.
43. Liu, B.; Yu, S.-H.; Li, L.; Zhang, F.; Zhang, Q.; Yoshimura, M.; Shen, P. Nanorod-Drect Oriented Attachment Growth and Promoted Crystallization Processes Evidence in Case of $ZnWO_4$ *J. Phys. Chem. B*, **2004**, *108*, 2788-2792.
44. Gao, B.; Fan, H.; Zhang, X.; Song, L. Template-Free Hydrothermal Synthesis and High Photocatalytic Activity of $ZnWO_4$ Nanorods. *Materials Science and Engineering: B* 2012, 177, 1126-1132.
45. Cheng, W.; Tang, K.; Liu, Z.; Sheng, J.; Qi, Y. Template-Free Synthesis of Monodisperse $Cu_2WO_4(OH)_2$ Round and Elliptical Hollow Spheres with a Ligand-Assisted Dissolution Process. *Chem. Commun.* **2009**, 7185-7187.
46. Zhao, X.; Zhu, Y. Synergistic Degradation of Rhodamine B at Porous ZnWO4 Film Electrode by a Combined Electro-Oxidation and Photocatalysis *Environ. Sci. Technol.* **2006**, *40*, 3367-3372.
47. Dai, Q.; Song, H.; Bai, X.; Pan, G.; Lu, S.; Wang, T.; Ren, X.; Zhao, H. Photoluminescence Properties of $ZnWO_4$:Eu^{3+} Nanocrystals Prepared by a Hydrothermal Method *J. Phys. Chem. C* **2007**, *111*, 7586-7592.

48. Nagirnyi, V.; Jönsson, L.; Kirm, M.; Kotlov, A.; Lushchik, A.; Martinson, I.; Watterich, A.; Zadneprovski, B. I. Luminescence Study of Pure and Fe- or Mo-Doped $ZnWO_4$ Crystals *Radiation Measurements* **2004**, *38*, 519-522.
49. Fu, H.; Pan, C.; Yao, W.; Zhu, Y. Visible-Light-Induced Degradation of Rhodamine B by Nanosized Bi_2WO_6 *J. Phys. Chem. B* **2005**, *109*, 22432-22439.
50. Tang, J.; Zou, Z.; Ye, J.; Photocatalytic Decomposition of Organic Contaminants by Bi_2WO_6 under visible light irradiation *Catal. Lett.*, **2004**, *92*, 53-56.
51. Zhang, Y.; Zhang, N.; Tang, Z.-R.; Xu, Y.-J. Identification of Bi_2WO_6 as a highly selective visible-light photocatalyst toward oxidation of glycerol to dihydroxyacetone in water *Chem. Sci.*, **2013**, *4*, 1820-1824.
52. Hill, J. C.; Choi, K.-S. Synthesis and Characterization of High Surface Area $CuWO_4$ and Bi_2WO_6 Electrodes for use as Photoanodes for Solar Water Oxidation *J. Mater. Chem. A* **2013**, *1*, 5006-5014.
53. Zhang, L.; Man, Y.; Zhu, Y. Effects of Mo Replacement on the Structure and Visible-Light Induced Photocatalytic Performances of Bi_2WO_6 Photocatalyst *ACS Catal.*, **2011**, *1*, 841-848.
54. Zhang, L.; Bahnemann, D.; Synthesis of Nanovoid Bi_2WO_6 2D Ordered Arrays as Photoanodes for Photoelectrochemical Water Splitting *ChemSusChem*, **2013**, *6*, 283-290.
55. Galceran, M.; Pujok, M. C.; Aguiló, M.; Díaz, F. Sol-Gel Modified Pechini Method for Obtaining Nanocrystalline $KRE(WO_4)_2$ (RE = Gd and Yb) *J. Sol-Gel Sci. Techn.* **2007**, *42*, 79-88.
56. Montini, T.; Gombac, V.; Hameed, A.; Felisari, L.; Adami, G.; Fornasiero, P. Synthesis, Characterization and Photocatalytic Performance of Transition Metal Tungstates *Chem. Phys. Lett.* **2010**, *498*, 113-119.

CHAPTER 6

PHOTOCATALYTIC WATER OXIDATION USING OXIDE POWDERS

Portions of this chapter have been published:
Reproduced with permission from Etacheri, V.; Yourey, J. E.; Bartlett, B. M. *ACS Nano* **2014**, *8*, 1491-1499. Copyright 2014 American Chemical Society
http://pubs.acs.org/doi/abs/10.1021/nn405534r

6.1 Introduction

This chapter presents research efforts toward the photocatalytic oxidation of water in the presence of an electron accepting species. Specifically, this chapter presents the formation of bronze-phase titania (TiO_2-B) chemically bonded to reduced graphene oxide (RGO) which is active as a water oxidation catalyst. TiO_2-B-RGO nanosheet composites are nearly 20 times more active over plain TiO_2-B nanosheets when performing photocatalytic water oxidation in the presence of an electron acceptor. This chapter also presents the rational for targeting a d^0/d^{10} ternary phase oxide, $PbCrO_4$. Hydrothermally formed $PbCrO_4$ rods can photocatalytically oxidize water in the presence of an e^- acceptor when properly loaded with co-catalysts.

Current research in this area of solar driven chemistry focuses on developing light absorbing materials for photocatalytic water splitting, photocatalytic water oxidation in the presence of an e^- acceptor, and proton reduction in the presence of an electron donor. Research is poised in several directions including the discovery of new light absorbing oxides/nitrides, controlling synthesis methods to form more active morphologies, and co-catalyst loading to improve rates of reactions. Powdered water catalysis is an attractive area of research because there are minimal device fabrication costs in comparison to thin films.

A technical and economic feasibility study on current methods for producing H_2 from water estimates a single particle system, containing photocatalysts that are suspended in baggies and capable of 10% STH efficiency at 1.60 \$/kg H_2 after a 10 year production lifetime.[1] This cost is significantly lower when compared to a thin-film fixed-panel array which at 10% STH is estimated to cost 10.40 \$/kg H_2 over the component lifetime. The major difference arises from the capital costs necessary for plant construction and device manufacturing; approximately 1 \$/kg H_2 compared to 8 \$/kg H_2 for the fixed bed and panel array systems, respectively. Of course, there is a safety concern with producing O_2 and H_2 in the same sealed vessel which is associated with the single particle fixed bed system. A dual-catalyst separated fixed-bed system circumvents this issue and was also evaluated in this feasibility study. The final cost was estimated to be 3.20 \$/kg H_2 using two catalysts, each 5 % efficient when performing their respective half reaction. In this system, an electron mediator is used to shuttle electrons between the two beds. The research presented in this chapter most closely resembles the dual-catalyst system, where we focus on forming materials capable of performing solar-driven water oxidation with concomitant IO_3^- reduction. Water oxidation (equation 1) with IO_3^- reduction (equation 2) is an endergonic process by 51 kJ/mol (equation 3).

$$2H_2O + 4h\nu \rightarrow O_2 + 4H^+ + 4e^- \quad 1)$$

$$4H^+ + \tfrac{2}{3}IO_3^- + 4e^- \rightarrow \tfrac{2}{3}I^- + 2H_2O \quad 2)$$

$$\tfrac{2}{3}IO_3^- \rightarrow \tfrac{2}{3}I^- + O_2 \quad 3)$$

IO_3^- is a suitable choice for an electron redox mediator because both the oxidized and reduced forms are colorless in solution the reaction is highly reversible. This is contrary to the traditional methanol electron donor and Ag^+ electron acceptor. Its redox chemistry is pH dependent, which does not allow one to tailor the pH of a solution to alter the driving forces of water oxidation and proton reduction and its formal reduction potential is 1.085 V, only slightly more negative than O_2/H_2O. Most importantly, properly chosen photocatalysts are selective for the desired chemical reactions in the presence of IO_3^-/I^- when placed in the right pH solution and properly co-catalyst loaded.[2] Pt-WO_3 and $BiVO_4$ have emerged as the most active and used water oxidation catalysts in Z-scheme water splitting systems.[3–6] The work presented in this chapter focuses on improving the rates of the classically studied TiO_2 by forming a composite catalyst using the bronze

phase as a UV light absorbing oxide along with the design strategy and formation $PbCrO_4$ rods used for solar driven water oxidation.

6.2 Synthesis, Characterization and Battery Performance of TiO_2-B Modified with Reduced Graphene Oxide

The photocatalysis studies on TiO_2-B-RGO composites began through collaboration with my post-doctoral labmate Vinod Etacheri. The nanosheet morphology of TiO_2-B forms a promising anode for Li-ion batteries due to the exposed (010) facets. Furthermore, anchoring TiO2 to electrically conductive RGO is another method used to improve the rate capability of these materials. Therefore, the collaboration began by combining the advantages of a nanosheet morphology with the RGO support as a composite material to serve as an anode in a Li-ion battery. My efforts in this collaboration were focused on the materials characterization, with specific contributions in collecting IR, XPS, and EPR spectra, which we used to understand the chemical bonding of TiO_2-B to RGO and the oxidation state of titanium. Therefore, in the thesis I will focus on the conclusions made from those experiments and how they were crucial to both battery performance and photocatalysis. The full battery study can be found as reference 7.

TiO_2-B sheets were formed hydrothermally during the slow hydrolysis and crystallization of $TiCl_3$ in an ethylene glycol/H_2O mixture. The RGO composite was formed through photocatalytic reduction of graphene oxide (GO) by TiO_2-B suspended in a ethanol solution. This method results in chemically bonded RGO to TiO_2-B through Ti^{3+}–C bonds, which are crucial for rapid interfacial charge transfer. By illuminating the ethanol suspension of TiO_2-B and GO, conduction band electrons from TiO2 reduce GO to RGO. Additionally, surface Ti^{4+} get reduced to Ti^{3+} during the long-term illumination (12 h), and further reaction of these surface states with defect carbon in GO gives rise to the Ti^{3+}–C bonds, as described in Figure 6.1.

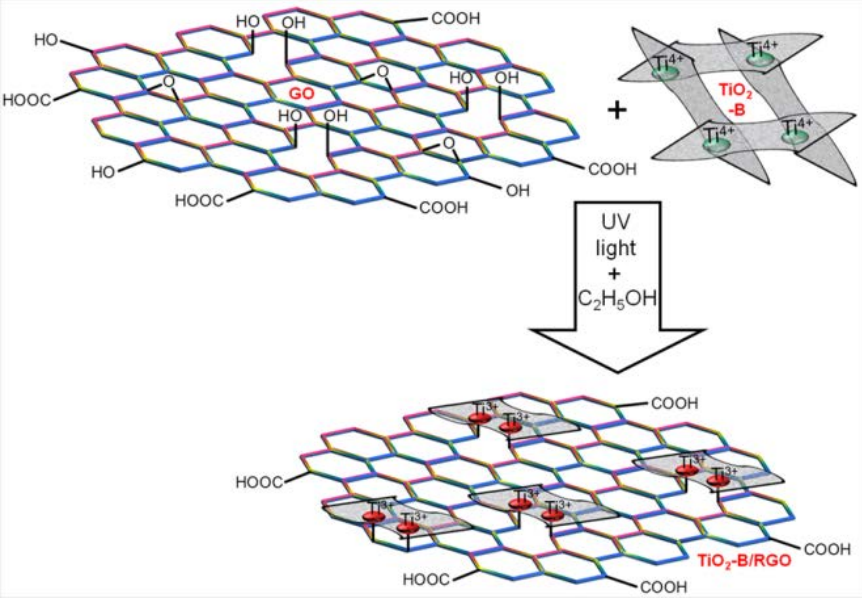

Figure 6.1 Synthesis of the TiO_2-B/RGO hybrid nanostructure through photocatalytic reduction.

The chemical nature at the surface of the composite material was probed by XPS. The results of the C(1s) peaks are presented in Figure 6.2.

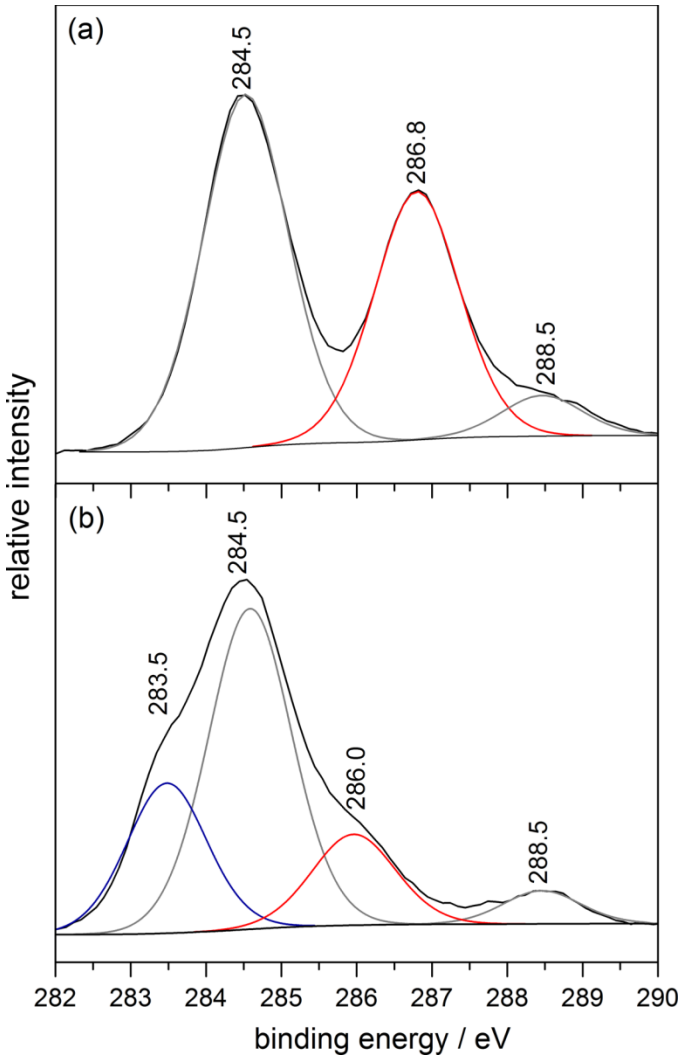

Figure 6.2 C(1s) XP spectra of a) GO and b) TiO_2-B/RGO composite

Three peaks are observed in GO, which represent chemically different carbon species, are located at 284.5, 286.8, and 288.5 eV, respectively (Figure 6.2a). These peaks correspond to elemental carbon/sp^2 hybridized carbon from GO, oxygen containing alcohol or ether linkages (C–OH and C–O) and carboxylate (O=C–O) respectively.[8–10] In the case of TiO_2-B/RGO hybrid nanostructures, the high intensity peak at 286.8 eV disappears, and an additional peak characteristic of defect-containing sp^2-hybridized carbon emerges at 286.0 eV (Figure 6.2b). This shift indicates that most of the oxygen containing functional groups of GO are efficiently reduced during the photocatalytic reduction reaction. A low intensity peak of carboxyl carbon (288.5 eV) is still present in the photoreduced sample. IR spectroscopy corroborates this result as the only C–O absorption band that persists

after photoreduction is due to the carboxyl groups. These reminiscent carboxyl groups provide a strong electron withdrawing effect on surface titanium as evidenced by the slight shift to higher energy of the Ti (2p) peaks in the XP spectra (Figure E.1).[11,12] An additional C(1s) peak at 283.5 eV emerges in Figure 6.2, which is at higher binding energy than the titanium carbide (Ti^{4+}–C) peak at 281.5 eV. It can be assigned to carbon from RGO bonded to Ti^{3+} of TiO_2-B nanosheets.[13,14]

The formation of Ti^{3+}–C bonds results is corroborated by the bathochromic shift observed in the Raman spectrum of TiO_2-B/RGO compared to that of bare TiO_2-B nanosheets and with EPR spectra identifying Ti^{3+} in TiO_2-B/RGO as seen in Figure 6.3.

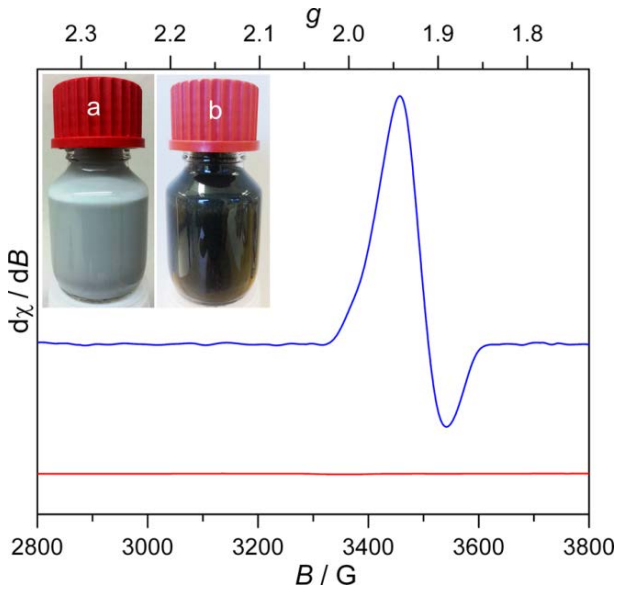

Figure 6.3 EPR spectrum of TiO_2-B/RGO (blue) and TiO_2-B (Red)
Inset: photograph of TiO_2-B/GO in absolute ethanol solution a) before and b) after photoreduction.

The TiO_2-B/GO sample has no characteristic EPR resonances at 77 K, whereas the TiO_2-B/RGO hybrid nanostructure shows an EPR resonance at g = 1.94, indicative of surface Ti^{3+}.[15] The photocatalytic reduction of GO is also evidenced by the color change from gray to black (Figure 6.3 inset), which has previously been observed during the chemical reduction of GO, and assigned to the partial restoration of the π conjugated network of graphene.[16] Comparing the signal intensity of the TiO_2-B/RGO hybrids to those of standard Ti^{3+} solutions reveal that one in 6.1×10^5 Ti^{4+} ions is reduced to Ti^{3+} during the photocatalytic reduction, which is comparable to the Ti^{3+} content present in chemically reduced TiO_2.[17] To probe the reaction mechanism, EPR spectra were collected for the

ethanol suspension of pure TiO_2-B nanosheets before and after the UV-light treatment. For a brief period of time after UV treatment, the EPR spectrum of the TiO_2-B nanosheets presents a band at g = 1.94, and the solution shows a corresponding blue color, all characteristic of surface Ti^{3+}. The chemical bonding of TiO_2-B to RGO proved to be valuable for performance both in a battery as well during photocatalytic water oxidation. The TiO_2-B/RGO hybrids possess faster rates and increased stability during cycling as a Li-ion electrode when compared to both plain TiO_2-B and physically mixed TiO_2-B + RGO. The rates of catalysis are also improved when forming a TiO_2-B/RGO hybrid photocatalyst for water oxidation.

6.3 Photocatalytic Water Oxidation on TiO_2-B/RGO

Fast electron transfer and chemical bond connectivity between the oxide electrode and carbonaceous conductor are desirable characteristics during cycling in a Li-ion battery. These desirable properties can be translated to photocatalysis, ensuring that excited electrons are driven to the surface before recombining. The chemically bonded RGO serves as a site for facile electron transfer and catalyst for IO_3^- reduction. This section presents the formation of TiO_2-B chemically bonded to various weight percent's of RGO and their resulting photocatalytic performances. Additionally, control experiments highlight that the presence of RGO is crucial for catalysis and chemically bonding RGO significantly enhances the rates of water oxidation.

The absorption spectra of TiO_2-B/RGO hybrids are presented in Figure 6.4.

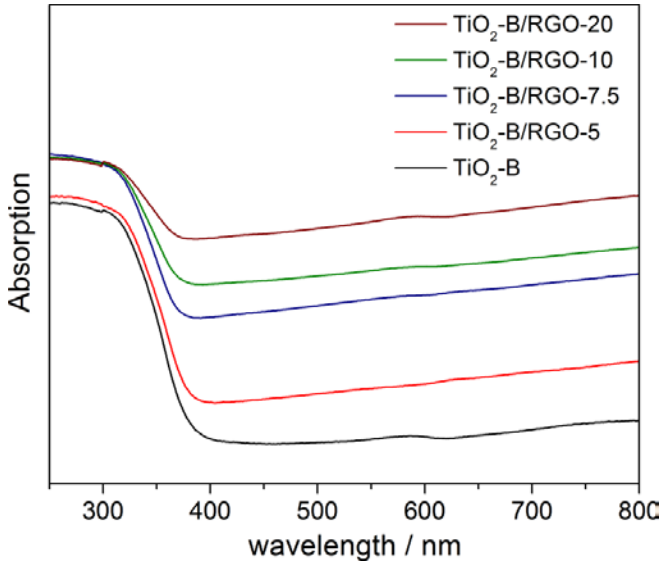

Figure 6.4 UV-Vis absorption spectra of TiO_2-B/RGO hybrids.

There is a significant increase in the black body absorption over the visible part of the solar spectrum due as the weight percent of RGO is increased. However, the absorption edge of TiO_2-B seen at approximately 400 nm does not significantly change, indicating that the presence of Ti^{3+} is not adding significant states and decreasing the band gap of TiO_2-B. Chemically bonded TiO_2-B/RGO demonstrates enhanced rates of photocatalytic water oxidation compared to pure TiO_2-B nanosheets, as seen in Figure 6.5.

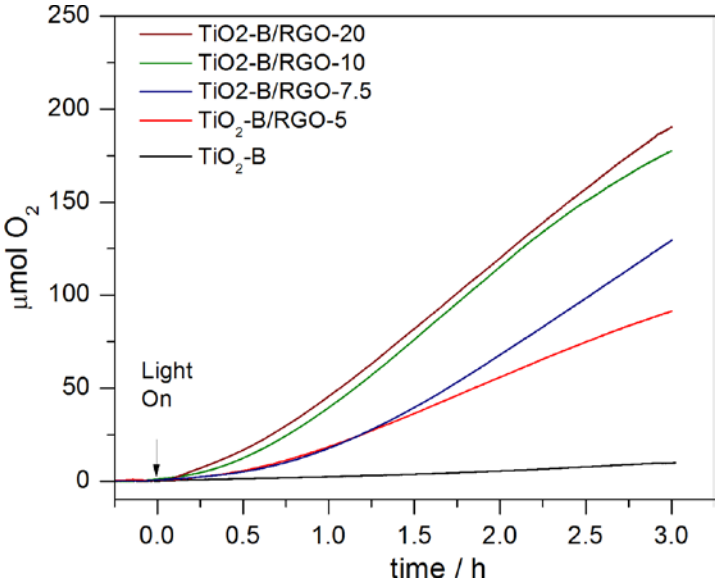

Figure 6.5 Photocatalytic Water Oxidation on TiO_2-B with various weight percent of RGO

Also, in Figure 6.5, the rates of water oxidation on TiO_2/RGO hybrids depend on the mass loading of RGO. The calculated rate constants for pure TiO_2-B, TiO_2-B/RGO-5, TiO_2-B/RGO-7.5, TiO_2-B/RGO-10, and TiO_2-B/RGO-20 are 1.1, 10.5, 16.4, 21.3, and 21.0 µmol/h, respectively. TiO_2-B/RGO-10 and TiO_2-B/20 show similar results, indicating that there is a maximum loading of RGO that is advantageous to catalysis. TiO2-B/RGO-10 was used in subsequent studies because this catalyst has the lowest possible loading amount which exhibits the fastest rates of catalysis.

The TiO_2-B/RGO-10 hybrid is compared to a sample of TiO_2-B physically mixed with 10 wt-% RGO to evaluate the importance of the Ti–C chemical bond for charge separation and catalysis. TiO_2-B/RGO-10 exhibits a 2-fold increase in the rate of water oxidation compared to physically mixed TiO_2-B/RGO-10, and 20-fold increase compared to native TiO_2-B, as seen in Figure 6.6.

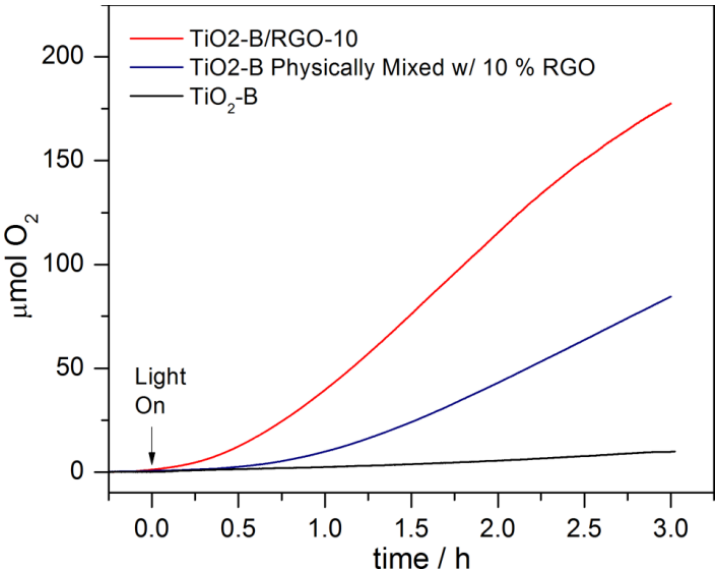

Figure 6.6 Photocatalytic Water Oxidation comparing TiO_2-B/RGO hybrid to TiO_2-B mixed with RGO and TiO_2-B

The enhancement in the rates of catalysis is explained by the formation of a Ti^{3+}–C bond, which facilitates efficient electron-hole separation in comparison to the physically mixed sample. RGO acts as an electron sink for charge separated electrons and subsequently a reaction site for IO_3^- reduction. The physically mixed samples are capable of the same process, but chemical bonding ensures that electrons are transferred to the RGO.

RGO has residual functional groups which may act as the oxygen source under illumination. This raises the question; is the blackbody absorption of RGO leading to decomposition under illumination and releasing O_2? To ensure that light absorption by TiO_2-B is providing the driving force for catalysis, and not the sensitizing mechanism, control experiments were conducted. As seen in Figure E.2, when TiO_2-B/RGO-10 is illuminated using a 458 nm cutoff, no oxygen is evolved. Additionally, when GO alone is illuminated, we observe no O_2 evolution. This ensures that the mechanism of electron transfer is commensurate with Figure 6.7. Light absorption takes place on TiO_2, surface holes perform water oxidation and conduction band electrons are transferred to RGO.

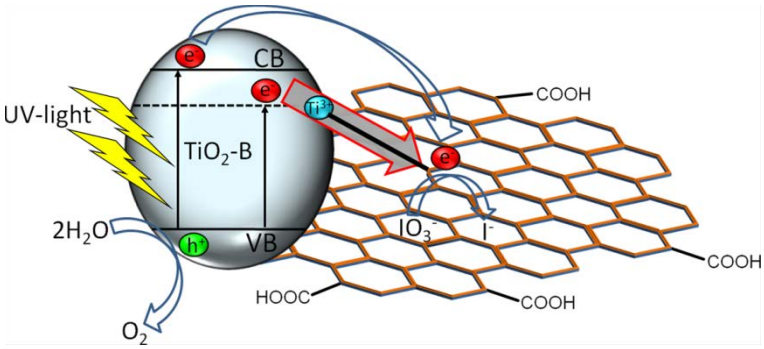

Figure 6.7 Mechanism of electron/hole transfer on TiO_2-B/RGO during photocatalytic water oxidation

Finally, in order to further confirm the fact that Ti^{3+}–C bonds are responsible for the superior photocatalytic activity, pure TiO_2-B, chemically bonded and physically mixed TiO_2-B/RGO hybrids were subjected to photoluminescence (PL) spectroscopy (Figure 6.8).

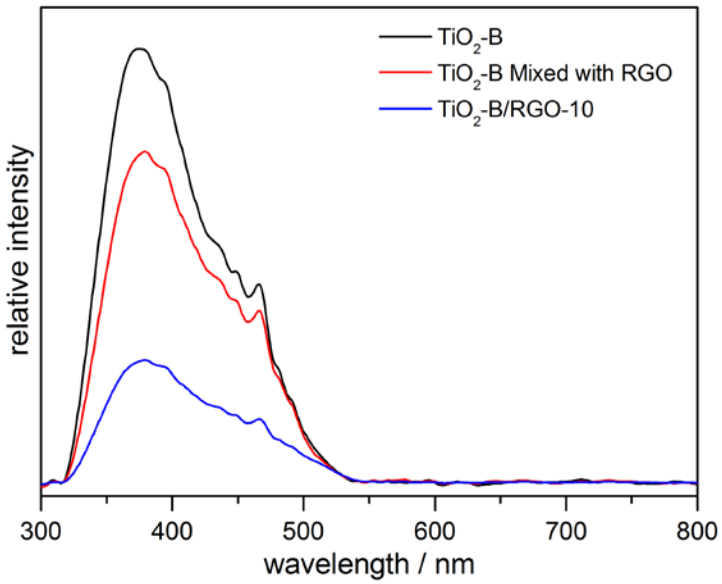

Figure 6.8 PL spectra comparing relative rates of recombination in TiO2-B, TiO2-B mixed with RGO, and TiO2-B/RGO-10

It is well known that PL emission results from the radiative recombination of photogenerated electron-hole pairs. As a result, details regarding the surface states and the kinetics of charge carrier trapping and recombination can be obtained from the PL spectra. This technique has been extensively used to investigate the fate of electron-hole pairs in TiO_2 nanoparticles, and a strong correlation between PL intensity and photocatalytic activity has been reported.[18–21] The PL spectra of all samples show

characteristic band-band peaks at 380 nm. Additional low-intensity excitonic emissions appear at higher wavelengths, 425 and 470 nm. Considerably higher band-band and excitonic PL intensities are observed for pure TiO_2-B nanosheets followed by less intense peaks of physically mixed and chemically bonded TiO_2-B/RGO-10 samples. This demonstrates that efficient electron hole separation enabled by RGO is responsible for the decreased PL intensities of TiO_2-B/RGO hybrids.

This section provides the photocatalysis experiments on a TiO_2-B/RGO hybrid catalyst capable of performing water oxidation. TiO_2-B hasn't been as thoroughly studied as a photocatalyst compared to the phases of titania, but these results indicate that it is in fact an active photocatalyst and worth further pursuit. The work conducted in this section provided me with the experience in conducting powdered catalysis experiments and more importantly, the value of collaboration.

6.4 New Design Criteria of Ternary Oxides for Photocatalytic Applications

When designing new materials for solar-driven water oxidation, a few criteria come into mind considering the lessons learned from $CuWO_4$. The first is that we still want valence bands containing predominantly metal character, thus requiring a ternary oxide. This leads to smaller band gaps than d^0/d^{10} binary oxides. The configuration must contain metals with a completely full or empty valence shell, precluding the formation of any empty or half empty orbitals within the forbidden region of the gap such as the d10s2 and d0 configurations for the valence and conduction bands, respectively in ternary oxides. An example of a material having this configuration that is used for PEC applications is $BiVO_4$. $BiVO_4$ possesses a predominantly Bi(6s) based valence band and V(3d) conduction band.

Moreover, it is a direct band gap material, which is another desired property in designing a material for use. Direct band gap materials have high absorptivity coefficients and are therefore common to thin-film applications. Coupling between Bi(6s) and O(2p) orbitals forces an upward dispersion of the valence band at the Brilliouin zone boundary, giving high mobility for the minority carriers.[22] Complimentarily, the direct band gap is maintained via coupling among V (3d), O(2p), which also lowers the conduction band minimum. With these design criteria in hand, we began looking throughout the literature for relatively unstudied materials for PEC applications. $PbCrO_4$,

chrome yellow, emerged as a possible candidate, and I prepared nanoparticulate $PbCrO_4$ to serve as an *n*-type semiconducting photocatalyst for solar-driven water oxidation in the presence of an electron acceptor.

6.5 Synthesis and Characterization of $PbCrO_4$ Rods

The synthesis method used throughout the catalysis experiments was adapted from reference 23. This method uses a precipitation reaction:

$$K_2CrO_{4(aq)} + Pb(NO_3)_{2(aq)} \rightarrow PbCrO_{4(s)} + 2\ KNO_{3(aq)} \qquad 1)$$

followed by hydrothermal treatment without any templates or additives. As per the literature, single-crystalline rods are formed which are microns in length and between 200 and 500 nm wide, confirmed by the SEM and TEM images in Figure 6.9.

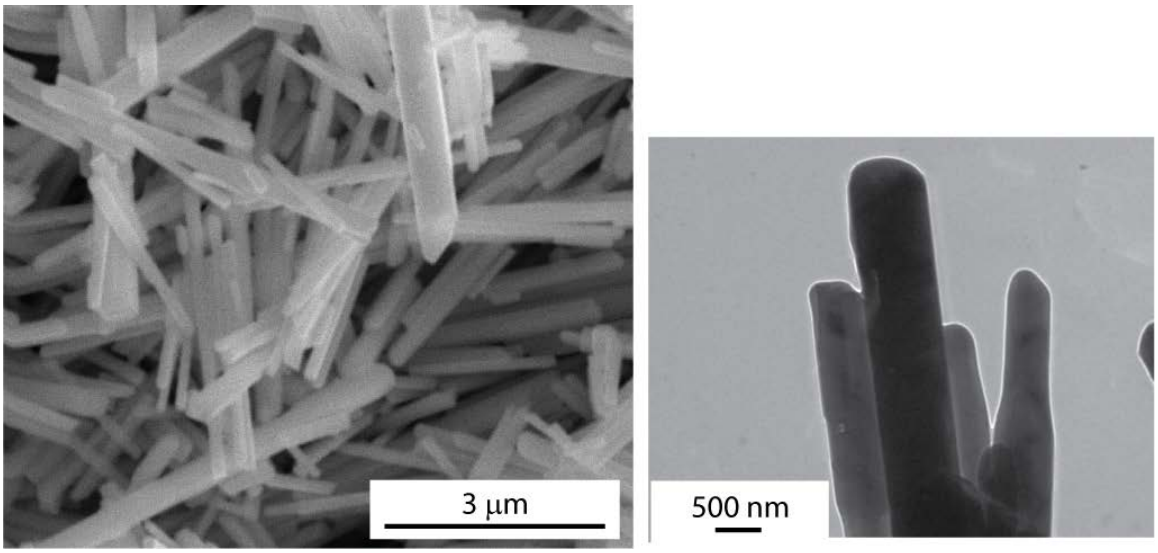

Figure 6.9 SEM and TEM images of $PbCrO_4$ rods

These rods are described as single crystalline in the literature, which is important for preventing recombination at grain boundaries during photocatalysis. Charge separation and migration may be improved compared to recombination in the bulk. Furthermore, the rod morphology provides orthogonal light absorption and charge separation. That is, there will be increased light absorption due to the long rod-like morphology, but the charges have a significantly shorter distance to travel to reach the surface.

UV-Vis spectroscopy confirms the high absorptivity of $PbCrO_4$ and also estimates the band gap. Figure 6.10 provides a comparative UV-Vis spectrum of $PbCrO_4$ and $CuWO_4$.

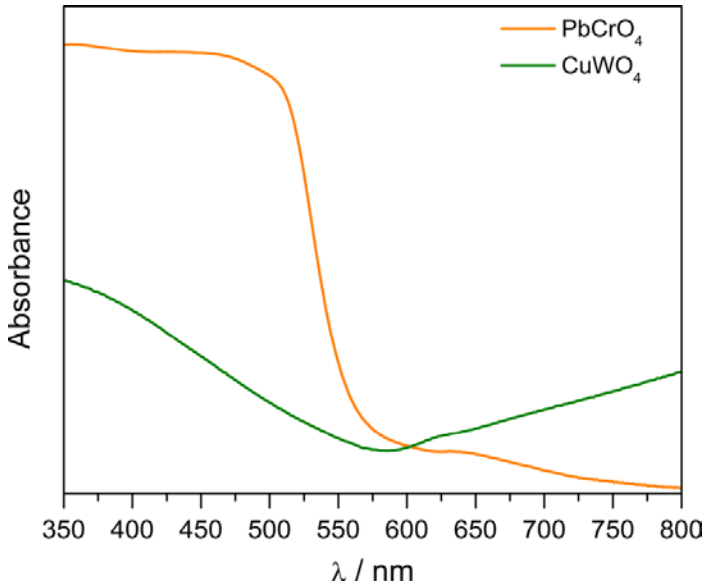

Figure 6.10 Absorption Spectrum comparing $PbCrO_4$ to $CuWO_4$

From the onset of absorption, $PbCrO_4$ is predicted to have a band gap about 2.3 eV, similar to $CuWO_4$. However, because $PbCrO_4$ is a direct band-gap semiconductor, unlike $CuWO_4$, the overall absorption is significantly enhanced. This is crucial for achieving high efficiencies at longer wavelengths; photon absorption must be efficient.

The electronic structure of PbCrO4 is predicted by DFT[24] to possess band edges as seen in Figure 6.11.

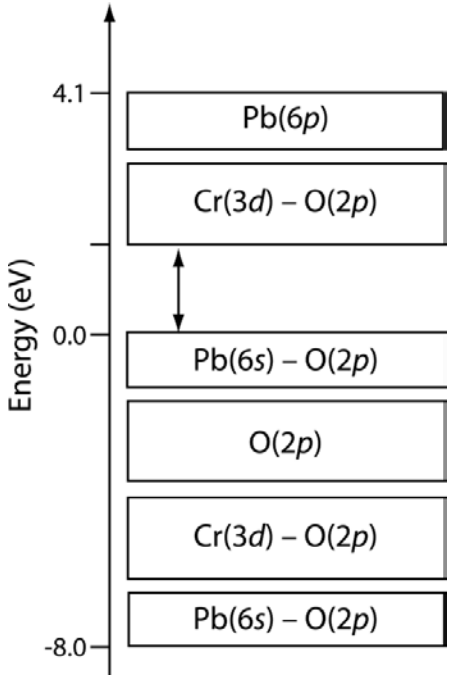

Figure 6.11 Band Structure of $PbCrO_4$

This band structure matches the $d^{10}s^2/d^0$ configuration of $BiVO_4$. 3d transition metal orbitals dominate the conduction band, where hybridized Pb(6s)/O(2p) orbitals comprise the top of the valence band. There has yet to be an experimental determination of the conduction band edge of $PbCrO_4$ published in the literature, but my colleague Charles Lhermitte has conducted this measurement. The results of his EIS experiments place E_{fb} in $PbCrO_4$ at +0.6 V RHE. This value is more positive than desired, probably due to the electronegativity of the Cr(3d) based orbitals. However, the rod morphology, direct band gap, and this band structure are desirable for performing spontaneous photo driven water oxidation with concomitant IO_3^- reduction. With a new target material and easily reproducible and scalable synthesis, we moved on to evaluate these materials for photocatalytic water oxidation.

6.6 Photocatalytic Water Oxidation on $PbCrO_4$ Rods

$PbCrO_4$ was surveyed once in the past literature as a possible photocatalyst for water oxidation.[25] It was concluded that $PbCrO_4$, in an aqueous solution containing Ag^+ as an electron acceptor, was incapable of performing photocatalytic water oxidation. We have seen similar results using bare $PbCrO_4$, but it is now understood that in order to see appreciable rates of catalysis for O_2 evolution from water, incorporation of a co-catalyst is necessary. These cocatalysts serve as either reduction sites for IO_3^- reduction (as seen on TiO_2-B/RGO), or oxidation sites for O_2 evolution. Materials that possess a strictly O(2p) based valence band can form $OH^{\bullet}$ and evolve O_2 without a cocatalyst, but materials that contain predominantly metal-based valence bands benefit from the rate enhancement that the co-catalyst provides. Ruthenium Oxide (RuO_2) is a typical cocatalyst used for O_2 photocatalysis.[26,27] Therefore, we use an impregnation method to adsorb RuO_2 nanoparticles onto the surface of $PbCrO_4$. Heating at 350 °C helps crystallize the hydrolyzed RuO_2 and form better contact between the catalyst and semiconductor. A TEM image of RuO_2 loaded $PbCrO_4$ is presented in Figure 6.12.

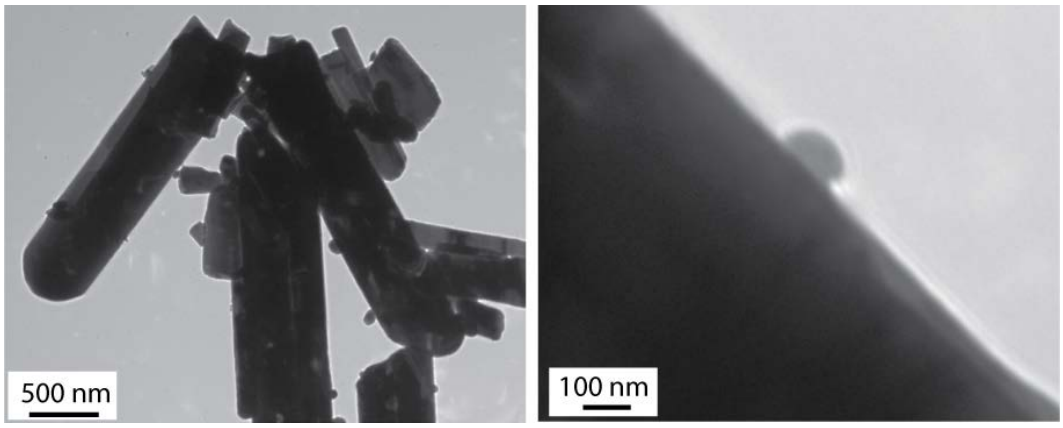

Figure 6.12 TEM images of $PbCrO_4$ showing small nanoparticulate RuO_2 on the surface

There are particles dispersed on the surface of $PbCrO_4$ which we assume are RuO_2 nanoparticles. Because of the thick $PbCrO_4$ rods, we were unable to produce a selected area diffraction pattern confirming the phase of the particles on the surface; however the presence of RuO_2 was identified using XPS as seen in Figure E.3. RuO_2 persists on the surface during photocatalysis.

Water oxidation experiments were conducted in a 10 mM IO_3^- solution containing suspended $PbCrO_4$ catalyst. The stirred solution is illuminated using AM1.5G light at 500 mW/cm^2 (~5 suns). Figure 6.13 compares the activity of $PbCrO_4$ loaded with 0.5 wt-% RuO_2 ($PbCrO_4$-0.5Ru) to native $PbCrO_4$.

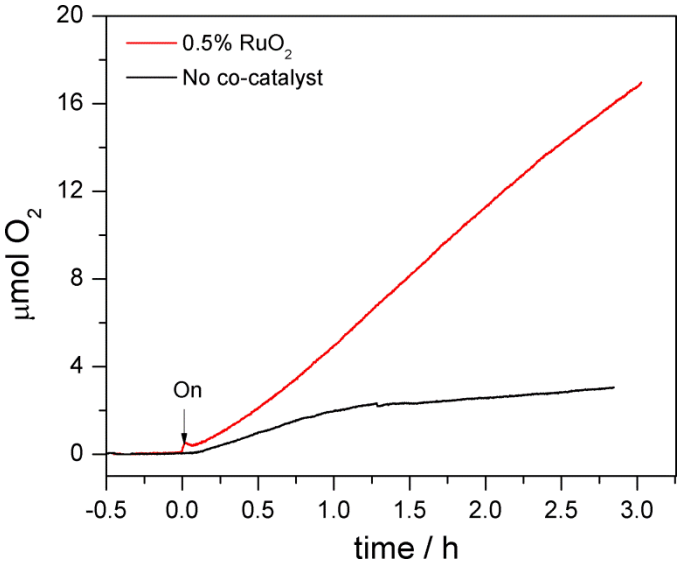

Figure 6.13 Comparing rates of photocatalytic water oxidation on $PbCrO_4$ (black) and $PbCrO_4$-0.5Ru (red).

Native $PbCrO_4$ shows minimal O_2 evolution, only 3 µmol after three hours of illumination. $PbCrO_4$-0.5Ru produces 17 µmol. This result shows that cocatalyst loaded $PbCrO_4$ is capable of photocatalytically decomposing water into O_2 in the presence of IO_3^-. As stated earlier, one advantage of $PbCrO_4$ is that its direct band gap results in higher absorptivity of longer wavelength light. Therefore, a wavelength dependence study was conducted using various optical filters to monitor O_2 production when certain areas of the solar spectrum were cut off. Figure 6.14 presents the relative rates of O_2 production using 530, 485, 425 and 380 nm long pass filters.

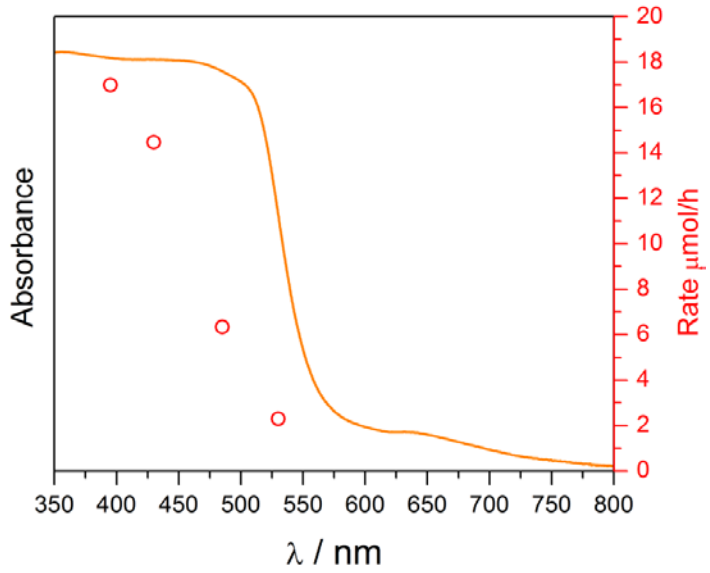

Figure 6.14 Rates of O_2 production on $PbCrO_4$ using various long pass filters

The results show that even using a 530 nm long pass filter, $PbCrO_4$ is capable of generating appreciable quantities of O_2. The rate of O_2 production increases significantly as shorter wavelengths of light are allowed to pass. The rate increases to 16 µmol/h using the Xe lamp, a water filter, and a 425 nm long pass filter (P_{in} = 600 mW/cm^2), equivalent to cutting the UV part of the solar spectrum.

The weight percent of RuO_2 was varied to evaluate the dependence of the loading amount on catalytic performance. Figure 6.15 shows the total amount of O_2 produced after three hours of illumination when the mass loading of RuO_2 was varied from 0 – 1 wt-%.

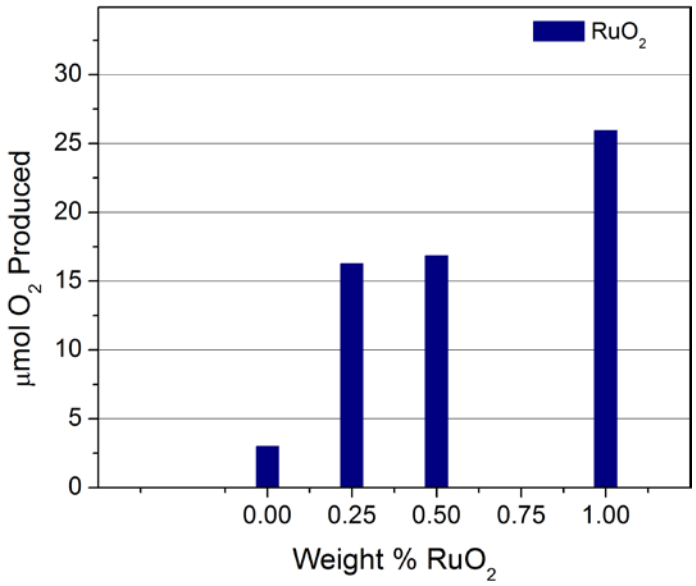

Figure 6.15 Amount of O_2 produced as a function of loaded RuO_2 on $PbCrO_4$

From Figure 6.15, 0.1 wt. % RuO_2 results in the greatest amount of O_2 produced over the 3-hour illumination period, showing a 5-fold increase in the rate of catalysis compared to plain $PbCrO_4$. We did not study higher amounts than 1 wt % RuO_2 because competing photon absorption becomes a significant issue as greater amounts of cocatalyst are added. Figure E.4 shows that at only 1 wt % RuO_2, there is a significant increase in the baseline absorption.

To enhance the reaction rate, it is reasonable to expect that loading both an oxidation and reduction catalyst onto the photocatalyst's surface would improve the activity compared to modification with only a single catalyst. [28] In the past few years, this approach has resulted in significant enhancement of rates.[29] We use a dual cocatalyst impregnation method to simultaneously form RuO_2 and PtO_x nanoparticles on the surface of PbCrO4. PtO_x is a common reduction catalyst for both H_2 evolution and IO_3^- reduction.[28,4] Both PtO_x and RuO_2 co-catalysts were co-impregnated onto $PbCrO_4$ and the resulting rates of water oxidation were measured. Figure 6.16 shows that by using dual co-catalysts, the rate of O_2 evolution is enhanced.

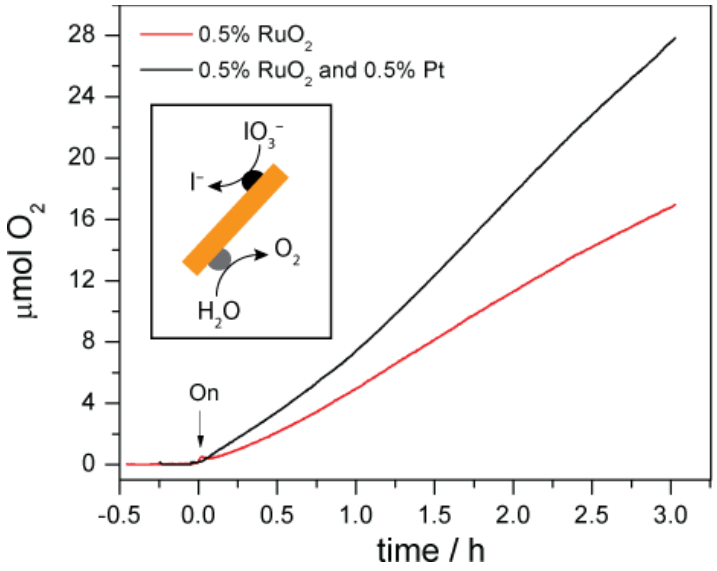

Figure 6.16 Rates of O_2 evolution on $PbCrO_4$-0.5RuO_2 compared to $PbCrO_4$-0.5Ru-0.5Pt.
Inset: A pictorial description of water oxidation and IO_3^- reduction taking place on $PbCrO_4$

$PbCrO_4$ loaded with 0.5 wt. % of both RuO_2 and PtO_x ($PbCrO_4$-0.5Ru-0.5pt) shows a 1.5-fold rate enhancement compared to $PbCrO_4$-0.5Ru. The inset of Figure 6.16 depicts photocatalytic IO_3^- reduction and H_2O oxidation taking place on the PtO_x (black) and RuO_2 (grey) sites. We then screened loading amount of RuO_2 while maintaining a 0.5 wt. % of Pt. Figure 6.17 compares the rates of varying the RuO_2 amount while maintaining 0.5 wt-% Pt.

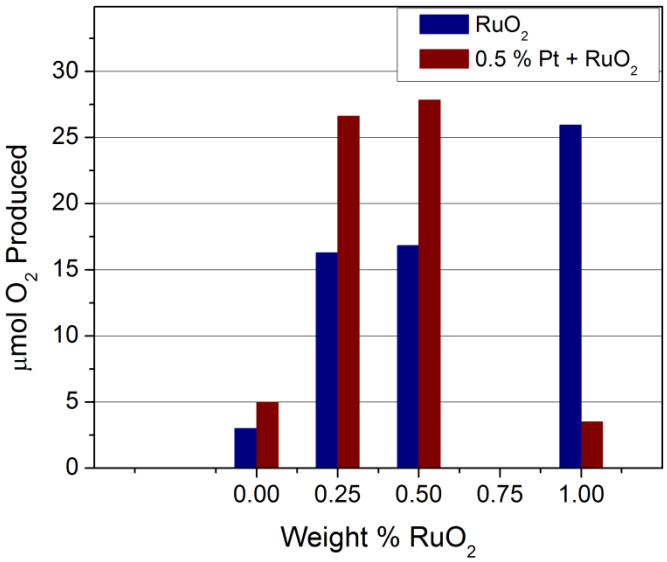

Figure 6.17 O_2 produced when $PbCrO_4$-0.5Pt was loaded with varying amounts of RuO_2.

From Figure 6.17, both $PbCrO_4$-0.25Ru-0.5-Pt and $PbCrO_4$-0.5Ru-0.5Pt show a similar 1.5-fold rate enhancement compared to only a single co-catalyst loading. However, when $PbCrO_4$-1Ru was loaded with PtO_x, there is a significant decrease in the rates of catalysis. These results are repeatable and by incorporating such a significant overall mass loading of catalysts (1.5 wt. % total), competing light absorption is an impediment to performance.

We designate the platinum catalysts as PtO_x, because after annealing at 350 °C, the Pt species is predominantly PtO_2, with a small amount of PtO. It is known in the literature that higher temperatures reduce Pt, leading to lower valent oxides and even metallic Pt.[30] However, $PbCrO_4$ is a metastable phase and at higher temperatures it decomposes to yield Pb_2CrO_5. There is variation in the literature, stating its decomposition temperature between 500 – 750 °C, with the annealing atmosphere playing a role.[31,32] We compared the photocatalytic performance of $PbCrO_4$-0.5Ru-0.5Pt when annealed at 500 °C for 30 minutes. Figure E.5 shows that the rate is significantly decreased; however by XRD no impurity phase is identified, hinting that $PbCrO_4$ is in fact stable up to 500 °C in air. In order to circumvent the need for high temperatures, a photodeposition approach was used to form PtO/Pt nanoparticles on the surface of PbCrO4-0.5Ru.[33] XPS confirms that Pt was deposited onto the surface of the oxide during photodeposition (Figure E.6). Figure E.7 compares the rates of O_2 evolution when Pt was deposited by impregnation or photodeposition. As seen in Figure E.7, the rate is not enhanced compared to the impregnation method. This result hints that we may not be optimally using the oxygen evolution cocatalyst, but many catalysts work synergistically on specific light absorbing oxides, and the deposition parameters as well as the catalyst identity can be further screened to optimize the photocatalysis.

6.7 Conclusions

This chapter presented the formation of two materials for photocatalytic water oxidation in the presence of an electron acceptor. TiO_2-B is a phase of titania that hasn't been as thoroughly studied as the anatase and rutile phases, however our results show that it is quite active when chemically bonded to RGO. The chemical bond between TiO2-B an RGO was evaluated using spectroscopic methods, and this bonding is critical for

achieving high rates of catalysis. Another phase, $PbCrO_4$ was prepared by a hydrothermal route. The resulting micron sized rods absorb out to 550 nm with high absorptivity due to PbCrO4's direct band gap. When PbCrO4 rods were loaded with a RuO_2 and PtO_x cocatalyst, they were capable of photocatalytically oxidizing water using simulated solar irradiation

6.8 Outlook

The loading amount required to realize a synergistic effect of both co-catalysts requires significant screening and variation of mass loading amounts.[34] To optimize $PbCrO_4$'s photocatalytic properties, I recommend a more full screening of the various possible oxidation and reduction catalysts, including MnO_x, CoO_x, and IrO_x.[35] This screening will help identify which catalyst, if any, is most compatible with $PbCrO_4$. Additionally, the impregnation method relies on proper adherence and contact formed during water evaporation and subsequent heating. A photodriven method to load these catalysts is another method commonly explored and more efficiently uses the catalysts, requiring significantly less mass loading compared to impregnation.[36] The formation of CoO_x and MnO_x nanoparticulate cocatalysts is feasible by photodeposition.[36] Future work should also be directed toward the photocatalytic formation of these cocatalysts on the surface of $PbCrO_4$. My efforts thus far have been replacing Co with Ru and following the same experimental procedure for impregnation. This work has not yet resulted in the desired rate enhancement, but the experimental parameters should be amended to make a more solid conclusion. Similar efforts are also feasible on the TiO_2-B/RGO catalysts discussed in the earlier part of this Chapter. Currently, RGO is presumably serving as an IO_3^- reduction catalyst, and I have experimentally shown that loading 0.5 wt-% RuO_2 enhances the rate of water oxidation on native TiO_2-B, therefore it is reasonable to expect enhancements when both co-catalysts are used simultaneously. Accomplishing this result will again require significant optimization since competing photon absorption is significant when using only RGO. This chapter shows conclusive results for photocatalytic water oxidation using powdered catalysts and the data herein is on progress for publication.

6.9 Experimental

Physical Characterization of TiO_2-B/RGO

Bruker EMX spectrometer was employed for collecting the X-band electron paramagnetic resonance (EPR) spectra of the samples at liquid nitrogen temperature. Quantification of Ti^{3+} species present in TiO_2-B/RGO hybrid was performed by comparing their EPR spectra with that of standard Ti^{3+} solutions (1 mM-10 mM $TiCl_3$). A Kratos Axis Ultra spectrometer equipped with an Al Kα X-ray radiation source (photon energy 1486.6 eV) was used for recording the X-ray photoelectron spectra (XPS). The CC/CH component of the C 1s peak was set at 284.5 eV for the binding energy measurement of elements. XPS spectra were deconvoluted into Gaussian/Lorenzian-shaped components using Vision software (Kratos). FTIR spectra of samples (in the range of 4000−400 cm^{-1}) were recorded using a Perkin Elmer GX spectrometer. UV-Vis spectra of samples were recorded using an Agilent-Cary 5000 spectrophotometer equipped with a Praying Mantis diffuse reflectance accessory. Photoluminescence experiments were conducted using dilute suspensions (10 mg/L) of the discussed samples. The excitation wavelength was 280 nm and the emission spectra were collected from 300 – 800 nm.

Water oxidation study on TiO_2-B/RGO and $PbCrO_4$

Oxygen detection was performed in a custom-built 72 mL Pyrex cell fitted with a quartz window. In a typical experiment, 50 mg of TiO_2/RGO hybrid was suspended in 40 mL of 5 mM $NaIO_3$ (Sigma Aldrich), and purged with N_2. A fluorescence probe (Ocean Optics Inc.) was used for O_2 detection. Before beginning the experiment, % O_2 was recorded for 20 min to ensure the cell was sealed completely from the atmosphere and to create a baseline. The sample was irradiated for 3 h using a Newport-Oriel 150 W Xe arc lamp passed through a water filter. The incident power was 2.4 W (750 mW/cm^2) measured using an optical power meter (Newport 1918-R) equipped with a thermopile detector (Newport 818P-015-19). The number of moles of O_2 produced was determined using the ideal gas law from the measured volume of the headspace, the temperature recorded using a NeoFox temperature probe, and the partial pressure of O_2 recorded by the fluorescence probe. Dissolved O_2 in the solution was accounted for through Henry's law using the measured partial pressure of O_2 and the volume of solution in the cell. Water oxidation experiments were duplicated, and the calculated rate constants were

within 5% error limit. Control photocatalytic experiments were performed with a UV-cutoff filter, and pure RGO.

The same experimental set up was used for the water oxidation experiments performed on PbCrO4. In these experiments, the incident light was passed through a AM1.5G filter and the irradiance was measured to be 500 mW/cm^2. The experimental suspensions contained 50 mg of PbCrO4 in 40 mL of 20 mM KIO_3.

Synthesis and Characterization of $PbCrO_4$ Rods

$PbCrO_4$ rods are synthesized by a co-precipitation reaction followed by hydrothermal crystallization. Eight mmol of $Pb(NO_3)_2$ and K_2CrO_4 were each dissolved separately in 32 mL of water forming a 0.25 M solution. The K_2CrO_4 solution was added to the $Pb(NO_3)_2$ solution by syringe pump at a rate of 36 mL/h. The resulting suspension of $PbCrO_4$ was allowed to stir for 30 minutes. The 64 mL suspension was divided into four Teflon-lined autoclaves (Parr instruments) and heated at 180 °C for 12 h; heating and cooling rates were 10 °C/min. After heating, the resulting precipitate was separated by centrifugation and washed three times with distilled water, then dried at 60 °C in a vacuum oven.

RuO_2 and PtO_x were impregnated using a slow evaporation method. The stated mass % was determined by comparing the amount RuO_2 and/or Pt to the $PbCrO_4$ sample. For example, 50 mg of $PbCrO_4$ loaded with 0.5 wt % RuO_2 would contain 0.25 mg of RuO_2. 50 mg of $PbCrO_4$ loaded with 0.5 wt % Pt would contain 0.25 mg of Pt. The impregnation was performed from 1 mg/mL $RuCl_3$ or $H_2PtCl_6 \bullet 6H_2O$ stock solutions. The required amount of the aqueous stock solutions was added to dry $PbCrO_4$ in a scintillation vial. The solution was put on a stir plate and stirred at approximately 300 rpm while being heated at approximately 80 °C. Evaporation typically takes about 1h for completion. The samples were removed from heat prior to complete drying to prevent uneven loading of the co-catalyst. Rather, after the solutions were about 90 % dry, the samples were removed from heat and allowed to finish drying in a vacuum oven at 60 °C. The resulting vials were heated at 350 °C for 1h to crystallize the cocatalysts.

XRD was collected using a Bruker D8 advanced diffractometer equipped with a Lynx-Eye detector and parallel beam optics using Cu-Kα (λ = 0.154184 nm). Microstructural and morphological investigations of the samples were conducted using

HR-SEM (Inspect FEI Nova-200) and TEM (JEOL JEM-3011). UV-Vis spectra of samples were recorded using an Agilent-Cary 5000 spectrophotometer equipped with a Praying Mantis diffuse reflectance accessory. Equal amounts of $PbCrO_4$ was mixed with $BaSO_4$ and the samples were scanned from 800 – 400 nm. BaSO4 was used as a baseline for the experiment.

6.10 References

1. Pinaud, B. A.; Benck, J. D.; Seitz, L. C.; Forman, A. J.; Chen, Z.; Deutsch, T. G.; James, B. D.; Baum, K. N.; Baum, G. N.; Ardo, S.; Wang, H.; Miller, E.; Jaramillo, T. F. Technical and Economic Feasibility of Centralized Facilities for Solar Hydrogen Production via Photocatalysis and Photoelectrochemistry *Energy Environ. Sci.* **2013**, *6*, 1983-2002
2. Abe, R.; Sayama, K.; Domen, K.; Arakawa, H. A New Type of Water Splitting System Composed of Two Different TiO_2 Photocatalysts (Anatase, Rutile) and a IO_3^-/I^- Shuttle Redox Mediator *Chem. Phys. Lett.* **2001**, *344*, 339-344

3 Abe, R.; Sayama, K.; Sugihara, H. Development of a New Photocatalytic Water Splitting into H_2 and O_2 using Two Different Semiconductor Photocatalysts and a Shuttle Redox Mediator IO_3^-/I^- *J. Phys. Chem. B*, **2005**, *109*, 16052-16061

4 Maeda, K.; Higashi, M.; Lu, D.; Abe, R.; Domen, K. Efficient Nonsacrificial Water Splitting through Two-Step Photoexcitation by Visible Light using a Modified Oxynitride as a Hydrogen Evolution Photocatalyst *J. Am. Chem. Soc.* **2010**, *132*, 5858-5868

5 Kudo, A.; Ueda, K.; Kato, H.; Mikami, I. Photocatalytic O_2 Evolution Under Visible Light on $BiVO_4$ in Aqueous $AgNO_3$ Solution *Catal. Lett.* **1998**, *53*, 229-230

6 Yu, J.; Kudo, A. Effects of Structural Variation on the Photocatalytic Performance of Hydrothermally Synthesized $BiVO_4$ *Adv. Funct. Mater.* **2006**, *16*, 2163-2169

7. Etacheri, V.; Yourey, J. E.; Bartlett, B. M. Chemically Bonded TiO2-Bronze Nanosheet/Reduced Graphene Oxide Hybrid for High-Power Lithium Ion Batteries *ACS Nano*, **2014**, *8*, 1491-1499
8. Xiang, Q.; Yu, J.; Jaroneic, M. Enhanced Photocatalytic H2-Production Activity of Graphene-Modified Titania Nanosheets *Nanoscale*, **2011**, *3*, 3670-3678
9. Xiang, Q. J.; Yu, J. G.; Jaroniec, M. Preparation and Enhanced Visible-Light Photocatalytic H2-Production Activity of Graphene/C_3N_4 Composites *J. Phys. Chem. C* **2011**, *115*, 7355-7363

10 Akhavan, O.; Gharderi, E. Photocatalytic Reduction of Graphene Oxide Nanosheets on TiO_2-Thin Film for Photoinactivation of Bacteria in Solar Light Irradiation *J. Phys. Chem. C* **2009**, *113*, 20214-20220

11 Dong, F.; Guo, S.; Wang, H.; Li, X.; Wu, Z., Enhancement of the Visible Light Photocatalytic Activity of C-Doped TiO_2 Nanomaterials Prepared by a Green Synthetic Approach *J. Phys. Chem. C* **2011,** *115*, 13285-13292.

12. Shah, M. S. A. S.; Park, A. R.; Zhang, K.; Park, J. H.; Yoo, P. J., Green Synthesis of Biphasic TiO_2–Reduced Graphene Oxide Nanocomposites with Highly Enhanced Photocatalytic Activity. *ACS Appl. Mater. Interfaces* **2012**, *4*, 3893-3901.
13. Park, J. H.; Kim, S.; Bard, A. J. Novel Carbon-Doped TiO2 Nanotube Arrays with High Aspect Ratios for Efficient Solar Water Splitting *Nano Lett.*, **2006**, *6*, 24-28
14. Wang, Y.; Li, H.; Jo, L.; Liu, X.; Wu, Y.; Lv, Y.; Fu, Y.; Zhou, H.; Chen, J. Synthesis and Characterization of Titanium-Containing Graphite-Like Carbon Films with Low Internal Stress and Superior Tribological Properties. *J. Phys. D: Appl. Phys.* **2012**, *45*, 295301-295310
15. Breault, T. M.; Bartlett, B. M. Lowering the Band Gap of Anatase-Structured TiO_2 by Coalloying with Nb and N: Electronic Structure and Photocatalytic Degradation of Methylene Blue *J. Phys. Chem. C* **2012**, *116*, 5986-5994
16. Becerril, H. A.; Mao, J.; Liu, Z.; Stoltenberg, R. M.; Bao, Z.; Chen, Y., Evaluation of Solution-Processed Reduced Graphene Oxide Films as Transparent Conductors. *ACS Nano* **2008,** *2*, 463–470.
17. Grabstanowicz, L. R.; Gai, S.; Li, T.; Rickard, R. M.; Rahj, T.; Liu, D.-J.; Zu, T. Facile Oxidative conversion of TiH_2 to High-Concentration Ti^{3+} Self-Doped Rutile TiO_2 with Visible-Light Photoactivity *Inorg. Chem.* **2013**, *52*, 3884-3890
18. Etacheri, V.; Seery, M. K.; Hinder, S. J.; Pillai, S. C. Oxygen Rich Titania: A Dopant Free, High Temperature Stable, and Visible-Light Active Anatase Photocatalyst *Adv. Funct. Mater.* **2011**, *21*, 3744-3752
19. Etacheri, V.; Seery, M. K.; Hinder, S. J.; Pillai, S. C., Highly Visible Light Active $TiO_{2-x}N_x$ Heterojunction Photocatalysts. *Chem. Mater.* **2010,** *22*, 3843-3853.
20. Etacheri, V.; Seery, M. K.; Hinder, S. J.; Pillai, S. C., Nanostructured $Ti_{1-x}S_xO_{2-y}N_y$ Heterojunctions for Efficient Visible-Light-Induced Photocatalysis. *Inorg. Chem.* **2012,** *51*, 7164-7173.
21. Etacheri, V.; Michlits, G.; Seery, M. K.; Hinder, S. J.; Pillai, S. C., A Highly Efficient $TiO_{2-x}C_x$ Nano-Heterojunction Photocatalyst for Visible Light Induced Antibacterial Applications. *ACS Appl. Mater. Interfaces* **2013,** *5*, 1663-1672.
22. Walsh, A.; Yan, Y.; Huda, M. N.; Al-Jassim, M. M.; Wei, S.-H. Band Edge Electronic Structure of BiVO4: Elucidating the role of the Bi s and V d Orbitals *Chem. Mater.* **2009**, *21*, 547-551
23. Cheng, B.; Guo, H.; Yu, J.; Zhao, X. Facile Preparation, Characterization, and Optical Properties of Rectangular $PbCrO_4$ Sing-Crystal Nanorods *J. Alloy Compd.* **2007**, *431*, L4-L7
24. Bandiello, E.; Errandonea, D.; Martinez-Garcia, D.; Santamaria-Perez, D.; Manjón, F. J. Effects of High-Pressure on the Structural, Vibrational, and Electronic Properties of Monazite-Type $PbCrO_4$ *Phys. Rev. B* **2012**, *85*, 024108-10
25. Kudo, A.; Steinbert, M.; Bard, A. J.; Campion, A.; Fox, M. A.; Mallouk, T. E.; Webber, S. E.; White, J. M. Photoactivity of Ternary Lead-Group IVB Oxides for Hydrogen and Oxygen Evolution *Catal. Lett.***1990**, *5*, 61-66
26. Maedoa, K.; Abe, R.; Domen, K. Role and Function of Ruthenium Species as Promoters with TaON-Based Photocatalysts for Oxygen Evolution in Two-Step Water Splitting under Visible Light *J. Phys. Chem. C* **2011**, *115*, 3057-3064

27. Breault, T. M.; Brancho, J. J.; Guo, P.; Bartlett, B. M. Visible Light Water Oxidation Using a Co-Catalyst Loaded Anatase Structured Ti_1-$(5_x/4)Nb_x)_{2-\gamma-\delta}N_\gamma$ Compound *J. Phys. Chem. C* **2013**, *52*, 9363-9368
28. Maeda, K.; Xiong, A.; Yoshinaga, T.; Ikeda, T.; Sakamoto, N.; Hisatomi, T.; Takashima, M.; Lu, D.; Kanehara, M.; Setoyama, T.; Teranishi, T.; Domen, K. Photocatalytic Overall Water Splitting Promoted by Two Different Cocatalysts for Hydrogen and Oxygen Evolution under Visible Light *Agnew. Chem. Int. Ed.*, **2010**, *49*, 4096-4099
29. Xiong, A.; Yoshinaga, T.; Ikeda, T.; Takashima, M.; Hisatomi, T.; Maeda, K.; Setoyama, T.; Teranishi, T.; Domen, K. Effect of Hydrogen and Oxygen Evolution Cocatalysts on Photocatalytic Activity of GaN:ZnO *Eur. J. Inorg. Chem.* **2014**, 767-772
30. Abe, R.; Higashi, M.; Domen, K. Overall Water Splitting under Visible Light through a Two-Step Photoescitation Between TaON and WO3 in the Presence of an Iodate-Iodide Shuttle Redox Mediator *ChemSusChem* **2011**, *4*, 228-237
31. Negas, T. The System PbO-Chromium Oxide in Air *J. Am. Ceram. Soc.* **1968**, *51*, 716-719
32. Gomez-Quero, S.; Hernandez-Mejia, C.; Hendrikx, R.; Rothenberg, G. Understanding the Redox Behaviour of $PbCrO_4$ and its Application in Selective Hydrogen Combustion *Dalton Trans.* **2012**, *41*, 12289-12295
33. Min, Y.; He, G. Xu, Q.; Chen, Y. UV Light Assisted Synthesis of Ternary Reduced Graphene Oxide Hybrid Materials and their Photocatalytic Performance *Dalton Trans.* **2013**, *42*, 12284-12292
34. Ma, S. S. K.; Maedo, K.; Abe, R.; Domen, K. Visible-Light Driven Nonsacrificial Water Oxidation over Tungsten Trioxide Powder Modified with Two Different Cocatalysts *Energy Environ. Sci.* **2012**, *5*, 8390-8397
35. Asai, R.; Nemoto, H.; Jia, Q.; Saito, K.; Iwase, A.; Kudo, A. A Visible Light Responsive Rhodium and Antimony-Codoped $SrTiO_3$ Powdered Photocatalyst Loaded with an IrOx Cocatalyst for Solar Water Splitting *Chem. Comm.* **2014**, *50*, 2543-2546
36. Li, R.; Han, H.; Zhang, F.; Wang, D.; Li, C. Highly efficiency Photocatalysts Constructed by Rational Assembly of Dual-Cocatalysts Separately on Different Facets of $BiVO_4$ *Energy. Environ. Sci*. **2014**, DOI: 10.1039/C3EE43304H

APPENDIX A

SUPPORTING DATA FOR CHAPTER 2

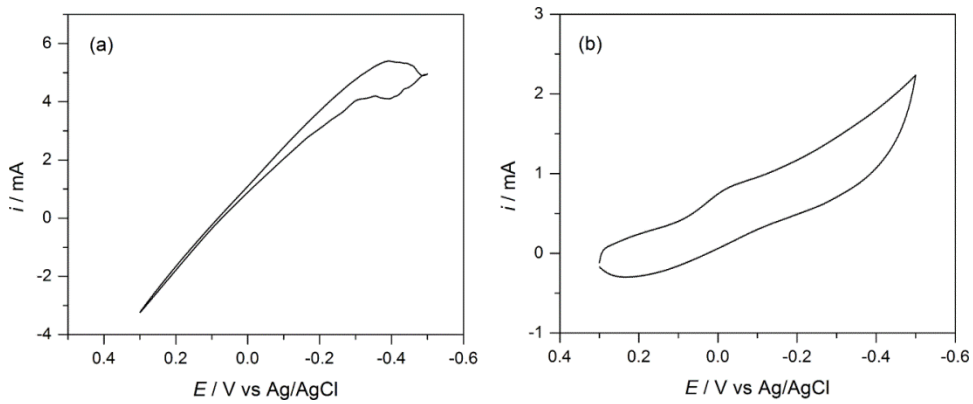

Figure A.1 Electrochemical deposition control experiments.
These experiments were conducted in the same potential window (+0.3 to –0.5 V vs Ag/AgCl) for (a) 0.25M Cu^{2+} in a pH 1.1 solution of 70:30 H_2O:2-propanol and (b) 0.25M $W_2O_{11}^{2-}$ in a pH 1.1 solution of 70:30 H_2O:2-propanol.

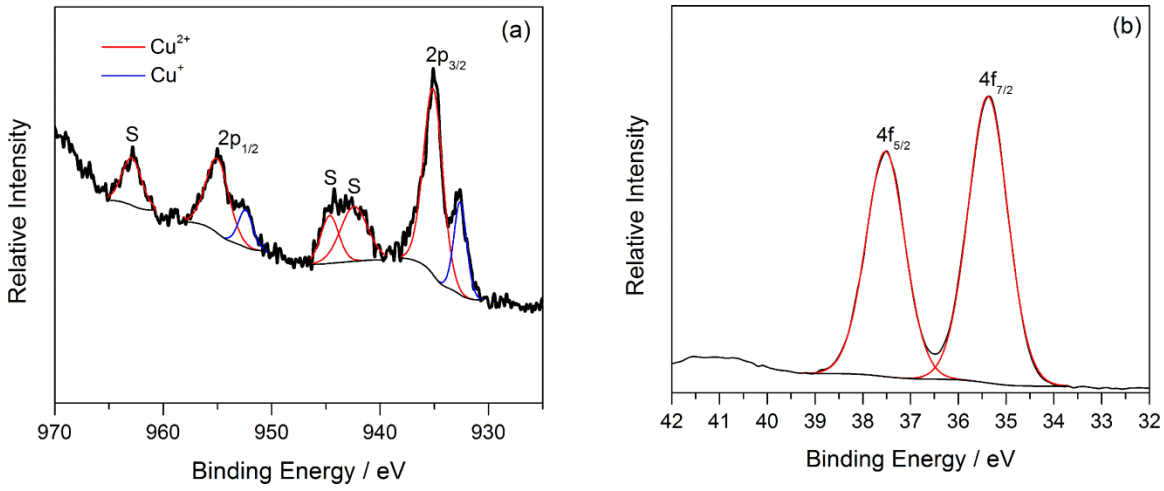

Figure A.2 X-ray photoelectron spectra for a) Cu(2p) and b) W(4f) in an amorphous, as deposited film

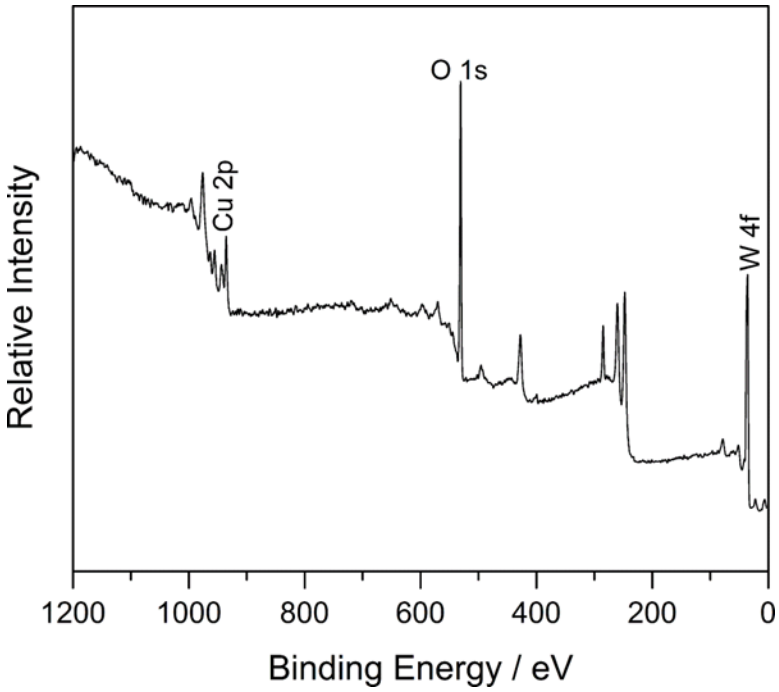

Figure A.3 X-Ray photoelectron survey scan of $CuWO_4$.
The Cu(2p), O(1s), and W(4f) binding energies are noted in the figure.

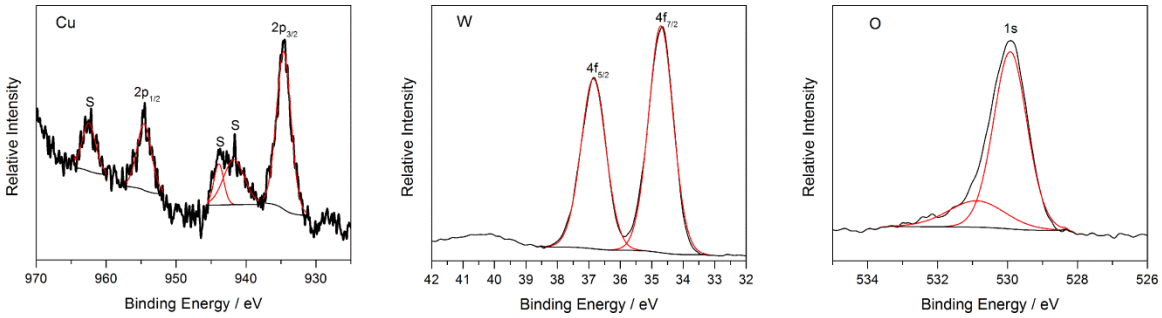

Figure A.4 Experimental X-ray photoelectron spectra of the Cu(2p), W(4f), and O(1s) (black) peaks with deconvolution (red).

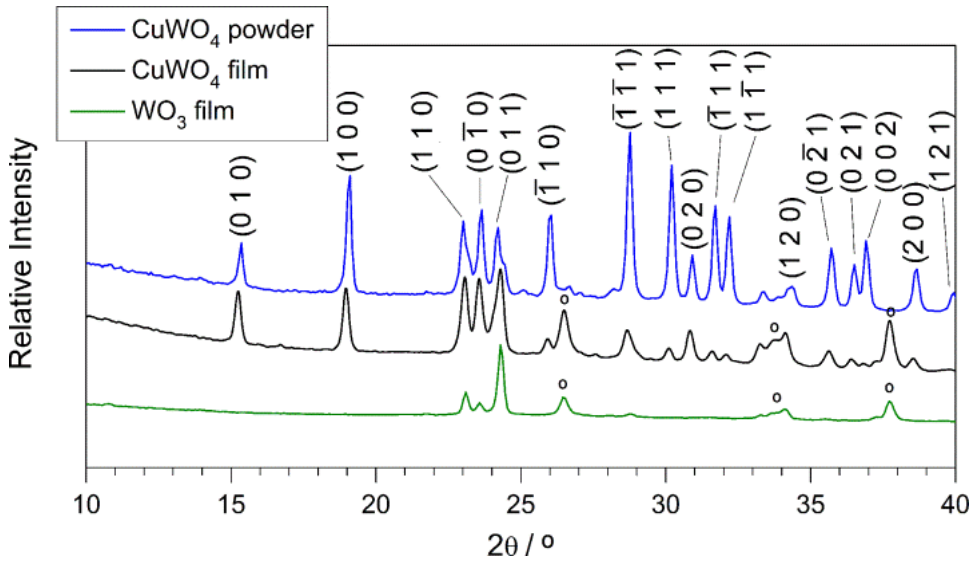

Figure A.5 X-ray diffraction pattern of crystalline $CuWO_4$ electrode, powder, and WO_3 thin film.
Note: The º'ed peaks are reflections associated with the FTO substrate.

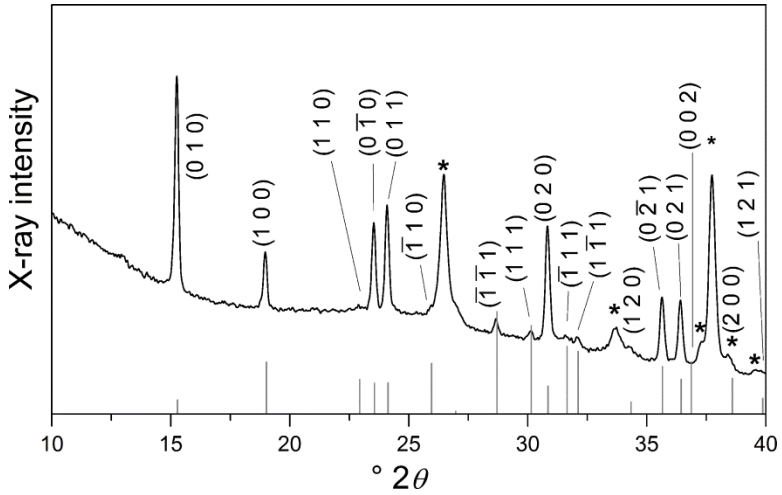

Figure A.6 X-ray diffraction pattern of $CuWO_4$ thin films.
The Bragg reflections from JCPDF 72-0616 are shown as gray lines. The FTO substrate is marked with an *.

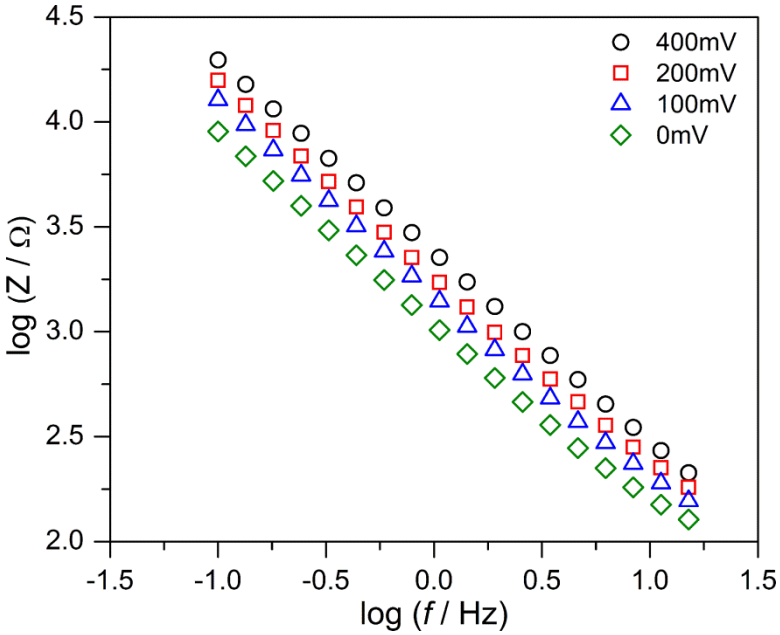

Figure A.7 Bode plot for a $CuWO_4$ film constructed from the impedance data taken in 0.1 M KP_i (pH 7).

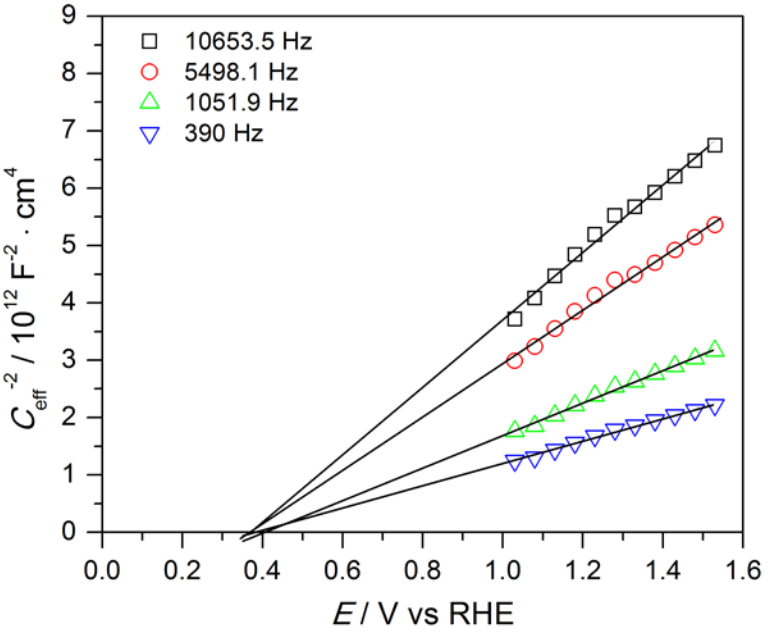

Figure A.8 Mott-Schottky plot of $CuWO_4$ single crystal in a 0.1 M $Fe(CN)_6^{3-/4-}$ at pH 9

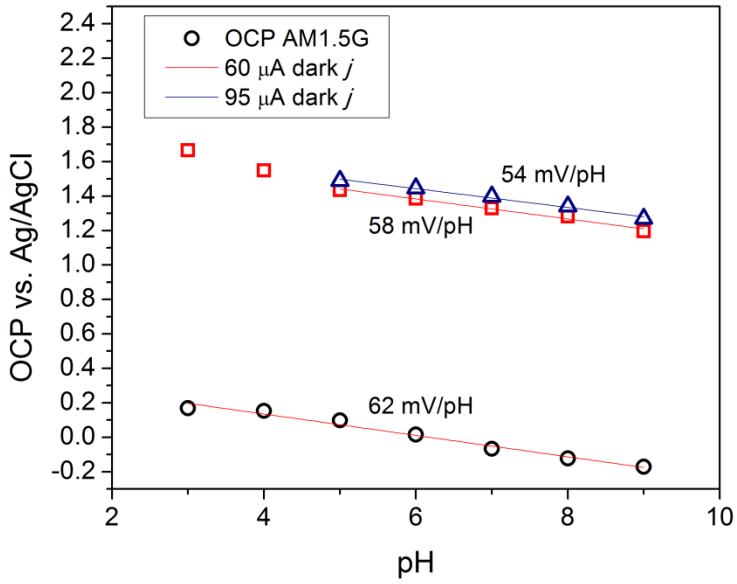

Figure A.9 pH dependence of the open-circuit voltage of $CuWO_4$ under illumination. The figure also presents the potential at which certain dark currents were generated as a function of pH during the electrolysis of water.

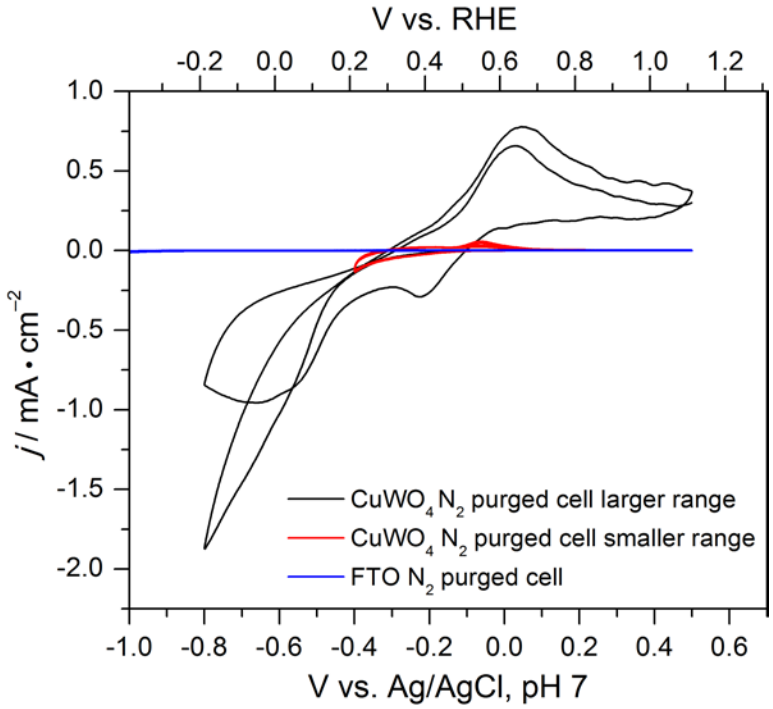

Figure A.10 CV traces of $CuWO_4$ and FTO in N_2 purged solutions

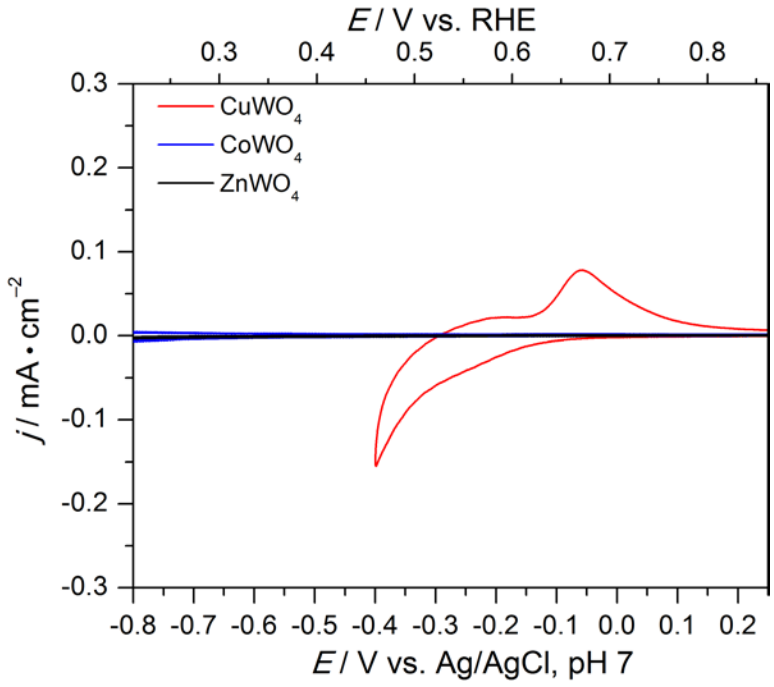

Figure A.11 CV traces of $CuWO_4$, $CoWO_4$, and $ZnWO_4$ in pH 7 KP_i under N_2

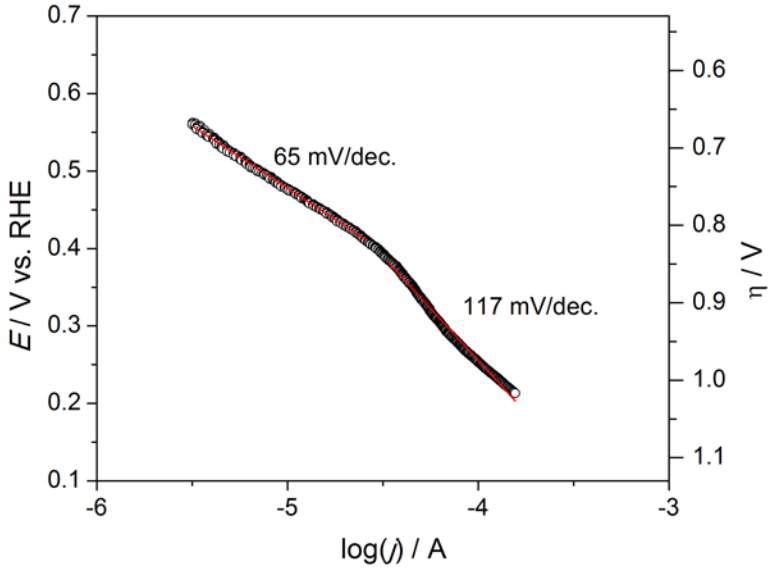

Figure A.12 Tafel Study on $CuWO_4$ from a LSV trace taken in pH 7 KP_i and 1 atm O_2

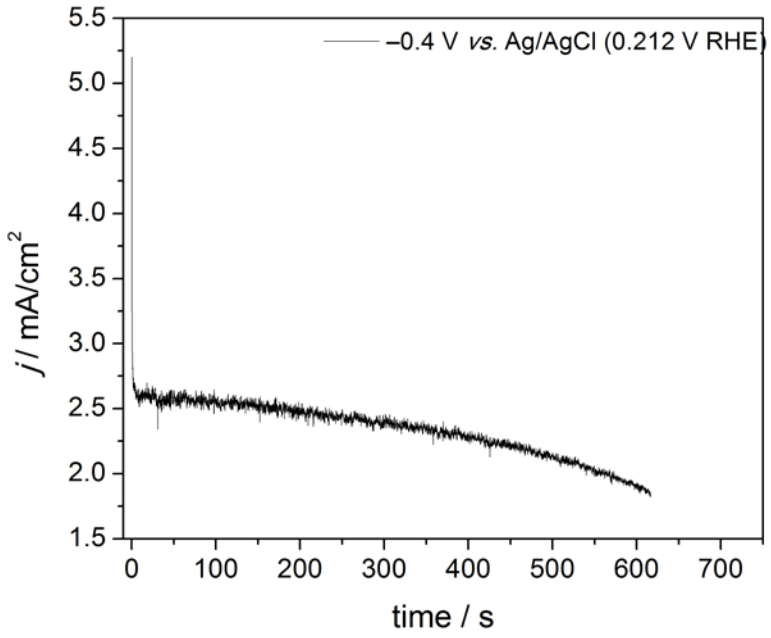

Figure A.13 BE study of ORR on $CuWO_4$ at -0.4 V vs. Ag/AgCl (0.212 V RHE) in pH 7 KP_i at 1 atm O_2

APPENDIX B

SUPPORTING DATA FOR CHAPTER 3

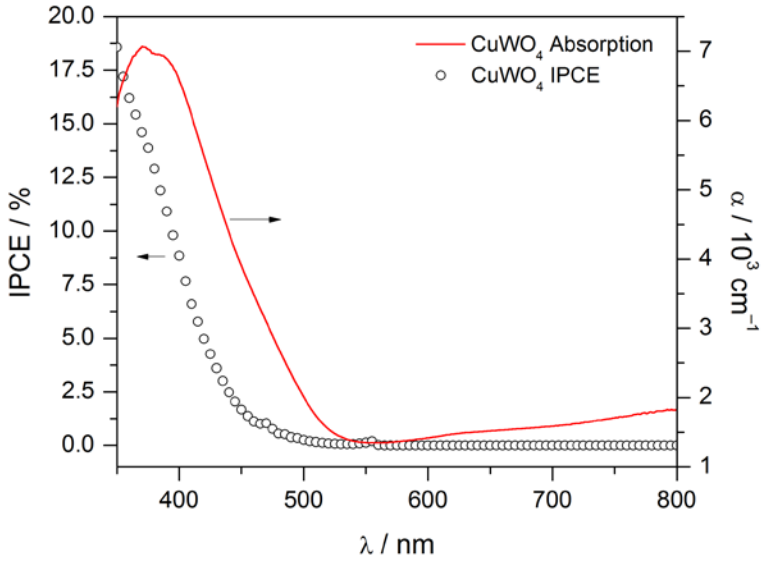

Figure B.1 Spectral Response and Absorption Spectrum of $CuWO_4$
The IPCE measurement was conducted at 0.5 V vs. Ag/AgCl in a 0.1 M Na_2SO_4 solution containing 10 % v/v MeOH
The absorptivity coefficient of $CuWO_4$ was determined from the thickness of the electrochemically deposited electrode as well as the %R of a thin film

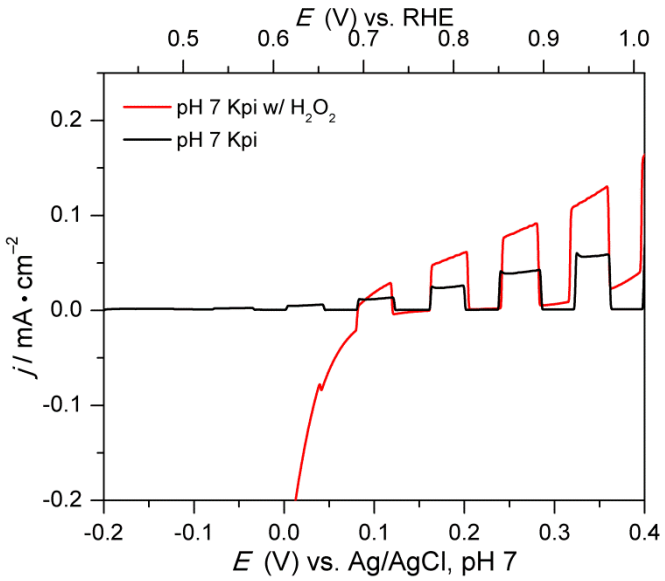

Figure B.2 Linear sweep voltammogram under AM1.5G illumination in pH 7 KP_i buffer with and without added H_2O_2.

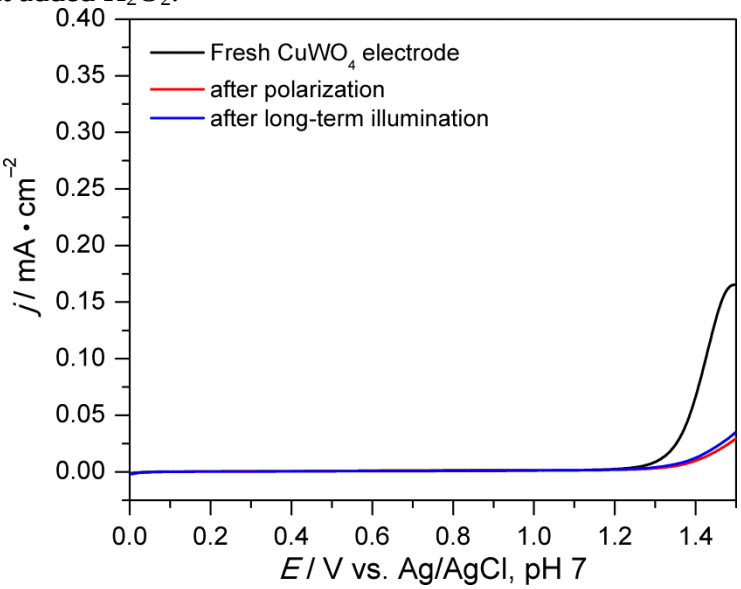

Figure B.3 Dark LSV trace of a sol-gel electrode before and after a polarization. The experiment was also conducted after an illuminated bulk electrolysis experiment

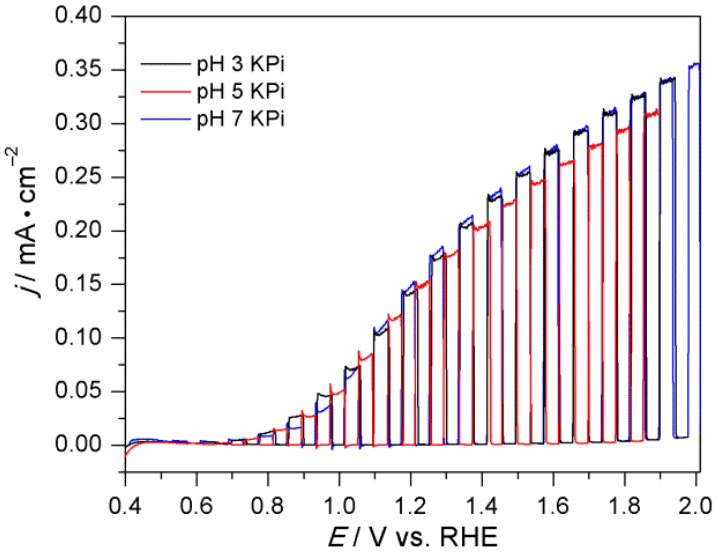

Figure B.4 LSV trace of sol-gel $CuWO_4$ in pH 3, 5, and 7 KP_i buffer under AM1.5G illumination at 100 mW/cm^2

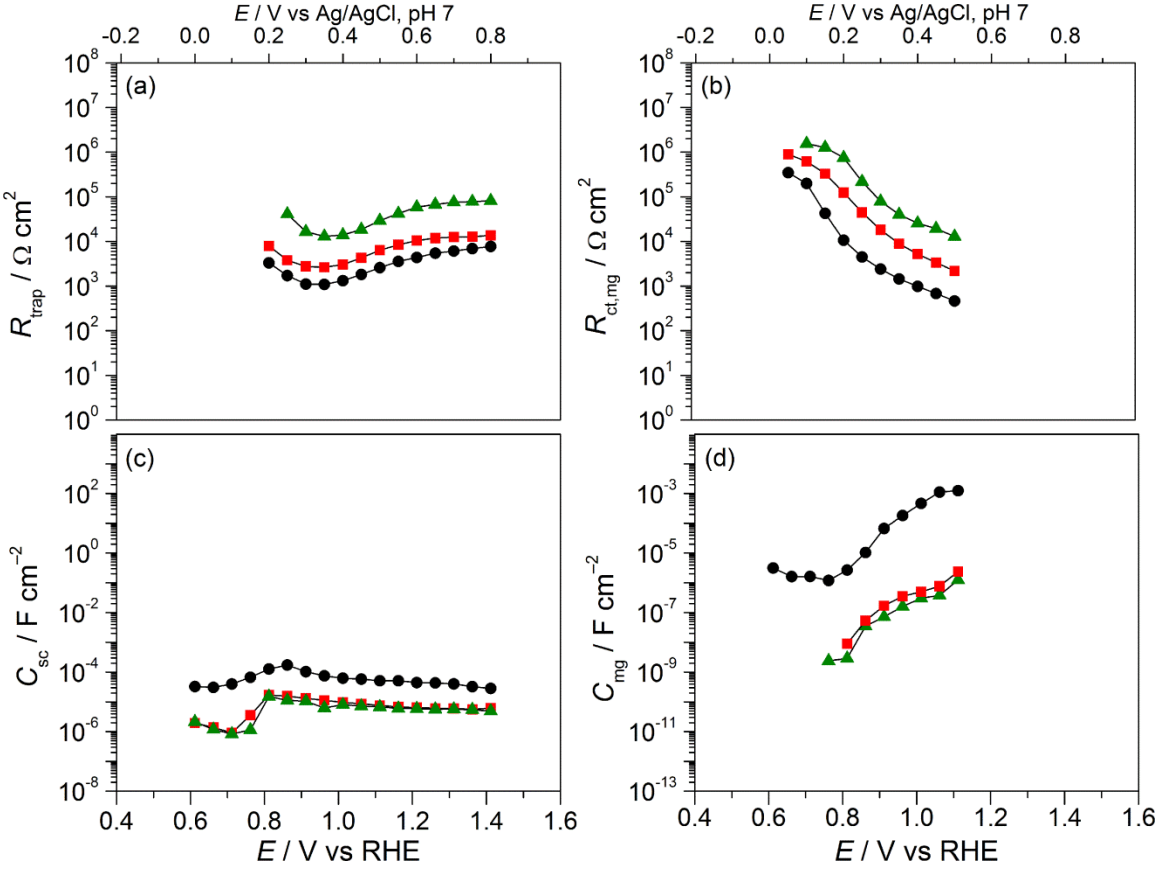

Figure B.5 Circuit elements as a function of potential and light intensity.
(a) R_{trap} (b) $R_{ct,mg}$ (c) C_{sc} (d) C_{mg}.
100 mW/cm^2, black circles; 50 mW/cm^2, red squares; and 15 mW/cm^2, green triangles

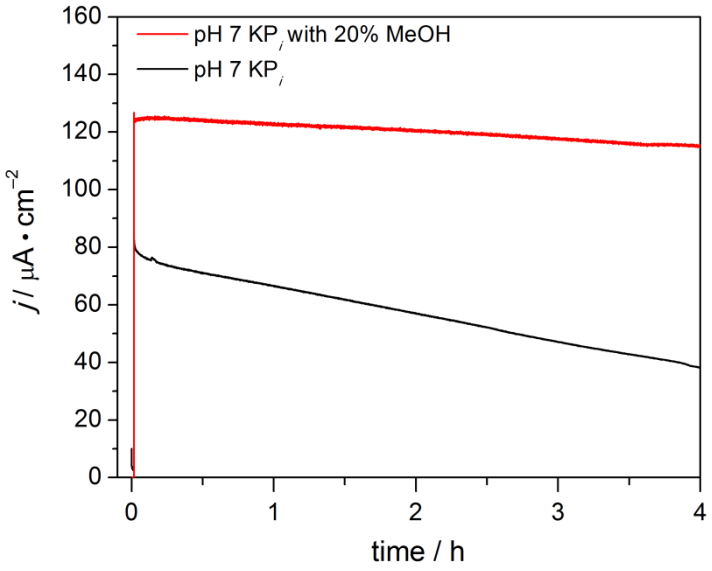

Figure B.6 *j*–t curve comparison between water oxidation (black) and methanol oxidation (red) in pH 7 KP_i
The experiment was conducted in 0.1 M KPi buffer at pH 7 and 1.23 V under AM1.5G illumination at 100 mW/cm2 with and without 20% MeOH present.

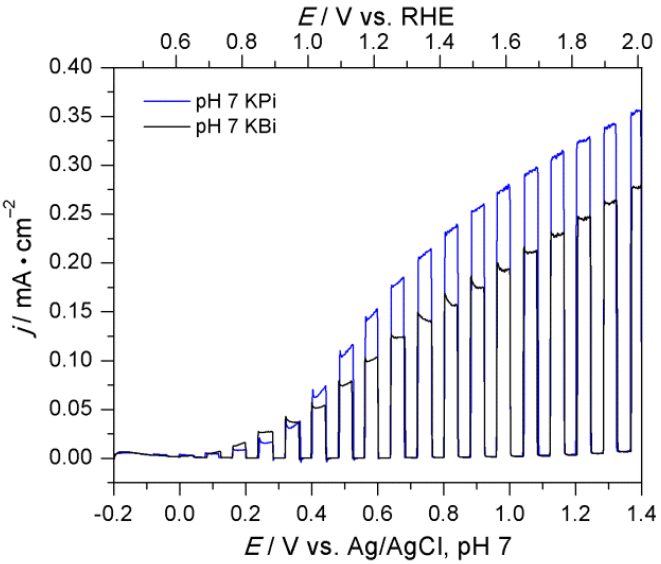

Figure B.7 LSV trace of $CuWO_4$ comparing various buffers

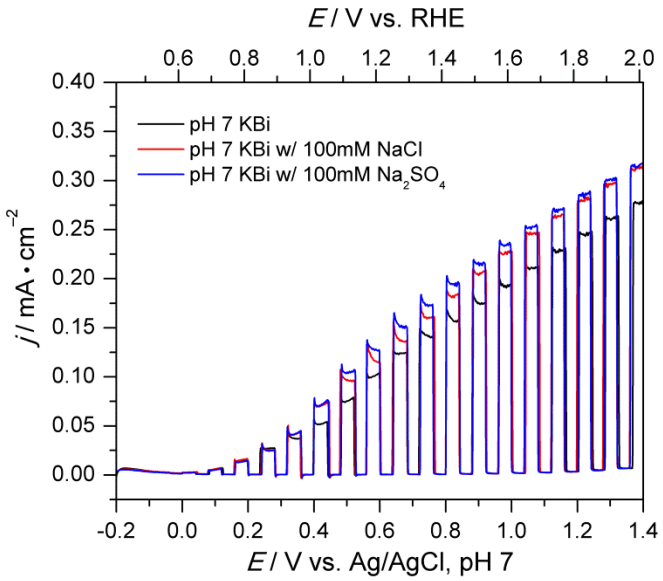

Figure B.8 LSV trace of $CuWO_4$ in KB_i containing supporting electrolytes.

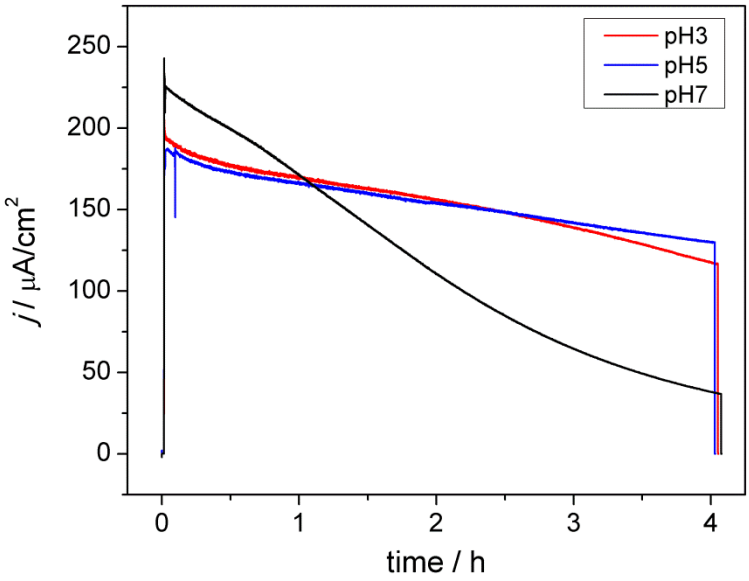

Figure B.9 *j*-t curve comparison under AM1.5G 300 mW/cm^2 illumination at in KP_i various pH

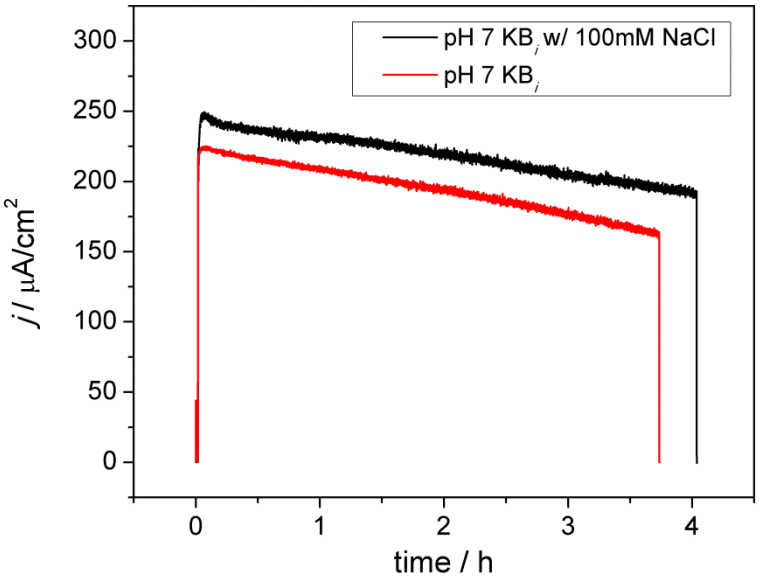

Figure B.10 *j*-t curve comparison under AM1.5G 300 mW/cm^2 illumination in a pH 7 KB$_i$ buffer

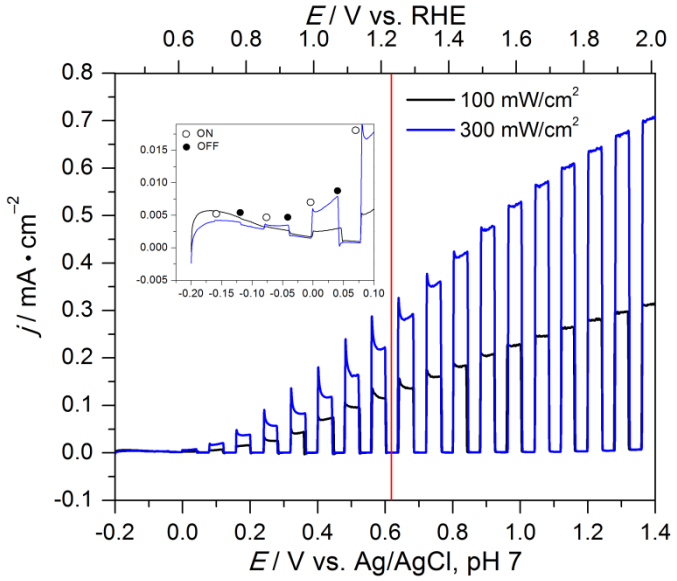

Figure B.11 LSV of $CuWO_4$ in 0.1 M KB$_i$ w/ 100 mM NaCl under AM1.5G illumination

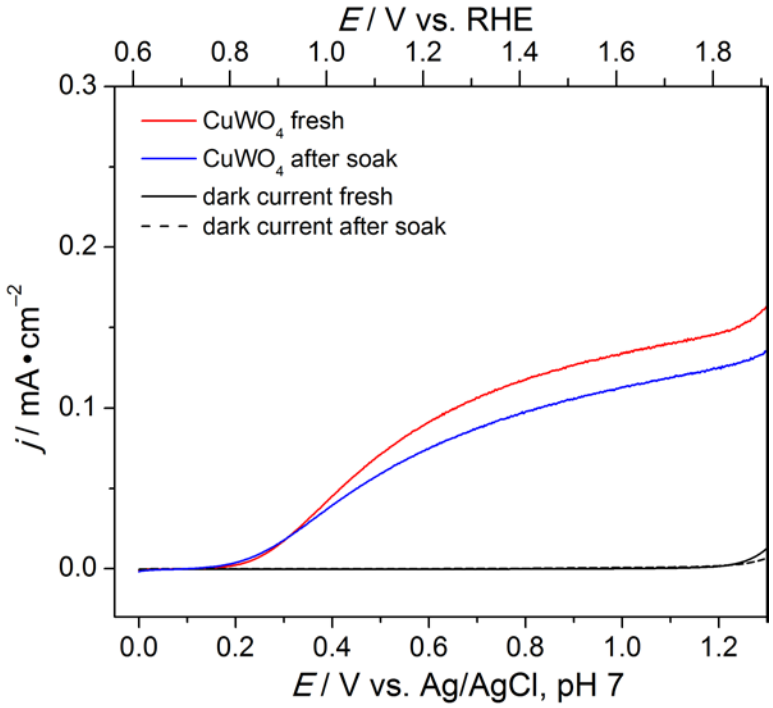

Figure B.12 LSV traces of sol-gel $CuWO_4$ on a fresh electrode and after soaking in pH 7 KP_i for 12 hours

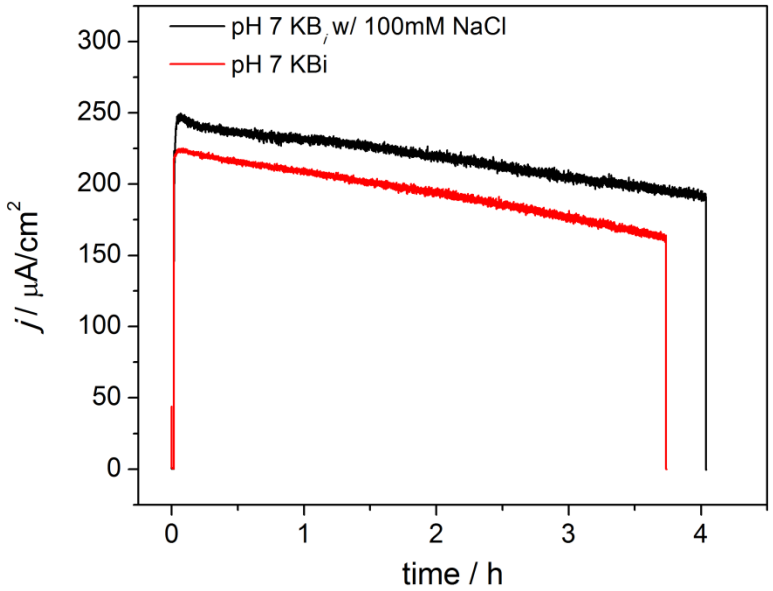

Figure B.13 *j*-t comparison of $CuWO_4$ electrodes in 0.1 M KB_i buffer at pH 7 with and without the presence of 100 mM NaCl
The experiment was conducted at 1.23 V RHE under 300 mW/cm^2 AM1.5G illumination

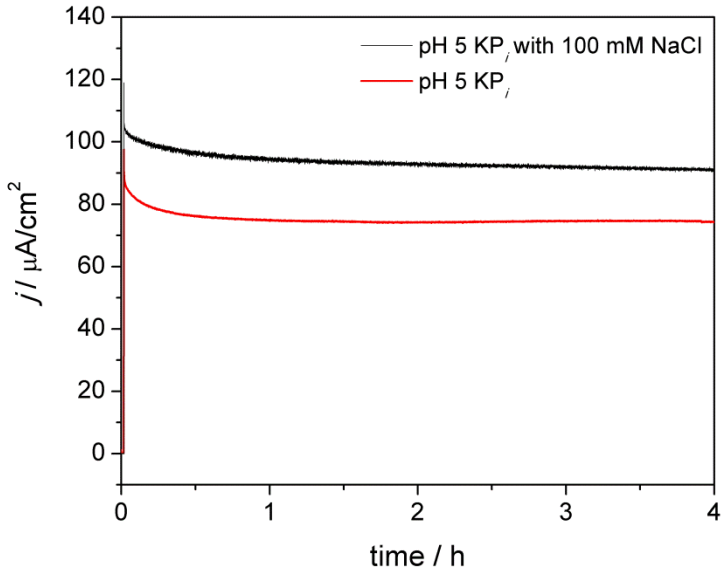

Figure B.14 j-t comparison of $CuWO_4$ electrodes in pH 5 KP_i buffer with NaCl under 100 mW/cm^2 illumination
The experiment was conducted at 1.23 V RHE in 0.1 M KPi buffer at pH 5 with and without the presence of 100 mM NaCl under 100 mW/cm2 AM1.5G illumination.

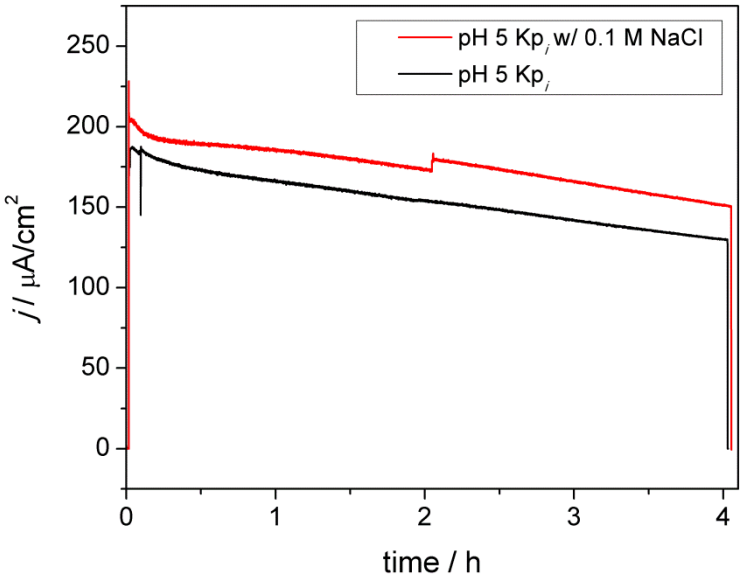

Figure B.15 j-t comparison of $CuWO_4$ electrodes in a pH 5 KP_i buffer with NaCl under 300 mW/cm^2 illumination
The experiment was conducted at 1.23 V RHE in a 0.1 M KP_i pH 5 buffer w and w/o the presence of 100 mM NaCl under 300 mW/cm^2 AM1.5G illumination.

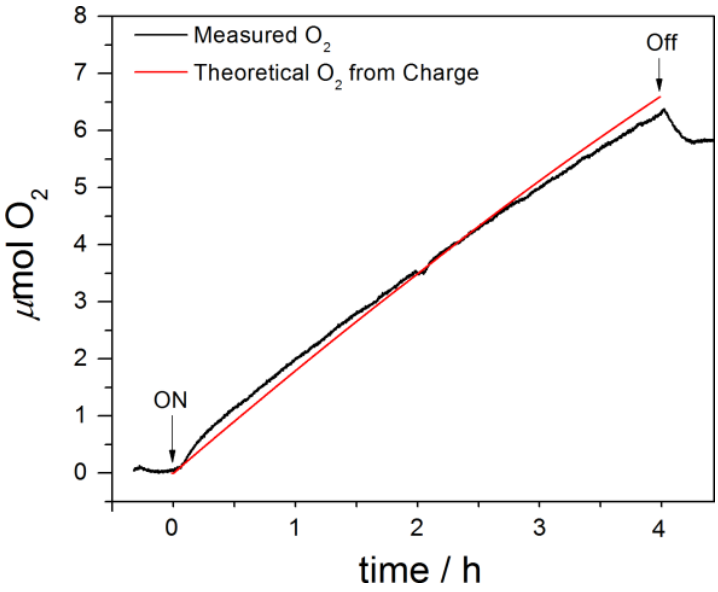

Figure B.16 O_2 detection on $CuWO_4$ at 1.23 V RHE in a 0.1 M KP_i buffer w/ 100 mM NaCl at pH 5
The experiment was conducted at 1.23 V RHE under 300 mW/cm2 AM1.5G illumination. The black line is the measured O_2 and the red line is theoretical based on coulometry.

APPENDIX C

SUPPORTING DATA FOR CHAPTER 4

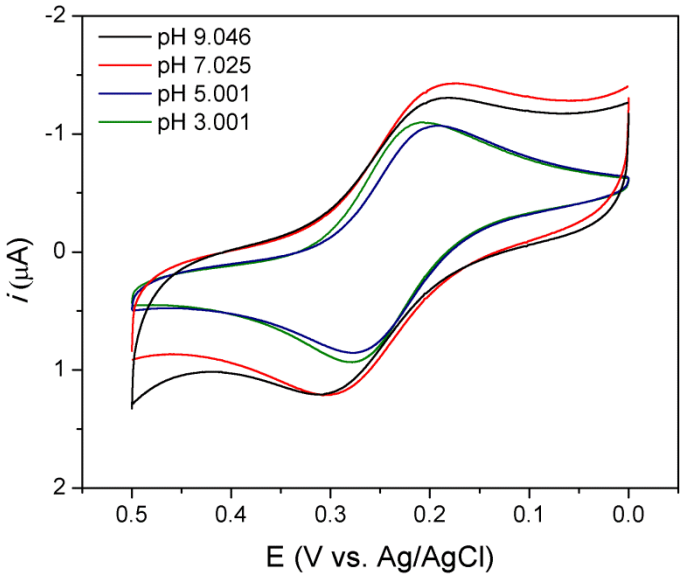

Figure C.1 Cyclic voltammogram of a 3-electrode cell using a glassy carbon working electrode, Ag/AgCl reference, and Pt mesh auxiliary electrode to identify $E^{o\prime}$ of the $[Fe(CN)_6]^{3-/4-}$ couple.

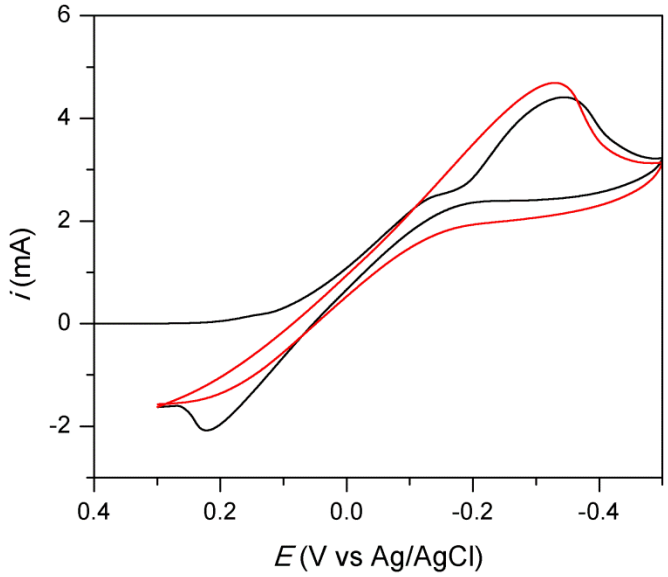

Figure C.2 Electrochemical deposition of amorphous $CuWO_4$-WO_3 composite photoanode by cyclic voltammetry.
Current was recorded as a function of potential as the potential was swept from 0.3 to -0.5 V (vs Ag/AgCl) at 10 mV/s in a 30% isopropanol solution containing 50 mM $W_2O_{11}^{2-}$ and 30 mM Cu^{2+}. The black line is the first cycle, and the red the second.

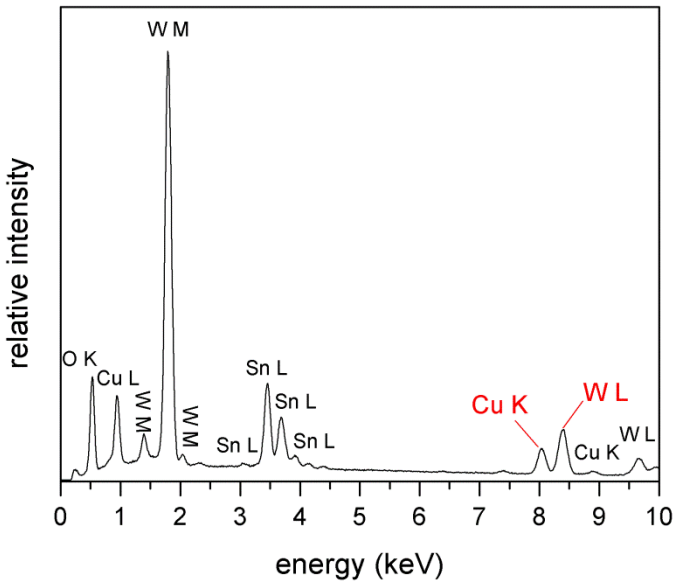

Figure C.3 EDX spectrum of a $CuWO_4$-WO_3 electrode.
The Cu K and W L lines (red) were used for quantifying the mole ratio of W to Cu.
We used the Cu K and W L emissions for quantifying the relative atomic ratio, as is the standard in EDX analysis. Additionally, EDX measurements taken on $CuWO_4$ powders prepared by traditional solid state methods show the W:Cu atomic ratio of 1:1 using these emission lines.

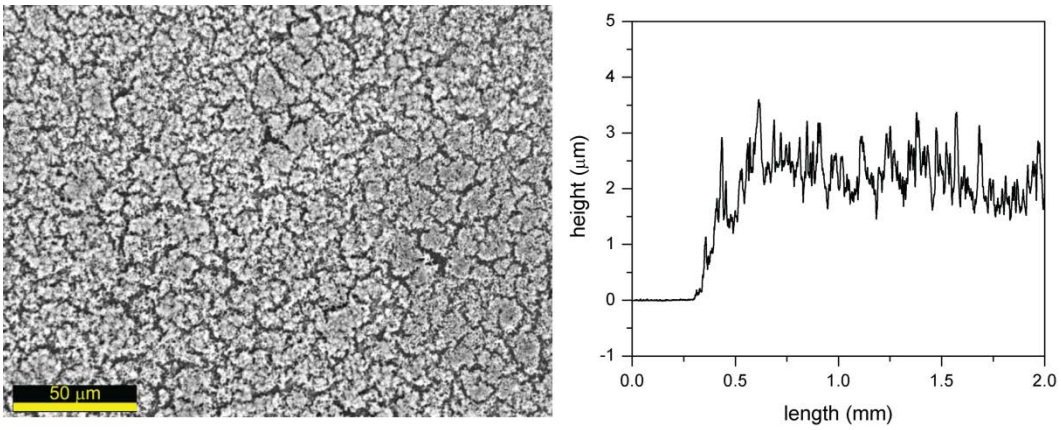

Figure C.4 Left) Scanning electron micrograph of a CuWO4-WO3 electrode. Right) Profile of a $CuWO_4$-WO_3 electrode.
Film thickness was 2-3 µm as determined by profilometry using a Dektak 6 M surface profilometer.

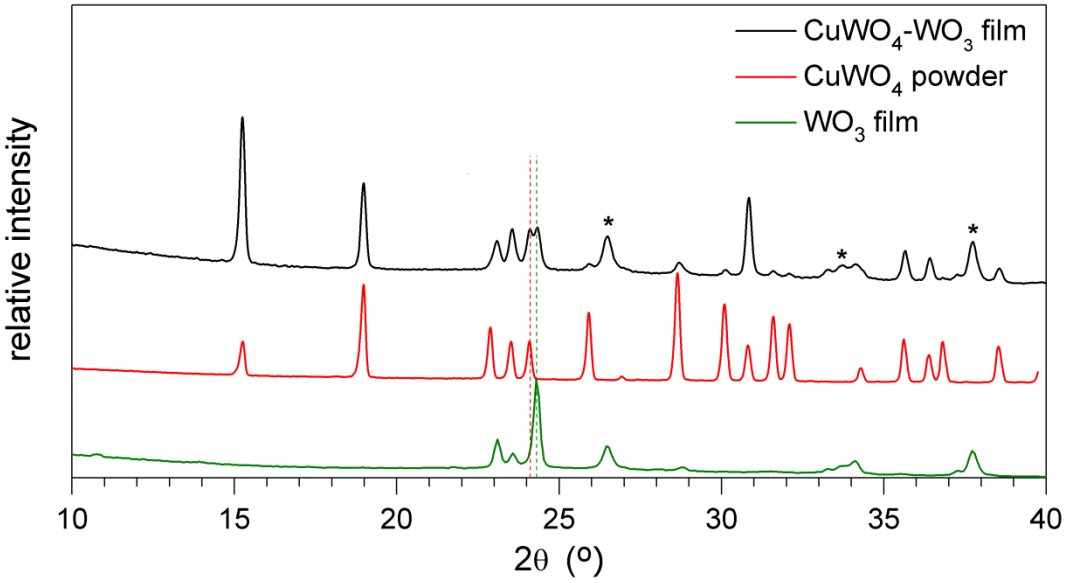

Figure C.5 X-ray diffraction pattern of $CuWO_4$-WO_3 film (black), $CuWO_4$ powder (red), and a WO_3 film (green).
The biphasic mixture is indicated by the peak splitting seen at 24° 2θ, the red dotted line is indicative of the (001) plane in $CuWO_4$ and the green dotted line represents the (200) plane in WO_3. Features associated with the, fluorinated tin oxide (FTO) substrate are indicated by * in the XRD pattern.

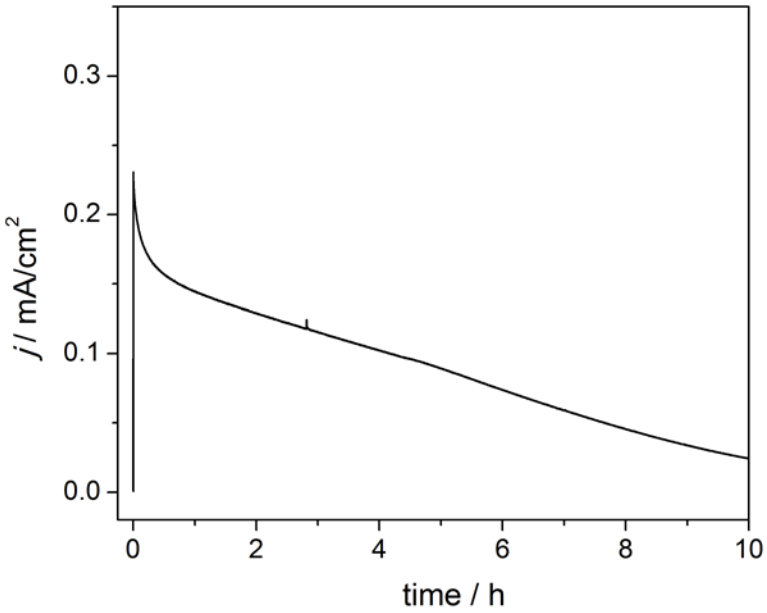

Figure C.6 *j*-t curve of a $CuWO_4$-WO_3 composite photoanode in pH 7 Kp_i under illumination
The experiment was conducted at 0.5 V vs. Ag/AgCl under AM1.5G illumination at 100 mW/cm^2.

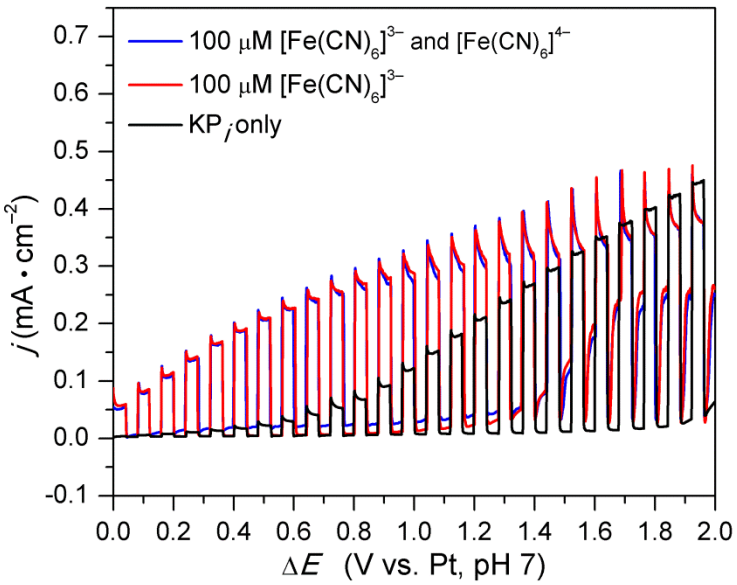

Figure C.7 LSV of a KPi electrolyte solution (black) containing 100 μM $[Fe(CN)_6]^{3-}$ (red) and 100 μM each of $[Fe(CN)_6]^{3-}$ and $[Fe(CN)_6]^{4-}$.
At these concentrations, there is no discernible difference the *j*-E characteristics of the system except for the slight increase in dark oxidative current from to the electrochemical oxidation of $[Fe(CN)_6]^{4-}$ by either the composite electrode or exposed FTO

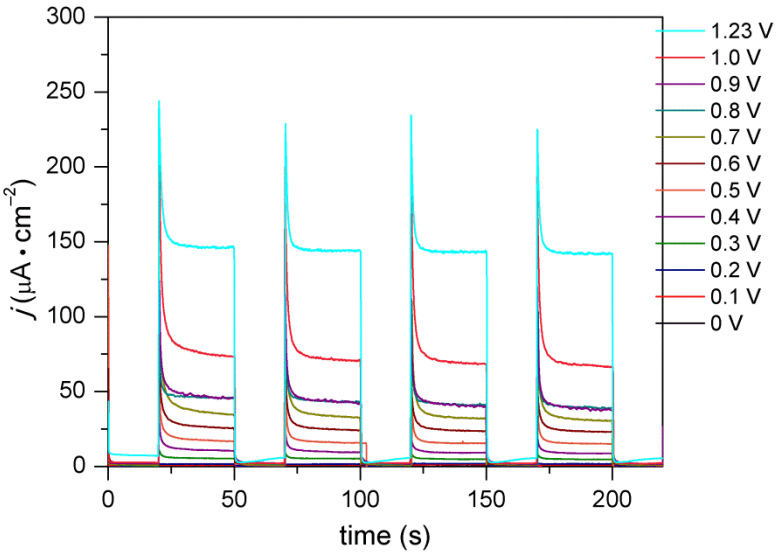

Figure C.8 Chopped light bulk electrolysis in a 100 mM KP_i solution in a 2-electrode cell using a $CuWO_4$-WO_3 working electrode and a Pt mesh auxiliary.
A bias was applied (ΔE vs. Pt) between the two electrodes and photocurrent was measured as the $CuWO_4$-WO_3 electrode was illuminated in 30 s intervals.

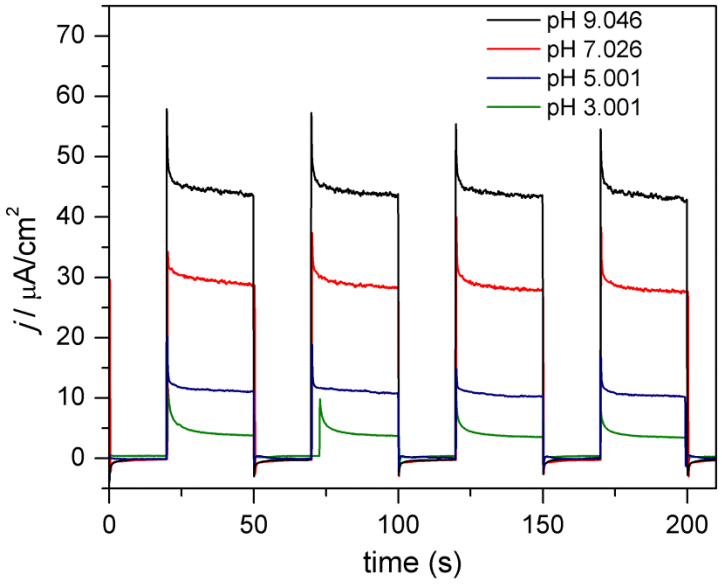

Figure C.9 Chopped light bulk electrolysis in a 2-electrode cell under chopped-light illumination equipped with a $CuWO_4$-WO_3 working electrode and a Pt mesh auxiliary electrode in a 100 mM KP_i solution containing 100 μM $[Fe(CN)_6]^{3-}$ at different pH. The initial electrolyte solution was 100 mM H_3PO_4. The pH of the solution was adjusted using 1 M KOH and allowed to equilibrate for 15 minutes before conducting the next chopped light bulk electrolysis experiment.

APPENDIX D

SUPPORTING DATA FOR CHAPTER 5

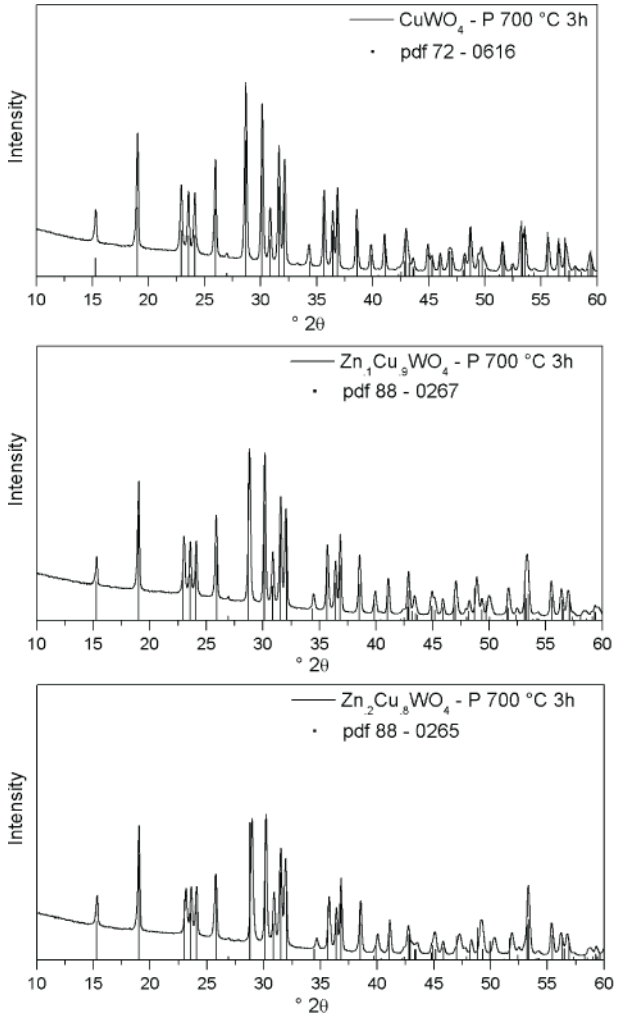

Figure D.1 X-ray diffraction patterns of Zn1-$_x$Cu$_x$WO$_4$ (x = 0.8, 0.9, 1) synthesized by the Pechini sol-gel method.
The relevant pdf cards are included in the figures.

Table D.1 ICP-AES results quantifying the mol ratio of the Cu, Zn, and W

x	Cu / mol	Zn / mol	W/ mol
0	0	1	0.98
0.1	0.091	0.909	0.99
0.2	0.185	0.815	0.98
0.3	0.279	0.721	1.01
0.4	0.373	0.627	1.01
0.5	0.471	0.529	1.03
0.6	0.572	0.428	1.05
0.7	0.676	0.324	1.05
0.8	0.787	0.213	1.06
0.9	0.896	0.104	1.08
1.0	1	0	1.01

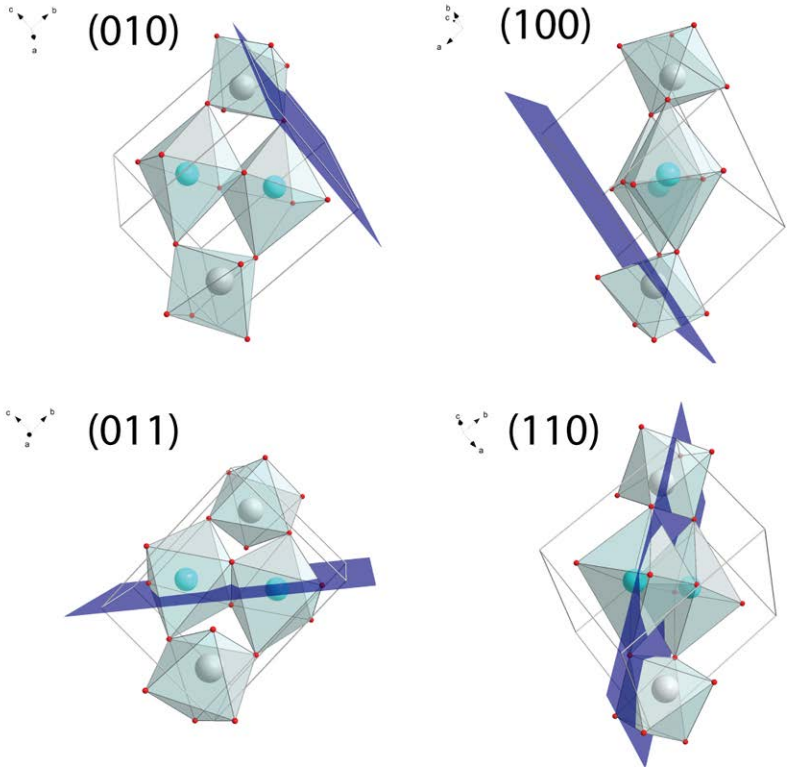

Figure D.2 Bragg planes of AWO_4.
Cu is light blue, W is grey, and O is red.

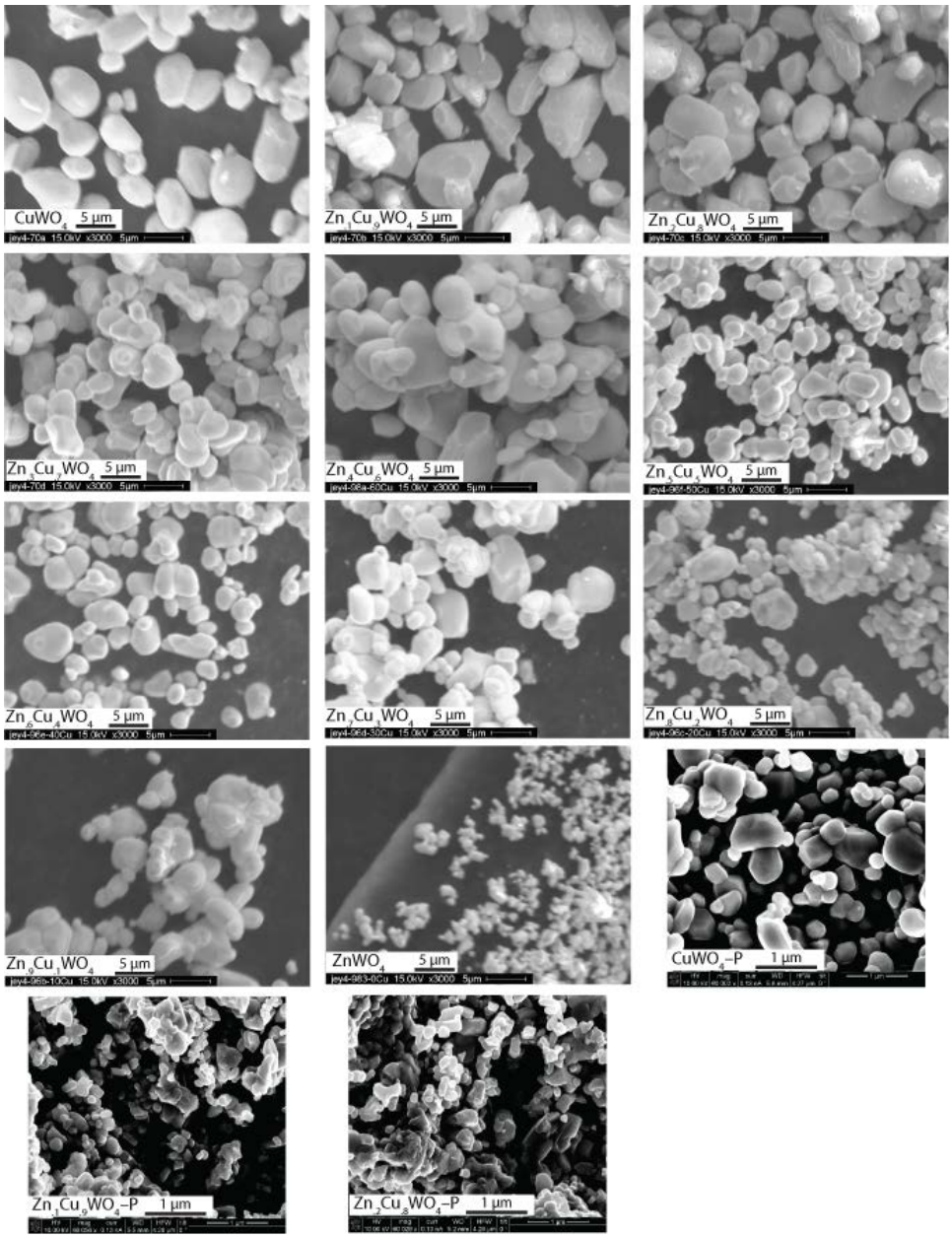

Figure D.3 SEM images of $Zn_{1-x}Cu_xWO_4$ ($0 \leq x \leq 1$) by solid state and $Zn_{1-x}Cu_xWO_4$ (x = 0.8, 0.9, 1) by Pechini sol-gel (-P).

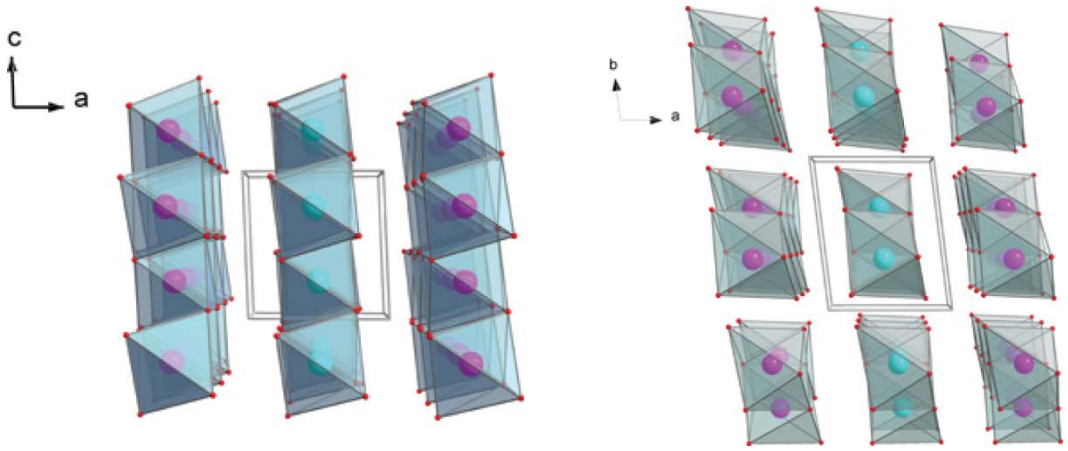

Figure D.4 Structure of $CuWO_4$ showing ferro- and antiferromagnetic interactions along different crystal vectors.
The alternating colors represent spin up and spin down Cu centers.

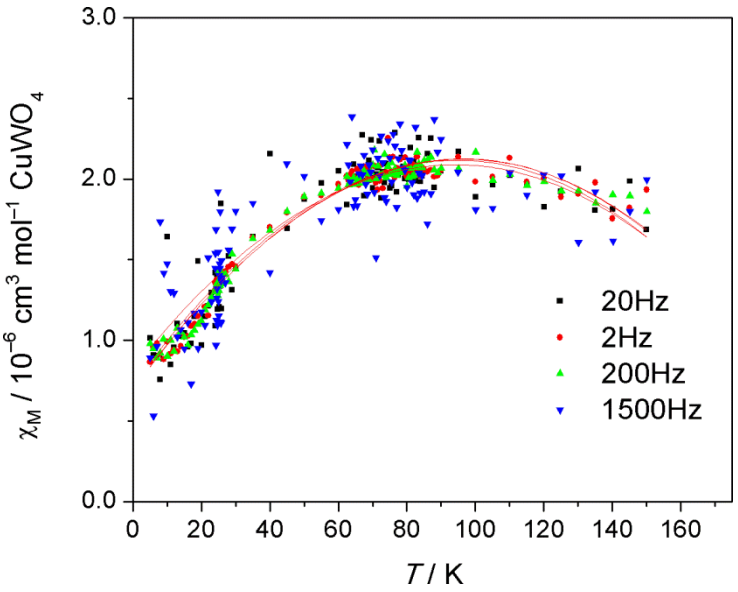

Figure D.5 AC susceptibility plot of $CuWO_4$ showing no frequency dependence.
Lines are included to guide the eye.

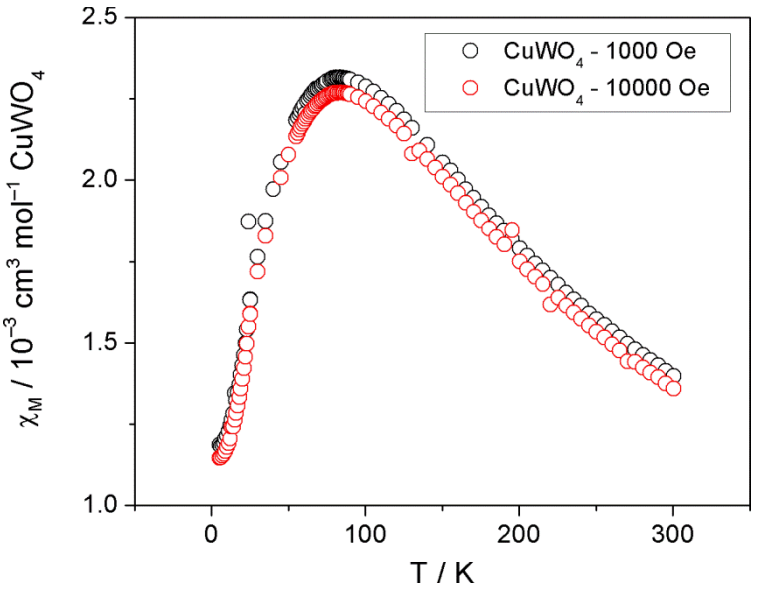

Figure D.6 DC susceptibility of $CuWO_4$ at 1000 Oe and 1000 Oe

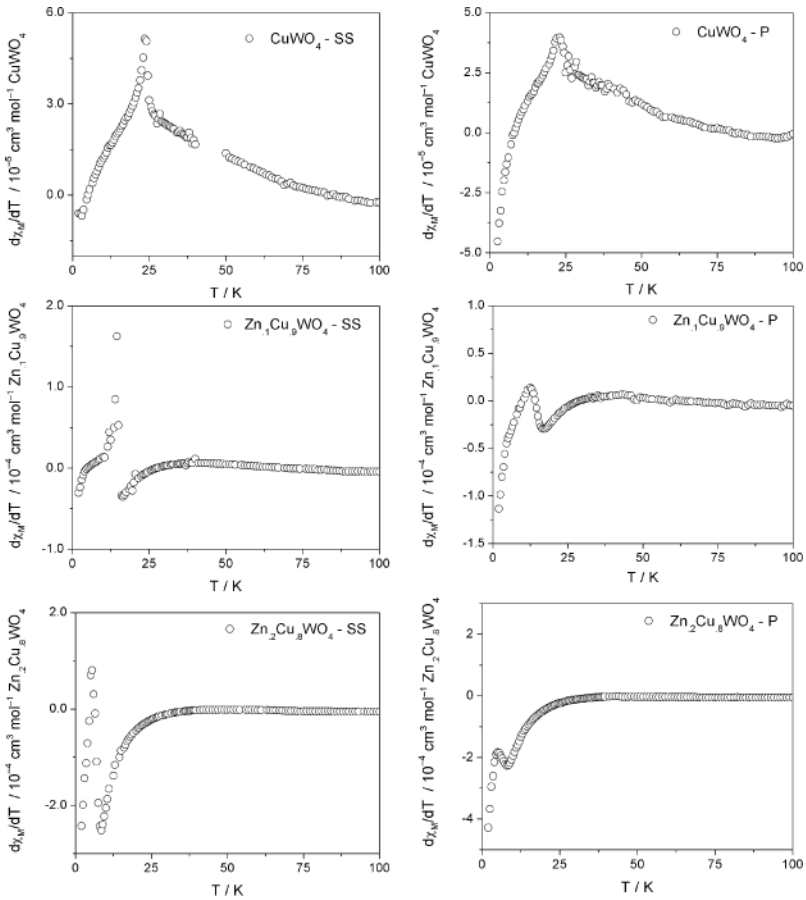

Figure D.7 dχ/dT plots for $Zn_{1-x}Cu_xWO_4$ (x = 0.8, 0.9, 1) prepared by both solid state (SS) and Pechini sol-gel (P)

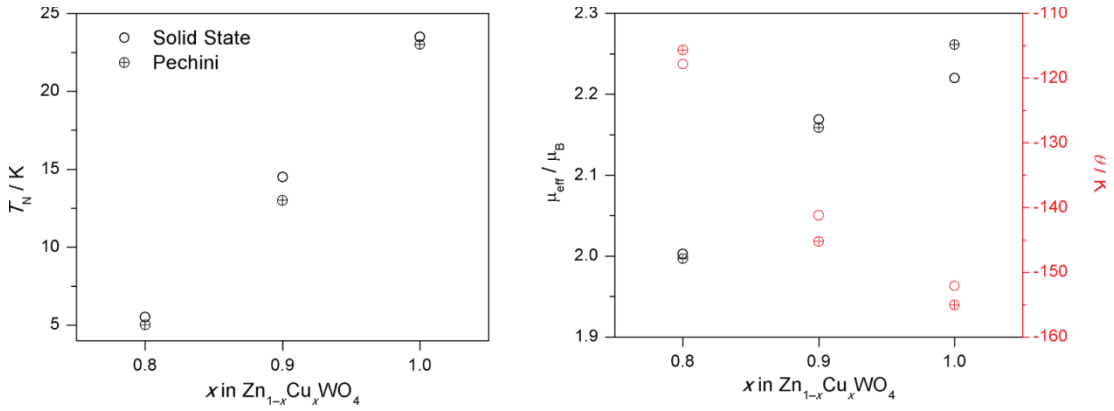

Figure D.8 Left: The Néel temperature (T_N) for both the solid-state and Pechini synthesized compounds $Zn_{1-x}Cu_xWO_4$ (x = 0.8, 0.9, 1). Right: μeff and Θ for both the solid-state and Pechini synthesized compounds $Zn_{1-x}Cu_xWO_4$ (x = 0.8, 0.9, 1). The empty circles represent the solid-state data and the crossed circles represent the Pechini data.

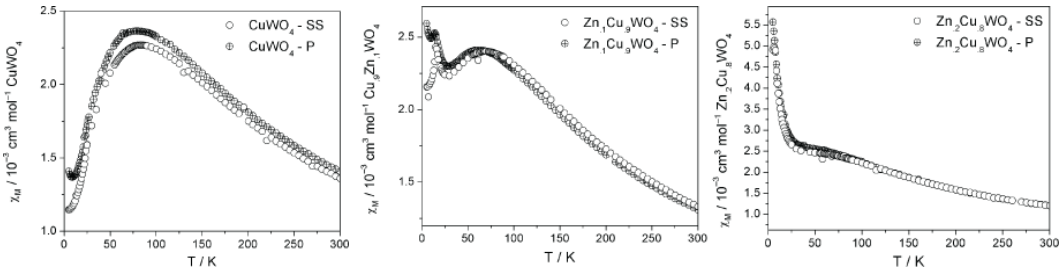

Figure D.9 χM(T) plots for $Zn_{1-x}Cu_xWO_4$ (x = 0.8, 0.9, 1) for the solid state (SS) and Pechini (P) compounds.

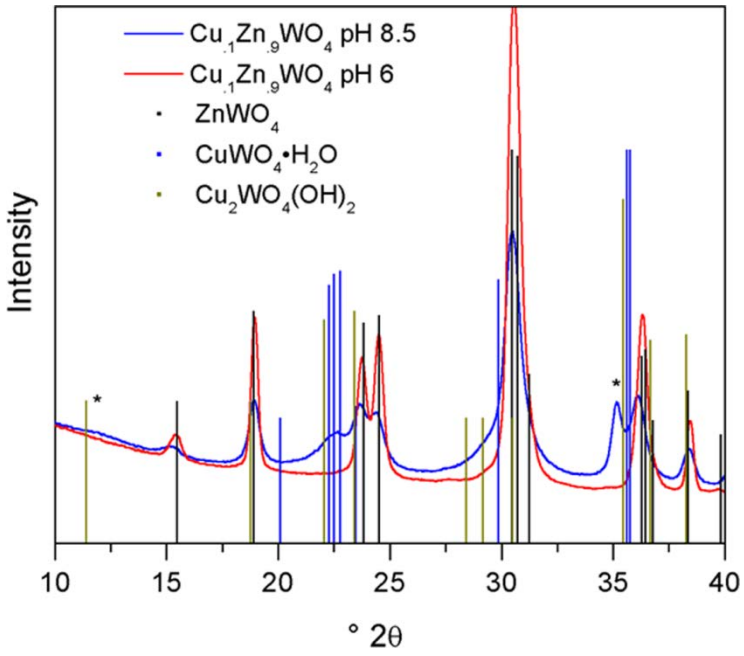

Figure D.10 XRD pattern of $Cu_{0.1}Zn_{0.9}WO_4$ prepared by HTR methods at pH 6 and 8.5 The phases are identified by the Bragg reflections presented from the pdf cards

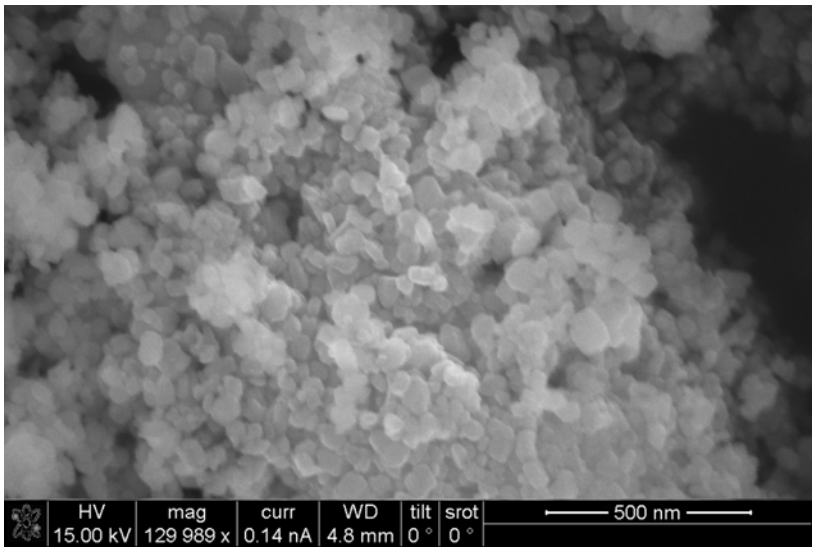

Figure D.11 SEM image of $Cu_{0.1}Cu_{0.9}WO_4$ prepared by HTR methods

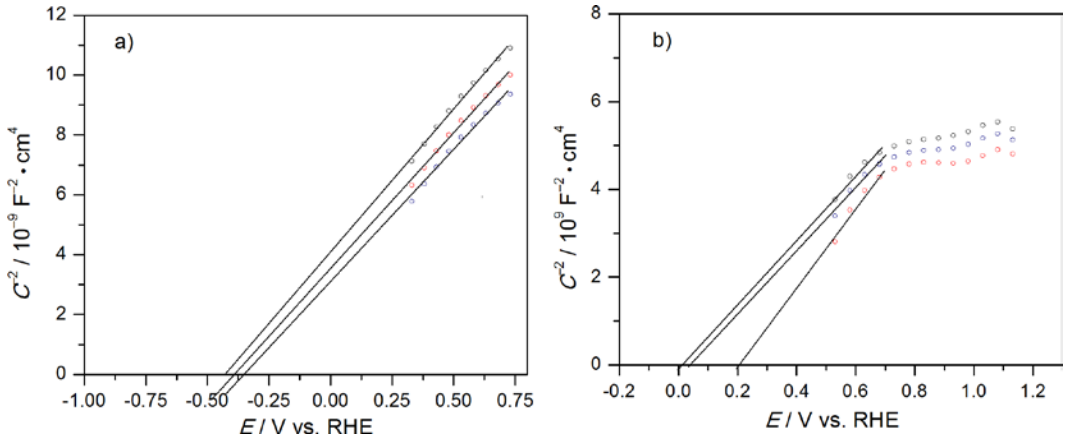

Figure D.12 Mott-Schottky plots of a) $ZnWO_4$ and b) $Zn_{0.5}Cu_{0.5}WO_4$

APPENDIX E

SUPPORTING DATA FOR CHAPTER 6

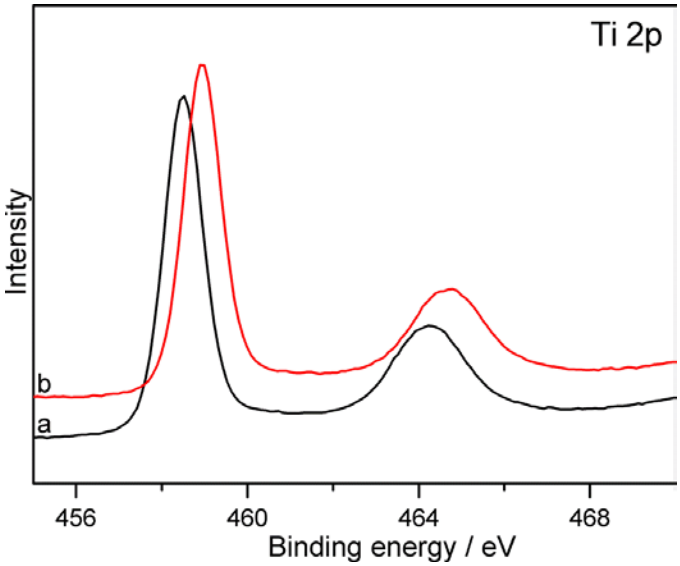

Figure E.1 Ti 2p XPS pattern of (a) TiO_2-B and (b) TiO_2-B/RGO

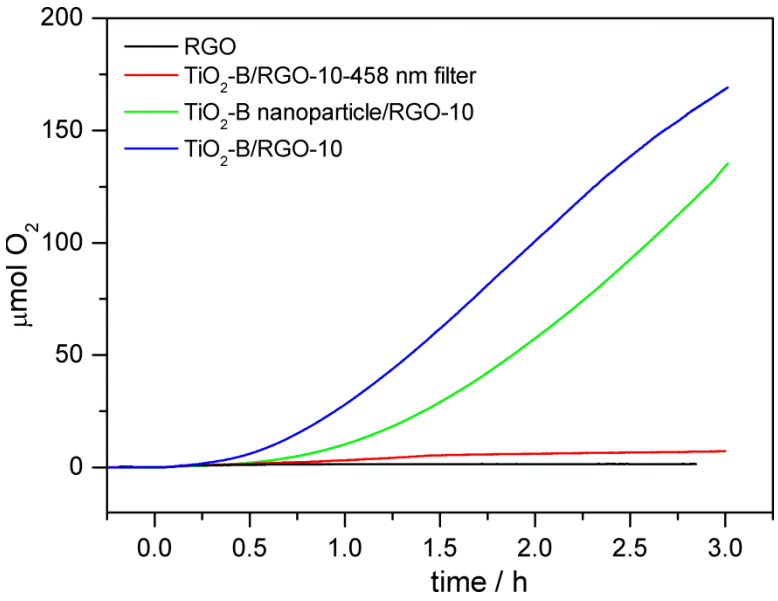

Figure E.2 Photocatalysis experiments comparing TiO_2-B/RGO nanosheets, TiO_2-B/RGO nanoparticles, RGO, and TiO_2-B/RGO nanosheets with a UV cutoff filter.

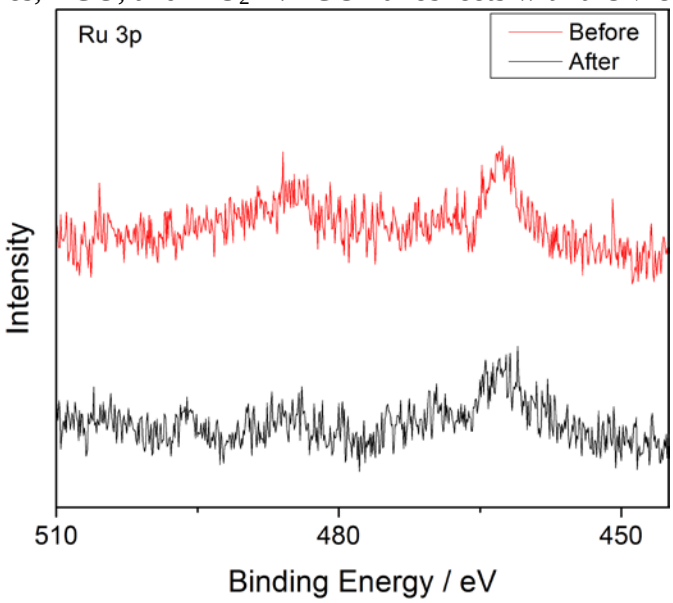

Figure E.3 Ru(3p) XP spectra before (red) and after (black) a photocatalytic water oxidation experiment

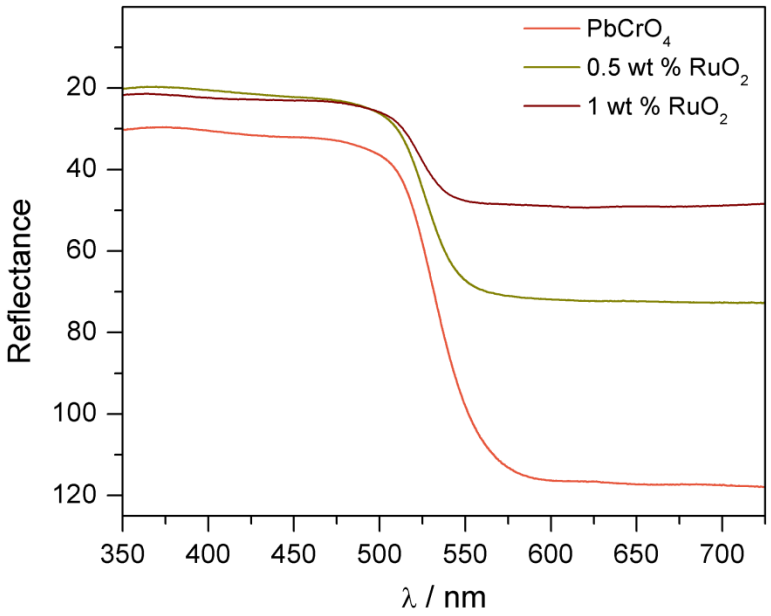

Figure E.4 Absorption Spectrum of $PbCrO_4$ with various loadings of RuO_2

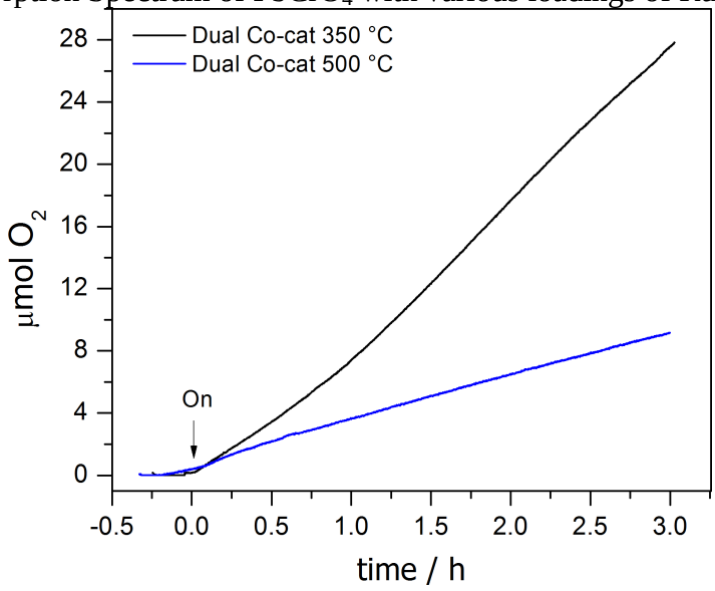

Figure E.5 Rates of O_2 evolution on $PbCrO_4$-0.5Ru-0.5Pt annealed at various temperatures

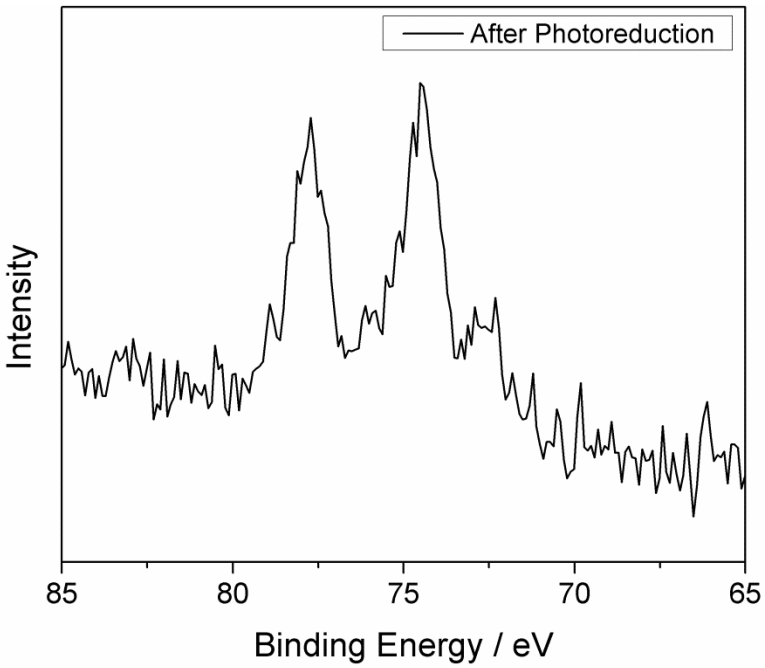

Figure E.6 Pt(4f) peaks in the XPS spectrum after photodeposition experiments by $PbCrO_4$

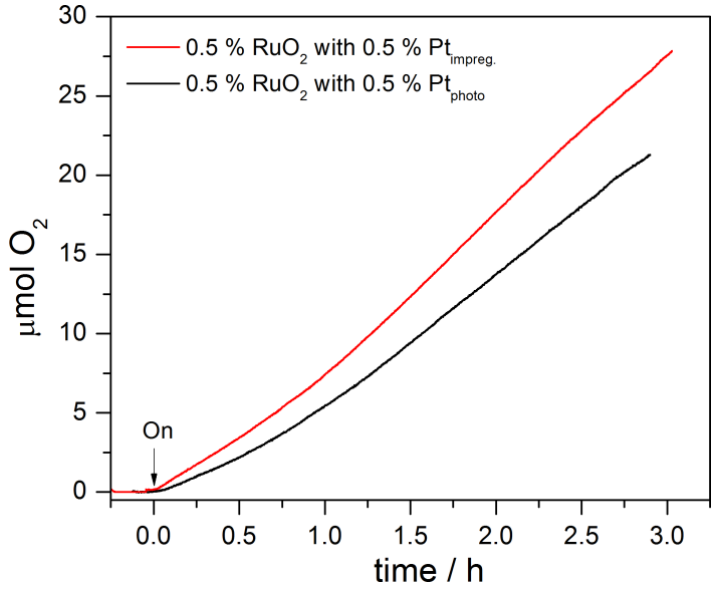

Figure E.7 Rates of O_2 evolution comparing $PbCrO_4$-0.5Ru with Pt deposited by various methods